School of Chemical and Petroleum Engineering

Fuels and Energy Technology Institute

Development of Novel Mesoporous Proton Exchange Membranes for Fuel Cells

Jin Zhang

This thesis is presented for the Degree of
Doctor of Philosophy
of
Curtin University

April 2016

Declaration

To the best of my knowledge and belief this thesis contains no material previously published by any other person except where due acknowledgement has been made.

This thesis contains no material which has been accepted for the award of any other degree or diploma in any university.

Signature:……

Date:……

Abstract

Proton exchange membrane fuel cells (PEMFCs) have attracted great attentions due to their high efficiency, environmental friendliness and fast start-up/shut-down for the portable electronic devices and vehicle applications. And the proton exchange membrane (PEM) is one of the critical components in PEMFCs. Nafion membrane is the state-of-the-art PEMs because of its high proton conductivity in fully hydrated state, good mechanical property, chemical stability and structural integrity. However, the high dependence of the proton mobility in Nafion membrane on high relative humidity (RH) makes the operation of fuel cells based on Nafion membranes highly relied on external humidification, which not only complicates the water management but also increases the cost.

There are two strategies to reduce and even diminish the dependence of PEMs on external humidification. The first one is to modify the Nafion membrane and achieve high water retention and proton conductivity at low relative humidity and even anhydrous conditions. And the other strategy is to employ high temperature proton conductors, such as phosphoric acid (PA), instead of hydrated water molecules, and develop alternative PEMs with high operation temperatures (100 – 200 ^{o}C). Polybenzimidazole (PBI) composite membrane is one of the most promising polymers that are able to operate at elevated temperatures with high thermal and chemical stability as well as high proton conductivity. However, the complex synthesis procedures impede the wild application of PBI in PEMFCs. Besides, the PA/PBI composite membrane suffers from severe PA leaching at high temperatures up to 190 ^{o}C, leading to a sharply drop of the proton conductivity and fuel cell performance at high temperatures.

Herein, following the first strategy, mesoporous structures were introduced into the Nafion membrane via a soft template method with the assistance of the silica colloidal mediator. Highly ordered mesoporous Nafion membranes were fabricated with different structure symmetries including 2D hexagonal, 3D face-centred, 3D cubic-bicontinuous and 3D body-centred. The Nafion electrolyte membranes derived from the self-assembly of mesoporous Nafion-silica pairs. After the removal of the structure directing agent and silica colloidal templates, highly ordered mesoporous structural Nafion ionomers were obtained. The proton conductivity of the

mesoporous Nafion membranes showed high independence upon the external humidity. And Nafion membrane with the 2D hexagonal structure showed the best performance among the four samples with an exceptional stability at anhydrous conditions.

For the second strategy, inorganic-organic nanostructured hybrid membranes of polyethersulfone (PES)-polyvinylpyrrolidone (PVP) were prepared. The PES-PVP composite membrane was employed as the PEM matrix rather than polybenzimidazole. That is due to the simple preparation method for the PES-PVP membranes. Silica materials including amino-functionalized mesoporous silica (NH_2-*meso*-silica) spheres, hollow mesoporous silica (HMS) spheres and amino-functionalized hollow mesoporous silica (NH_2-HMS) spheres were incorporated into the PES-PVP membranes. All the inorganic-organic composite membranes showed the superior proton conductivity and cell performance than that of the pristine PES-PVP membrane. That is due to the facilitated proton transportation in the ordered mesoporous channels via the hydrogen bonds between the $–NH_2$ groups and H_3PO_4. The highest peak power density at 180 ^oC was 480 mW cm^{-2} for the composite membrane based on NH_2-HMS, which is 92.7 % higher than that of the PA-doped PES-PVP membrane at the identical condition.

Nevertheless, there are three disadvantages for NH_2-HMS in the application of PES-PVP membranes, including complex synthesis procedures, low proton conductivity and limited operation temperature ($\leq$ 180 ^oC). A novel method was developed to simplify the synthesis method of NH_2-HMS. Different from the reported approaches, NH_2-HMS in the present study was transformed from NH_2-*meso*-silica/CTAB induced by a Na_2CO_3 solution. During the transformation, the interior parts of the NH_2-*meso*-silica/CTAB hybrid particles were removed by the enriched OH^- ions in the mesoporous channels, while the shell of the particles was remained intact. Besides the novelty and simplicity, the novel method also reveals a new self-etching mechanism for the functionalization of mesoporous silica.

Moreover, in order to improve the proton conductivity of NH_2-HMS in PES-PVP membranes, a solid proton conductor, phosphotungstic acid (PWA), was incorporated into the mesopores of NH_2-HMS nanoparticles (PWA-NH_2-HMS). The PWA in the mesopores of NH_2-HMS facilitated the proton transportation, and consequently enhanced the proton conductivity and performance of the PES-PVP composite membrane cells. The best performance was obtained on a PES-PVP

polymer membrane with an optimum loading of 10 wt.% PWA-NH_2-HMS.

Finally, PES-PVP matrix was replaced by PBI for the fuel cell application at higher temperatures than 180 ^oC, resulting from the high glass transition temperature and thermal stability of PBI. Efforts were conducted to improve the stability of PA/PBI composite membranes at elevated high temperature of 200 ^oC by modifying the PBI membrane with inorganic fillers. Phosphotungstic acid functionalized mesoporous silica (PWA-*meso*-silica) was incorporated into the PA/PBI membrane and exceptional performance durability up to 2700 h was achieved (27 $\mu V\ h^{-1}$) at 200 ^oC. The exceptional durability for the composite membrane is due to the *in situ* formation of phosphosilicate in the PA/PBI composite membranes with mesoporous silica filler, and the high stability of the Pt catalyst in the electrode, especially in the cathode. The successful demonstration of PWA-*meso*-silica-PA/PBI membrane based fuel cells at 200 ^oC represents a significant milestone in the development of the PA/PBI based high temperature fuel cells.

In addition to the project on the mesoporous membranes for PEMFCs, work has also been carried on the synthesis and development of novel Pd electrocatalyst on carbon nanotubes (CNTs) with different number of inner tubes or walls. The number of walls or inner tubes has a significant promotion effect on the activity of supported Pd nanoparticles for alcohol oxidation reactions of direct alcohol fuel cells. A facile charge transfer mechanism via electron tunnelling between the outer wall and inner tubes of CNTs under the electrochemical driving force is proposed for the significant promotion effect of CNTs for the alcohol oxidation reactions in alkaline solutions. However, the work on electrocatalyst of fuel cells is not included in this thesis in order to keep the focus of the thesis on mesoporous PEMs. Nevertheless, the details of the work in this part can be found in paper published in journals, ***Chemical Communications***, 2014, 50(89), 13732-13734 and ***Chemsuschem***, 2015, 8(17), 2956-2966.

Acknowledgements

I would like to sincerely thank to my supervisor, Prof. San Ping Jiang, who supported me throughout the whole PhD project with great patience and expertise. I made great progress in scientific research under his guidance. He gave me huge amount of help and opportunities for the developing of my academic career. Besides, I want to thank to the director of our institute, Prof. Chun-zhu Li for supplying us excellent research facilities. I also want to thank to Ms. Angelina Rossiter and Mrs. Tasneem Dawood for supporting me in safety and administrative issues.

I would like to thanks our current and previous group members for their friendship and help (in no particular order): Dr.Yi Cheng, Dr. Lichao Jia, Dr. Kongfa Chen, Dr. Na Ai, Dr. Ling Zhao, Dr. Beibei He, Dr. Weiyong Yuan, Dr. Bo Wei, Dr. Shikui Yao, Dr. Jian Pan, Ms Chengcheng Wang, Ms Meng Li, Ms Yiming Zhong, Mr. Shuai He, and Mr. Haohua Kuang.

Thanks to Dr. Jian Liu in Curtin University, Australia for the discussion about the synthesis of mesoporous silica materials. Also thanks for the discussion with Prof. Shanfu Lu and Prof.Yan Xiang in Beihang University, China, Dr.David Alili and Prof.Qingfeng Li in Techincal University of Denmark, Denmark and Dr.Haijin Zhu and Prof.Maria Foryth in Deakin University, Australia.

This work is financially supported by Australian Research Council *Discovery Project funding scheme* (project number: DP120102325, DP150102025, DP150102044 and DP120204932), the National Natural Science Foundation of China (61274135, 51272200), Program for New Century Excellent Talents in University (NCET-12-0911) and the Fundamental Research Funds for the Central Universities (WUT: 2013-IV-037, 2013-II-011). And also thanks the assistance on STEM provide by Dr. Martin Sunders in University of Western Australia.

The authors acknowledge the facilities, and the scientific and technical assistance of the National Imaging Facility at the Centre for Microscopy, Characterization& Analysis, the University of Western Australia, a facility funded by the University, State, and Commonwealth Government as well as the facilities, scientific and technical assistance of the Curtin University Microscopy & Microanalysis Facility, which is partially funded by the University, State and Commonwealth Governments. The synchrotron SAXS was carried out on the SAXS beamline at the Australian Synchrotron, Victoria, Australia.

Finally, I would like to thank my parents and young sister for being such as huge support through my experiences. I couldn’t have made it without you all. Love you.

List of Publications

Journals

1. Alili D., **Zhang J.**, Mark T. D. J., Zhu H.J., Yang T.Y., Liu J., Forsyth M., Pan C., Jensen J. O., Cleemann L. N., Jiang S. P. and Li Q.F. Exceptional durability enhancement of PA/PBI based polymer electrolyte membrane fuel cells for high temperature operation at 200 ^{o}C. Journal of Materials Chemistry A, 2016, **4**, 4019-4024.(Alili D. and Zhang J. contribute equally).
2. Yuan, W.Y., **Zhang, J**., Shen, P.K., Li, C.M., Jiang, S.P., Self-assembled CeO_2 on Carbon Nanotubes Supported Au Nanoclusters as Superior Electrocatalysts for Glycerol Oxidation Reaction of Fuel Cells, Electrochimica Acta, 2016, 190, 817-828.
3. Wei, J., Liang, Y., Hu, Y.X., Kong, B., Simon, G.P., **Zhang, J.,** Jiang, S.P., Wang, H.T., A versatile Iron-Tannin-Framework Ink Coating Strategy to Fabricate Biomass-Derived Iron Carbide/Fe-N-Carbon Catalysts for Efficient Oxygen Reduction, Angewandte Chemie International Edition, 2016, 55, 1355-1359.
4. **Zhang, J**.; Lu, S.; Xiang, Y.; Shen, P. K.; Liu, J.; Jiang, S. P., Carbon-Nanotubes- Supported Pd Nanoparticles for Alcohol Oxidations in Fuel Cells: Effect of Number of Nanotube Walls on Activity. Chemsuschem 2015, 8(17), 2956-2966.
5. Cheng, Y.; **Zhang, J**.; Jiang, S. P., Are metal-free pristine carbon nanotubes electrocatalytically active? Chemical Communications 2015, 51(72), 13764-13767.
6. Wei J.; Hu Y.X.; Liang Y.; Kong B.; **Zhang J**.; Song J.C.; Bao Q.L.; Simon G.P.; Jiang S.P.; Huang T.W.; Nitrogen doped nanoporous carbon/graphene nano-sandwiches: synthesis and application for efficient oxygen reduction. Advanced Functional Materials, 2015, 25(36), 5768-5777.
7. Wei J.; Liang Y.; Zhang X.Y.; Simon G.P.; Zhao D.Y.; **Zhang J**.; Jiang S.P.; Wang H.T.; Controllable synthesis of mesoporous carbon nanospheres and Fe-N/Carbon nanospheres as efficient oxygen reduction electrocatalysts. Nanoscale 2015, 7(14), 6247-6254.

8. **Zhang, J**.; Li, J.; Tang, H.; Pan, M.; Jiang, S. P., Comprehensive strategy to design highly ordered mesoporous Nafion membranes for fuel cells under low humidity conditions. Journal of Materials Chemistry A 2014, 2(48), 20578-20587.
9. **Zhang, J.;** Cheng, Y.; Lu, S.; Jia, L.; Shen, P. K.; Jiang, S. P., Significant promotion effect of carbon nanotubes on the electrocatalytic activity of supported Pd NPs for ethanol oxidation reaction of fuel cells: the role of inner tubes. Chemical Communications 2014, 50(89), 13732-13734.
10. Lu, S.; Xu, X.; **Zhang, J**.; Peng, S.; Liang, D.; Wang, H.; Xiang, Y., A Self-Anchored Phosphotungstic Acid Hybrid Proton Exchange Membrane Achieved via One-Step Synthesis. Advanced Energy Materials 2014, 4, 1400842.
11. Peng, S.; Lu, S.; **Zhang, J**.; Sui, P.-C.; Xiang, Y., Evaluating the interfacial reaction kinetics of the bipolar membrane interface in the bipolar membrane fuel cell. Physical Chemistry Chemical Physics 2013, 15(27), 11217-11220.
12. Lan, F.; Wang, D.; Lu, S**.; Zhang, J**.; Liang, D.; Peng, S.; Liu, Y.; Xiang, Y., Ultra-low loading Pt decorated coral-like Pd nanochain networks with enhanced activity and stability towards formic acid electrooxidation. Journal of Materials Chemistry A 2013, 1(5), 1548- 1552.

Book Chapters

1. **Zhang, J.,** Jiang S.P., Mesoporous materials for fuel cells, 2016, Springer publication.
2. **Zhang, J.,** Jiang S.P., Self-assembly in fuel cells, Comprehensive supramolecular chemistry II, 2016, Elsevier publication.

Table of Contents

Declaration i

Abstract ii

Acknowledgements v

List of Publications vii

Table of Contents ix

List of Figures xiii

List of Tables xxi

List of Abbreviations xxii

Chapter 1 ..... ***1***

1.1 Background 1

1.2 Objectives and outline of the thesis 2

Chapter 2 Literature review ***5***

2.1 Introduction 5

2.2 Mesoporous block copolymer based PEMs 6

2.3 Functionalized mesoporous silica based PEMs 9

2.3.1 Sulfonated mesoporous silica fillers for Nafion membranes 9

2.3.2 Sulfonated mesoporous silica for alternative PEMs 13

2.3.3 Sulfonation of mesoporous silica 16

2.3.4 Pore structure and acidity of mesoporous silica 19

2.4 High temperature proton conductors for PEMs 21

2.4.1 Imidazole 22

2.4.2 Triazole 23

2.4.3 Protic ionic liquids 24

2.4.4 Phosphoric acid 25

2.4.5 Alternative mesoporous materials for PEM 27

2.5 Conclusions 29

Chapter 3 Comprehensive strategy to design highly ordered mesoporous Nafion membranes for fuel cells under low humidity conditions ***36***

3.1 Introduction 36

3.2 Experimental 38

3.2.1 Materials 38

3.2.2 Synthesis of Nafion membranes with different structure symmetries 38
3.2.3 Characterization 39
3.2.4 Cell preparation and electrochemical characterization 40
3.3 Results and discussion 41
3.3.1 Formation and characterizations of ordered mesoporous Nafion membranes 41
3.3.2 Fuel cell performance of mesoporous Nafion membranes 48
3.4 Conclusions 52
Chapter 4 Amino-functionalized mesoporous silica based polyethersulfone-polyvinylpyrrolidone composite membrane for elevated temperature fuel cells ***56***
4.1 Introduction 56
4.2 Experimental 58
4.2.1 Mesoporous silica fabrication 58
4.2.2 Amino-functionalization of mesoporous silica 59
4.2.3 PES-PVP composite membranes 59
4.2.4 Characterizations 59
4.3 Results and discussion 60
4.3.1 Formation of amino-functionalized mesoporous silica materials 60
4.3.2 Properties of amino-functionalized mesoporous silica based PES-PVP composite membranes 64
4.3.3 Proton conductivity and cell performance of PES-PVP composite membranes 69
4.4 Conclusions 73
Chapter 5 Facile synthesis of amino-functionalized hollow mesoporous silica with oriented mesoporous channels ***77***
5.1 Introduction 77
5.2 Experiment section 78
5.2.1 NH_2-HMS synthesis procedures 78
5.2.2 Characterizations 79
5.3 Results and discussions 79
5.3.1 Synthesis of NH_2-HMS 79
5.3.2 Factors for the synthesis of NH_2-HMS 83
5.3.3 Formation mechanism 97
5.4 Conclusions 101

Chapter 6 Phosphotungstic acid impregnated amino-functionalized hollow mesoporous silica particles for the elevated temperature fuel cells application ***.....104***
6.1 Introduction 104
6.2 Experimental section 106
6.2.1 HPW-NH_2-HMS preparation 106
6.2.2 Membrane preparation 106
6.2.3 Characterizations 106
6.3 Results and discussion 106
6.3.1 Morphology and structure 106
6.3.2 Thermal stability 110
6.3.3 ATR-FTIR 111
6.3.4 PA uptake, volume swelling and mechanical stability 112
6.3.5 Proton conductivity 115
6.3.6 Cell performance 117
6.4 Conclusions 119
Chapter 7 Phosphotungstic acid impregnated mesoporous silica for polybenzimidazole based polymer electrolyte membrane fuel cells at 200 ^oC ***122***
7.1 Introduction 122
7.2 Experimental 123
7.2.1 Membrane preparation 123
7.2.2 PWA-meso-SiO_2 and composite Membrane characterization 124
7.2.3 Proton conductivity and fuel cell tests 125
7.3 Results 125
7.3.1 Morphology of the inorganic particles and membranes 125
7.3.2 PA uptake and mechanical properties 127
7.3.3 Proton conductivity 129
7.3.4 Durability 131
7.4 Discussion 133
7.4.1 Effects of the proton exchange membrane 133
7.4.2 Effects of the catalysts 137
7.5 Conclusions 139
Chapter 8 Conclusions and Recommendations for future work ***143***
8.1 Conclusions and achievements 143
8.2 Recommendations for future work 144

Appendix 146

List of Figures

Figure 2.1 Scheme of the MEA for a proton exchange membrane fuel cell. 5

Figure 2.2 TEM images of vapor annealing samples: (a) sPS-PMMA, SI_20 (LAM); (b) sPS-PMMA, S2_17 (HEX); (c) sPS-PMMA S2_35 (HPL); (d) PS-PMMA, lamellar structure and (e) the normalized proton conductivity σ/Ø as a function of sulfonation degree. Ø refers to the volume fraction of the PS + sPS + water domains.[17].....8

Figure 2.3 TEM images of (a) solid SiO_2; (b) core-shell SiO_2; (c) hollow mesoporous silica (HMS); (d) sulfonic acid functionalized HMS. (e) is the schematic for the water reservoir of functionalized HMS in Nafion composite membrane [39, 40]. 11

Figure 2.4 The proton conductivity of native and modified *meso*-silica in Nafion membranes under 100 % RH, 60 ^{o}C [41].....13

Figure 2.5 Proton conductivity of sPEEK65/OSPN/SMBS composite membranes at different relative humidity (100 °C).[57] 15

Figure 2.6 Co-condensation and post synthesis for the functionalization of mesoporous silica materials. 16

Figure 2.7 Interactions of (A) water and hydroxyl species and (B) grafted PFSA and triflic acid with ^{29}Si and ^{27}Al moieties.(C) proton conductivities against temperature (50 % RH) and (D) triflic acid concentrations at ambient condition (20 ^{o}C, ~40 % RH).[72] 18

Figure 2.8 Water uptake (a) of sulfonic acid functionalized mesoporous silica films at 25 ^{o}C against RH values. Water sorption at high (b) and low (c) acid density at low RH and proton channel formation.[75].....20

Figure 2.9 Three types of imidazole groups grafted on mesoporous silica surface (A) N-imi-MCM-41, (B) imi-MCM-41 and (C) pep-imi-MCM-41.[80].....22

Figure 2.10 (A) The proton conductivity of composite membranes against temperature under anhydrous condition (PBI/PA membrane from [107]). (B) Single cell performance of PA/meso-silica membrane based fuel cell in H_2/O_2 at 190 ^{o}C. [104].....26

Figure 3.1 SAXS spectra of (A) mesoporous Nafion-silica composites with 2D-H, 3D-FC, 3D-CB and 3D-BC mesoporous structures after removal of the structure directing agents, and (B) corresponding mesoporous Nafion

membranes after removal of silica. The SAXS pattern of pristine Nafion 112 membrane is shown in B. 41

Figure 3.2 TEM morphologies of mesoporous Nafion with (A) 2D hexagonal (2D-H, *P6mm*) in the [110] direction, (B) 3D body-centred (3D-BC, $Im\bar{3}m$) in the [111] direction, (C) 3D face-centred (3D-FC, $Fm\bar{3}m$) in the [100] direction, (D) 3D cubic-bicontinuous (3D-CB, $Ia\bar{3}d$) mesoporous structure in the [311] direction and (E) the pristine Nafion membrane.[F] TGA profiles of mesoporous Nafion membranes with different space symmetries and the pristine Nafion membrane as the control group is shown in (F). 42

Figure 3.3 Nitrogen sorption isotherms and pore size distributions of mesoporous Nafion membranes with different structure symmetries. 43

Figure 3.4 (A) Time-resolved synchrotron SAXS diffractograms and (B) 100 s and 3000s SAXS curves of the silica colloid-mediated synthesis of 2D hexagonal mesoporous Nafion-silica composite (10 wt.% Nafion) in P123 + HCl + Nafion ionomers + TEOS solution without stirring.....45

Figure 3.5 Schematic of surfactant-directed and soft template method with the assistance of silica colloidal mediator for the formation of mesoporous Nafion (2D-H structured Nafion was selected as a representative). The transformation from random micelles to an ordered hexagonal structure phase in solution occurs at ~ 600 s.....46

Figure 3.6 Synchrotron SAXS profiles of 2D hexagonal Nafion-silica powders with Nafion ratio of 10 %, 50 % and 70 %, measured at room temperature...47

Figure 3.7 Polarization and power output of cells, measured at 60 ^{o}C, H_2/O_2 with (a) 2D-H Nafion membrane, (b) 3D-CB Nafion membrane, (c) 3D-FC Nafion membrane, (d) 3D-BC Nafion membrane, (e) Nafion 112 membrane. Peak power density of mesoporous Nafion membranes against various relative humidity at 60 ^{o}C is given in (f).....49

Figure 3.8 (A) Plots of cell voltages measured under different RH levels for 2D-H Nafion and Nafion 112 membrane based fuel cells. (B) and (C) are the enlarged portion of the voltage curves of the cell under 60 % RH and 0 % RH, respectively. The cells were tested at 60 ^{o}C in H_2/O_2 under a

constant discharge current density of 100 mA cm^{-2}. 51
Figure 4.1 TEM images of (A, B) HMS, (C, D) NH_2-HMS and (E, F) NH_2-*meso*-silica. 61
Figure 4.2 (A) N_2 adsorption isotherms, (B) pore size distributions and (C) SAXS profiles of mesoporous silica and amino-functionalized mesoporous silica materials. 62
Figure 4.3 (A) ^{13}C CP/MAS and (B) ^{29}Si MAS NMR of NH_2-HMS and (C) ATR-FTIR spectra of mesoporous silica and amino-functionalized mesoporous silica. 63
Figure 4.4 Cross-sectional SEM images of the PES-PVP composite membranes with (A) pristine PES-PVP, (B) PES-PVP-H, (C) PES-PVP-NS and (D) PES-PVP-NH. Insets are cross-section images of the composite membranes in large scale. 65
Figure 4.5 ATR-FTIR profiles of (A) PES-PVP composite membranes and (B) PA-doped PES-PVP composite membranes with different silica materials. .66
Figure 4.6 TGA profiles of the PES-PVP composite membranes with different types of silica fillers. Inset is the image of derivation weight as a function of temperatures. 68
Figure 4.7 (A) Proton conductivity and (B) activation energy for proton transportation of PA-doped based PES-PVP composite membranes under anhydrous conditions. 69
Figure 4.8 Single cell performance of PA-doped silica/PES-PVP composite membranes for (A) PA/PES-PVP, (B) PA/PES-PVP-H, (C) PA/PES-PVP-NS, and (D) PA/PES-PVP-NH. (E) is the comparison of the cell performance at 180 ^oC and (F) is the peak power density as a function of temperature. 71
Figure 4.9 The scheme for the formation and proton transportation of mesoporous silica based PES-PVP composite membranes.(Take PA/PES-PVP-NH as example.) 72
Figure 5.1 TEM images of NH_2-*meso*-silica (A and B) and NH_2-HMS spheres (C, and D) fabricated via co-condensation method with 8 mmol L^{-1} CTAB and 10 % molar ratio APTES. Etching condition: 0.2 M Na_2CO_3, 60 ^oC 2h. 79
Figure 5.2 (A) SAXS profiles and (B) N_2 isotherms of NH_2-*meso*-silica and NH_2-

HMS particles. Synthesis condition: 8 mmol L^{-1} CTAB and 10 % molar ratio APTES. Etching condition: 0.2 M Na_2CO_3, 60 ^oC, 2h. 80

Figure 5.3 (A) ^{13}C CP/MAS, (B) ^{29}Si MAS NMR spectra and (C) ATR-FTIR spectra of NH_2-*meso*-silica (a) and NH_2-HMS(b). Synthesis condition: 8 mmol L^{-1} CTAB and 10 % molar ratio APTES. Etching condition: 0.2 M Na_2CO_3, 60 ^oC, 2h. 82

Figure 5.4 (A) TGA profiles of NH_2-*meso*-silica/CTAB and NH_2-*meso*-silica spheres. (B) The TEM image of NH_2-*meso*-silica. TEM images of (C) NH_2-*meso*-silica and (D) NH_2-*meso*-silica/CTAB etched at 0.2 M Na_2CO_3 at 60 ^oC for 10 h. The molar ratio of APTES is 10 %. 83

Figure 5.5 TEM images of NH_2-*meso*-silica/CTAB synthesised by the CTAB concentration of (A) 4 mmol L^{-1}, (C) 8 mmol L^{-1}, (E) 12 mmol L^{-1} and (G) 16 mmol L^{-1}. (B), (D), (F) and (H) are the TEM images for the corresponding samples etched at 0.2 M Na_2CO_3, 60 ^oC for 2h. The molar ratio of APTES is 10 %. 84

Figure 5.6 SAXS profiles of NH_2-*meso*-silica/CTAB spheres before (red line) and after etching (black line) against CTAB concentration. Etching condition: 0.2 M Na_2CO_3, 60 ^oC for 2h. The molar ratio of APTES is 10 %.....85

Figure 5.7 Effects of molar ratios of APTES for the synthesis of the NH_2-*meso*-silica/CTAB spheres before (red line) and after etching (black line) at 0.2 M Na_2CO_3, 60 ^oC for 2h. 86

Figure 5.8 TEM images of the NH_2-*meso*-silica/CTAB spheres etched at various Na_2CO_3 concentrations at 60 ^oC for 2h (A) 0.1 M, (B) 0.2 M (C), 0.3 M (D) 0.4 M. (E) and (F) are the shell/core ratio and the SAXS profile of NH_2-HMS/CTAB against the concentration of Na_2CO_3, respectively. ...87

Figure 5.9 Solid state ^{29}Si MAS NMR spectra of NH_2-HMS obtained from different concentrations of etching agent at 60 ^oC for 2h. 88

Figure 5.10 (A) N_2 adsorption isotherms and (B) pore size distributions of NH_2-HMS etched from different concentrations of the Na_2CO_3 solution. 90

Figure 5.11 TGA profiles of the NH_2-HMS obtained from different concentration of etching agents. 91

Figure 5.12 Particle size distributions of NH_2-*meso*-silica/CTAB after 0.3 M Na_2CO_3 etching under different time. (A) 0 min, (B) 60 min, (C) 120 min and (D) 2-20 h. (D) also includes the shell/diameter ratio of the particles.

The Insets are corresponding TEM images of the particles in difference etching time. 92

Figure 5.13 Scheme of the time-resolved synchrotron SAXS characterization.[26] 93

Figure 5.14 (A) *In situ* time-resolved synchrotron SAXS for the formation of the NH_2-*meso*-silica/CTAB material. SAXS curves comparison of the NH_2-*meso*-silica/CTAB material against the time in (B) the (100) plane and (C) the (110) and (200) planes. The inset in (B) is the peak position *vs.* time. 94

Figure 5.15 (A) *In situ* time-resolved synchrotron SAXS for NH_2-*meso*-silica/CTAB etching process under 0.1 M Na_2CO_3 at 60 ^oC, (B) TEM image of the particle in A at t = 130 min. (C) *In situ* time-resolved synchrotron SAXS for NH_2-*meso*-silica/CTAB etching process under 0.3 M Na_2CO_3 at 60 ^oC, and (D) TEM image of the particle in C at t = 130 min. Black line in A and C shows the lowest peak intensity during the etching process. 95

Figure 5. 16 The peak position and intensity of the NH_2-*meso*-silica/CTAB particles against etching time in (A) 0.1 M Na_2CO_3, and (C) 0.3 M Na_2CO_3. The particle size comparison before and after the etching treatment under (B) 0.1 M Na_2CO_3, and (D) 0.3 M Na_2CO_3 96

Figure 5. 17 The scheme for the cross-sectional image of a NH_2-*meso*-silica/CTAB particles; B, the particle of NH_2-*meso*-silica/CTAB after the OH^- ions exchange via CTAB molecules; C, the enlarged tubes for the mesopores in the NH_2-*meso*-silica/CTAB particles. 99

Figure 5.18 Proposed mechanism for the formation of NH_2-*meso*-silica/CTAB nanoparticles. 100

Figure 6.1 (A), (B) and (C) Bright field TEM images, and (D) HAADF STEM images of a PWA-NH_2-HMS particle. (E), (F) and (G) are the Si, O, and W element mapping for a PWA-NH_2-HMS particle, respectively. 107

Figure 6.2 (A) SAXS profiles and (B) BET characterizations of NH_2-HMS particles impregnated by HPW. 108

Figure 6.3 Cross section SEM images of the PES-PVP composite membranes with various PWA-NH_2-HMS loading (A) pristine PES-PVP, (B) 5 wt.%, (C) 10 wt.%, and (D) 15 wt.%. Inset images are the picture of the corresponding membranes at large scales. 109

Figure 6.4 TGA profiles of the PWA-NH_2-HMS based PES-PVP composite

membrane (A) weight and (B) derivation weight as a function of temperature. 110

Figure 6.5 ATR-FTIR profiles of the PES-PVP composite membranes with different inorganic fillers.(A) pristine PES-PVP; (B) PES-PVP with PWA; (C) pristine PWA; (D) PA-PES-PVP; and (E) PA-PES-PVP with PWA-NH_2-HMS. 111

Figure 6.6 The PA uptake and volume swelling for the PES-PVP composite membranes with various loading of PWA-NH_2-HMS filler. 112

Figure 6. 7 (A) Selection of stress-strain curves for the composite membranes with PWA-NH_2-HMS loading of 0 – 15 wt.% after PA doping and (B) the corresponding elastic modulus for each membrane. The standard deviations are indicated by the error bars. 114

Figure 6.8 (A) Proton conductivity and (B) activation energy for proton transportation in PA-doped PES-PVP composite membranes. (a) ● 10 % PWA-NH_2-HMS; (b) ■ 5 % PWA-NH_2-HMS; (c) ▲ 15% PWA-NH_2-HMS; (d) ♦ 10 % NH_2-HMS; (e) ▼ pristine PES-PVP composite membrane. 116

Figure 6.9 Single cell performance of PA-doped PES-PVP composite membranes with (A) pristine PES-PVP; (B) 5 % PWA-NH_2-HMS; (C) 10 % PWA-NH_2-HMS; (D) 15 % PWA-NH_2-HMS; (E) 10 % NH_2-HMS pristine and (F) peak power density conclusion of PES-PVP based composite membranes. 117

Figure 6.10 Durability test of PES-PVP based composite membranes with different loading of PWA-NH_2-HMS filler in the range of 0 to 15 wt.%. Both H_2 and O_2 have flow rate of 100 mL min^{-1}, 0 % RH, 90 ^oC, while the fuel cell was tested at 200 ^oC. 118

Figure 7.1 Chemical structure of the poly[2,2′-m-(phenylene)-5,5′-bibenzimidazole] (*m*PBI) repeat unit and dequalinium chloride hydrate modifier. 124

Figure 7.2 (A) Bright field TEM, (B) HAADF STEM image and corresponding (C) Si and (D) W element mapping for the PWA-*meso*-SiO_2; (E) large scale HAADF STEM image for PWA-*meso*-SiO_2; (F) SAXS patterns and (G) N_2 adsorption isotherm of *meso*-SiO_2 and PWA-*meso*-SiO_2 126

Figure 7.3 Cross sectional SEM images of (A) PBI, and PBI membranes with (B) 5 wt.%, (C) 10 wt.% and (D) 15 wt.% PWA-*meso*-silica. 127

Figure 7.4 Tensile strength of PBI composite membranes with different PWA-*meso*-silica loading before (A1 and A2) and after (B1 and B2) PA-doping. ..128

Figure 7.5 *In situ* proton conductivity PA-doped membranes with PWA-*meso*-SiO_2 loadings ranging from 0 – 40 wt.%; (B) ^1H chemical shift of *meso*-SiO_2 and (C) Proton diffusion coefficient in PA-*meso*-SiO_2 and PA-PWA-*meso*-SiO_2 at different temperatures. 129

Figure 7.6 (A) Long-term stability tests of corresponding fuel cell operated at 200 mA cm^{-2} and 200 °C; (B) Variation of the *in situ* membrane conductivity and (C) open circuit voltage with time. 131

Figure 7.7 (A) Polarization curves and (B) power output curves for fuel cells based on the composites with PWA-*meso*-SiO_2 loadings of 0, 5 and 15 wt.%. 133

Figure 7.8 TEM images of (A) the PWA-*meso*-silica/PBI composite membrane, and (B) the composite membrane after 2700 h fuel cell test. (C) and (D) are the SEM images of the PWA-*meso*-silica/PBI composite membrane before and after the 2700 h fuel cell test, respectively, while (E) and (F) are the corresponding EDS for the selected area in (C) and (D). The loading for the filler is 15 wt.%.....134

Figure 7.9 SAXS profiles of a PA-doped PWA-*meso*-silica/PBI composite membranes before and after 2700 h fuel cell test. The loading for the inorganic filler is 15 wt.%. 135

Figure 7.10 XRD profiles of various PA/PBI composite membranes with 0, 5 and 15 wt.% PWA-*meso*-SiO_2 after durability test. 136

Figure 7.11 Scheme of proton conduction paths through the attached and stabilized PA and PWA anchored inside the mesoporous channels of *meso*-silica at high temperatures. 136

Figure 7.12 (A) XRD patterns of the Pt catalyst after the durability operation with a current load of 200 mA cm^{-2} at 200 ^oC. a, 15 % PBI, anode; b, 15% PBI, cathode; c, 5 % PBI, anode; d, 5% PBI, cathode; e, PBI, anode; f, PBI, cathode. (B) The particle size of Pt catalysts derived from the XRD pattern by the Scherrer equation.....138

Figure 7.13 TEM images of Pt catalysts after over 2700 h operation with a current load of 200 mA cm^{-2} at 200 ^oC. A, the pristine PBI, anode; B, the pristine PBI, cathode. C, 5 wt.% PBI, anode; D, 5 wt.% PBI, cathode; E, 15 wt.%

PBI, anode; F, 15wt.% PBI, cathode. 139

List of Tables

Table 2.1 Proton conductivities of Nafion based hybrid membrane with different fillers, and functional groups. 13

Table 2.2 The properties of mesoporous materials for proton exchange membranes. 28

Table 3.1 Peak position q, d spacing and lattice parameter a for the mesoporous Nafion-silica and mesoporous Nafion membranes. 43

Table 3.2 BET surface area S_{BET}, pore diameter d_{pore}, wall thickness d_{wall} and hydrogen crossover current density j, the proton conductivity σ of diverse mesoporous Nafion and pristine Nafion. 44

Table 4.1 Physical properties of mesoporous silica and amino-functionalized mesoporous silica materials. 63

Table 4. 2 Peaks of PES-PVP membranes with different fillers. 67

Table 4.3 Volume swelling, acid doping of the blend composite membranes and proton conductivity of PA-doped PES-PVP composite membranes under anhydrous condition at different temperatures. 68

Table 5.1 Physical properties for the mesoporous NH_2-*meso*-silica/CTAB spheres with various CTAB concentrations in terms of particle size and d spacing before and after etching process. d_1 before etching process, and d_2 after etching process. 85

Table 5.2 Contents of amine groups and Si groups analysed from NMR results. 89

Table 5.3 Physical properties of NH_2-*meso*-silica sphere after etching by Na_2CO_3 with different concentrations. 90

Table 6.1 Physical properties of NH_2-HMS and PWA-NH_2-HMS with 40 wt.% PWA loading. 109

Table 6.2 Properties of the PES-PVP composite membranes with various loading of PWA-NH_2-HMS filler. NH_2-HMS was employed as the control group. 112

Table 7.1 Phosphoric acid uptake and volume swelling after doping in 85 wt.% H_3PO_4 at room temperature for at least 2 weeks. 128

List of Abbreviations

APTES	3-Thiopropyltrimethoxysilane
AST	Accelerated stress test
ATMP	Amino tris(methylene phosphonic acid)
BCPs	Block copolymers
BMIm-BF4	1-Butyl-3-methylimidazolium tetrafluoroborate
BMIm-TFSI	1-Butyl-3-methylimidazolium bis(trifluoromethane sulfone) imide
BTCA	Benzotriazole-5-carboxylic acid
CIM	Conventional impregnation method
CMETCS	2-(Carbomethoxy)ethyltrichloro silane
CSPTMS	2-(4-Chlorosulfonylphenyl)ethyltrimethoxysilane
DEPTES	Diethylphosphatoethyltriethoxy silane
DFT	Density functional theory
EIm-TfO	N-Ethylimidazolium Trifluoromethanesulfonate
EISA	Evaporation-induced self-assembly
FSAS	1,2,2-Trifluoro-2-hydroxy-1-trifluoromethyl-ethanesulfonic acid sultone
HEX	Hexagonally packed cylinders
HMS	Hollow mesoporous silica
HPL	Hexagonally perforated lamellae
HPAs	Heteropolyacids
IEC	Ion exchange capacity
IPN	Interpenetrating polymer network
KU	Keggin unit
LAM	Lamellae
MEA	Membrane-electrode-assembly
MPTMS	Mercaptopropyltrimethoxy silane
MSA	Methane sulphuric acid
OSPN	Organosiloxane network
PA	Phosphoric acid
PAC	Proton acceptance capacity
PBI	Polybenzimidazole
PEM	Proton exchange membrane

PEMFC	proton exchange membrane fuel cell
PESf	Polyethersulfone
PETMS	Phenethytrimethoxy silane
PFS	Poly(4-fluorostyrene)
PFSA	Perfluorosulfonic acid
PILs	Protic ionic liquids
PMMA	Poly(methyl methacrylate)
PMO	Periodic mesoporous organic silica
PS-*b*-sPHS	Poly(styrene-block-sulfonated hydrostyrene
PSS-PMB	Poly(styrenesulfonate-methylbutylene)
PTES	Phenyltriethoxysilane
PVP	Polyvinylpyrrolidone
PWA	Phosphotungstic acid
RH	Relative humidity
SAN	Poly(styrene-co-acrylonitrile)
SAXS	Small angle x-ray scattering
SDAs	Structural directing agents
SPEEK	Sulfonated poly(ether ether keton)
sPHS	Sulfonated polyhydroxystyrene
SMBS	Sulfonated cube mesoporous benzene-silica
SPI	Sulfonated polyimide
sPPO	Sulfonated poly(2,6-dimethyl-1,4-phenylene oxide)
SPPSU	Sulfonated poly(phenylsulfone)
sPS-PMMA	Sulfonated polystyrene-poly(methyl methacrylate)

Chapter 1

1.1 Background

Fuel cells are energy conversion devices that directly transfer the chemical energy of the fuels such as hydrogen and alcohols etc. into electricity. They show high efficiency, low pollution, environmental friendliness, quite operation and flexible modulability in comparison with the conventional internal combustion engine. Fuel cells, therefore, are considered as one of the most promising power generation devices.[1] Fuel cells are divided into low temperature fuel cells such as proton exchange membrane fuel cells (PEMFCs) and high temperature (500-1000^{o}C) solid oxide fuel cells (SOFCs) according to the operation temperature. Among various types of fuel cells, the proton exchange membrane fuel cell is considered to be the leading power source because of its low operation temperature and fast start-up and shut down cycle. It is a versatile device with various applications ranging from portable electronic devices, transportation vehicles to power stations.

The critical component of PEMFCs is a membrane electrode assembly (MEA). It consists of a proton exchange membrane (PEM) and the electrocatalytic electrodes including the anode and cathode. The development of PEMs is essential for PEMFCs. PEMs not only show essential function for proton transport, but also function as separator to prevent the fuel and oxidant from mixing. High proton conductivity and chemical and thermal stability, therefore, are the critical criteria for PEMs.[2] Perfluorosulfonic acid (PFSA) membranes such as Nafion are the state-of-the-art PEMs with high chemical and thermal stability as well as outstanding proton conductivity at full hydration condition. However, the proton conductivity of Nafion is sensitive to the hydration of the membrane, and external humidification is required for the stable operation of Nafion membrane based fuel cells to maintain the full hydration of the Nafion membrane.[3] The external humidification system not only complicates the water management but also increases the cost. Herein, improving the proton conductivity of PEMs at low hydration is the most critical challenge for PEMFCs.

Porosity is singular in PEMs in terms of transportation of mass to reactive sites. Mesoporous materials with well-defined and ordered pore arrays in the range of 2 – 50 nm in diameter [4, 5], show unique properties of capillary condensation effect [6].

Thus, mesoporous materials can store and release water at low relative humidity (RH) [7]. When the mesoporous structure is introduced in the PEMs, it could facilitate water-assisted proton transportation at low RH and high temperatures. Moreover, high surface area and highly ordered mesoporous channels of mesoporous materials not only increase the utilization of catalysts, but also facilitate the mass transfer in the electrode.

In this regard, the aim of this project is to develop alternative PEMs with high proton conductivity at low RH and high temperatures by introducing mesoporous structures in PEMs, and by developing alternative PEMs based on amino or heteropolyacid functionalized mesoporous silica/polymer like polyethersulfone (PES)-polyvinylpyrrolidone (PVP) or phosphoric acid (PA)/polybenzimidazole (PBI) composite. The overall objective is to develop high temperature PEMs with high proton conductivity and low RH dependence or anhydrous conditions for elevated high temperature applications.

1.2 Objectives and outline of the thesis

Based on the above mentioned objectives, this thesis has 8 chapters. Chapter 2 focuses on the literature review of the state-of-the-art in the field. The experiment results and discussion are presented in chapter 3-7. In Chapter 8, conclusions are made and the suggestions for future work are proposed.

Chapter1 Introduction

The chapter briefly introduced the challenges of proton exchange membranes and the advantages of incorporating mesoporous structures in PEMs. Then the objectives and the outline of the thesis were presented.

Chapter 2 Literature Review

This chapter started with a brief introduction of PEMFCs, followed by a detailed description and discussion of the advances in the synthesis and applications of the mesoporous structured materials in PEMFCs, including mesoporous polymer membranes and mesoporous inorganic-organic hybrid membranes.

Chapter 3 Comprehensive strategy to design highly ordered mesoporous Nafion membranes for fuel cells (*This chapter is based on the paper published on* ***Journal of Materials Chemistry A)***

Highly ordered mesoporous Nafion membranes were developed with different

structure symmetries including 2D hexagonal, 3D face-centred, 3D cubic-bicontinuous and 3D body-centred. The membranes were synthesized via a soft template method with the assistance of the silica colloidal mediator. Mesoporous Nafion membranes showed the high proton conductivity at low RH and fuel cell stability even at anhydrous conditions.

Chapter4 Amino-functionalized mesoporous silica based polyethersulfone-polyvinylpyrrolidone composite membrane for elevated temperature fuel cells

Inorganic-organic nanostructured hybrid membranes of PES-PVP were prepared with mesoporous silica materials. After the addition of mesoporous silica and amino-functionalized mesoporous silica into the matrix of PA-doped PES-PVP composite membranes, the proton conductivity and cell performance of the composite membranes were significantly increased.

Chapter 5 Facile synthesis of amino-functionalized hollow mesoporous silica with oriented mesoporous channels

A novel method was revealed to synthesize amino-functionalized hollow mesoporous silica (NH_2-HMS). Different from the research in the literature, NH_2-HMS was transformed from amino-factionalized mesoporous silica spheres via the enrichment of OH^- induced by the cationic surfactant. This novel method not only simplifies the procedures for the fabrication of NH_2-HMS, but also suggests a new self-etching mechanism for the functionalization of mesoporous silica materials.

Chapter 6 Phosphotungstic acid impregnated amino-functionalized hollow mesoporous silica particles for the elevated temperature fuel cells application

Novel proton exchange membranes based on phosphotungstic acid (PWA) impregnated amino-functionalized hollow mesoporous silica were fabricated for elevated temperature fuel cells. PWA and the mesopores of NH_2-HMS facilitated the proton transportation in the membrane, resulting in the improved proton conductivity and cell performance for the polymer host of PES and PVP.

Chapter 7 Phosphotungstic acid impregnated mesoporous silica for polybenzimidazole based polymer electrolyte membrane fuel cells at 200 ^oC(*This chapter is based on the paper published on* ***Journal of Materials Chemistry A)***

Phosphotungstic acid functionalized mesoporous silica particles were incorporated into PA/PBI membranes and exceptional durability up to 2700 h was achieved at 200 ^oC. Such enhancement is most likely due to the *in situ* formation of phosphosilicate and the high stability of the Pt/C catalyst.

Chapter 8 Conclusions and recommendations for future work

The overall achievements of this thesis were summarized and the recommendations for future studies were listed in this chapter.

References

[1] S.P. Jiang, P.K. Shen, Nanostructured and Advanced Materials for Fuel Cells, CRC Press, London, 2013.

[2] M.A. Hickner, H. Ghassemi, Y.S. Kim, B.R. Einsla, J.E. McGrath, Alternative Polymer Systems for Proton Exchange Membranes (PEMs), Chemical Reviews 104 (10) (2004) 4587-4612.

[3] K.A. Mauritz, R.B. Moore, State of Understanding of Nafion, Chemical Reviews 104 (10) (2004) 4535-4586.

[4] J.S. Beck, J.C. Vartuli, W.J. Roth, M.E. Leonowicz, C.T. Kresge, K.D. Schmitt, C.T.W. Chu, D.H. Olson, E.W. Sheppard, A new family of mesoporous molecular sieves prepared with liquid crystal templates, Journal of the American Chemical Society 114 (27) (1992) 10834-10843.

[5] C.T. Kresge, M.E. Leonowicz, W.J. Roth, J.C. Vartuli, J.S. Beck, Ordered mesoporous molecular sieves synthesized by a liquid-crystal template mechanism, Nature 359 (6397) (1992) 710-712.

[6] Y. Wan, Zhao, On the Controllable Soft-Templating Approach to Mesoporous Silicates, Chemical Reviews 107 (7) (2007) 2821-2860.

[7] Y. Ye, C. Jo, I. Jeong, J. Lee, Functional mesoporous materials for energy applications: solar cells, fuel cells, and batteries, Nanoscale 5 (11) (2013) 4584-4605.

Chapter 2 Literature review

2.1 Introduction

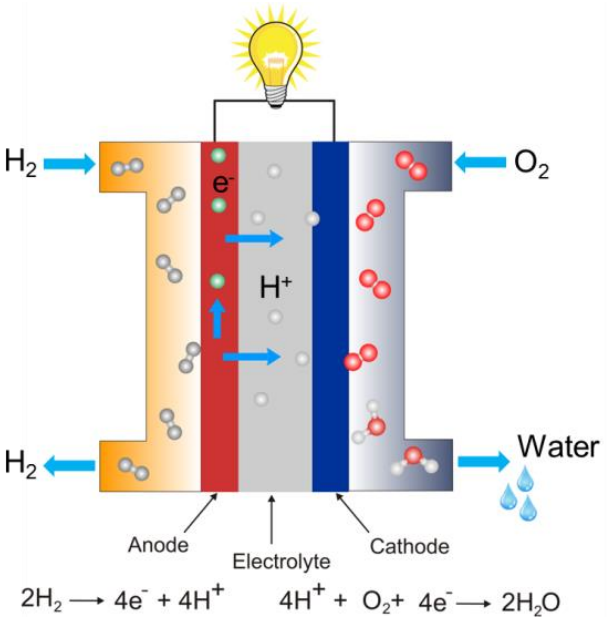

Figure 2.1 Scheme of the MEA for a proton exchange membrane fuel cell.

Proton exchange membrane fuel cell shows superiorities of low operation temperatures and fast start-up and shut-down cycles in comparison with other types of fuel cells. It is, therefore, considered to be one of the most promising power sources for applications ranging from portable electronic devices, transportation vehicles to power stations. Figure 2.1 shows the operation principle of a PEMFC. The critical component of the PEMFC is the membrane electrode assembly composed of a proton exchange membrane sandwiched between the electrocatalytic anode and cathode. In the case of H_2 fuel, H_2 is oxidized at the anode and the proton is transported to the cathode through the PEM. The electrons produced flow to the cathode through an external load, reducing ambient oxygen to water.

A PEM has the essential functions as a proton transporter as well as a separator to prevent the mixing between fuels and oxidants. Perfluorosulfonic acid membranes such as Nafion are the state-of-the-art PEMs with high chemical stability and outstanding proton conductivity at hydrous conditions. The high proton conductivity of Nafion results from microphase separation derived from the unique skeleton of hydrophobic C–F backbone grafted with hydrophilic $–SO_3H$ side chains. However, the proton conductivity of Nafion is extremely dependent on the hydration of the

membrane, which requires a high level of relative humidity for the stable operation of Nafion membrane based fuel cells. It not only complicates the water management but also increases the cost. Herein, the development of PEMs with high proton conductivity at elevated temperatures or/and low humidity is one of the most critical challenges for PEMFCs.

In fuel cells, porosity is a singular attribute, which controls not only the transportation of fuels/oxidants to reactive sites but also the length or area of the three phase boundary or the electrode/electrolyte interface where the electrochemical reaction occurs. Mesoporous materials, characterized by well-defined and ordered pore arrays in the range of 2 – 50 nm in diameter, were first reported by the scientists in Mobil on the MCM-41S series of mesoporous silica materials [1, 2]. Mesoporous materials show unique properties including high hydrophilicity because of the –OH groups arranged on the highly ordered *meso*-channels and the capillary condensation effect of the mesopores [3]. Thus, mesoporous materials can store and release water at elevated temperatures [4]. When the mesoporous structure is introduced in the PEMs, it can facilitate water-assisted proton transportation at high temperatures and low RH. Therefore, mesoporous materials, as a kind of versatile materials, have been extensively used in PEMFCs to reduce the RH dependence of PEMs, simplify the water management system, and reduce the cost of fuel cells.

In this chapter, the emphasis will be put on the progress in the development of various types of mesoporous materials including mesoporous organic polymers and mesoporous organic/inorganic materials for low temperature and elevated temperature PEMFCs. The structure-activity relationship of the mesoporous materials based PEMs and their cell performance will be discussed.

2.2 Mesoporous block copolymer based PEMs

Mesoporous sulfonated block copolymers (BCPs) have been widely investigated as potential PEMs because of their well-ordered nanostructures with precisely controlled structure and morphology [5-8]. Generally, sulfonated block copolymer molecules have long C-C backbones grafted by $–SO_3H$ terminated side chains. The side chains not only improve the movement of the $–SO_3H$ groups, but also block the methanol crossover of the membranes. Moreover, the thermodynamic incompatibility between the hydrophilic chains and the hydrophobic chains

maximizes the contact between similar blocks, while minimizes the contact among dissimilar blocks [9, 10]. Thus, mesoporous structures are achieved in block copolymers by the microphase separation of hydrophilic and hydrophobic segments. For instance, when hydrophilic sulfonated polyhydroxystyrene (sPHS) was grafted onto the backbone of polystyrene to form poly(styrene-*block*-sulfonated hydrostyrene) (PS-*b*-sPHS), the membrane with ordered proton conductive channels possessed higher proton conductivities than sulfonated polystyrene-*block*-poly(ethylene-*ran*-butylene)-*block*-polystyrene (sSEBS) membranes with random proton channels[11]. Moreover, when the sulfonated poly(2,6-dimethyl-1,4-phenylene oxide) (sPPO) was grafted by hydrophobic poly(4-fluorostyrene) (PFS) side chains, well-ordered mesoporous structure with cylindrical *meso*-channels were formed for the proton transportation[12].

Molecular weight and temperature affect the mesoporous structure of block copolymers. Lamellae (LAM) morphology is discovered in the low molecular weight copolymer of poly(styrenesulfonate-methylbutylene) (PSS-PMB), while mesoporous structures, such as hexagonally perforated lamellae (HPL) and hexagonally packed cylinders (HEX), are found for the high molecular weight copolymer [13]. The effect of molecular weight on the morphology of the block copolymers is consistent with the self-consistent field theory for the phase behaviour of copolymers [14]. Moreover, the low molecular weight copolymer of PSS-PMB shows phase transitions from HPL to LAM when the temperature is changed. On the other hand, high molecular weight copolymers constantly express the mesoporous structure against the temperature [15].

The proton conductivity of the PSS-PMB membranes under low RH depends strongly on the size of the mesopores. The vapour pressure of water confined in *meso*-channels, p_W^{vap}, is given by Kelvin and Young-Laplace equation[16]:

$$\ln\left(\frac{p_{\mathrm{w}}^{\mathrm{vap}}}{p_{\mathrm{w,o}}^{\mathrm{vap}}}\right) = -\frac{2aV_{\mathrm{w}}\gamma\cos\theta}{wRT} \qquad (2.1)$$

where $p_{\mathrm{w,o}}^{\mathrm{vap}}$, γ and V_{w} are the normal vapor pressure, the surface tension and the molar volume of water, respectively. R is the ideal-gas constant and T is the absolute temperature. θ is the contact angle between water and the pore surface, while w is the pore size (diameter of cylindrical pores and width of lamellar pores). The value of a is 1 for lamellae, and 2 for cylinders. Given that the pores in PSS-PMB membrane are perfectly wetting, that is, $\theta = 0$, calculation indicates that a rapid

decrease of the pressure within the hydrophilic pores occurs when the pore size is close to 5 nm; that is, when the width of hydrophilic ionic channels is lower than 5nm, the membrane tends to retain water at low RH and elevated temperatures [13]. Besides the pore size, the proton conductivity of block copolymer membranes is also dominated by the morphology of the membrane. For instance, sulfonated polyestyrene-poly(methyl methacrylate) (sPS-PMMA) self-assembled into LAM (Figure 2.2 A), HEX (Figure 2.2 B), and HPL (Figure 2.2 C) morphologies, while the pristine PS-PMMA formed a lamellar structure (Figure 2.2 D). The proton conductivity of sPS-PMMA diblock copolymers followed the trend of ISO<HEX<HPL<LAM, when the proton conductivity of the copolymers was normalized by the volume fraction of the conductive domains, as shown in Figure 2.2 E [17]. This is due to the fact that the lamellar phase possesses a larger swelling and greater water uptake than the other morphologies, leading to the high efficiency in proton diffusion from $-SO_3H$.

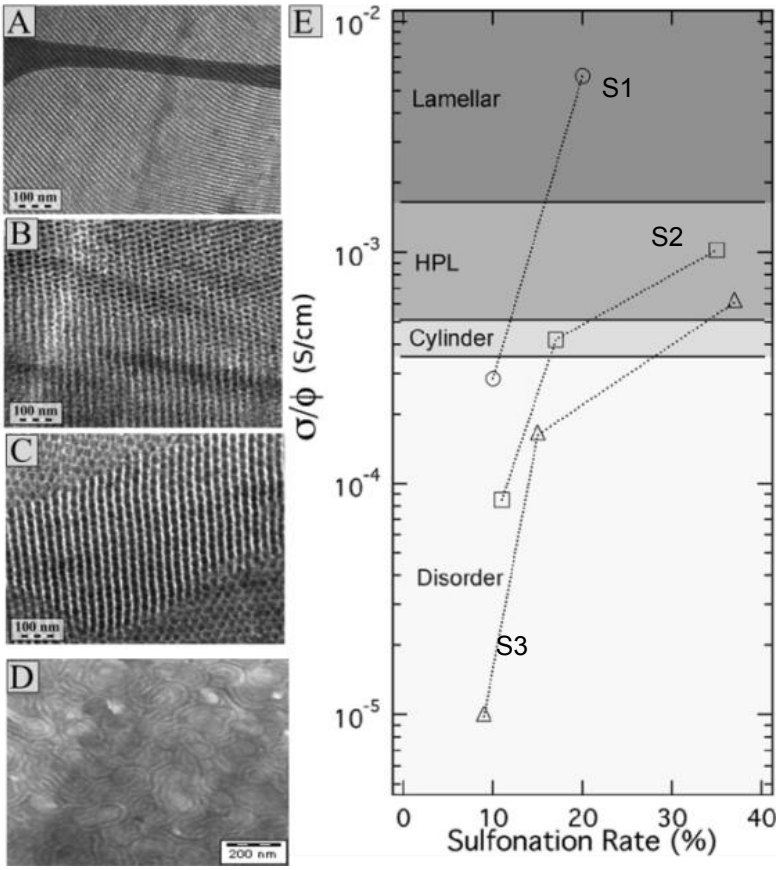

Figure 2.2 TEM images of vapor annealing samples: (a) sPS-PMMA, SI_20 (LAM); (b) sPS-PMMA, S2_17 (HEX); (c) sPS-PMMA S2_35 (HPL); (d) PS-PMMA, lamellar structure and (e) the normalized proton conductivity σ/Ø as a function of sulfonation degree. Ø refers to the volume fraction of the PS + sPS + water domains.[17]

2.3 Functionalized mesoporous silica based PEMs

Mesoporous inorganic materials possess desirable properties including the large surface area, chemical inertness and mechanically stable framework. These materials have been extensively studied as potential PEM candidates. Mesoporous materials can be embedded in polymeric membranes to form the organic/inorganic composite PEMs. The addition of mesoporous materials enhances the water uptake of polyelectrolyte membranes and increases their proton conductivity as well as the cell performance at high temperatures and low RH [18]. Moreover, the functionalized mesoporous materials form effective proton conducting paths through their highly ordered channels, which also improve the proton conductivity of the polyelectrolyte membranes. Mesoporous silica is one of the commonly investigated mesoporous materials with highly ordered mesopores and high thermal stability [19]. Pure mesoporous silica shows negligible proton conductivity. For instance, the conductivity of a mesoporous silica film was lower than 10^{-5} S cm^{-1} at 90 % RH,[20] which is too low to be used in PEMs. However, when the mesoporous silica materials were functionalized by proton carriers or conductors, the proton conductivity of the materials was significantly increased [21, 22]. Thus, functionalization is essential to enhance the proton conductivity of the inorganic mesoporous materials or fillers for the potential application as PEMs in fuel cells.

2.3.1 Sulfonated mesoporous silica fillers for Nafion membranes

Because of the high surface area, mesoporous silica contains a large number of OH groups, which is a promising property for water adsorption. Thus, the introduction of hexagonal mesoporous silica MCM-41 into a Nafion membrane improves its thermal stability and enhances its water retention [23]. However, the *meso*-silica/Nafion composite membrane generally shows lower proton conductivity than the pristine Nafion membrane, as the conductivity of the mesoporous silica filler is much lower than that of the Nafion membrane. The decrease in conductivity becomes more severe as the content of the silica fillers increases.

In order to improve the proton conductivity of *meso*-silica/Nafion composite membranes while maintain the high water uptake, mesoporous silica can be functionalized by proton conducting groups or proton carriers prior to being introduced into the polymer matrix [24]. For instance, the proton conductivity of a

composite membrane filled with sulfonated mesoporous silica (SMPS) was 50 times higher than that of the composite membrane with pristine mesoporous silica [25]. This is also confirmed by the result that the proton conductivity was increased by over one order of magnitude at 40 % RH, 80 ^{o}C when 1 wt.% of sulfonated mesoporous organosilicate was added into the PA/PBI membrane [26]. That is attributed to the fact that the $–SO_3H$ groups in SMPS create efficient proton diffusion channels by the hydrogen bond network in the interior surface of the mesopores of *meso*-silica.

There are two types of proton diffusion mechanisms, namely, vehicle [27] and Grotthuss mechanisms [28]. For vehicle mechanism, protons are diffused with the aid of water molecules. In Nafion membranes, proton diffusion in the highly hydrated state is primarily assumed as the vehicle mechanism. For the Grotthuss mechanism, protons transfer by hopping from one site to the neighbouring site by the hydrogen bond construction and reorientation of the water molecules. When the RH decreases from 98 % to 80 %, the activation energy of Nafion membrane calculated in the range of 20 to 95 ^{o}C doubles from 9.1 to 18.2 kJ mol^{-1}, which is in the range of characteristic of the Grotthuss mechanism (14 - 40 kJ mol^{-1}) [29]. This is due to the fact that when RH decreases, the number of hydrated proton carriers is also reduced. Consequently, the Grotthuss mechanism will be a preferential pathway for proton transportation with minimum hydration water molecules. On the other hand, sulfonated mesoporous silica has a high propensity to retain water and inhibits the volatility of water in the Nafion membrane at high temperatures and low RH. And then the composite membrane shows low dependence of the proton conductivity on hydration. The proton activation energy of the composite membrane only slightly increases from 7.1 to 7.6 kJ mol^{-1} when the RH decreases from 98 to 80%. Therefore, proton diffusion in the sulfonated mesoporous silica based composite membranes is most likely to occur via the vehicle mechanism even at critical conditions.

Besides mesoporous silica, hollow silica can also be incorporated into proton exchange membranes as a *micro*-water reservoir [30], resulting in the improved water uptake of the composite membranes. Moreover, by combining the water reservoir of hollow materials and the periodic proton diffusion paths of mesopores, hollow mesoporous silica (HMS) has been developed as a superior proton conductive filler under high temperatures and low RH [31]. Hollow mesoporous sili-

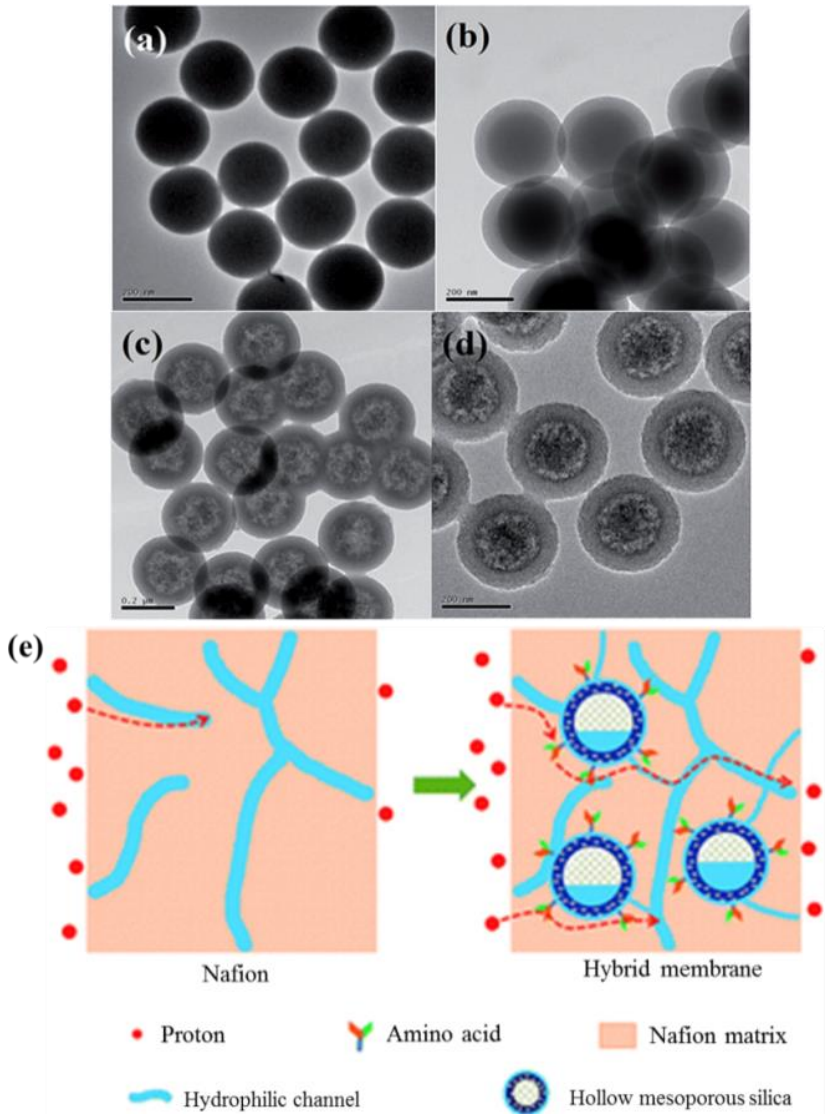

Figure 2.3 TEM images of (a) solid SiO_2; (b) core-shell SiO_2; (c) hollow mesoporous silica (HMS); (d) sulfonic acid functionalized HMS. (e) is the schematic for the water reservoir of functionalized HMS in Nafion composite membrane [39, 40].

ca is synthesized via two protocols: the template method and the self-templating etching method. Hard templates including SiO_2 [32], carbon [33], polystyrene (PS) [34] and soft templates such as emulsion droplets and vesicles are used as the core [35], followed by coverage with a mesoporous silica shell. When the core is etched by HF, NaOH or Na_2CO_3 solutions or calcined at high temperatures, HMS is obtained. Self-templating etching includes surface-protected etching [36, 37] and structural difference-based selective etching [38]. Different from the hard template method, the template, SiO_2 for instance, is dissolved in an alkaline solution and redeposited into HMS via the assistance of surfactant micelles. Jiang et al. synthesized HMS via hard template method (SiO_2 as the template, Figure 2.3 a and

b) and functionalized it by amino acids with sulfonic acid, phosphoric acid and carboxylic acid groups on the surface, as shown in Figure 2.3 d [39]. The acid-based HMS particles were incorporated into the Nafion matrix and the composite membranes possessed a high proton conductivity up to 1.02×10^{-2} S cm^{-1} at 26.1% RH, 80 ^{o}C, which is 11.1 times higher than that of the recast Nafion membrane. However, the water uptake of Nafion/HMS (4.0 wt.%) increased from 19.9 % to 41.2 %, while the swelling ratio slightly raised from 7.42 % to 8.11 %, from 25 ^{o}C to 80 ^{o}C, respectively. That is due to the water reservoir of HMS microspheres with large volume of lumen, leading to the water retention under low RH, as shown in Figure 2.3 e. [40]

The filler content significantly affects the performance of the composite membranes. When 3 wt.% of sulfonated mesoporous silica was embedded into the Nafion membrane, the conductivity of the composite membrane increased from 1.0 to 1.2×10^{-1} S cm^{-1} at 100 % RH, 60 ^{o}C [41]. On the contrary, the proton conductivity of the pristine Nafion membrane decreased to 8.7×10^{-1} S cm^{-2} at the same condition when 3 wt.% pristine mesoporous silica was added [41]. However, when a large amount of sulfonated mesoporous silica (> 10 wt.%) was added into the Nafion matrix, the excessive fillers formed the insulative phase by agglomerations, which hinders the proton transportation in the Nafion matrix (Figure 2.4). Therefore, it is of critical importance to optimize the filler content in the Nafion membrane via improved methods for the synthesis, in order to minimize the detrimental effects. Pereira et al. [29] synthesized perfluorosulfonic acid/mesoporous silica hybrid membranes using evaporation-induced self-assembly (EISA). The silica phase grew in the Nafion matrix in the presence of the surfactant, water, the solvent, and the catalyst. And mesoporous silica nanoparticles with the average size of 50 nm were homogenously dispersed in the Nafion matrix with dense and smooth cross-sectional images even when the filler content increased to 13 wt.%. That is presumably due to the *in situ* growth of the inorganic phase entrapped in the polymeric network and well-dispersed at the submicronic level creating strong interaction with Nafion.

Table 2.1 summarizes the proton conductivities of the inorganic/organic hybrid membranes based on the Nafion matrix.

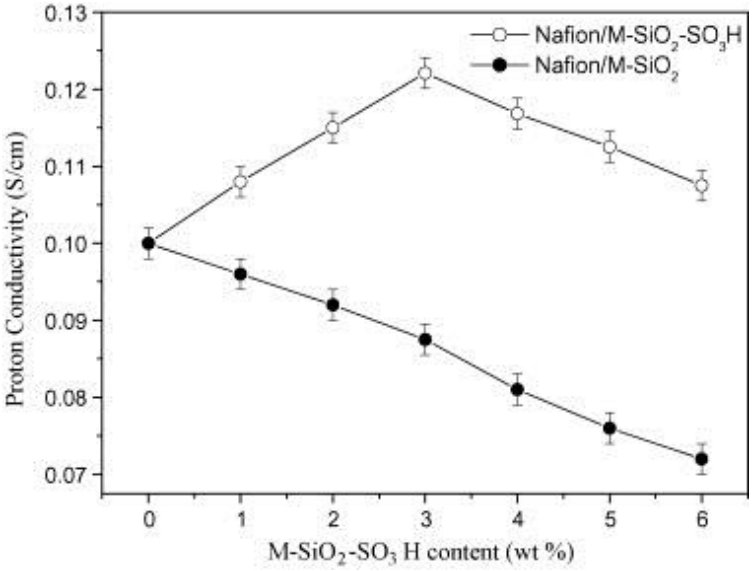

Figure 2.4 The proton conductivity of native and modified *meso*-silica in Nafion membranes under 100 % RH, 60 ^{o}C [41].

Table 2.1 Proton conductivities of Nafion based hybrid membrane with different fillers, and functional groups.

Fillers and content	Function groups	Agents	Conductivity, × 10^{-3} S cm^{-1}	Ref
MCM-41, 3%	–	–	~100 @100 ^{o}C, 80%RH	[23]
Mesoporous silica, 3%	–	–	87@60 ^{o}C, 100% RH	[41]
Mesoporous silica, 3%	-SO_3H	FSAS	108@60 ^{o}C, 100% RH	[41]
Mesoporous silica, 5%	-SO_3H	TPS	94@40 ^{o}C, 95%	[42]
Mesoporous silica, 13%	-SO_3H	CSPTMS	22@RT, 100%	[29]
KIT-6, 2.5%	-SO_3H	FSAS	–	[43]
MCM-41, MCM 48	-SO_3H -PO_3H_2	PETMS MPTMS	–	[44]
Mesoporous silica, 5%	-SO_3H	MPTMS	–	[24]
Al-MCM-41, 0.5%	-SO_3H	H_2SO_4	291@80 ^{o}C,100 %RH	[45]
phenyl-*meso*-silica, 3%	-SO_3H	H_2SO_4	12.9@RT, 100 %RH	[46]
HMS	-SO3H	Cysteine	10.2@80 ^{o}C, 21.6 %	[39]
	-PO_3H_2	Phosphoserine	7.91@80 ^{o}C, 21.6 %	
	-COOH	Aspartic acid	4.85@80 ^{o}C, 21.6 %	

2.3.2 Sulfonated mesoporous silica for alternative PEMs

Although the Nafion membrane is the state-of-the-art proton exchange membrane for

PEMFCs, its fell-scale application is largely limited by factors including high cost, complicated synthesis procedures and being toxic to the environment. Therefore, it is essentially important to develop alternative PEMs with high performance, low cost and simple methods for the synthesis. Sulfonated aromatic polymers such as sulfonated polyimide (SPI), sulfonated polyetheretherketon (SPEEK) and sulfonated poly(phenylsulfone) (SPPSU) are the polymer candidates to replace Nafion in PEMFCs.

Sulfonated polyimide membranes demonstrate excellent thermal and chemical stability, high ion exchange capacity (IEC) as well as the outstanding proton conductivity in hydrated conditions. The effects of mesoporous silica on SPI have been comprehensively investigated by Liu's group in terms of the filler contents and the fabrication methods [47-49]. Similar to the fillers in the Nafion membrane, sulfonated mesoporous silica in SPI indicates the same bell-shape for the proton conductivity against the filler content. Liu et al. indicated that 7.0 wt.% was the optimum filler content for sulfonated mesoporous silica with the particle size of ~ 300 nm and pore size of 2.6 nm in the SPI matrix for the proton conductivity at temperatures ranging from 25 ^{o}C to 80 ^{o}C, 100 % RH [48].

Sulfonated mesoporous silica has two functions for the incorporation in SPI membranes. First, sulfonated mesoporous silica has a high surface area; that is, a large number of Si-OH groups are exposed to water absorption. Second, the embedded sulfonated mesoporous silica limits the mobility of the polymer chains due to the strong interaction between the mesoporous silica particles and the SPI molecules. With the increase of the filler content, *micro*-phases with connected structures form in the SPI composite membrane, leading to improvements of the water retention and proton conductivity of SPI membranes. On the other hand, when excess fillers are embedded into the matrix, they tend to aggregate and consequently reduce the water uptake and decrease IEC of the composite membranes [47].

Generally, due to the aggregations of the sulfonated mesoporous silica at high content in SPI matrix by the simple blending and casting method, the content of the material in SPI is limited. In order to eliminate the aggregations of the nanoparticles, *in situ* synthesis of mesoporous silica in SPI was developed [49]. In comparison with the blending method, the amount of mesoporous silica reached up to 30 wt.% in the SPI matrix via the *in situ* sol-gel and self-assembly approach; and the properties of the composite membrane in terms of water uptake and proton conductivity improved

with the increase of the filler content in SPI [49].

Similar to SPI, proton exchange membranes such as SPEEK and SPPSU, fabricated via simple procedures at low cost, have also shown the excellent proton conductivity and stability [50-52]. The mesoporous structure of sulfonated mesoporous silica maintains the water content at a high level even at a low RH because of the capillary condensation effect. Moreover, the periodic sulfonated proton diffusion channels facilitate the proton transportation. Herein, blending of sulfonated mesoporous silica into SPEEK and SPPSU improves the thermal properties, water uptake, proton conductivity and cell performance of the pure membrane. For instance, when sulfonated SBA-15 particles were added into SPPSU, the composite membrane had a high proton conductivity of 5.9×10^{-3} S cm^{-1} after 130 min elapsed time under a dehydrated condition (50 % RH) at 80 ^{o}C, higher than 3.6×10^{-3} S cm^{-1} of the pristine SPPSU membrane[53]. Moreover, when sulfonated cube mesoporous benzene-silica (SMBS) ($Im\bar{3}m$) was added in SPEEK, the proton conductivity of the composite membrane increased up to 70 ^{o}C at 40 % RH; by comparison, the proton conductivity of Nafion 117 membrane sharply dropped when the temperature was raised beyond 60 ^{o}C under the same RH[54].

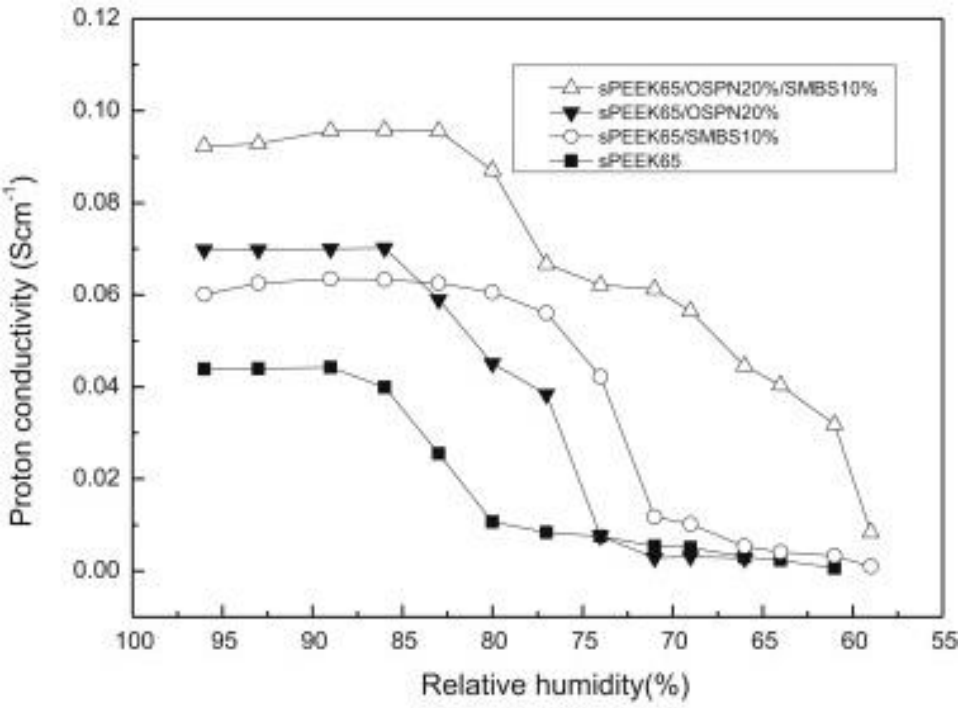

Figure 2.5 Proton conductivity of sPEEK65/OSPN/SMBS composite membranes at different relative humidity (100 °C).[57]

In order to further increase the conductivity of the composite membrane, a high degree of sulfonation for SPEEK is required. However, the high level of sulfonation results in high water uptake, leading to the decrease of the mechanical strength of SPEEK. The membrane becomes too brittle in the dry condition to make the MEA. One classic approach to increase the mechanical strength of SPEEK at the high level of sulfonation is to employ an interpenetrating polymer network (IPN) [55, 56]. For instance, when 10 wt.% SMBS was added into the IPN structure with an organosiloxane network (OSPN, 20 wt.%) and SPEEK (65% in sulfonation degree), the ternary composite membrane showed a higher elongation before breaking than SPEEK.[57] Besides, it exhibited higher water uptake than that of the pristine SPEEK membrane [57]. Furthermore, the ternary composite membrane showed higher proton conductivity than that of the pristine SPEEK membrane and that of the binary composite membrane either with OSPN or SMBS, especially in the low RH (Figure 2.5).[57] This is due to the high water retention at low RH, derived from the capillary condensation effect of the 2D periodic cylindrical channels of SMBS.

2.3.3 Sulfonation of mesoporous silica

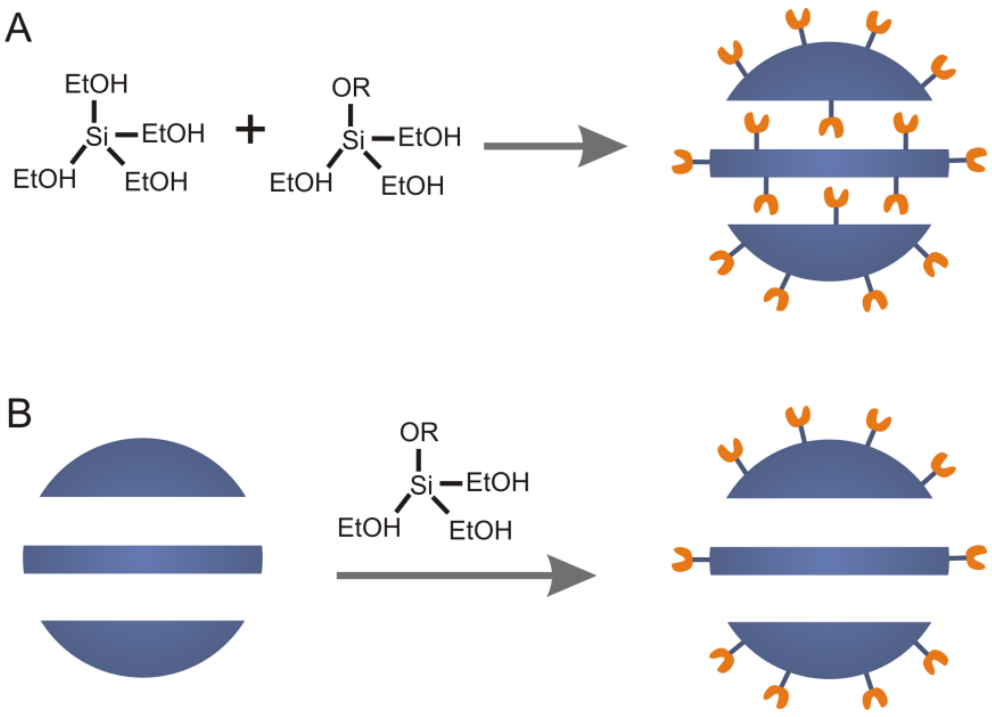

Figure 2.6 Co-condensation and post synthesis for the functionalization of mesoporous silica materials.

The organic functionalization of mesoporous silica generally follows two protocols, either by post-grafting of the functional groups to accessible pore surfaces after the formation of inorganic framework [58, 59] or by co-condensation of the functional species as the inorganic framework [60], as shown in Figure 2.6. The post-grafting functionalization method is based on the reaction of organic silanes with the framework of mesoporous silica [61]. Sulfonation of *meso*-silica is generally achieved by a thiol path [62] such as 3-(trihydroxysilyl)-1-propanesulfonic acid (TPS), mercaptopropyltrimethoxy silane (MPTMS) and a sulfonic path [63, 64] such as 1,2,2-trifluoro-2-hydroxy-1-trifluoromethyl-ethanesulfonic acid sultone (FASA) under a relatively harsh condition for a comparatively long reaction time. This protocol allows for a wide range of functional groups to be anchored on the surface of mesoporous silica with weak deterioration effects on the periodical properties of the silica support. Moreover, alternative groups can be anchored on the surface of the silica support (*i.e.* $-NH_2$) to bridge the functional organic groups and the silica support if appropriate silane moieties are not available [39]. However, the major challenges for the post-grafting protocol are the control of the acid density and the distributions of grafted functional groups.

The other protocol is the co-condensation one-step method that involves the self-assembly of hydrolyzed tetraalkoxysilanes ($(RO)_4Si$) with hydrolyzed trialkoxyorganosilane s($(RO)_3SiR'$), where R and R' are organic species, via structural-directing agents (SDAs) to functionalize mesoporous silica. However, the loading and diversity of the functionalities are limited by the collective compatibility of various components under the synthesis conditions. Furthermore, high concentration of the silane precursor species are detrimental for the mesoporous structural ordering of the materials [65]. The co-condensation method achieves a large number of functional sites with higher IEC for mesoporous silica, larger uniform pores, higher surface area and better long-range order than the post-grafting method. Moreover, it can be conducted under mild and simple synthesis conditions; and is less time-consuming, involving less material consumptions, than the post grafting method [66].

In comparison with the sulfonation of mesoporous silica, sulfonation of periodic mesoporous organosilica (PMO) is simpler and can be carried out under relatively mild conditions [67]. PMO was discovered by three independent research groups, Ozin et al.[68], Stein et al.[69], and Inagaki et al.[70] in 1999. PMO has both organic

and inorganic groups as the integral part of the porous framework where organic groups are located within the pore walls as bridges between Si centres. Tsai et al. synthesized the PMO of mesoporous phenyl-silica via both TEOS and phenyltriethoxysilane (PTES) as the precursors; and then PMO was sulfonated by concentrated sulfuric acid to form the sulfonated PMO [46]. When 3 wt.% of sulfonated mesoporous phenyl-silica was added into the Nafion matrix, the composite membrane expressed 2 times higher water uptake and a slightly higher ion exchange capacity in comparison with the pristine Nafion 212 membrane. Moreover, the composite membrane achieved the power density of 414 mW cm^{-2} at 65 ^{o}C under a dry condition [46], which is regarded as a milestone for the application of Nafion-based composite membranes without external humidification.

The introduction of heterogeneities in the silica support, such as Al, significantly improved the water retention of the mesoporous matrix materials at elevated temperatures (100 – 200 ^{o}C) because of the strong Brønsted acidity [71]. 2D ^{27}Al {^{1}H} HETCPR NMR spectra showed a dominant 2D intensity correlation at 3.0 ppm in the ^{27}Al dimension and 4.0 ppm in the ^{1}H dimension, indicating the interactions between adsorbed water and Al^{IV} aluminosilica species (Figure 2.7A) [72]. On the contrary, the 2D ^{29}Si {^{1}H} HETCPR NMR spectra demonstrated the strong dipole-dipole couplings between the Q^3 ^{29}Si species and the hydroxyl groups by the strong

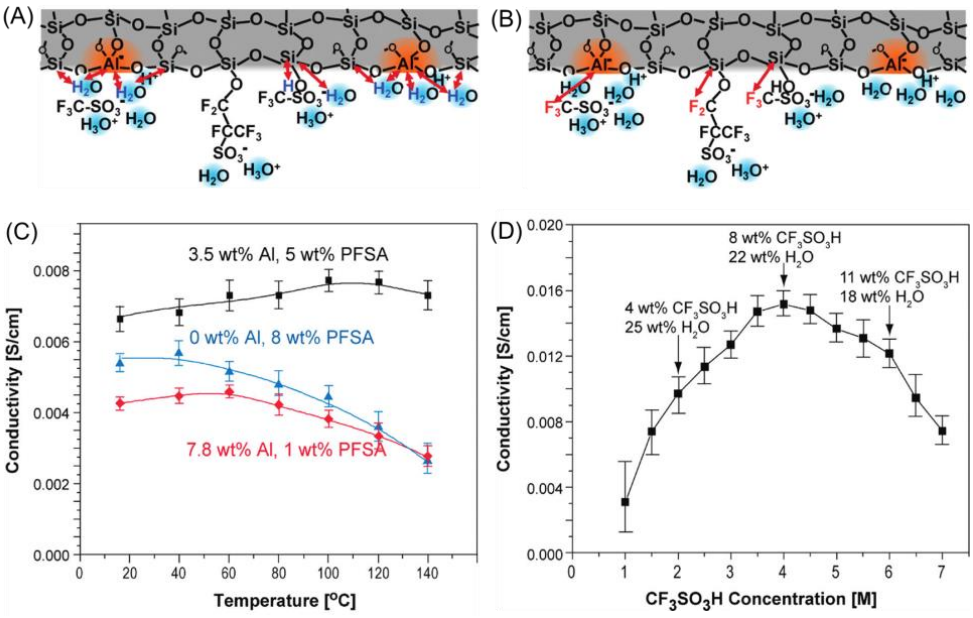

Figure 2.7 Interactions of (A) water and hydroxyl species and (B) grafted PFSA and triflic acid with ^{29}Si and ^{27}Al moieties.(C) proton conductivities against temperature (50 % RH) and (D) triflic acid concentrations at ambient condition (20 ^{o}C, ~40 % RH).[72]

correlated signal intensity at 1.6 ppm in the ^{1}H dimension and -102 ppm in the ^{29}Si dimension. The covalently grafted PFSA moieties interacted strongly with the Q^3 ^{29}Si sites, as the position of Q^3 ^{29}Si shifted from -115 ppm to -102 ppm[73]. By comparison, triflic acid species showed a selective interaction with ungrafted Q^3 or $Q^4(^{1}Al)$ ^{29}Si species and interactions with six-coordinate aluminosilica ^{27}Al mesopores surface sites, as shown in Figure 2.7B.

The proton diffusion rate in aluminosilicate is expected to be similar with that in the aqueous solutions, where protons move along the hydrogen bonds [45]. However, the replacement of Si atoms by Al atoms in the interior mesopores surface is at the cost of surface silanol sites available for proton conductive functional groups, independent of the temperature or RH. Nevertheless, the trade-off relationship between the proportion of the functional groups and aluminosilicate content of the silica support can be optimized. Athens et al.[72] optimized the contents for silanol sites replaced by aluminosilicate and PFSA, corresponding to high hydrophilicity and strong acidity (Figure 2.7C and D), respectively. The optimized content for aluminosilicate and perfluorosulfonic-acid surface grafting densities in the multifunctionalized mesoporous silica film with 3.5 wt.% Al and 5 wt.% PFSA yielded the maximum proton conductivity of 7.7×10^{-3} S cm^{-1} at temperatures ranging from 20 to 140 ^{o}C under 50 % RH, higher than the pure PFAS-grafted *meso*-silica and high aluminosilicate replaced cubic mesoporous films.

2.3.4 Pore structure and acidity of mesoporous silica

Pore structures in terms of dimensionality, pore size and morphology also influence the proton transportation under the conditions of similar acid loading. Mesoporous MCM-48 with a large pore size and three dimensional (3D) interconnected pore structures displayed higher proton conductivity than small pore zeolite beta and one dimensional pore structure MCM-41 with a pore size less than 4 nm [44]. To further improve the proton conductivity, sulfonated KIT-6 with a pore size of 8 nm and three dimensional interconnected pore structures were incorporated into the Nafion membrane with superior properties in terms of proton conductivity and cell performance under 72 % RH at 120 ^{o}C [43]. The enhanced water uptake, provision of strong acid sites and high bulk to surface water ratio are the critical factors for the high proton conductivity at low RH conditions.

The acidity of the organic groups in mesoporous silica materials is a critical factor that affects the activity of Nafion-based hybrid membranes. Aryl sulfonic acid (S-MP) mesoporous silica exhibits the highest conductivity followed by the propyl sulfonic acid (S-PE) containing samples, phosphonic acid (P) functionalized mesoporous silica, and finally carboxylic acid (C) functionalized mesoporous silica, where these four types of organic functional groups have the similar acid loading in MCM-41[44]. Tominaga et al. [42] synthesized three types of silica materials, including SiO_2 sphere (p-SiO_2), mesoporous silica (Ne-MPSi) and sulfonated mesoporous silica (Su-MPSi) with the acidity of 0.06, 0.38 and 0.46 mmol g^{-1}, respectively. With 5wt.% of the fillers embedded in the Nafion matrix, the Nafion/Su-MPSi composite showed the highest proton conductivity at 40 ^{o}C, 95% RH, which is attributed to the strong acid sites mainly located on the internal surface.[42]

The pore size and the acidity control the relationship between the proton conductivity and the water sorption process in the mesopores via Kelvin equation [74]. According to the Kelvin equation, the relative vapour pressure at the capillary condensation increases with the increase of the contact angel between the pore surface and water molecules and of the diameter of pores. The increase of acidity in the mesopores decreases the contact angle due to the hydrophilicity of the sulfonic acid groups. Thus, the conductivity of the mesoporous silica thin film drops steeply at medium RH with the steep decrease of water adsorption, respectively (Figure 2.8a

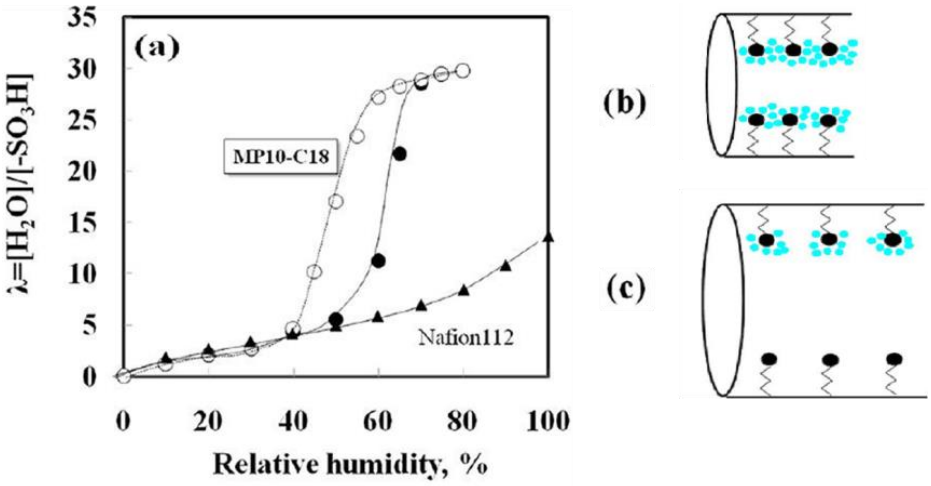

Figure 2.8 Water uptake (a) of sulfonic acid functionalized mesoporous silica films at 25 ^{o}C against RH values. Water sorption at high (b) and low (c) acid density at low RH and proton channel formation.[75]

)[75]. Moreover, the RH with the steep change in proton conductivity shifts lower with the decrease in the pore size and increase in the acid density, which corresponds well with the water vapour adsorption-desorption isotherms. Shannon and his colleges revealed that the proton conductivity of the sulfonated mesoporous silica films was almost independent of RH which can be as low as 20%, while the membrane with large pores showed a decline, beginning at a high level of humidity (50 – 60 %)[74]. The small pore size and high density of sulfonic acid groups can effectively conduct protons in the presence of a small amount of water (Figure 2.8b), while the large pore size and low density of sulfonic acid groups require a large amount of water to form proton channels (Figure 2.8c). Thus, the pore size and acidity of mesoporous silica controls the RH position at the steep change by the Kelvin equation, and the mesoporous electrolyte with small pore size and high acid density achieves high proton conductivity at low RH.

Overall, the confinement of $–SO_3H$ groups in the mesopores of silica materials reduces the dependence of proton conductivity on hydration. And the water retention of the sulfonated mesoporous silica could be tuned by the pore size, space symmetries of the pore structure, and the acidity density of acid groups. However, the intrinsic proton conduction mechanism of $–SO_3H$ groups requires the incorporation of water molecules. The boiling point of water limits the proton transportation at elevated temperatures. By comparison, non-aqueous mediators are able to transfer protons at elevated temperatures and anhydrous conditions. In this regard, the replacement of water with non-aqueous mediators, such as imidazole, triazole, phosphoric acid and ionic liquids for proton transportation has attracted great attention.

2.4 High temperature proton conductors for PEMs

Heterocyclic compounds such as imidazole and triazole play a role of proton transport mediator similar to water. The proton transport in the heterocyclic moieties is determined by the Grotthuss-type mechanism where a proton transports from one heterocyclic ring to a neighbour one via hydrogen bond construction and deconstruction, and subsequent reorientation of the heterocycle [76]. Low dependence on humidity and the high proton conductivity at high temperatures and low humidity, therefore, are expected for the heterocyclic moieties [77].

2.4.1 Imidazole

Imidazole groups are known to be involved in proton transferring biological systems; and according to the *ab-initio* calculation, they can act as proton acceptors, donors and proton shuttle species because of their amphoteric and self-dissociation character with acidic protons at –NH- and basic sites at =N- [78, 79]. Accordingly, protonation of imidazole gives symmetrical imidazolium cations; and protons are transferred from one imidazole group to the other imidazole group [77]. Moreover, imidazole based materials (*i.e.* polybenzenemidazole) combined with phosphoric acid have been employed as PEMs for the fuel cell application at high temperatures and anhydrous conditions [81-83].

Three types of imidazole groups have been grafted on the interior mesopores surface of MCM-41, as shown in Figure 2.9 [80]. Because of the occupation of one N atom in N-imi-MCM-41 for the anchorage of the imidazole group, the proton acceptance capacity (PAC) of N-imi-MCM-41 is lower than that of imi-MCM-41 with two N-atoms for the proton uptake, resulting in a lowered conductivity by two orders of magnitude compared with that of imi-MCM-41. Furthermore, when the fle xible chain was lengthened from 3 carbon atoms to five carbon atoms by combining the imidazole group via forming a peptide bond on amino-anchors (pep-imi-MCM-41), the PAC and the proton conductivity of MCM-41 were significantly improved from 0.21 mmol g^{-1} to 0.79 mmol g^{-1} and from 10^{-5} S cm^{-1} to 10^{-4} S cm^{-1} (100 % RH,

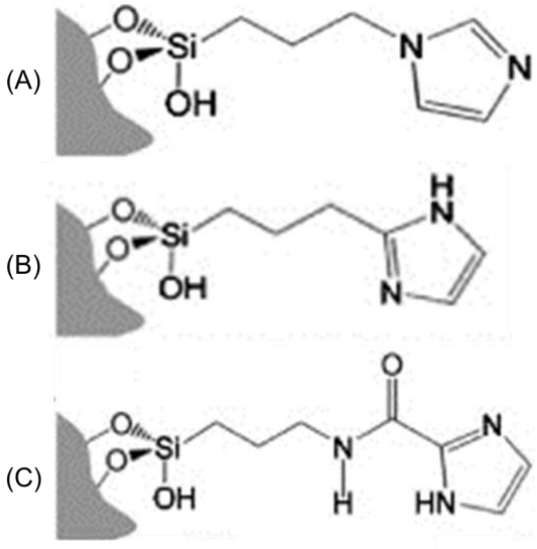

Figure 2.9 Three types of imidazole groups grafted on mesoporous silica surface (A) N-imi-MCM-41, (B) imi-MCM-41 and (C) pep-imi-MCM-41.[80]

140 ^{o}C), respectively. This is most likely due to the high imidazole loadings (PAC values) and long spacing between the silica host and the protonic groups, which allows the anchored imidazole group to reach each other easily[84].

Moreover, as the amphoteric character of imidazole diminishes the dependence of proton conductivity on humidity, imidazole functionalized mesoporous silica can be employed as fillers in sulfonated polymers for the proton conductivity improvement. Furthermore, ionic paths are formed by the hydrogen bonding interactions between the imidazole moieties and the sulfonic acid groups, which also enhances the proton diffusion [85]. For instance, when imidazole functionalized mesoporous silica was introduced into the Nafion membrane, a maximum conductivity of 1.06×10^{-2} S cm^{-1} was achieved at 130 ^{o}C under anhydrous condition with a 5 wt.% filler loading. Moreover, the conductivity of the composite membrane was stable under such as the harsh condition for 76 h [86]. However, the proton conductivity dropped for the further durability test due to the structural reconfiguration process above the glass transition point of the Nafion membrane (~126 ^{o}C), ending a distorted cross-linking geometry of the polymer matrix and discontinuity of proton conducting network paths [86].

2.4.2 Triazole

Triazole has a similar molecular structure to imidazole, and hence may transfer protons via a similar mechanism. 1H-1,2,4-triazole (mp: 120 ^{o}C and bp: 256 ^{o}C) has a proton conductivity of 1.2×10^{-3} S cm^{-1} at 120 ^{o}C under the anhydrous state[87], while 1H-1,2,3-triazole (mp: 23 ^{o}C and bp: 203 ^{o}C) has proton conductivity of 1.5×10^{-4} S cm^{-1} at the room temperature in the liquid phase[88]. This indicates that self-dissociation of 1H-1,2,4-triazole and 1H-1,2,3-triazole generates protons and the proton diffusion rate is considerably high, similar to the case of imidazole. Moreover, the acidity of 1H-1,2,3-triazole ($pK_a1 = 1.17$, $pK_a2 = 9.26$) is higher than imidazole ($pK_a1 = 7.18$, $pK_a2 = 14.52$), indicating higher proton conductivity than imidazole[89]. Triazole is a small molecular and is also susceptible to the leaching problem during the fuel cell operation, resulting in the continuous decrease in the conductivity. Nevertheless, triazole molecules could be fixed on silica materials to efficiently relieve the leaching problem.

Generally, triazole molecules are grafted on the interior pore surface of

mesoporous silica by chemical bonds via the reaction between the triazole precursor and the hydroxyl groups in mesoporous silica. For instance, benzotriazole-5-carboxylic acid (BTCA) was anchored onto SBA-15 by the groups of carboxylic acid and hydroxyl group[90]. The addition of BTCA/SBA-15 particles into the Nafion membrane significantly enhanced the proton conductivity of the matrix under 10 % RH, 150 ^{o}C and the proton conductivity increased with the increase of the filler content in the range of 2.3 – 5.6 wt.%[90]. The enhancement effect is due to the guide effect in the aligned mesoporous channels of SBA-15 by the intermolecular proton transportation among the adjacent BTCA molecules, and the improved water retention of mesoporous silica.

2.4.3 Protic ionic liquids

Protic ionic liquids (PILs) are non-aqueous proton carriers with a high ionic conductivity, non-volatility and chemical stability as well as thermal stability up to 300 ^{o}C [91, 92]. Ionic liquids consist of Brønsted acids and bases and the interacted hydrogen bond acts as the proton carrier path. They have been extensively introduced into polymer to improve their conductivity at anhydrous conditions [93]. However, ionic liquids are relatively small molecules in the form; and therefore, can be easily leached out the composite membrane [94]. On the other hand, mesoporous materials are able to confine the ionic liquid in the mesopores, which hinders the release of ionic liquid [95]. For instance, the pure PILs/poly(styrene-co-acrylonitrile) (SAN) and SiO_2 sphere composite membrane almost lost all the ionic liquid after a 4 h extraction by distilled water, while the mesoporous PILs/*meso*-silica/SAN composite membrane retained 20 wt.% of the ionic liquid under the same extraction process [96].

Considering the proton conductivity, the addition of mesoporous materials into the PILs/polymer composite has two competing effects [97]. The periodic channels in the mesoporous materials facilitate the proton transportation in the inorganic materials. At the same time, mesoporous inorganic fillers block the movement of polymer molecular chains and make the proton channels in the matrix tortuous, resulting in a disturbance in proton diffusion. That is why the proton conductivity of PILs composite membrane shows a volcano shape against the addition of mesoporous silica [97]. Generally, the optimum filler content is in the range of 1 – 5

wt.%, depending on the properties of the polymer matrix [98].

Moreover, the pore size of mesoporous silica affects the proton diffusion of ionic liquids in the mesopores of the inorganic fillers. The higher the ratio of surface area/pore volume, that is, the smaller the pore size, the higher the proton conductivity obtained, as the small pores favour the formation of PIL conductive channels. For instance, when the pore size of SBA-15 decreased from 17.4 nm to 9.5 nm, the proton conductivity of poly(methyl methacrylate) (PMMA)/PIL/SBA-15 composite membrane increased from 2.8×10^{-3} S cm^{-1} to 9.4×10^{-3} S cm^{-1} at 160 ^{o}C, 0 % RH [99]. Furthermore, the mesopores in small sizes favour the PIL retention because of the strong capillary forces within the mesoporous silica materials.

The morphology of mesoporous silica will also affect the proton conductivity of PILs based composite membranes. Hwang et al. [99] discovered that platelet-shaped SBA-15 with short pore channels was more effective in improving the proton conductivity of the PMMA/IL/SBA-15 composite membrane than fibre-shaped SBA-15 with long channels, probably due to the shortened distance and improved efficiency for proton diffusion in the platelet of SBA-15.

2.4.4 Phosphoric acid

Similar to protonic small molecules including imidazole, triazole and ionic liquids, phosphoric acid also shows the high proton conductivity and thermal stability at elevated temperatures and low RH [100]. Phosphoric acid has been extensively applied in PEMs combined with basic polymers, such as PBI [101]. However, the acid-base composite membrane suffers from the acid leaching problem during the prolonged operation in fuel cells [102]. Impregnating PA into the mesopores of mesoporous silica is a good way to solve the leaching problem of PA. Zhao et al.[103] introduced phosphorated mesoporous silica into the Nafion membrane, and the proton conductivity of the Nafion membrane was substantially increased to 3.39 $\times 10^{-1}$ S cm^{-1} at 100 %RH, 115 ^{o}C by an addition of 5.0 wt.% of fillers. In addition to mesoporous silica, hollow mesoporous silica was also employed by Jiang et al. as a PA reservoir because of the large volume to improve the conductor adsorption. When HMS was impregnated by amino tri(methylene phosphoric acid) (ATMP), the addition of HMS-ATMP with a loading of 7.5 wt.% significantly increased the proton conductivity of chitosan by two orders of magnitude from 1.1×10^{-4} S cm^{-1} to

1.2×10^{-2} S cm^{-1} [31].

Zeng et al. [104, 105] fabricated a novel PA/*meso*-silica composite membrane based on the sintered mesoporous silica disks. They found that the sintering treatment for the *meso*-silica disk significantly increased the mechanical strength of mesoporous silica disks and improved the operation temperatures by getting rid of the polymeric binder. After PA being impregnated into the mesopores of the sintered mesoporous silica disk (PA/*meso*-silica) with a loading of 27.7 wt.%, superior conductivity was achieved in comparison with the PA/PBI membrane and the PA-porous-silica membrane at a range of elevated temperatures (Figure 2.10A). Outstanding proton conductivity of 6.0×10^{-2} S cm^{-1} was achieved at 200 ^{o}C under the anhydrous condition while excellent power output of 689 and 200 mW cm^{-2} was obtained in the H_2/O_2 and the methanol/O_2 systems without humidification at 190 ^{o}C, respectively.

The PA/*meso*-silica membrane meets with two critical challenges. One is the sintering temperature. When the silica membrane is treated at temperature higher than 650 ^{o}C, the mesoporous structure remains intact at 750 ^{o}C and completely collapses at 850 ^{o}C[104]. The other one is the degradation of PA during the operation at high temperatures. However, the degradation of PA is determined by the water content and the temperatures. Thus, when external water is added into the fuel cell, the PA degradation is impeded. The hypothesis was confirmed by the superior performance of PA/*meso*-silica by adding 1 or 3 % water content, otherwise the performance decreased along with the fuel cell operation, as shown in Figure 2.10B.

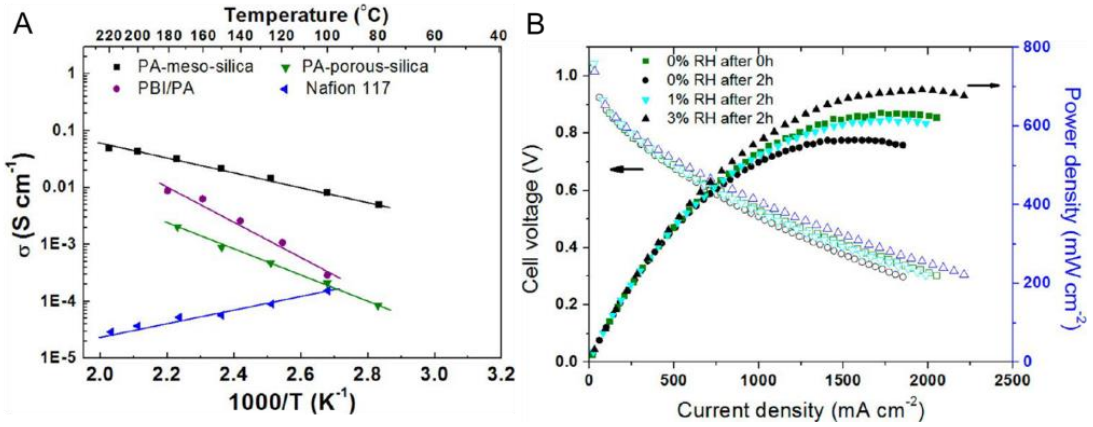

Figure 2.10 (A) The proton conductivity of composite membranes against temperature under anhydrous condition (PBI/PA membrane from [107]). (B) Single cell performance of PA/meso-silica membrane based fuel cell in H_2/O_2 at 190 ^{o}C. [104]

Although the PA/*meso*-silica based fuel cell demonstrates the excellent cell performance, the thermal and chemical stability of PA/*meso*-silica composite particles are not satisfactory for a long-term use at elevated temperatures. Yi et al. [106] found out that the structure of mesoporous silica remained intact under the heat treatment below 80 ^{o}C for 24 h; while the structure completely collapsed along with a growth of the particle size when the composite particles were annealed above 200 ^{o}C for 24 h. The Fourier Transform Infrared Spectroscopy (FT-IR) results showed that the Si-O-Si asymmetric stretching band at 1086 cm^{-1} blue shifted with the increase of the annealing temperatures due to the characteristic vibration peak of P-O-P and Si-O-P.[106] Besides the peak at round 110 ppm of amorphous silica (Si-$(OSi)_4$) by ^{29}Si MAS NMR, a new peak was detected at around 210 ppm, corresponding to the presence of ($Si_3(PO_4)_4$ or $Si(HPO_4)_2$).[106] That is due to the formation of phosphor silicate between PA and mesoporous silica.

2.4.5 Alternative mesoporous materials for PEM

Besides highly ordered mesoporous silica, mesoporous structures have also been introduced into other materials including titanium dioxide (TiO_2) [107], zirconium phosphate ($Zr_3(PO_4)_4$) [108], iron phosphate ($FePO_4$) [109], lanthanum phosphate ($LaPO_4$) [110, 111] and titanium phosphate ($Ti_3(PO_4)_4$) [112] as PEMs. Mesoporous anatase TiO_2/Nafion composite membrane (3.0 wt.%) shows 5.7 times higher performance (669 mW cm^{-2}) than the recast Nafion membrane at 50% RH, 120 ^{o}C, as mesoporous anatase TiO_2 confines a high content of water in its mesopores [107]. The surface area of the filler in the composite membrane determines the performance of the composite membrane based cells at low temperatures (< 90 ^{o}C), while the amount of water in the mesopores of the fillers plays a critical role in improving the cell performance at high temperatures (120 ^{o}C).

Acid metal phosphates are solid proton conductors, while proton diffusion of metal acid phosphate is determined by the surface functional group -OH in the interlay with the presence of water [113]. Given that the mesoporous structure is introduced into the acid metal phosphate, its surface area could be significantly enlarged. Thus, the proton conductivity of the acid metal phosphate could be substantially increased due to the large number of exposed –OH groups. For instance, when a worm-like mesoporous structure was introduced into $Zr_3(PO_4)_4$

with pore size in the range of 2 – 4 nm and surface area between 78 - 174 $m^2 g^{-1}$, the conductivity of the material reached up to 4.1×10^{-6} S cm^{-1} at 84 % RH, 22 ^oC [108]. Generally, the mesoporous acid metal phosphate materials are synthesized by the acid-based pair synthesis way via templates, such as Pluroic, P123, F127 and F108, C14-Br, cetytrimethylammonium (CTAB), and sodium dodecyl sulfate (SDS).

Moreover, organic groups can also be embedded into the framework of metal phosphate to improve the conductivity of the substrate, similar to the PMO. For instance, sulfonated mesoporous iron oxophenyl phosphate was produced via the oxophenyl sulfonation by fuming sulfuric acid for mesoporous iron oxophenyl phosphate. And proton conductivity of 1.0×10^{-2} S cm^{-1} was obtained for sulfonated mesoporous oxophenyl phosphate at 100 % RH and room temperature [109].

Table 2.2 The properties of mesoporous materials for proton exchange membranes.

Matrix	Fillers and content	Function groups	agents	Conductivity, mS cm^{-1}	Ref
N/A	SBA-15, 5.6 wt.%	triazole	BTCA	0.852@150 ^oC, 10 % RH	[90]
N/A	Sulfonated SBA-16 disk	Ionic liquid	BMIm-BF4	11.4@160 ^oC, 0 % RH	[95]
	MCM-41, 6.0 wt.%	Ionic liquid	EIm-TfO	12@160 ^oC, 0 % RH	[96]
Nafion	*Meso*-silica, 3.0 wt.%	Ionic liquid	N/A	54.6@90 ^oC, 30 % RH	[97]
	Platelet SBA-15, 5.0 wt.%	Ionic liquid	BMIm-TFSI	5.3@160 ^oC, 0 % RH	[99]
N/A	MCM-41, 5.0 wt.%	Ionic liquid	N/A	67.4@150 ^oC, 0 % RH	[98]
SAN	Sintered *meso*-silica disk	PA	PA	60@190 ^oC, 0 % RH	[105]
Nafion	Hollow mesoporous	$-PO_3H_2$	ATMP	12@80 ^oC, 78 % RH	[31]
PMMA	MCM-41, 5.0 wt.%	$-PO_3H_2$	$POCl_3$	339@80 ^oC, 100 % RH	[103]
Nafion	HMS, 4.0 wt.%	$-SO_3H$	Cysteine	10.2@80 ^oC, 21.6 % RH	[39]
		$-PO_3H_2$	Phosphoserine	7.91@80 ^oC, 21.6 % RH	
		-COOH	Aspartic acid	4.85@80 ^oC, 21.6 % RH	
SPI	*Meso*-silica, 7.0 wt.%	$-SO_3H$	MPTMS	42.5@80 ^oC, 100 % RH	[48]
SPEEK	*Meso*-silica, 10.0 wt.%	$-SO_3H$	H_2SO_4	17@70 ^oC, 40 % RH	[54]
SPPSU	SBA-15, 0.5 wt.%	$-SO_3H$	MPTMS	5.9@80 ^oC, 50% RH	[53]

In order to further increase the proton conductivity of the mesoporous metal phosphate materials, proton conductors such as PA have been impregnated into the mesopores. The impregnation of PA significantly increased the proton conductivity of metal phosphate to around 1.0×10^{-2} S cm^{-1} at elevated temperatures between 120 – 180 ^{o}C, 20% RH with a PA content as low as 5.0 wt.%. And the conductivity value is comparable with the Nafion membrane at a fully hydrated state[110]. Properties of selected mesoporous PEM materials are listed in Table 2.

2.5 Conclusions

Mesoporous materials possess periodic and interconnected channels and high surface areas. Because of the capillary condensation effect of mesoporous channels, they show strong capability to retain water at low RH and high temperatures. Moreover, water molecules confined in the mesopores induce the proton transportation by forming protonic charge carriers through hydrogen bonding. Herein, the introduction of mesoporous structure into PEMs not only facilitates the proton conductivity but also alleviates the dependence of proton conductivity of PEMs on RH. Mesoporous polymer membranes, such as mesoporous sulfonated block copolymers and mesoporous inorganic-polymer composite membranes, such as sulfonated mesoporous silica based composite membranes are directly employed as the PEMs for fuel cells. The space symmetry, pore size, porosity and ordering level of the mesoporous materials and functionalized mesoporous materials are the critical factors to obtain the optimum performance of PEMs for fuel cells.

References

[1] J.S. Beck, J.C. Vartuli, W.J. Roth, M.E. Leonowicz, C.T. Kresge, K.D. Schmitt, C.T.W. Chu, D.H. Olson, E.W. Sheppard, A new family of mesoporous molecular sieves prepared with liquid crystal templates, Journal of the American Chemical Society 114 (27) (1992) 10834-10843.

[2] C.T. Kresge, M.E. Leonowicz, W.J. Roth, J.C. Vartuli, J.S. Beck, Ordered mesoporous molecular sieves synthesized by a liquid-crystal template mechanism, Nature 359 (6397) (1992) 710-712.

[3] Y. Wan, Zhao, On the Controllable Soft-Templating Approach to Mesoporous Silicates, Chemical Reviews 107 (7) (2007) 2821-2860.

[4] Y. Ye, C. Jo, I. Jeong, J. Lee, Functional mesoporous materials for energy applications: solar cells, fuel cells, and batteries, Nanoscale 5 (11) (2013) 4584-4605.

[5] N.W. DeLuca, Y.A. Elabd, Polymer electrolyte membranes for the direct methanol fuel cell: A review, Journal of Polymer Science Part B: Polymer Physics 44 (16) (2006) 2201-2225.

[6] M.A. Hickner, H. Ghassemi, Y.S. Kim, B.R. Einsla, J.E. McGrath, Alternative Polymer Systems for Proton Exchange Membranes (PEMs), Chemical Reviews 104 (10) (2004) 4587-

4612.
[7] P.V. Komarov, I.N. Veselov, P.P. Chu, P.G. Khalatur, Mesoscale simulation of polymer electrolyte membranes based on sulfonated poly(ether ether ketone) and Nafion, Soft Matter 6 (16) (2010) 3939-3956.
[8] W.H. Choi, W.H. Jo, Preparation of new proton exchange membrane based on self-assembly of Poly(styrene-co-styrene sulfonic acid)-b-poly(methyl methacrylate)/Poly(vinylidene fluoride) blend, Journal of Power Sources 188 (1) (2009) 127-131.
[9] S.B. Darling, Directing the self-assembly of block copolymers, Progress in Polymer Science 32 (10) (2007) 1152-1204.
[10] J. Won, H.H. Park, Y.J. Kim, S.W. Choi, H.Y. Ha, I.-H. Oh, H.S. Kim, Y.S. Kang, K.J. Ihn, Fixation of Nanosized Proton Transport Channels in Membranes†, Macromolecules 36 (9) (2003) 3228-3234.
[11] H.-C. Lee, H. Lim, W.-F. Su, C.-Y. Chao, Novel sulfonated block copolymer containing pendant alkylsulfonic acids: Syntheses, unique morphologies, and applications in proton exchange membrane, Journal of Polymer Science Part A: Polymer Chemistry 49 (11) (2011) 2325-2338.
[12] M. Ingratta, E.P. Jutemar, P. Jannasch, Synthesis, Nanostructures and Properties of Sulfonated Poly(phenylene oxide) Bearing Polyfluorostyrene Side Chains as Proton Conducting Membranes, Macromolecules 44 (7) (2011) 2074-2083.
[13] M.J. Park, K.H. Downing, A. Jackson, E.D. Gomez, A.M. Minor, D. Cookson, A.Z. Weber, N.P. Balsara, Increased water retention in polymer electrolyte membranes at elevated temperatures assisted by capillary condensation, Nano Letters 7 (11) (2007) 3547-3552.
[14] E. Helfand, Z.R. Wasserman, Block Copolymer Theory. 4. Narrow Interphase Approximation, Macromolecules 9 (6) (1976) 879-888.
[15] M.J. Park, N.P. Balsara, Phase behavior of symmetric sulfonated block copolymers, Macromolecules 41 (10) (2008) 3678-3687.
[16] S. Ge, X. Li, B. Yi, I.-M. Hsing, Absorption, Desorption, and Transport of Water in Polymer Electrolyte Membranes for Fuel Cells, Journal of The Electrochemical Society 152 (6) (2005) A1149-A1157.
[17] L. Rubatat, C.X. Li, H. Dietsch, A. Nykanen, J. Ruokolainen, R. Mezzenga, Structure-Properties Relationship in Proton Conductive Sulfonated Polystyrene-Polymethyl Methacrylate Block Copolymers (sPS-PMMA), Macromolecules 41 (21) (2008) 8130-8137.
[18] H. Tang, Z. Wan, M. Pan, S.P. Jiang, Self-assembled Nafion-silica nanoparticles for elevated-high temperature polymer electrolyte membrane fuel cells, Electrochemistry Communications 9 (8) (2007) 2003-2008.
[19] D. Zhao, Y. Wan, W. Zhou, Ordered Mesoporous Materials, Wiley-VCH Verlag GmbH & Co. KGaA, 2013, pp. 5-54.
[20] H. Li, M. Nogami, Pore-Controlled Proton Conducting Silica Films, Advanced Materials 14 (12) (2002) 912-914.
[21] Y.G. Jin, S.Z. Qiao, Z.P. Xu, J.C. Diniz da Costa, G.Q. Lu, Porous Silica Nanospheres Functionalized with Phosphonic Acid as Intermediate-Temperature Proton Conductors, The Journal of Physical Chemistry C 113 (8) (2009) 3157-3163.
[22] A. Matsuda, Y. Nono, T. Kanzaki, K. Tadanaga, M. Tatsumisago, T. Minami, Proton conductivity of acid-impregnated mesoporous silica gels prepared using surfactants as a template, Solid State Ionics 145 (1–4) (2001) 135-140.
[23] Y. Jin, S. Qiao, L. Zhang, Z.P. Xu, S. Smart, J.C.D. da Costa, G.Q. Lu, Novel Nafion composite membranes with mesoporous silica nanospheres as inorganic fillers, Journal of Power Sources 185 (2) (2008) 664-669.
[24] Y. Choi, Y. Kim, H.K. Kim, J.S. Lee, Direct synthesis of sulfonated mesoporous silica as inorganic fillers of proton-conducting organic-inorganic composite membranes, Journal of Membrane Science 357 (1-2) (2010) 199-205.
[25] Y. Chiba, Y. Tominaga, Poly(ethylene-co-vinyl alcohol)/sulfonated mesoporous organosilicate composites as proton-conductive membranes, Journal of Power Sources 203 (2012) 42-47.
[26] Y. Tominaga, T. Maki, Proton-conducting composite membranes based on polybenzimidazole and sulfonated mesoporous organosilicate, International Journal of Hydrogen Energy 39 (6) (2014) 2724-2730.

[27] K.-D. Kreuer, A. Rabenau, W. Weppner, Vehicle Mechanism, A New Model for the Interpretation of the Conductivity of Fast Proton Conductors, Angewandte Chemie International Edition in English 21 (3) (1982) 208-209.
[28] L. Bernard, A. Fitch, A.F. Wright, B.E.F. Fender, A.T. Howe, Proceedings of the International Conference on Fast Ionic Transport in SolidsMechanisms of hydrogen diffusion and conduction in DUO2AsO4·4D2O as inferred from neutron diffraction evidence, Solid State Ionics 5 (1981) 459-462.
[29] F. Pereira, K. Vallé, P. Belleville, A. Morin, S. Lambert, C. Sanchez, Advanced Mesostructured Hybrid Silica−Nafion Membranes for High-Performance PEM Fuel Cell, Chemistry of Materials 20 (5) (2008) 1710-1718.
[30] H. Pu, L. Lou, Y. Guan, Z. Chang, D. Wan, Proton exchange membranes based on semi-interpenetrating polymer networks of polybenzimidazole and perfluorosulfonic acid polymer with hollow silica spheres as micro-reservoir, Journal of Membrane Science 415–416 (2012) 496-503.
[31] Y. Zhao, H. Yang, H. Wu, Z. Jiang, Enhanced proton conductivity of hybrid membranes by incorporating phosphorylated hollow mesoporous silica submicrospheres, Journal of Membrane Science 469 (2014) 418-427.
[32] X. Fang, C. Chen, Z. Liu, P. Liu, N. Zheng, A cationic surfactant assisted selective etching strategy to hollow mesoporous silica spheres, Nanoscale 3 (4) (2011) 1632-1639.
[33] R. Deshmukh, U. Schubert, Synthesis of CuO and Cu3N Nanoparticles in and on Hollow Silica Spheres, European Journal of Inorganic Chemistry 2013 (14) (2013) 2498-2504.
[34] G. Qi, Y. Wang, L. Estevez, A.K. Switzer, X. Duan, X. Yang, E.P. Giannelis, Facile and Scalable Synthesis of Monodispersed Spherical Capsules with a Mesoporous Shell, Chemistry of Materials 22 (9) (2010) 2693-2695.
[35] Y. Dai, H. Jiang, Y. Hu, Y. Fu, C. Li, Controlled Synthesis of Ultrathin Hollow Mesoporous Carbon Nanospheres for Supercapacitor Applications, Industrial & Engineering Chemistry Research 53 (8) (2014) 3125-3130.
[36] T. Zhang, J. Ge, Y. Hu, Q. Zhang, S. Aloni, Y. Yin, Formation of Hollow Silica Colloids through a Spontaneous Dissolution–Regrowth Process, Angewandte Chemie International Edition 47 (31) (2008) 5806-5811.
[37] Q. Zhang, T. Zhang, J. Ge, Y. Yin, Permeable Silica Shell through Surface-Protected Etching, Nano Letters 8 (9) (2008) 2867-2871.
[38] Y. Chen, H. Chen, L. Guo, Q. He, F. Chen, J. Zhou, J. Feng, J. Shi, Hollow/Rattle-Type Mesoporous Nanostructures by a Structural Difference-Based Selective Etching Strategy, ACS Nano 4 (1) (2010) 529-539.
[39] Y. Yin, W. Deng, H. Wang, A. Li, C. Wang, Z. Jiang, H. Wu, Fabrication of hybrid membranes by incorporating acid-base pair functionalized hollow mesoporous silica for enhanced proton conductivity, Journal of Materials Chemistry A 3 (31) (2015) 16079-16088.
[40] K. Feng, B. Tang, P. Wu, A "H2O donating/methanol accepting" platform for preparation of highly selective Nafion-based proton exchange membranes, Journal of Materials Chemistry A (2015).
[41] Y.-F. Lin, C.-Y. Yen, C.-C.M. Ma, S.-H. Liao, C.-H. Lee, Y.-H. Hsiao, H.-P. Lin, High proton-conducting Nafion (R)/-SO3H functionalized mesoporous silica composite membranes, Journal of Power Sources 171 (2) (2007) 388-395.
[42] Y. Tominaga, I.-C. Hong, S. Asai, M. Sumita, Proton conduction in Nafion composite membranes filled with mesoporous silica, Journal of Power Sources 171 (2) (2007) 530-534.
[43] Z. Chen, R.S. Hsu, Nafion/Acid Functionalized Mesoporous Silica Nanocomposite Membrane for High Temperature PEMFCs, Proton Exchange Membrane Fuel Cells 9 25 (1) (2009) 1151-1157.
[44] J.C. McKeen, Y.S. Yan, M.E. Davis, Proton Conductivity of Acid-Functionalized Zeolite Beta, MCM-41, and MCM-48: Effect of Acid Strength, Chemistry of Materials 20 (16) (2008) 5122-5124.
[45] S. Meenakshi, A.K. Sahu, S.D. Bhat, P. Sridhar, S. Pitchumani, A.K. Shukla, Mesostructured-aluminosilicate-Nafion hybrid membranes for direct methanol fuel cells, Electrochimica Acta 89 (2013) 35-44.
[46] C.-H. Tsai, H.-J. Lin, H.-M. Tsai, J.-T. Hwang, S.-M. Chang, Y.-W. Chen-Yang, Characterization and PEMFC application of a mesoporous sulfonated silica prepared from two

precursors, tetraethoxysilane and phenyltriethoxysilane, International Journal of Hydrogen Energy 36 (16) (2011) 9831-9841.
[47] L. Geng, Y. He, D. Liu, C. Lu, New organic-inorganic hybrid membranes based on sulfonated polyimide/aminopropyltriethoxysilane doping with sulfonated mesoporous silica for direct methanol fuel cells, Journal of Applied Polymer Science 123 (5) (2012) 3164-3172.
[48] D. Liu, L. Geng, Y. Fu, X. Dai, C. Lue, Novel nanocomposite membranes based on sulfonated mesoporous silica nanoparticles modified sulfonated polyimides for direct methanol fuel cells, Journal of Membrane Science 366 (1-2) (2011) 251-257.
[49] L. Geng, Y. He, D. Liu, X. Dai, C. Lu, Facile in situ template synthesis of sulfonated polyimide/mesoporous silica hybrid proton exchange membrane for direct methanol fuel cells, Microporous and Mesoporous Materials 148 (1) (2012) 8-14.
[50] D.X. Luu, E.-B. Cho, O.H. Han, D. Kim, SAXS and NMR Analysis for the Cast Solvent Effect on sPEEK Membrane Properties, The Journal of Physical Chemistry B 113 (30) (2009) 10072-10076.
[51] S. Zhou, D. Kim, Cross-linked aryl-sulfonated poly(arylene ether ketone) proton exchange membranes for fuel cell, Electrochimica Acta 63 (2012) 238-244.
[52] J.-R. Lee, J.-H. Won, K.-S. Yoon, Y.T. Hong, S.-Y. Lee, Multilayer-structured, SiO2/sulfonated poly(phenylsulfone) composite membranes for proton exchange membrane fuel cells, International Journal of Hydrogen Energy 37 (7) (2012) 6182-6188.
[53] J.-H. Won, H.-J. Lee, K.-S. Yoon, Y.T. Hong, S.-Y. Lee, Sulfonated SBA-15 mesoporous silica-incorporated sulfonated poly(phenylsulfone) composite membranes for low-humidity proton exchange membrane fuel cells: Anomalous behavior of humidity-dependent proton conductivity, International Journal of Hydrogen Energy 37 (11) (2012) 9202-9211.
[54] L. Xie, E.-B. Cho, D. Kim, Sulfonated PEEK/cubic (Im3m) mesoporous benzene-silica composite membranes operable at low humidity, Solid State Ionics 203 (1) (2011) 1-8.
[55] V. Delhorbe, X. Thiry, C. Cailleteau, E. Mourier, M. Bathfield, L. Chikh, O. Fichet, B. Ameduri, R. Mercier, S. Vidal, L. Augier, E. Espuche, F. Gouanve, G. Gebel, A. Morin, Fluorohexane network and sulfonated PEEK based semi-IPNs for fuel cell membranes, Journal of Membrane Science 389 (2012) 57-66.
[56] D.X. Luu, D. Kim, Semi-interpenetrating polymer network electrolyte membranes composed of sulfonated poly(ether ether ketone) and organosiloxane-based hybrid network, Journal of Power Sources 196 (24) (2011) 10584-10590.
[57] S.Y. Han, J. Park, D. Kim, Proton-conducting electrolyte membranes based on organosiloxane network/sulfonated poly(ether ether ketone) interpenetrating polymer networks embedding sulfonated mesoporous benzene-silica, Journal of Power Sources 243 (2013) 850-858.
[58] R. Marschall, J. Rathousky, M. Wark, Ordered functionalized silica materials with high proton conductivity, Chemistry of Materials 19 (26) (2007) 6401-6407.
[59] R. Marschall, I. Bannat, J. Caro, M. Wark, Proton conductivity of sulfonic acid functionalised mesoporous materials, Microporous and Mesoporous Materials 99 (1-2) (2007) 190-196.
[60] Q. Yang, J. Liu, L. Zhang, C. Li, Functionalized periodic mesoporous organosilicas for catalysis, Journal of Materials Chemistry 19 (14) (2009) 1945-1955.
[61] E.-B. Cho, D.X. Luu, D. Kim, Enhanced transport performance of sulfonated mesoporous benzene-silica incorporated poly(ether ether ketone) composite membranes for fuel cell application, Journal of Membrane Science 351 (1-2) (2010) 58-64.
[62] M. Wilhelm, M. Jeske, R. Marschall, W.L. Cavalcanti, P. Tölle, C. Köhler, D. Koch, T. Frauenheim, G. Grathwohl, J. Caro, M. Wark, New proton conducting hybrid membranes for HT-PEMFC systems based on polysiloxanes and SO3H-functionalized mesoporous Si-MCM-41 particles, Journal of Membrane Science 316 (1–2) (2008) 164-175.
[63] G.L. Athens, Y. Ein-Eli, B.F. Chmelka, Acid-Functionalized Mesostructured Aluminosilica for Hydrophilic Proton Conduction Membranes, Advanced Materials 19 (18) (2007) 2580-2587.
[64] M. Alvaro, A. Corma, D. Das, V. Fornes, H. Garcia, Single-step preparation and catalytic activity of mesoporous MCM-41 and SBA-15 silicas functionalized with perfluoroalkylsulfonic acid groups analogous to Nafion[registered sign], Chemical Communications (8) (2004) 956-957.

[65] F. Hoffmann, M. Cornelius, J. Morell, M. Froeba, Silica-based mesoporous organic-inorganic hybrid materials, Angewandte Chemie-International Edition 45 (20) (2006) 3216-3251.
[66] D. Margolese, J.A. Melero, S.C. Christiansen, B.F. Chmelka, G.D. Stucky, Direct Syntheses of Ordered SBA-15 Mesoporous Silica Containing Sulfonic Acid Groups, Chemistry of Materials 12 (8) (2000) 2448-2459.
[67] E.-B. Cho, H. Kim, D. Kim, Effect of Morphology and Pore Size of Sulfonated Mesoporous Benzene-silicas in the Preparation of Poly(vinyl alcohol)-Based Hybrid Nanocomposite Membranes for Direct Methanol Fuel Cell Application, Journal of Physical Chemistry B 113 (29) (2009) 9770-9778.
[68] T. Asefa, M.J. MacLachlan, N. Coombs, G.A. Ozin, Periodic mesoporous organosilicas with organic groups inside the channel walls, Nature 402 (6764) (1999) 867-871.
[69] B.J. Melde, B.T. Holland, C.F. Blanford, A. Stein, Mesoporous Sieves with Unified Hybrid Inorganic/Organic Frameworks, Chemistry of Materials 11 (11) (1999) 3302-3308.
[70] S. Inagaki, S. Guan, Y. Fukushima, T. Ohsuna, O. Terasaki, Novel Mesoporous Materials with a Uniform Distribution of Organic Groups and Inorganic Oxide in Their Frameworks, Journal of the American Chemical Society 121 (41) (1999) 9611-9614.
[71] S. Meenakshi, A. Manokaran, S.D. Bhat, A.K. Sahu, P. Sridhar, S. Pitchumani, Impact of Mesoporous and Microporous Materials on Performance of Nafion and SPEEK Polymer Electrolytes: A Comparative Study in DEFCs, Fuel Cells 14 (6) (2014) 842-852.
[72] G.L. Athens, D. Kim, J.D. Epping, S. Cadars, Y. Ein-Eli, B.F. Chmelka, Molecular Optimization of Multiply-Functionalized Mesoporous Films with Ion Conduction Properties, Journal of the American Chemical Society 133 (40) (2011) 16023-16036.
[73] M. Alvaro, A. Corma, D. Das, V. Fornés, H. García, "Nafion"-functionalized mesoporous MCM-41 silica shows high activity and selectivity for carboxylic acid esterification and Friedel–Crafts acylation reactions, Journal of Catalysis 231 (1) (2005) 48-55.
[74] S. Moghaddam, E. Pengwang, Y.-B. Jiang, A.R. Garcia, D.J. Burnett, C.J. Brinker, R.I. Masel, M.A. Shannon, An inorganic-organic proton exchange membrane for fuel cells with a controlled nanoscale pore structure, Nature Nanotechnology 5 (3) (2010) 230-236.
[75] S. Fujita, A. Koiwai, M. Kawasumi, S. Inagaki, Enhancement of Proton Transport by High Densification of Sulfonic Acid Groups in Highly Ordered Mesoporous Silica, Chemistry of Materials 25 (9) (2013) 1584-1591.
[76] Z. Zhou, R. Liu, J. Wang, S. Li, M. Liu, J.-L. Brédas, Intra- and Intermolecular Proton Transfer in 1H(2H)-1,2,3-Triazole Based Systems, The Journal of Physical Chemistry A 110 (7) (2006) 2322-2324.
[77] S. Liu, Z. Yue, Y. Liu, Incorporation of imidazole within the metal-organic framework UiO-67 for enhanced anhydrous proton conductivity, Dalton Transactions 44 (29) (2015) 12976-12980.
[78] S. Scheiner, M. Yi, Proton Transfer Properties of Imidazole, The Journal of Physical Chemistry 100 (22) (1996) 9235-9241.
[79] W. Munch, K.D. Kreuer, W. Silvestri, J. Maier, G. Seifert, The diffusion mechanism of an excess proton in imidazole molecule chains: first results of an ab initio molecular dynamics study, Solid State Ionics 145 (1-4) (2001) 437-443.
[80] R. Marschall, M. Sharifi, M. Wark, Proton conductivity of imidazole functionalized ordered mesoporous silica: Influence of type of anchorage, chain length and humidity, Microporous and Mesoporous Materials 123 (1–3) (2009) 21-29.
[81] Q. Li, J.O. Jensen, R.F. Savinell, N.J. Bjerrum, High temperature proton exchange membranes based on polybenzimidazoles for fuel cells, Progress in Polymer Science 34 (5) (2009) 449-477.
[82] R. He, Q. Li, J.O. Jensen, N.J. Bjerrum, Doping phosphoric acid in polybenzimidazole membranes for high temperature proton exchange membrane fuel cells, Journal of Polymer Science Part a-Polymer Chemistry 45 (14) (2007) 2989-2997.
[83] R.H. He, Q.F. Li, A. Bach, J.O. Jensen, N.J. Bjerrum, Physicochemical properties of phosphoric acid doped polybenzimidazole membranes for fuel cells, Journal of Membrane Science 277 (1-2) (2006) 38-45.
[84] W.L. Cavalcanti, R. Marschall, P. Tölle, C. Köhler, M. Wark, T. Frauenheim, Insight into Proton Conduction of Immobilised Imidazole Systems Via Simulations and Impedance Spectroscopy, Fuel Cells 8 (3-4) (2008) 244-253.

[85] K.A. Sung, K.-H. Oh, W.-K. Kim, M.-J. Choo, K.-W. Nam, J.-K. Park, Proton Exchange Membrane Using Imidazole-Functionalized Silica to Enhance Proton Conductivity at Lower Humidity, Electrochemical and Solid State Letters 14 (10) (2011) B114-B116.
[86] I.S. Amiinu, W. Li, G. Wang, Z. Tu, H. Tang, M. Pan, H. Zhang, Toward Anhydrous Proton Conductivity Based on Imidazole Functionalized Mesoporous Silica/Nafion Composite Membranes, Electrochimica Acta 160 (2015) 185-194.
[87] S. Li, Z. Zhou, Y. Zhang, M. Liu, W. Li, 1H-1,2,4-Triazole: An Effective Solvent for Proton-Conducting Electrolytes, Chemistry of Materials 17 (24) (2005) 5884-5886.
[88] Z. Zhou, S. Li, Y. Zhang, M. Liu, W. Li, Promotion of Proton Conduction in Polymer Electrolyte Membranes by 1H-1,2,3-Triazole, Journal of the American Chemical Society 127 (31) (2005) 10824-10825.
[89] D. Basak, C. Versek, J.A. Harvey, S. Christensen, J. Hillen, S.M. Auerbach, M.T. Tuominen, D. Venkataraman, Enhanced anhydrous proton conduction in binary mixtures of 1H-imidazole-1H-1,2,3-triazole based compounds, Journal of Materials Chemistry 22 (38) (2012) 20410-20417.
[90] S.J. Park, D.H. Lee, Y.S. Kang, High temperature proton exchange membranes based on triazoles attached onto SBA-15 type mesoporous silica, Journal of Membrane Science 357 (1-2) (2010) 1-5.
[91] F. Yan, S. Yu, X. Zhang, L. Qiu, F. Chu, J. You, J. Lu, Enhanced Proton Conduction in Polymer Electrolyte Membranes as Synthesized by Polymerization of Protic Ionic Liquid-Based Microemulsions, Chemistry of Materials 21 (8) (2009) 1480-1484.
[92] S. Subianto, M.K. Mistry, N.R. Choudhury, N.K. Dutta, R. Knout, Composite Polymer Electrolyte Containing Ionic Liquid and Functionalized Polyhedral Oligomeric Silsesquioxanes for Anhydrous PEM Applications, Acs Applied Materials & Interfaces 1 (6) (2009) 1173-1182.
[93] S.S. Sekhon, J.-S. Park, E. Cho, Y.-G. Yoon, C.-S. Kim, W.-Y. Lee, Morphology Studies of High Temperature Proton Conducting Membranes Containing Hydrophilic/Hydrophobic Ionic Liquids, Macromolecules 42 (6) (2009) 2054-2062.
[94] Y.-S. Ye, J. Rick, B.-J. Hwang, Ionic liquid polymer electrolytes, Journal of Materials Chemistry A 1 (8) (2013) 2719-2743.
[95] I.S. Amiinu, X. Liang, Z. Tu, H. Zhang, J. Feng, Z. Wan, M. Pan, Anhydrous Proton Conducting Materials Based on Sulfonated Dimethylphenethylchlorosilane Grafted Mesoporous Silica/Ionic Liquid Composite, Acs Applied Materials & Interfaces 5 (22) (2013) 11535-11543.
[96] B. Lin, S. Cheng, L. Qiu, F. Yan, S. Shang, J. Lu, Protic Ionic Liquid-Based Hybrid Proton-Conducting Membranes for Anhydrous Proton Exchange Membrane Application, Chemistry of Materials 22 (5) (2010) 1807-1813.
[97] A.K. Mishra, T. Kuila, D.-Y. Kim, N.H. Kim, J.H. Lee, Protic ionic liquid-functionalized mesoporous silica-based hybrid membranes for proton exchange membrane fuel cells, Journal of Materials Chemistry 22 (46) (2012) 24366-24372.
[98] A.K. Mishra, N.H. Kim, J.H. Lee, Effects of ionic liquid-functionalized mesoporous silica on the proton conductivity of acid-doped poly(2,5-benzimidazole) composite membranes for high-temperature fuel cells, Journal of Membrane Science 449 (2014) 136-145.
[99] Y.-S. Ye, G.-W. Liang, B.-H. Chen, W.-C. Shen, C.-Y. Tseng, M.-Y. Cheng, J. Rick, Y.-J. Huang, F.-C. Chang, B.-J. Hwang, Effect of morphology of mesoporous silica on characterization of protic ionic liquid-based composite membranes, Journal of Power Sources 196 (13) (2011) 5408-5415.
[100] E. Quartarone, P. Mustarelli, Polymer fuel cells based on polybenzimidazole/H3PO4, Energy & Environmental Science 5 (4) (2012) 6436-6444.
[101] C. Laberty-Robert, K. Valle, F. Pereira, C. Sanchez, Design and properties of functional hybrid organic-inorganic membranes for fuel cells, Chemical Society Reviews 40 (2) (2011) 961-1005.
[102] S. Yu, L. Xiao, B.C. Benicewicz, Durability Studies of PBI-based High Temperature PEMFCs, Fuel Cells 8 (3-4) (2008) 165-174.
[103] Y. Zhao, H. Yang, H. Wu, Z. Jiang, Enhanced proton conductivity of the hybrid membranes by regulating the proton conducting groups anchored on the mesoporous silica, Journal of Power Sources 270 (2014) 292-303.
[104] J. Zeng, B. He, K. Lamb, R. De Marco, P.K. Shen, S.P. Jiang, Anhydrous Phosphoric Acid Functionalized Sintered Mesoporous Silica Nanocomposite Proton Exchange Membranes

for Fuel Cells, Acs Applied Materials & Interfaces 5 (21) (2013) 11240-11248.
[105] J. Zeng, B. He, K. Lamb, R. De Marco, P.K. Shen, S.P. Jiang, Phosphoric acid functionalized pre-sintered meso-silica for high temperature proton exchange membrane fuel cells, Chemical Communications 49 (41) (2013) 4655-4657.
[106] T. Xue, X. Wang, J.-M. Lee, Dual-template synthesis of Co(OH)(2) with mesoporous nanowire structure and its application in supercapacitor, Journal of Power Sources 201 (2012) 382-386.
[107] S.Y. Chen, C.C. Han, C.H. Tsai, J. Huang, Y.W. Chen-Yang, Effect of morphological properties of ionic liquid-templated mesoporous anatase TiO2 on performance of PEMFC with Nafion/TiO2 composite membrane at elevated temperature and low relative humidity, Journal of Power Sources 171 (2) (2007) 363-372.
[108] W.H.J. Hogarth, J.C.D. da Costa, J. Drennan, G.Q. Lu, Proton conductivity of mesoporous sol-gel zirconium phosphates for fuel cell applications, Journal of Materials Chemistry 15 (7) (2005) 754-758.
[109] N.K. Mal, A. Bhaumik, M. Matsukata, M. Fujiwara, Syntheses of mesoporous hybrid iron oxophenyl phosphate, iron oxophosphate, and sulfonated oxophenyl phosphate, Industrial & Engineering Chemistry Research 45 (23) (2006) 7748-7751.
[110] Z. Chai, Q. Suo, H. Wang, X. Wang, Mesoporous lanthanum phosphate nanostructures containing H3PO4 as superior electrolyte for PEM fuel cells, Rsc Advances 3 (44) (2013) 21928-21935.
[111] Z. Chai, L. Gao, C. Wang, H. Zhang, R. Zheng, P.A. Webley, H. Wang, Synthesis of mesoporous LaPO4nanostructures with controllable morphologies, New Journal of Chemistry 33 (8) (2009) 1657-1662.
[112] E. Rodríguez-Castellón, J. Jiménez-Jiménez, A. Jiménez-López, P. Maireles-Torres, J.R. Ramos-Barrado, D.J. Jones, J. Rozière, Proton conductivity of mesoporous MCM type of zirconium and titanium phosphates, Solid State Ionics 125 (1–4) (1999) 407-410.
[113] M. Casciola, D. Bianchi, Frequency response of polycrystalline samples of α−Zr(HPO4)2·H2O at different relative humidities, Solid State Ionics 17 (4) (1985) 287-293.

Chapter 3 Comprehensive strategy to design highly ordered mesoporous Nafion membranes for fuel cells under low humidity conditions

3.1 Introduction

Nafion membrane is the state-of-the-art proton exchange membrane because of its high proton conductivity in fully hydrated state, good mechanical property, chemical stability and structural integrity.[1-3] However, the high dependence of the proton mobility in Nafion membrane on high relative humidity requires the high level of RH for the stable operation of Nafion membrane based fuel cells, which not only complicates the water management but also increases the cost.[4] The high sensitivity of Nafion membrane to RH is mainly due to the fact that Nafion membrane has a non-ordered nanostructure consisting of hydrophobic perfluorinated main chains surrounded by hydrophilic ionic domains that swell upon hydration.[5-7] The growth of ionic domains during water sorption induces a phase-separation, where water-swollen ionic domains tend to interconnect with nanochannels and thus facilitate water and ion transport through the hydrophobic polymer matrix.[8] However, the water channels in the Nafion membrane are random, which results in inherent limitations in the relatively low water retention ability of conventional Nafion membrane.[9]

We have shown early that mesoporous structures could be introduced into the Nafion membrane via a soft template method.[10, 11] In this method, a non-ionic block copolymer surfactant, PEO_{127}-PPO_{48}-PEO_{127} (Pluronic F108) was introduced during the formation of Nafion membranes and the surfactant embedded in the synthesized Nafion membranes was removed by reflux with hot water, forming mesoporous structures in Nafion. The mesoporous Nafion membranes synthesized by a soft template method show higher water retention and proton conductivity than the pristine Nafion membrane due to the vapour condensation effect within the confined space of the mesoporous channels.[12, 13] However, the degree of order of the mesoporous structure is rather low because it is difficult to form highly ordered micelles in the solution due to the flexible non-ionic block polymer chains. That is indicated by the low resolution and broad small-angle x-ray scattering (SAXS) peak of as-synthesized mesoporous Nafion.[11] In order to increase significantly the long-

range period and ordered mesoporous structures, we employed silica colloidal as the mediator in addition to the non-ionic surfactant to facilitate the formation of highly ordered mesoporous Nafion membranes.[14] The presence of silica colloidal mediator significantly increased the degree of order of mesoporous structure of Nafion membrane. However, the formation of a mesoporous Nafion nanostructure and the interactions between non-ionic block copolymer surfactant, silica colloidal and Nafion ionomers are largely unknown although the formation of mesoporous silica materials via the nonionic block polymer template has been extensively studied [15-17].

Therefore, a fundamental understanding of the interaction among nonionic block copolymer micelles, Nafion ionomers and silica precursor is of scientific and technological importance in order to optimize the structure and proton conductivity properties of PFSA-based membranes like Nafion for fuel cells applications. On the other hand, although the presence of highly ordered mesoporous structures in Nafion membrane enhances the water retention and proton conductivity of the membranes under reduced RH [11, 18], the relationship between the performance of the highly ordered mesoporous Nafion membrane based fuel cells and structural symmetries needs to be identified in order to evaluate the external humidity dependence of the mesoporous Nafion membranes. Consequently, understanding the effect of morphology and microstructure on the proton transportation and the water retention capability of the Nafion membrane is crucial in the development of efficient Nafion membrane-based energy-conversion and storage devices such as fuel cells and electrolysis.

Here, the SAXS technique was applied to analyse the microstructures of as-synthesized mesoporous Nafion membranes. Furthermore, we employed *in situ* time-resolved synchrotron SAXS to study the micelles and mesoporous structure formation assisted with silica colloids. The microstructure, mesoporous symmetry, pore size, proton conductivity and performance of the mesoporous Nafion membranes were studied in detail. Cell performance results showed that highly ordered mesoporous Nafion membranes possessed substantially high tolerance towards RH fluctuation as compare to the pristine Nafion membranes, and could be operated under anhydrous conditions.

3.2 Experimental

3.2.1 Materials

All reagents were used as received without further purification. Nonionic triblock copolymers, including poly(ethylene oxide)-*b*-poly(propylene oxide)-*b*-poly-(ethylene oxide) copolymer $EO_{20}PO_{70}EO_{20}$ (Pluronic® P123, MW = 5800) and $EO_{106}PO_{70}EO_{106}$ (Pluronic® F127, MW = 12600), TEOS and n-butanol (99.4%) were purchased from Sigma-Aldrich. 1,3,5-trimethylbenzene (TMB, 99%), concentrated HCl (AR), HF (40%), KCl (AR) and ethanol (AR) were purchased from Shanghai Chemical Company. Nafion 520 ionomers (EW = 1000, 5 wt %) was purchased from DuPont, USA.

3.2.2 Synthesis of Nafion membranes with different structure symmetries

Mesoporous Nafion with four different mesoporous structure symmetries, including 2D hexagonal (denoted as 2D-H), 3D face-centred cubic (denoted as 3D-FC), 3D body-centred cubic (denoted as 3D-BC), and 3D cubic-bicontinuous (donated as 3D-CB) was synthesized from the Nafion-silica composites. The synthesis procedures for the Nafion-silica composites are as follows:

2D-H Nafion-silica. Typically, 2.0 g of P123 and 10.3 mL concentrated HCl solution were mixed in 62.5 g distilled water. Nafion ionomers was then added dropwise under a stirring condition to obtain a homogeneous solution. TEOS (4.16 g) was added and stirred for 24 h. Then the mixture was transferred into an autoclave reactor and kept at 100 ^{o}C for 24 h.

3D-FC Nafion-silica. 2.0 g of F127, 2.0 g of TMB and 5.0 g of KCl were dissolved in a HCl solution (2.0 M, 120 mL) under stirring for 24 h. Nafion ionomers was then added dropwise under a stirring condition to obtain a homogeneous solution. TEOS (8.3 g) was added and stirred for 24 h. The mixture was transferred into an autoclave reactor and kept at 40 ^{o}C for 72 h.

3D-BC Nafion-silica. 1.07 g of F127 and 2.12 g concentrated HCl were mixed in 51.44 g distilled water. The solution was heated to 45 ^{o}C before adding 3.21 g n-butanol. Nafion ionomers was then added dropwise under stirring condition to obtain a homogeneous solution. TEOS (5.09 g) was added and stirred for 24 h. The mixture was transferred into an autoclave reactor and kept at 100 ^{o}C for 24h.

3D-CB Nafion-silica. 2.0 g of P123 and 3.7 g of concentrated HCl solution were mixed to distilled water. The solution was heated to 35 ^{o}C before adding 2.0 g of n-butanol. Nafion ionomers was then added dropwise under stirring condition to obtain a homogeneous solution. TEOS (5.2 g) was added and stirred for 24 h. The mixture was transferred into an autoclave reactor and kept at 100 ^{o}C for 24h.

Without specification, the Nafion content in the Nafion-silica composites was 10 wt.%. Structure directing agents, namely triblock copolymers in the as-synthesized Nafion-silica composites as described above, were removed by refluxing in ethanol for 48 h at 70 ^{o}C. Then the Nafion-silica composites were then mixed with HF solutions under stirring for 48 h to remove the silica template. Then Nafion ionomer was isolated and collected by centrifugation treatment at 4000 rpm for 5 min. Mesoporous Nafion membranes were obtained by recasting the mesoporous Nafion ionomers and heat-treated at 60 ^{o}C for 8 h, 80 ^{o}C for 8 h and 100 ^{o}C for 2 h.

3.2.3 Characterization

Small-Angle X-ray Diffraction (SAXRD) profiles were recorded on a Rigaku D/MAX-RB diffractometer with a CuKα radiation (λ = 1.5419 Å) operating at 40 kV, 50 mA. A linear position-sensitive Dectris-Pilatus detector was used, and the photo energy was 12 keV. Before the test, Nafion-silica composites were grinded finely into powder and the Nafion suspensions were transferred into transparent tubes.

Transmission electron microscopy (TEM) was used to characterize the morphology of Nafion by depositing of the Nafion suspension on a lacey carbon grid via electron microscopy (JEOL JEM-2100F) at an accelerating voltage of 200 kV.

A Q500 (TA instrument) thermogravimetric analyser was employed to investigate the thermal and water retention of the pristine and mesoporous Nafion membrane samples. The as-prepared membranes were immersed in water at room temperature for 24 h before the test. Then TGA measurement was conducted from room temperature to 800 ^{o}C at 10 ^{o}C min^{-1} under air flow of 50 mL min^{-1}.

Nitrogen adsorption isotherms, Brunauer-Emmett-Teller (BET) specific surface areas (S_{BET}) and the porosity of the samples were measured at -196 ^{o}C using Micromeritics ASAP 2020 gas adsorption apparatus. Before adsorption measurement the membranes were cut into small pieces and degassed at 100 ^{o}C for 9 h.

The *in situ* time-resolved synchrotron SAXS measurements were performed with a camera length of 650 mm on the Australian synchrotron SAXS beamline with a 3 GeV electron storage ring, Melbourne, Australia. The *q* range was 0.015 – 0.95 $Å^{-1}$. Mesoporous Nafion-silica composite powders were confined in the holes of a flat plate sample holder which were covered with Kapton tape. The sample plates were then placed on the beamline. In the present study, a precursor solution with appropriate compositions of P123, Nafion ionomers and TEOS in HCl solution for 2D-H Nafion-silica composite was selected in the *in situ* time-resolved synchrotron SAXS study. The solution was confined in a transparent homemade apparatus and then it was placed on the sample holder on the beamline. The synchrotron SAXS of solutions was carried out at room temperature without stirring due to the restriction of the sample holder.

3.2.4 Cell preparation and electrochemical characterization

Pt/C catalysts (50 % Pt/C, E-TEK, USA) were used for the anode and cathode. Pt/C catalyst layers were transferred onto the mesoporous Nafion membrane at 125 ^{o}C and 10 MPa by the decal method to form the catalyst-coated-membrane (CCM). Then the CCM was sandwiched between two gas diffusion layers based on Toray® TGP-H-060 carbon paper to form the membrane-electrode-assembly. The loading for Pt and mesoporous Nafion ionomers in both the anode and the cathode was 0.2 mg cm^{-2} and 0.4 mg cm^{-2}, respectively. The MEA was then placed in a single-cell hardware (active area 6.25 cm^{-2}) for the cell performance measurement using a Greenlight G20 fuel cell test station. H_2 and O_2 flow rates were 50 mL min^{-1}. The stability of mesoporous Nafion membranes was studied on cells with 2D-H Nafion and Nafion 112 membranes at 60 ^{o}C and different RH under a discharge current density of 100 mA cm^{-2}. The proton conductivity of mesoporous Nafion membranes was measured using electrochemical impedance spectroscopy (EIS) technique at frequencies ranging from 100 KHz to 1 Hz.

Hydrogen crossover across of the membranes was evaluated at ambient condition by an electrochemical method. Pure hydrogen and nitrogen (99.9999%) were fed without humidification to the anode and the cathode, respectively, at 300 mL min^{-1}. The potential of the cathode (in nitrogen) was swept at 2 mV s^{-1} in a potential range of 0 mV to 700 mV against the anode (H_2/H^+) using a voltammetry station (Autolab,

PGSTAT30). Hydrogen crossover was evaluated in diffusion-limited hydrogen oxidation current density obtained in the range of 300 – 350 mV.

3.3 Results and discussion

3.3.1 Formation and characterizations of ordered mesoporous Nafion membranes

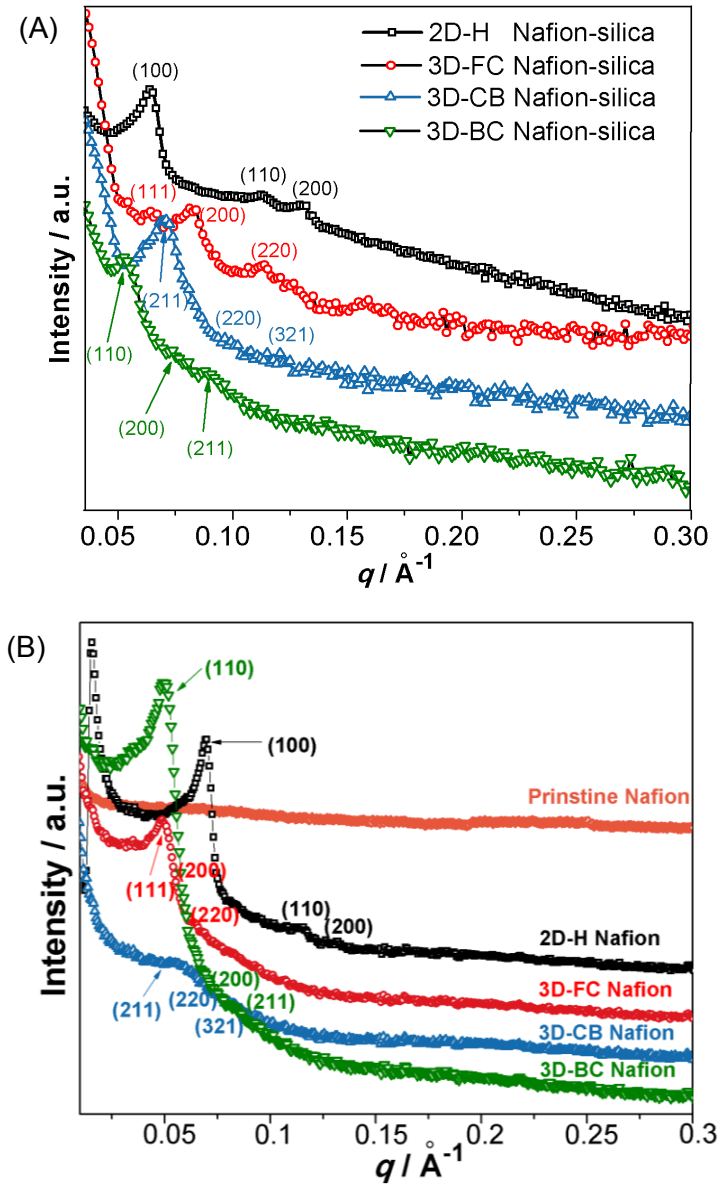

Figure 3.1 SAXS spectra of (A) mesoporous Nafion-silica composites with 2D-H, 3D-FC, 3D-CB and 3D-BC mesoporous structures after removal of the structure directing agents, and (B) corresponding mesoporous Nafion membranes after removal of silica. The SAXS pattern of pristine Nafion 112 membrane is shown in B.

The strategy to design highly ordered mesoporous Nafion membranes is based on the co-assembly of Nafion, silica and SDAs to form the onion-like Nafion-silica-SDAs composites.[14] After removal of the SDAs, the Nafion-silica composites show characteristic SAXS diffraction peaks of well-ordered 2D hexagonal (structural symmetry *P6mm*) [19], 3D face-centred cubic (structural symmetry $Fm\overline{3}m$) [20], 3D body-centred cubic (structural symmetry $Im\overline{3}m$) [21] and 3D cubic bicontinuous (structural symmetry $Ia\overline{3}d$) [22] mesoporous silica (as shown in Figure 3.1A). Moreover, the as-synthesized Nafion membranes after the removal of the mesoporous silica templates show sharp and typical SAXS peaks in the region of $q < 0.2$ Å^{-1} (Figure 3.1B), characteristics of the corresponding Nafion-silica mesoporous structure symmetries but with an increased intensity. In contrast, the pristine Nafion 112 membrane, as the control group, is generally featureless under the present study conditions, indicating that Nafion structure has no long-range and ordered mesopores shown by the SAXS and TEM characterization.[23, 24]

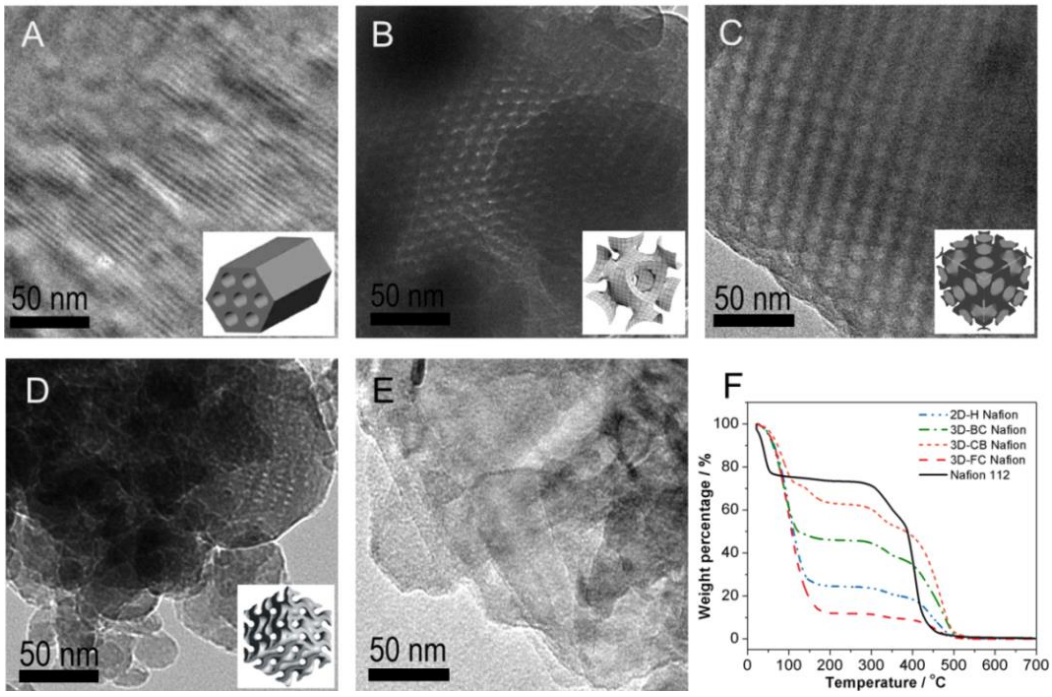

Figure 3.2 TEM morphologies of mesoporous Nafion with (A) 2D hexagonal (2D-H, *P6mm*) in the [110] direction, (B) 3D body-centred (3D-BC, $Im\overline{3}m$) in the [111] direction, (C) 3D face-centred (3D-FC, $Fm\overline{3}m$) in the [100] direction, (D) 3D cubic-bicontinuous (3D-CB, $Ia\overline{3}d$) mesoporous structure in the [311] direction and (E) the pristine Nafion membrane.[F] TGA profiles of mesoporous Nafion membranes with different space symmetries and the pristine Nafion membrane as the control group is shown in (F).

The very different SAXS patterns between the mesoporous Nafion and the pristine Nafion are also confirmed by the TEM images as well as TGA profiles in Figure 3.2. The lattice parameter, *a*, of mesoporous Nafion and mesoporous Nafion-silica composites was calculated from SAXS profiles and the data are shown in Table 3.1. The results indicate that highly ordered mesoporous structures with long-range periodicity remain stable and intact in mesoporous Nafion membranes after the removal of SDA and silica colloids. However, without the assistance of silica colloids, the degree of order of the mesoporous structure is much lower, as shown in previous studies.[10, 11] Silica colloids, therefore, plays an important role for the formation of highly ordered mesoporous structured phase in Nafion-SDA-silica precursor solutions with controlled structure symmetries.

Table 3.1 Peak position *q*, *d* spacing and lattice parameter *a* for the mesoporous Nafion-silica and mesoporous Nafion membranes.

Space symmetries	Mesoporous Nafion-silica			Mesoporous Nafion		
	q / Å^{-1}	*d* / nm	*a* / nm	*q* / Å^{-1}	*d* / nm	*a* / nm
2D-H	0.065	9.7	11.2	0.068	9.2	10.6
3D-FC	0.064	9.8	13.9	0.051	12.3	17.4
3D-CB	0.071	8.8	21.6	0.058	10.8	26.7
3D-BC	0.053	11.8	20.6	0.051	12.3	21.3

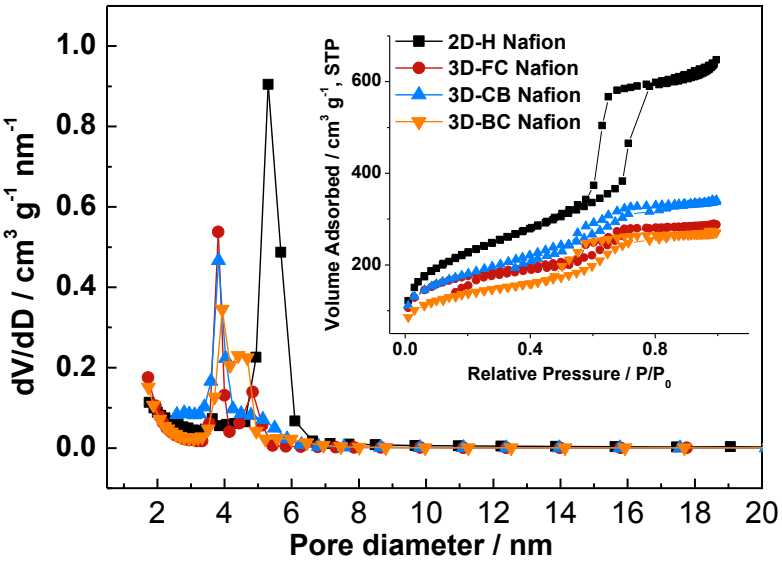

Figure 3.3 Nitrogen sorption isotherms and pore size distributions of mesoporous Nafion membranes with different structure symmetries.

Table 3.2 BET surface area S_{BET}, pore diameter d_{pore}, wall thickness d_{wall} and hydrogen crossover current density j, the proton conductivity σ of diverse mesoporous Nafion and pristine Nafion.

Type of Nafion	S_{BET} / m^2 g^{-1}	d_{pore} / nm	d_{wall} / nm	j / mA cm^{-2}	σ / × 10^{-2} Scm^{-1} (60 °C)		
					0 %RH	40 % RH	100 %RH
2D-H Nafion	609	5.3	2.7	1.15	3.8	6.2	8.0
3D-FC Nafion	447	3.8	8.5	0.85	2.4	5.0	7.0
3D-CB Nafion	781	3.8	7.0	1.54	1.9	3.3	7.2
3D-BC Nafion	554	4.7	10.3	0.88	2.7	4.4	6.9
Pristine Nafion	—	—	—	0.69	1.5	0.42*	7.2

* Measured on Nafion 115 at 30 °C.[25]

The pore size and specific surface area of the mesoporous Nafion membranes were also measured using N_2 adsorption isotherm and the results are shown in Figure 3.3. Mesoporous Nafion membranes with different symmetries have typical type-IV curves and capillary condensation steps. The 2D-H Nafion shows capillary condensation at relative pressures of 0.55 – 0.8, while typical type-IV curves with a clear condensation step at $P/P_0 = 0.4 – 0.7$ were observed in 3D-FC, 3D-CB and 3D-BC Nafion membranes. The mesoporous Nafion samples generally give the H1-type hysteresis loop, suggesting the uniform pore sizes distribution and an ordered pore shape of the mesoporous Nafion.[26] The mesoporous Nafion shows a rather narrow pore size distributions and the average pore diameter, d_{pore}, is 5.3 nm, 3.8 nm, 3.8 nm and 4.7 nm for 2D-H, 3D-FC, 3D-CB and 3D-BC Nafion, respectively. Based on the d_{pore} and lattice parameter, a (see Table 3.1), the pore wall thickness, d_{wall}, can be calculated. For 2D-H, $d_{\text{wall}} = a - d_{\text{pore}}$;[27] for 3D-FC, $d_{\text{wall}} = \frac{\sqrt{2}}{2}a - d_{\text{pore}}$;[28] for 3D-CB, $d_{\text{wall}} = \frac{a}{3.0919} - \frac{1}{2}d_{\text{pore}}$, where 3.0919 is a constant representing the minimal surface area for the $Ia\overline{3}d$ space group; for 3D-BC, $d_{\text{wall}} = \frac{\sqrt{3}}{2}a - d_{\text{pore}}$.[28] The obtained BET surface area, pore diameter and wall thickness of the mesoporous Nafion were calculated and are listed in Table 3.2. Mesoporous Nafion with structure symmetry 3D-CB, exhibits the highest BET surface area of 781 m^2 g^{-1}. 3D-FC Nafion shows lowest specific surface area of 447 m^2 g^{-1}, which may be due to the low order of mesoporous structure as shown by SAXS (Figure 3.1).

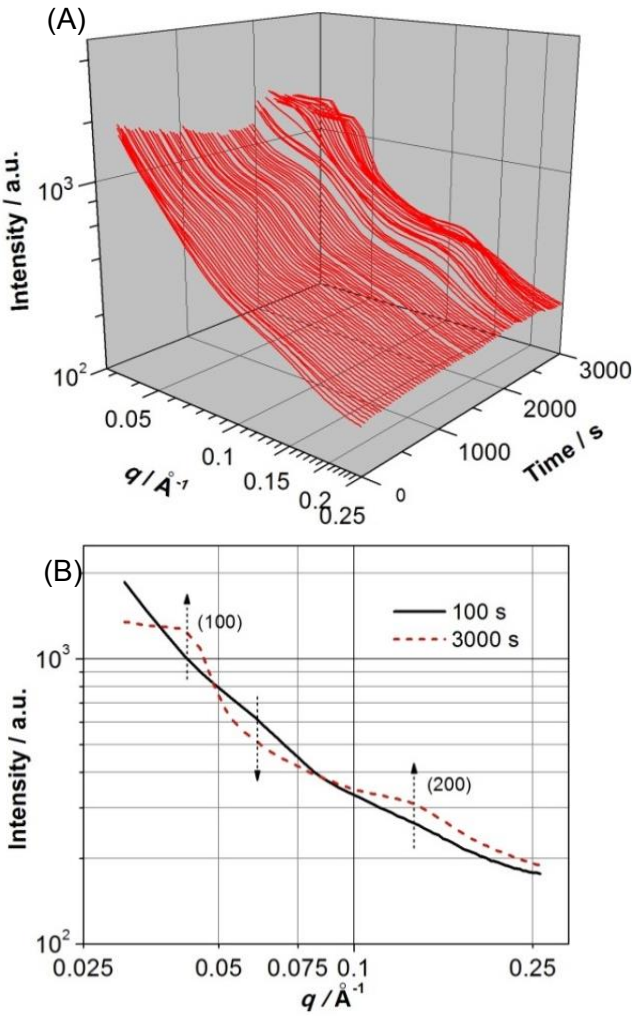

Figure 3.4 (A) Time-resolved synchrotron SAXS diffractograms and (B) 100 s and 3000s SAXS curves of the silica colloid-mediated synthesis of 2D hexagonal mesoporous Nafion-silica composite (10 wt.% Nafion) in P123 + HCl + Nafion ionomers + TEOS solution without stirring.

The formation mechanism and interaction among Nafion molecules, SDAs and silica colloids were further studied by *in situ* time-resolved synchrotron SAXS, using 2D-H structured Nafion as an example. In the initial stage of the self-assembly process, the SAXS signal is typical of a micellar solution with broad oscillation as a function of the scattering vector q as shown in Figure 3.4A. A broad peak centred around 0.06 Å^{-1} occurs at t = 600 s, which is most likely resulted from scattering of associated unordered globular micelles of Nafion-silica nanoparticles.[29] The peak becomes more pronounced with the reaction time because of the stabilizing functions of Nafion ionomers, that is, further agglomeration and grain growth of silica nanoparticles will be inhibited.[30] As the hydrolysis of TEOS only takes a few minutes to complete in the P123 micellar solution,[15] shape evolution and formation of 2D-hexagonal phase would occur between P123 and Nafion-silica

pairs. Then, the structure transforms from the unordered micelles directly to the ordered hexagonal structured phase in solution, and such transformation occurs at ~ 600 s. As shown in Figure 3.4A, the intensity of the Bragg peaks of (100) reflection (0.04 $Å^{-1}$) increases with time, while the intensity of the micellar peak (0.06 $Å^{-1}$) decreases. The continuous increase in the intensity of the (100) reflection reflects an increase in the amount of ordered phase. This indicates the transformation process from the spherical micelles to the ordered and rod-shaped 2D-hexagonal structured phase. Moreover, the comparison of the diffractograms of the Nafion-silica composite taken at 100 s and 3000 s shows the evolution of the Bragg peaks of the hexagonal structure in solution (Figure 3.4B). The silica nanoparticle colloid that attached both at Nafion ionomers and P123 expands the Nafion ordered arrays, and creates an electrostatic-induced reorientation of sulfonic groups towards the ordered silica-P123 micelles. Through cooperative hydrogen bonding self-assembly of the Nafion-silica pairs and P123, a highly 2D-H ordered mesoporous structures is formed. The *in situ* time-resolved synchrotron SAXS results on the 2D-H Nafion-silica also imply that Nafion-silica with different mesoporous structure symmetries can be achieved by adjusting the reagents ratio and employing structure directing agents, SDAs, with different ether blocks.[31]

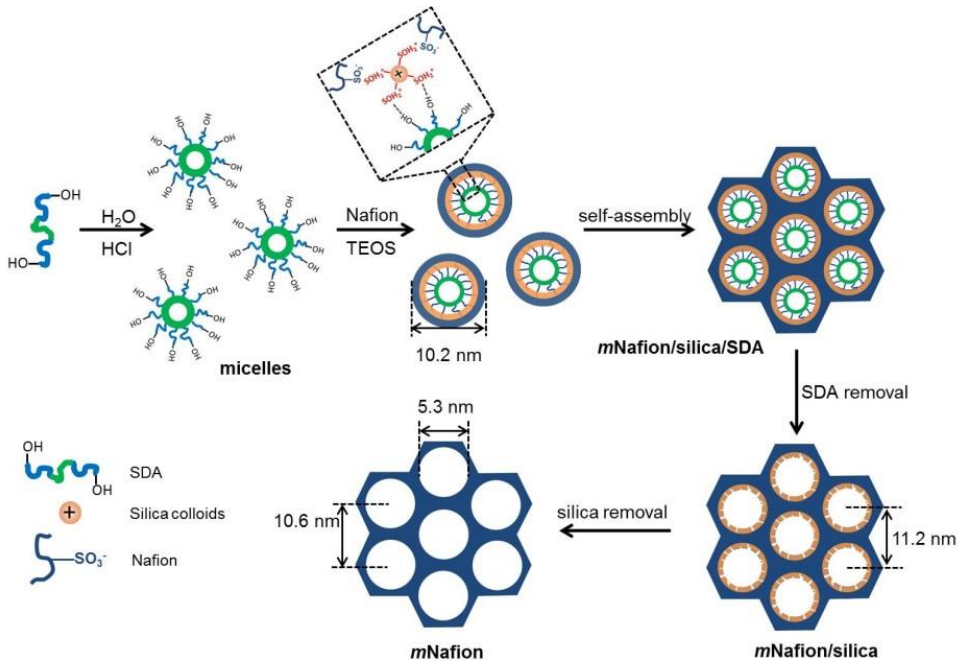

Figure 3.5 Schematic of surfactant-directed and soft template method with the assistance of silica colloidal mediator for the formation of mesoporous Nafion (2D-H structured Nafion was selected as a representative). The transformation from random micelles to an ordered hexagonal structure phase in solution occurs at ~ 600 s.

Based on the *in situ* time-resolved SAXS data, we proposed the process of the silica-mediator assisted formation of mesoporous Nafion membrane (see Figure 3.5 for the typical 2D-H structured Nafion). In the initial stage, the presence of acidic HCl solution initiates and promotes the hydrolysis of TEOS, forming protonated and positively charged silica particles that play the role as bonding sites between Nafion ionomers and the SDAs, *i.e.*, P123 in this case. Driven by the electrostatic forces between the positively charged silica nanoparticles and the negatively charged SO_3^- functional groups of Nafion ionomers, self-assembly of Nafion and silica particles occurs instantaneously, forming Nafion-silica pairs. Then, the Nafion-silica pairs will anchor to the ether block of the SDAs through hydrogen bonding. The Nafion ionomers attached to the silica nanoparticles will stabilize the silica nanoparticles, inhibiting the agglomeration and grain growth of silica nanoparticles and forming the ordered and mesoporous structured phase. Based on the *in situ* time-resolved synchrotron SAXS (Figure 3.4A), the transformation from random micelles to ordered mesoporous phase occurs at ~ 600 s. The highly ordered and mesoporous Nafion ionomers are obtained after removal of both SDAs and silica mediators. The resulting mesoporous orientation would lead to the increasing exposure of sulfonic groups to the hydrophilic phase and the formation of highly ordered proton transporting channels, promoting fast proton conduction process.[32]

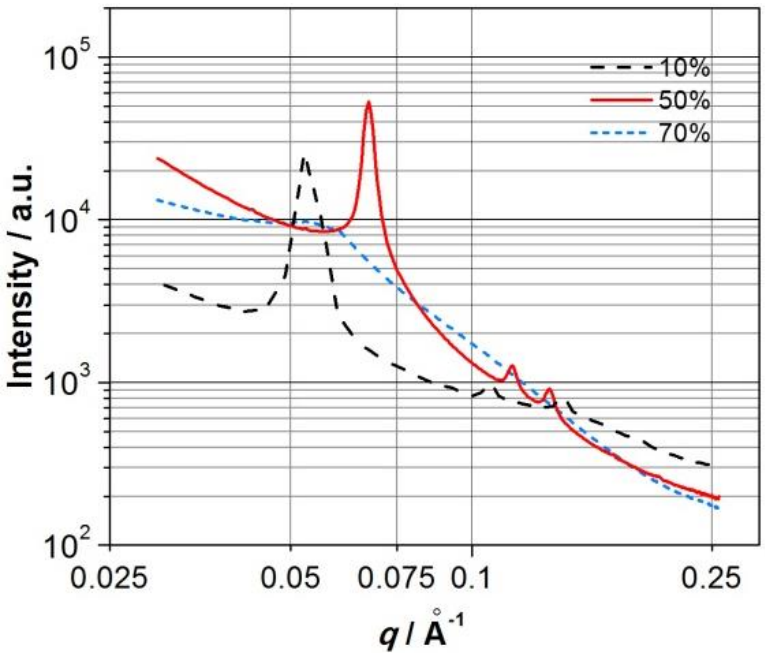

Figure 3.6 Synchrotron SAXS profiles of 2D hexagonal Nafion-silica powders with Nafion ratio of 10 %, 50 % and 70 %, measured at room temperature.

Besides, the formation of ordered mesoporous Nafion-silica composites depends on the Nafion to silica ratio. Figure 3.6 shows the synchrotron SAXS profiles of 2D-H Nafion-silica powders with different contents of Nafion, measured at room temperature. The main (100) reflection was red-shifted from 0.053 $Å^{-1}$ to 0.067 $Å^{-1}$ when the Nafion increased from 10 % to 50 %, that is, the d_{100} spacing value reduced from 11.8 nm to 9.3 nm, respectively. When the Nafion content increased to 70 %, the silica became disordered and the mesoporous Nafion-silica structure could not be obtained. The increase in the content of Nafion decreases the degree of order since the intensive interplay of amphipathic Nafion molecules with the silica-P123 micelles may interrupt significantly the self-assembly procedure of the ordered silica-SDAs framework.[32] Nafion molecules cover the surface of silica colloids, forming Nafion-silica pairs because of self-assembly between the positively charged silica nanoparticles and the negatively charge Nafion ionomers by the electrostatic force. With the increase of the Nafion ionomers, the increasing polymer network would interrupt the assembly of silicate species to the PEO groups of the amphiphile and impede the phase separation. Excess Nafion ionomers would interact with the P123, interrupting the formation of ordered and mesoporous phase in the Nafion-silica-P123 precursor solution. Thus, in the present study, the amount of Nafion in the Nafion-silica composites was controlled to 10 wt.%.

3.3.2 Fuel cell performance of mesoporous Nafion membranes

To assess the hydrogen gas permeability of the mesoporous Nafion membranes, the hydrogen crossover current density was measured and the results are given in Table 3.2. Hydrogen crossover currents were in the range of 0.85 mA cm^{-2} to 1.54 mA cm^{-2} for mesoporous Nafion membranes, which is slightly higher than 0.69 mA cm^{-2} measured on pristine Nafion 112 membrane. This indicates that the detrimental effect of the presence of ordered mesoporous channels on the gas permeability of mesoporous Nafion membranes is relatively low, indicating the applicability of the mesoporous Nafion membranes synthesized in this study as PEMs for fuel cells.

High proton conductivity is an important property of PEMs for fuel cells. Proton conductivities of mesoporous Nafion membrane samples were measured *in situ* during fuel cell operation by electrochemical impedance spectroscopy at 60 ^{o}C under different RH and the results are summarized in Table 3.2. The proton conductivity of

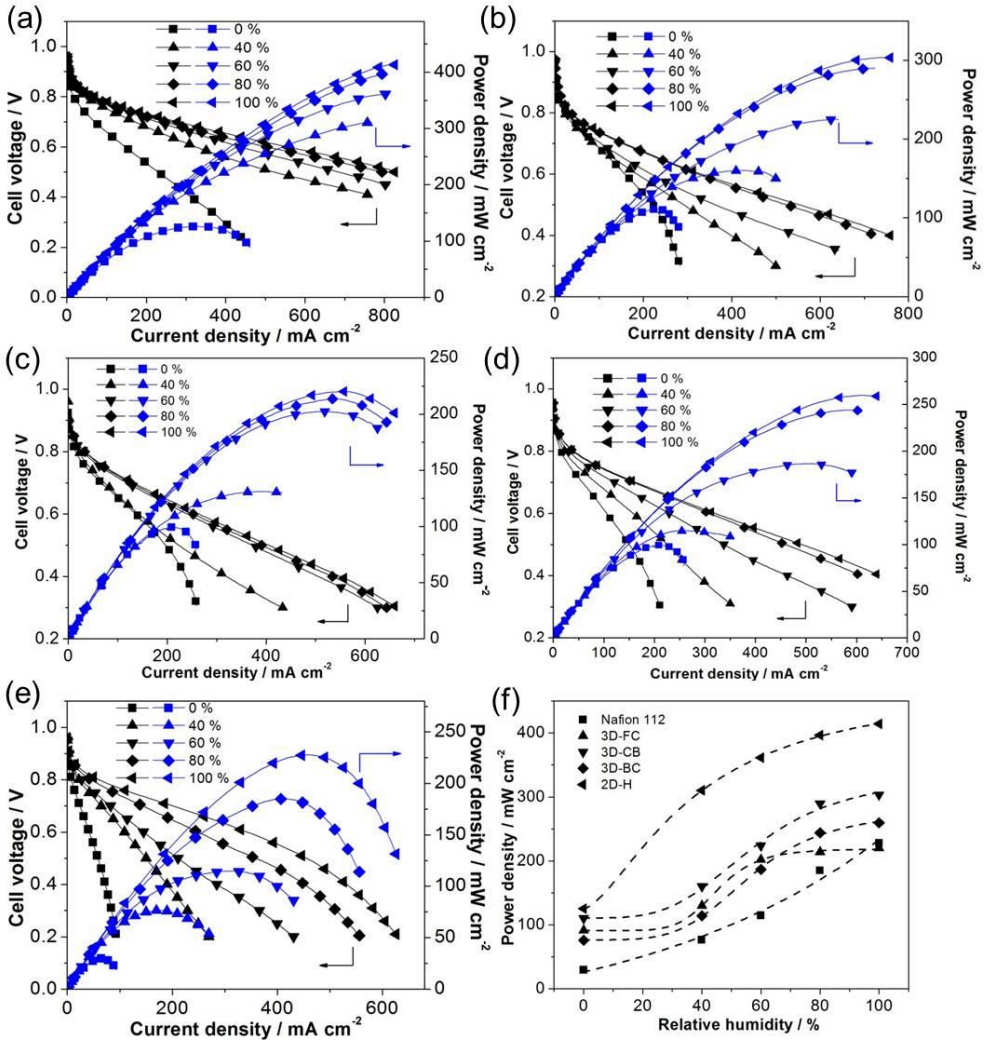

Figure 3.7 Polarization and power output of cells, measured at 60 ^{o}C, H_2/O_2 with (a) 2D-H Nafion membrane, (b) 3D-CB Nafion membrane, (c) 3D-FC Nafion membrane, (d) 3D-BC Nafion membrane, (e) Nafion 112 membrane. Peak power density of mesoporous Nafion membranes against various relative humidity at 60 ^{o}C is given in (f).

mesoporous Nafion membranes shows a very low sensitivity to the change in RH. For example, the proton conductivity for Nafion membrane with 2D-H structure was 8.0×10^{-2} Scm^{-1} at 100 % RH, similar to 7.2×10^{-2} S cm^{-1} measured on Nafion 112 membrane, but slightly lower than 1.0×10^{-1} S cm^{-1} reported on Nafion 115 membranes under 100 % RH at 30 ^{o}C.[25] When the RH was reduced to 40 %, the proton conductivity of 2D-H Nafion membrane was 6.2×10^{-2} Scm^{-1}, a reduction of 22.5 %. In contrast the proton conductivity of conventional Nafion 115 was 4.2×10^{-3} S cm^{-1} at 40 % RH, a reduction of 95.8 % as compared to the value measured at 100 % RH.[25] Most important, under 0 % RH, the proton conductivity of mesoporous Nafion was in the range of 1.9×10^{-2} to 3.8×10^{-2} Scm^{-1}. Consequently, the most significant benefit of the mesoporous Nafion with different structural

symmetries is the substantially enhanced proton conductivity at reduced RH.

Figure 3.7 is the polarization and power output performance of cells with mesoporous Nafion and Nafion 112 membranes, measured at 60 ^{o}C under various RH conditions. The open circuit voltage of all five Nafion membranes was in the range of 0.95 - 0.98 V. The polarization performance of cells with mesoporous Nafion membranes is considerably higher than that of the cells with the pristine Nafion membrane, particularly under reduced RH. For example, under 60 % RH, the power density of the cells with 2D-H, 3D-CB, 3D-BC, and 3D-FC Nafion membranes was 362 mW cm^{-2}, 224 mW cm^{-2}, 185 mW cm^{-2}, and 203 mW cm^{-2}, respectively, higher than 115 mW cm^{-2} obtained on Nafion 112. The cell with 2D-H Nafion membrane produced the highest power output.

The peak power density of cells with 2D-H, 3D-BC, 3D-CB and 3D-FC mesoporous Nafion membranes shows a very different dependence on RH, as compared to the cell with pristine Nafion 112 (Figure 3.7f). The peak power density of Nafion 112 reduced linearly with the decrease in RH. At 100 % RH, the power density of the Nafion membrane cell was 228 mW cm^{-2} and decreased to 77 mW cm^{-2} when the RH was reduced to 40%, a 66.2% reduction in power output. The significant reduction in power output of Nafion 112 membrane cell is clearly due to the fact that the proton conductivity of Nafion membranes decreases significantly with decreasing RH.[33-35]

In the case of the cells with mesoporous Nafion membranes, the dependence of the power density on RH follows a S-type curve. The S-type dependence of the polarization performance on the RH has also been observed on functionalized mesoporous silica cells.[18, 36] The S curves indicate that the power output of the mesoporous Nafion membrane cells is less sensitive to the change in RH. That is likely due to the fact that ordered mesoporous channels have a much better water retention ability as compared to the random nanostructures associated with pristine Nafion membranes. The reduced sensitivity of the power performance of the cells to RH is an important factor for practical operations as this will allow more stable power output under conditions of RH fluctuation. The cell with a 2D-H mesoporous Nafion membrane produced the best performance; 414 mW cm^{-2} under 100% RH and 310 mW cm^{-2} under 40% RH. Fukuda et al.[37] showed that variation of power density with the RH is consistent with the tendency of the amount of H_2O adsorbed on the Nafion membrane. Thus the low sensitivity or dependence on RH of

mesoporous Nafion membrane cells is most likely due to the water capillary condensation effect of the mesoporous structure at reduced relative humidity. On the other hand, the hydrophilic clusters of Nafion 112 membrane with -SO_3H group have to adsorb a large amount of water in order to form the continuous proton transportation channels, resulting in high dependence on external humidification and RH.[38] Consequently, the highest performance of 2D-H mesoporous Nafion based fuel cell indicates the effectiveness of the highly ordered hexagonal cylinders structure for the water retention.

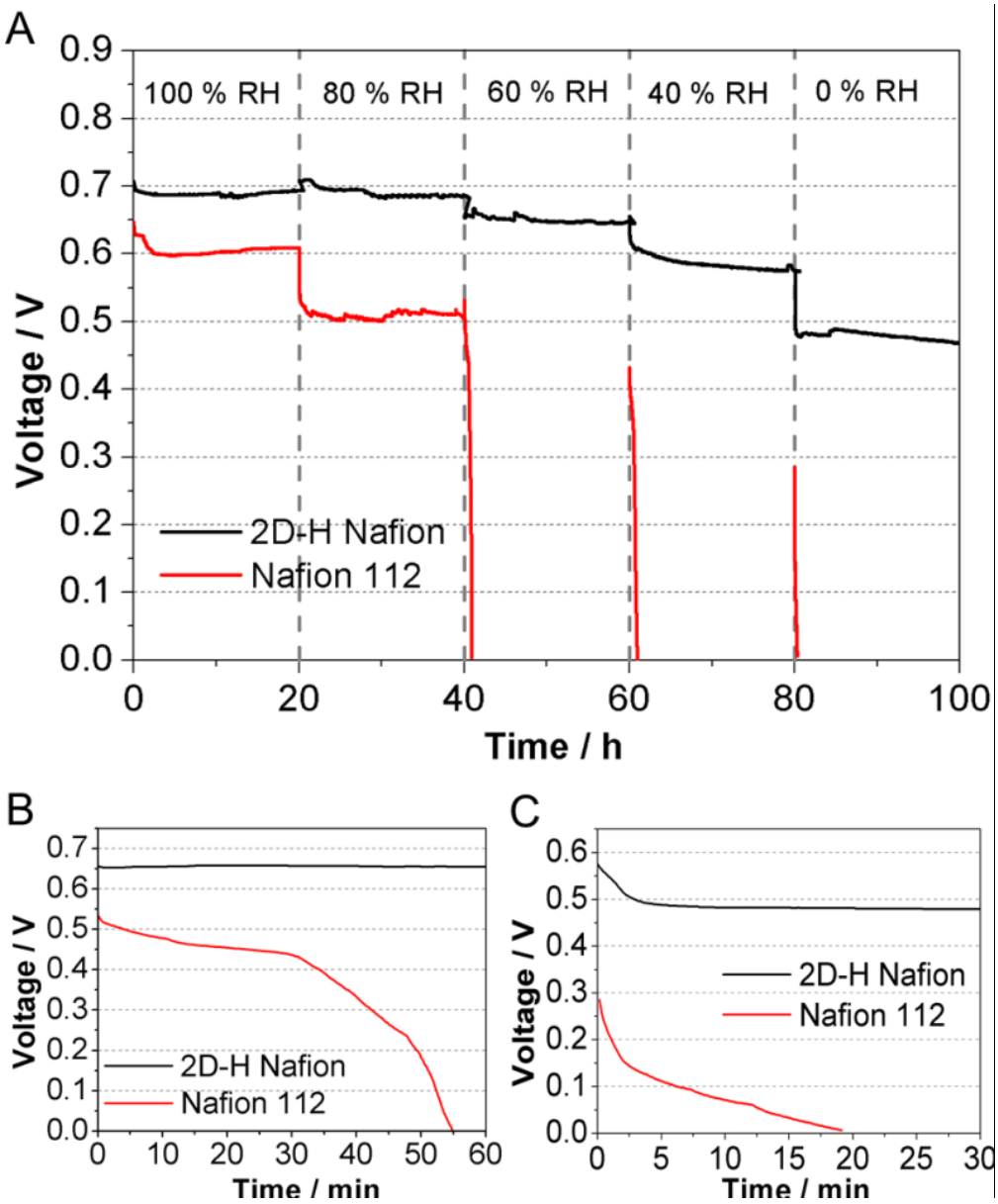

Figure 3.8 (A) Plots of cell voltages measured under different RH levels for 2D-H Nafion and Nafion 112 membrane based fuel cells. (B) and (C) are the enlarged portion of the voltage curves of the cell under 60 % RH and 0 % RH, respectively. The cells were tested at 60 ^{o}C in H_2/O_2 under a constant discharge current density of 100 mA cm^{-2}.

The stability of mesoporous Nafion and Nafion 112 membrane based fuel cells was evaluated as a function of RH. Figure 3.8 shows the cell voltage, measured at a constant discharge current density of 100 mA cm^{-2} and 60 ^{o}C under different RH. The RH decreased from 100 % to 0 % in decrements of 20 % every 20 h. For the 2D-H Nafion based fuel cell, the initial voltage was ~0.68 V at 100 % RH and 80 % RH was more or less stable. When RH descended to 60 %, the cell voltage slightly dropped to 0.65 V. The most interest observation is the stable performance observed on 2D-H Nafion membrane based fuel cell under 0 % RH. The initial cell voltage was 0.56 V and decreased to 0.47 V after 20 h of operation. This demonstrates that the highly ordered mesoporous Nafion membrane is able to operate under anhydrous conditions, clearly due to the extraordinary water retention ability of the ordered mesopores. This is consistent with the high proton conductivities of mesoporous Nafion at 0 % RH ($1.9 \times 10^{-2} - 3.8 \times 10^{-2}$ S cm^{-1} at 60 ^{o}C, Table 3.2). On the contrary, the cell of the conventional Nafion 112 membrane can only operate at high RH of 100 and 80 %. When the RH decreased to 60 %, the initial cell voltage was 0.54 V, and dropped very quickly to zero in 55 min (Figure 3.8). Under anhydrous conditions (*e.g.*, 0 % RH), the cell ceased to operate within 20 min (Figure 3.8 C). The rapid failure of cells based on conventional Nafion membrane under reduced RH clearly indicates the poor water retention properties of conventional Nafion membranes with random nanostructures. The stable cell performance of cells with a mesoporous Nafion membrane under low RH and anhydrous conditions confirms again the extraordinarily high water retention capacity of ordered mesoporous structured Nafion membranes, most likely due to the effective capillary condensation effect in ordered mesopores, as discussed above.

3.4 Conclusions

The formation of ordered and mesoporous structured phase in solution in Nafion-silica-SDA precursor solutions was studied for the first time using *in situ* time-resolved synchrotron SAXS technique. The results clearly demonstrate the formation of highly ordered and mesoporous Nafion-silica-SDA (P123 was used as the SDA in this study) structures in the presence of a silica colloidal mediator. Such formation of an ordered mesoporous phase in the solution is critical for the formation of a highly ordered mesoporous Nafion membrane with controlled structure symmetry from 2D

hexagonal, 3D face-centred, 3D cubic-bicontinuous to 3D body-centred.

The present study reported an effective synthesis strategy to introduce and control the mesoporous structure symmetry of PFSA-based membranes such as Nafion. The ability to introduce and control the mesoporous structure symmetries is important in the development of highly effective and functional PEMs for fuel cells. The results demonstrate that highly ordered mesoporous Nafion membranes have superior proton conductivity and enhanced electrochemical performance as compared to the pristine Nafion. Most importantly, the present study also demonstrated that mesoporous structured Nafion membranes based fuel cells can be operated under 0 % RH, *i.e.*, anhydrous conditions, an unique advantage over conventional Nafion membranes. Among the ordered mesoporous structures, 2D hexagonal exhibit the highest proton conductivity and the highest cell performance due to *meso*-morphology and the long-range periodicity which is facile for the proton transport and mass transfer.

References

[1] Y. Sone, P. Ekdunge, D. Simonsson, Proton conductivity of Nafion 117 as measured by a four-electrode AC impedance method, Journal of the Electrochemical Society 143 (4) (1996) 1254-1259.

[2] M.N. Silberstein, P.V. Pillai, M.C. Boyce, Biaxial elastic-viscoplastic behavior of Nafion membranes, Polymer 52 (2) (2011) 529-539.

[3] R. Solasi, X.Y. Huang, K. Reifsnider, Creep and stress-rupture of Nafion (R) membranes under controlled environment, Mechanics of Materials 42 (7) (2010) 678-685.

[4] H.W. Zhang, P.K. Shen, Advances in the high performance polymer electrolyte membranes for fuel cells, Chemical Society Reviews 41 (6) (2012) 2382-2394.

[5] L. Rubatat, O. Diat, Stretching effect on Nafion fibrillar nanostructure, Macromolecules 40 (26) (2007) 9455-9462.

[6] S.S. Jang, V. Molinero, T. Çağın, W.A. Goddard, Nanophase-Segregation and Transport in Nafion 117 from Molecular Dynamics Simulations: Effect of Monomeric Sequence, The Journal of Physical Chemistry B 108 (10) (2004) 3149-3157.

[7] K. Schmidt-Rohr, Q. Chen, Parallel cylindrical water nanochannels in Nafion fuel-cell membranes, Nature Materials 7 (1) (2008) 75-83.

[8] M.-H. Kim, C.J. Glinka, S.A. Grot, W.G. Grot, SANS Study of the Effects of Water Vapor Sorption on the Nanoscale Structure of Perfluorinated Sulfonic Acid (NAFION) Membranes, Macromolecules 39 (14) (2006) 4775-4787.

[9] O. Diat, G. Gebel, Fuel cells: Proton channels, Nature materials 7 (1) (2008) 13-14.

[10] J.L. Lu, S.F. Lu, S.P. Jiang, Highly ordered mesoporous Nafion membranes for fuel cells, Chemical Communications 47 (11) (2011) 3216-3218.

[11] J. Lu, H. Tang, C. Xu, S.P. Jiang, Nafion membranes with ordered mesoporous structure and high water retention properties for fuel cell applications, Journal of Materials Chemistry 22 (12) (2012) 5810-5819.

[12] G. Armatas, C. Salmas, M. Louloudi, G. Androutsopoulos, P. Pomonis, Relationships among pore size, connectivity, dimensionality of capillary condensation, and pore structure tortuosity of functionalized mesoporous silica, Langmuir 19 (8) (2003) 3128-3136.

[13] S. Dourdain, A. Gibaud, On the capillary condensation of water in mesoporous silica

films measured by x-ray reflectivity, Applied Physics Letters 87 (22) (2005) 223105-223105-223103.
[14] J. Li, H. Tang, L. Chen, R. Chen, M. Pan, S.P. Jiang, Highly ordered and periodic mesoporous Nafion membranes via colloidal silica mediated self-assembly for fuel cells, Chemical Communications 49 (58) (2013) 6537-6539.
[15] S. Manet, J. Schmitt, M. Imperor-Clerc, V. Zholobenko, D. Durand, C.L.P. Oliveira, J.S. Pedersen, C. Gervais, N. Baccile, F. Babonneau, I. Grillo, F. Meneau, C. Rochas, Kinetics of the Formation of 2D-Hexagonal Silica Nanostructured Materials by Nonionic Block Copolymer Templating in Solution, Journal of Physical Chemistry B 115 (39) (2011) 11330-11344.
[16] F. Michaux, N. Baccile, M. Imperor-Clerc, L. Malfatti, N. Folliet, C. Gervais, S. Manet, F. Meneau, J.S. Pedersen, F. Babonneau, In Situ Time-Resolved SAXS Study of the Formation of Mesostructured Organically Modified Silica through Modeling of Micelles Evolution during Surfactant-Templated Self-Assembly, Langmuir 28 (50) (2012) 17477-17493.
[17] Y. Wan, D.Y. Zhao, On the controllable soft-templating approach to mesoporous silicates, Chemical Reviews 107 (7) (2007) 2821-2860.
[18] J. Zeng, P.K. Shen, S.F. Lu, Y. Xiang, L. Li, R. De Marco, S.P. Jiang, Correlation between proton conductivity, thermal stability and structural symmetries in novel HPW-meso-silica nanocomposite membranes and their performance in direct methanol fuel cells, Journal of Membrane Science 397 (2012) 92-101.
[19] D. Zhao, J. Feng, Q. Huo, N. Melosh, G.H. Fredrickson, B.F. Chmelka, G.D. Stucky, Triblock Copolymer Syntheses of Mesoporous Silica with Periodic 50 to 300 Angstrom Pores, Science 279 (5350) (1998) 548-552.
[20] J. Fan, C. Yu, F. Gao, J. Lei, B. Tian, L. Wang, Q. Luo, B. Tu, W. Zhou, D. Zhao, Cubic Mesoporous Silica with Large Controllable Entrance Sizes and Advanced Adsorption Properties, Angewandte Chemie 115 (27) (2003) 3254-3258.
[21] D. Zhao, Q. Huo, J. Feng, B.F. Chmelka, G.D. Stucky, Nonionic Triblock and Star Diblock Copolymer and Oligomeric Surfactant Syntheses of Highly Ordered, Hydrothermally Stable, Mesoporous Silica Structures, Journal of the American Chemical Society 120 (24) (1998) 6024-6036.
[22] X. Liu, B. Tian, C. Yu, F. Gao, S. Xie, B. Tu, R. Che, L.-M. Peng, D. Zhao, Room-Temperature Synthesis in Acidic Media of Large-Pore Three-Dimensional Bicontinuous Mesoporous Silica with Ia3d Symmetry, Angewandte Chemie International Edition 41 (20) (2002) 3876-3878.
[23] G. Gebel, P. Aldebert, M. Pineri, Structure and Related Properties of Solution-cast Perfluorosulfonated Ionomer Films, Macromolecules 20 (6) (1987) 1425-1428.
[24] M. Fujimura, T. Hashimoto, H. Kawai, Small-Angle X-ray Scattering Study of Perfluorinated Ionomer Membranes. 1. Origin of 2 Scattering maxima, Macromolecules 14 (5) (1981) 1309-1315.
[25] J. Zeng, Y. Zhou, L. Li, S.P. Jiang, Phosphotungstic acid functionalized silica nanocomposites with tunable bicontinuous mesoporous structure and superior proton conductivity and stability for fuel cells, Physical Chemistry Chemical Physics 13 (21) (2011) 10249-10257.
[26] Y. Meng, D. Gu, F. Zhang, Y. Shi, L. Cheng, D. Feng, Z. Wu, Z. Chen, Y. Wan, A. Stein, D. Zhao, A Family of Highly Ordered Mesoporous Polymer Resin and Carbon Structures from Organic−Organic Self-Assembly, Chemistry of Materials 18 (18) (2006) 4447-4464.
[27] E.-B. Cho, S. Yim, D. Kim, M. Jaroniec, Surfactant-assisted synthesis of mesoporous silica/ceria-silica composites with high cerium content under basic conditions, Journal of Materials Chemistry A 1 (40) (2013) 12595-12605.
[28] D. Carmona, F. Balas, A. Mayoral, R. Luque, E.P. Urriolabeitia, J. Santamaria, Al-promoted increase of surface area and adsorption capacity in ordered mesoporous silica materials with a cubic structure, Chemical Communications 47 (45) (2011) 12337-12339.
[29] K. Flodstrom, C.V. Teixeira, H. Amenitsch, V. Alfredsson, M. Linden, In situ synchrotron small-angle X-ray scattering/X-ray diffraction study of the formation of SBA-15 mesoporous silica, Langmuir 20 (12) (2004) 4885-4891.
[30] H. Tang, Z. Wan, M. Pan, S.P. Jiang, Self-assembled Nafion-silica nanoparticles for elevated-high temperature polymer electrolyte membrane fuel cells, Electrochemistry Communications 9 (8) (2007) 2003-2008.

[31] Y. Wan, Zhao, On the Controllable Soft-Templating Approach to Mesoporous Silicates, Chemical Reviews 107 (7) (2007) 2821-2860.
[32] L. Chen, H. Tang, M. Pan, Periodic Nafion-silica-heteropolyacids electrolyte t for PEM fuel cell operated near 200 degrees C, International Journal of Hydrogen Energy 37 (5) (2012) 4694-4698.
[33] T.A. Zawodzinski, T.E. Springer, J. Davey, R. Jestel, C. Lopez, J. Valerio, S. Gottesfeld, A Comparative-Study of Water-Uptake by and Transport through Ionomeric Fuel-Cell Membranes, Journal of the Electrochemical Society 140 (7) (1993) 1981-1985.
[34] X.M. Yan, P. Mei, Y.Z. Mi, L. Gao, S.X. Qin, Proton exchange membrane with hydrophilic capillaries for elevated temperature PEM fuel cells, Electrochemistry Communications 11 (1) (2009) 71-74.
[35] F.N. Buchi, G.G. Scherer, Investigation of the transversal water profile in nafion membranes in polymer electrolyte fuel cells, Journal of the Electrochemical Society 148 (3) (2001) A183-A188.
[36] J. Zeng, S.P. Jiang, Characterization of High-Temperature Proton-Exchange Membranes Based on Phosphotungstic Acid Functionalized Mesoporous Silica Nanoconnposites for Fuel Cells, Journal of Physical Chemistry C 115 (23) (2011) 11854-11863.
[37] S. Fukada, K. Ohba, A. Nomura, Relation between water adsorption in polymer-electrolyte fuel cell and its electric power, Energy Conversion and Management 71 (0) (2013) 126-130.
[38] G.S. Hwang, M. Kaviany, J.T. Gostick, B. Kientiz, A.Z. Weber, M.H. Kim, Role of water states on water uptake and proton transport in Nafion using molecular simulations and bimodal network, Polymer 52 (12) (2011) 2584-2593.

Chapter 4 Amino-functionalized mesoporous silica based polyethersulfone-polyvinylpyrrolidone composite membrane for elevated temperature fuel cells

4.1 Introduction

The proton exchange membrane fuel cell shows superiorities of fast start-up and shut-down cycle in comparison with other fuel cells. It is, therefore, considered to be the most promising power generation technology for applications ranging from portable electronic devices, transportation vehicles to power stations. On the other hand, the low operation temperature (<80 ^{o}C) results in complex water managements [1] and CO poisoning to Pt catalysts from fuel gases [2]. However, the problems are diminished at elevated high temperatures (100 – 200 ^{o}C) for PEMFCs with improved catalyst kinetics, high fuel impurity tolerance as well as simplified water management systems.[3] Different from hydrated H^+ ions as proton conductor for PEMFCs operated at low temperatures, phosphoric acid (H_3PO_4) [4], ionic liquids [5] and heterocyclic compounds including imidazole [6] and triazole [7] have been investigated as alternative proton conductors in proton exchange membranes at elevated temperatures. Those alternative proton conductors allow for the reduced dependence on humidity and show the high proton conductivity at elevated temperatures. Among them, PA is probably one of the most promising proton conductors in that connection and has been extensively used in basic polymer-based PEMs such as polybenzimidazole [8-10] and pyridine containing aromatic polyethers [11]. PA-doped PBI membrane is the state-of-the-art PEMs operated at elevated temperatures, showing the high proton conductivity at low relative humidity as well as good thermal and oxidative stability.[12] However, the high proton conductivity of PA/PBI composite membrane strongly depends on high PA doping levels at temperatures above 160 ^{o}C, resulting in deterioration in the mechanical and thermal stability [13, 14]. Nevertheless, the fabrication of PBI is complex, impeding the wild application of the materials in fuel cells.

Recently, other basic polymer membranes were also employed as alternative high temperature proton transfer media, such as polyvinylpyrrolidone (PVP), and poly(4-vinylpyridine). Lu et al. synthesized the PA-doped polymer composite membrane by blending PVP with polyvinylidene fluoride (PVDF) [15] or poly(ether sulfone)

(PES) [16]. These membranes showed the excellent thermal stability and high proton conductivity at temperatures up to 180 ^{o}C.[16] Generally, for basic polymer based composite membranes, one phase supports the mechanical stability for the composite membrane, such as PVDF and PES, while the second phase plays the role as proton transportation network with liquid-like dynamics in nanoscale channels or pores formed in miscible blends, such as PVP.[13] Although the high amount of PVP content up to 80 wt.% guarantees the high proton conductivity comparable with the PA/PBI composite membrane at anhydrous conditions, it deteriorates the mechanical strength of the composite membrane with a tensile strength as low as 1.3 MPa [16].

The proton conductivity and mechanical strength of composite membranes can be improved by incorporating functionalized nano- or mesoporous silica materials such as phosphorylated hollow mesoporous silica (HMS) submicrospheres [17], PBI-functionalized silica nanoparticles [18], ionic liquid-functionalized mesoporous silica [19], phosphotungstic acid functionalized mesoporous silica [20], and proton conducting groups functionalized mesoporous silica [21]. Among them, functionalized HMS shows the high water uptake due to a large amount of lumen and facilitated proton transportation in the functionalized mesoporous silica channels. Jiang et al. found that the proton conductivity of recast Nafion membrane at low relativity humidity was improved 10 times after the addition of functionalized HMS with sulfonic acid, phosphoric acid and carboxylic acid groups.[22] Moreover, the phosphorylated HMS embedded chitosan membrane showed the high proton conductivity both at 100 % and 40 % RH in comparison with the pristine chitosan membrane.[17] In addition, an enhanced interfacial interaction and control over the interface can be achieved by grafting amino-groups on silica surface.[23] The amine-tailored silica material improves the interfacial compatibility between the PBI membrane and silica particles by the hydrogen bonding interaction between polybenzimidazole and amino-functionalized silica materials.[24] It has been reported that self-assembled amino-functionalized silica particle clusters enhanced the mechanical and thermal stability of PBI matrix, and the PA uptake as well as proton conductivity [25].

Herein, hollow mesoporous silica (HMS), amino-functionalized hollow mesoporous silica (NH_2-HMS) and mesoporous silica spheres (NH_2-*meso*-silica) were incorporated into the PES-PVP matrix to form nanostructured inorganic-organic composite membranes. The interfacial interaction of silica inorganic fillers

and polymer matrix were investigated in details. And the effects of morphology and functional groups of silica fillers on the proton conductivity of the composite membranes and the performance of the PES-PVP membrane fuel cells had been investigated. The results indicate that NH_2-HMS is the most promising filler for the PES-PVP based composite PEMs in the elevated temperature proton exchange membrane fuel cells.

4.2 Experimental

4.2.1 Mesoporous silica fabrication

Mesoporous silica (*meso*-silica) was prepared by mixing 2.5g CTAB and 15.2 g ammonium hydroxide solution ($NH_3 \bullet H_2O$, 28 wt.%) in 50 g Milli-Q water and 60 g ethanol, followed by an addition of 5 mL TEOS and vigorous stirred at room temperature for 2 h. The suspension was then centrifuged at 8000 rpm for 10 min, and the solid was washed twice by water and ethanol. The as-synthesized mesoporous silica powders were dried at 90 ^oC overnight, and then calcined in air at 550 ^oC for 6 h to remove the surfactant.

To synthesize HMS, the silica sphere template was obtained by a modified Stöber method.[26] Typically, 12 mL TEOS was added into a solution with 150 mL ethanol, 20 mL Milli-Q water and 6.3 mL $NH_3 \bullet H_2O$ (28 wt.%) and stirred at room temperature for 1h. After the centrifuge treatment, the solid silica spheres were washed by water and ethanol twice. Then the silica spheres were ultrasonicated at 500 mL water and 150 mL ethanol for 0.5 h. And the suspension was transferred into the CTAB solution with 3.0 g CTAB, 40 mL Milli-Q water, 20 mL ethanol, and 7.0 mL $NH_3 \bullet H_2O$ (28 wt.%). TEOS (4.5 mL) was added dropwise and stirred at room temperature overnight. Then the suspension was centrifuged at 8000 rpm for 5 min and the solid was redispersed at 500 mL water. After the addition of 10.5 g sodium carbonate (Na_2CO_3), the solution was etched at 60 ^oC for 12 h. Finally, the mesoporous silica powder was dried at 90 ^oC overnight, and the templates in the silica particles were removed by calcination in air at 550 ^oC for 6 h.

All the above chemicals were purchased from Sigma-Aldrich, Australia.

4.2.2 Amino-functionalization of mesoporous silica

Amino-functionalization *meso*-silica or HMS were prepared by dispersing 2.0 g mesoporous silica powder in 75 mL toluene. The suspension was refluxed at 110 ^{o}C in an oil bath for 20 h after the addition of 3.0 mL (3-aminopropyl)triethoxysilane (APTES) in 5 mL toluene under N_2 protection. The solid materials were finally washed by toluene for twice, and it was dried for future use. The amino-functionalized *meso*-silica and HMS were denoted as NH_2-*meso*-silica and NH_2-HMS, respectively.

4.2.3 PES-PVP composite membranes

Certain amount of mesoporous silica or amino-functionalized mesoporous silica materials were added into PES (Radel® A300, Solvay, Belgium) and PVP (PVP360, M_w = 360 000, Sigma-Aldrich, Australia) solution in N-methyl-2-pyrrolidone (NMP, Sigma-Aldrich, Australia) to form a slurry. The weight ratio for PVP to PES is 7:3, while the weight ratio of silica powders in the PES-PVP composite membranse is fixed at 2.0 wt.%. The slurry was poured into a petri dish and dried in the oven at 80 ^{o}C for 48 h. Membranes were peeled off from the petri dish and immersed in a 85 wt.% H_3PO_4 solution (Lab Service, Australia) for one week for PA doping.

The PES-PVP membranes with HMS, NH_2-HMS and NH_2-*meso*-silica were denoted as PES-PVP-H, PES-PVP-NH, and PES-PVP-NS, respectively, while the PA-doped PES-PVP composite membranes were denoted as PA/PES-PVP-H, PA/PES-PVP-NH, and PA/PES-PVP-NS.

4.2.4 Characterizations

Characterizations including synchrotron small-angle X-ray scattering, nitrogen adsorption isotherms, and thermogravimetric analysis are the same way as described in Section 3.2.3. Transmission electron microscopy (TEM) characterization is the same way as described in Section 3.2.3, except for the accelerating voltage of 120 kV.

Attenuated total reflectance Fourier Transform Infrared spectroscopy (ATR-FTIR) (zinc selenide top plate, Perkin-Elmer spectrum 100) was employed to record the grafting of the amino-functionalization of mesoporous silica materials, and the

interaction between the mesoporous silica materials and the PES-PVP matrix.

All nuclear magnetic resonance (NMR) spectra were measured at Bruker Avance III 500 MHz widebore NMR spectrometer equipped with a 4mm MAS probe. ^{13}C CP-MAS NMR spectra were recorded at 10 kHz MAS, while ^{29}Si MAS NMR spectra were measured using single pulse excitation sequence, with a small flip angle of 5 o and recycle delay of 40s, under 10 kHz MAS.

Scanning electron microscopy (SEM, Zeiss Neon 40 EsB) with accelerating voltage of 5 kV was employed to measure the cross-sectional morphology of the composite membranes.

Pt/C catalysts (50 % Pt/C, Alfa Aesar, USA) were used for the anode and cathode. Pt/C catalyst layers on Toray® TGP-H-060 carbon paper were hot pressed with PES-PVP composite membranes at 180 ^{o}C and 10 MPa to form the MEA. The loading for Pt and PVP ionomers (PVP40, Mw = 40 000, Sigma-Aldrich, Australia) in both anode and cathode was 0.35 and 0.18 mg cm^{-2}, respectively. Then the MEA was placed in a single-cell hardware (active area 4.0 cm^{-2}) for the cell performance measurement using a Greenlight G20 fuel cell test station. H_2 and O_2 (dry gas) flow rates were 50 and 100 mL min^{-1}, respectively. The proton conductivity of PES-PVP based composite membranes was measured using electrochemical impedance spectroscopy technique at frequencies ranging from 100 KHz to 10 Hz.

4.3 Results and discussion

4.3.1 Formation of amino-functionalized mesoporous silica materials

Figure 4.1 shows the TEM micrographs of HMS, NH_2-HMS and NH_2-*meso*-silica. For the fabrication of HMS, solid silica spheres with an average size of 260 nm derived from the Stöber method [26] were covered by mesoporous silica shells with the surfactant of CTAB in the mesopores. When the core-shell particles were exposed to the Na_2CO_3 solution, the solid SiO_2 core was selectively etched out while the shell remained intact with oriented mesoporous structure with thickness of 60 nm, forming hollow mesoporous silica (Figure 4.1A). That is due to the fact that the silicate-CTAB mesoporous shell is more stable than the inner solid SiO_2 core at the alkaline condition.[26] The pore channels in HMS were aligned perpendicularly to the surface of the spheres, as shown in Figure 4.1B. After the post-grafting of amino-groups, the morphology of HMS was still intact with mesoporous shell and hollow

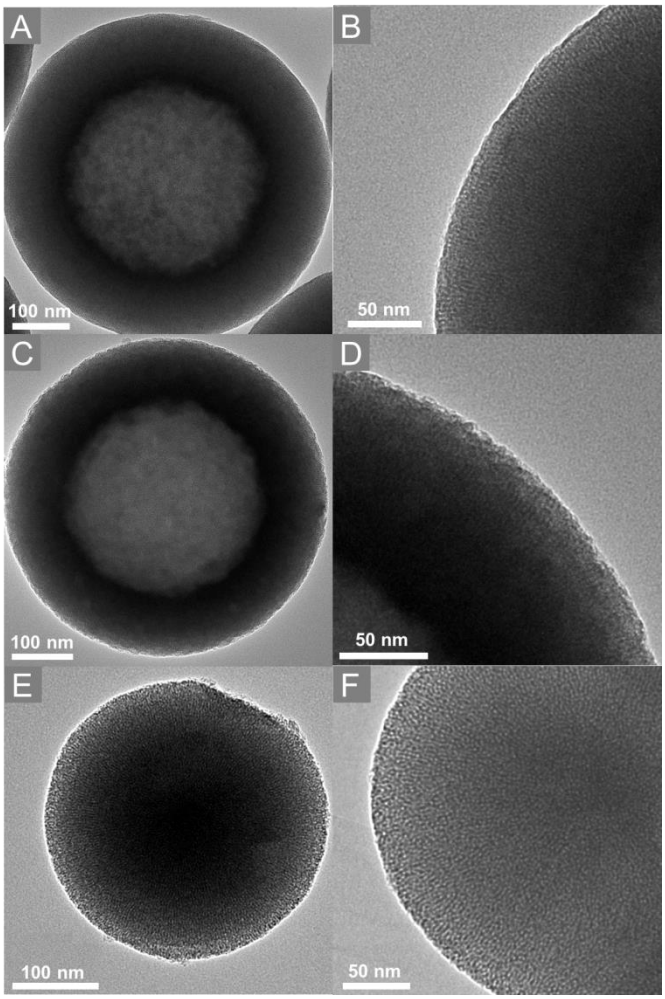

Figure 4.1 TEM images of (A, B) HMS, (C, D) NH_2-HMS and (E, F) NH_2-*meso*-silica.

structure (Figure 4.1C and D). Worm-like mesoporous channels directed from the centre to the edge of the spheres were observed for NH_2-*meso*-silica, as shown in Figure 4.1E and F. The average particle size was 350 nm.

Figure 4.2 shows N_2 adsorption/desorption isotherms of mesoporous silica and amino-functionalized mesoporous silica materials. The adsorption isotherms show type IV adsorption curves with H2 type hysteresis, characteristic of mesoporous materials (Figure 4.2A) [27]. The BET surface area of HMS was 1275 m^2g^{-1}. After the amino-functionalization, the surface area of NH_2-HMS was reduced to 1069 m^2g^{-1}, which is higher than 592 m^2g^{-1} for NH_2-*meso*-silica. This may be due to the large lumen of NH_2-HMS.[28] Moreover, the pore size of HMS decreased from 2.9 to 2.6 nm (Figure 4.2B), while the pore volume dropped from 1.03 cm^3g^{-1} for HMS to 0.72 cm^3g^{-1} after the amino-functionalization. The reduced pore size and pore volume indicate the successful grafting of $–NH_2$ group on the surface of the mesoporous channels of HMS [29]. Based on the TGA analysis, the content of amino-groups in

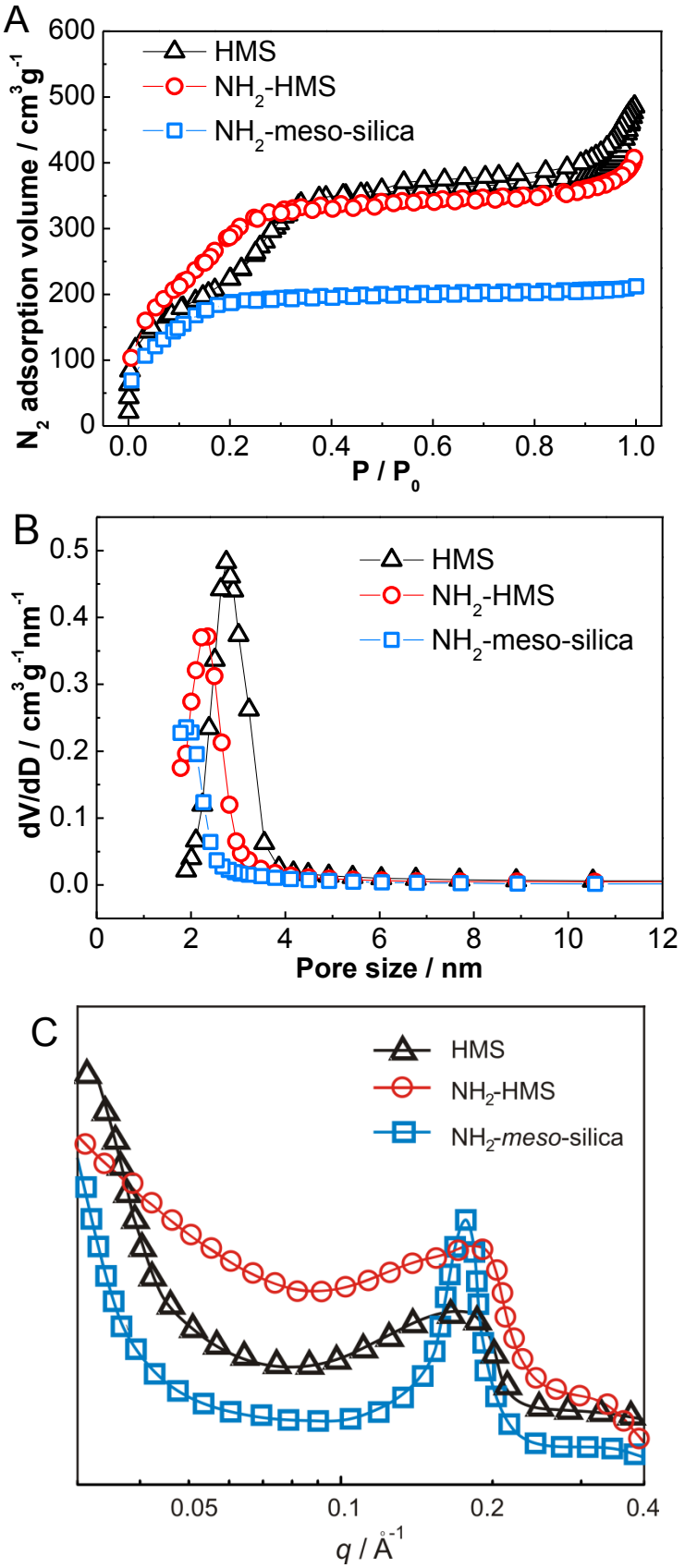

Figure 4.2 (A) N_2 adsorption isotherms, (B) pore size distributions and (C) SAXS profiles of mesoporous silica and amino-functionalized mesoporous silica materials.

Table 4.1 Physical properties of mesoporous silica and amino-functionalized mesoporous silica materials.

samples	-NH_2 content (wt.%)	BET surface area (m^2 g^{-1})	Pore size (nm)	Pore volume (cm^3g^{-1})
HMS	–	1275	2.9	1.03
NH_2-HMS	9.8 (1.69 mmol)	1069	2.6	0.72
NH_2-*meso*-silica	9.2 (1.58 mmol)	592	2.2	0.32

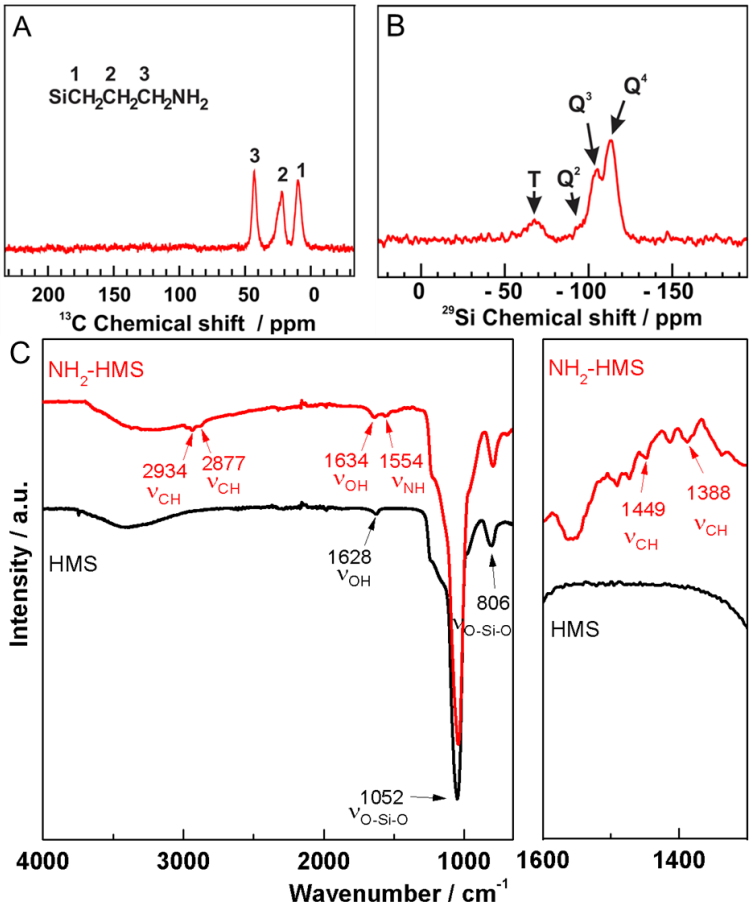

Figure 4.3 (A) ^{13}C CP/MAS and (B) ^{29}Si MAS NMR of NH_2-HMS and (C) ATR-FTIR spectra of mesoporous silica and amino-functionalized mesoporous silica.

NH_2-HMS and NH_2-*meso*-silica was 9.8 and 9.2 %, respectively, corresponding to 1.69 and 1.58 mmol. Physical properties of HMS, NH_2-HMS and NH_2-*meso*-silica were listed in Table 4.1.

The mesoporous structure of amino-functionalized mesoporous silica was confirmed by synchrotron small angle X-ray scattering, as shown in Figure 4.2C. A broad peak was observed in the SAXS curve of HMS, indicating the oriented pore structure of the mesoporous silica materials. That is consistent with the observation of ordered mesoporous shell structure in the TEM image in Figure 4.1 [30]. After

grafting of $–NH_2$ groups, the scattering peak increased to a high q value, indicating the decrease of the pore size. On the other hand, NH_2-*meso*-silica shows a sharp peak in comparison with HMS and NH_2-HMS, suggesting higher level of orientation of the mesoporous channels [31].

The successful incorporating of amine group on HMS has been confirmed by solid-state ^{13}C CP/MAS NMR as shown in Figure 4.3A. The relevant carbon signals at 10, 22, 42 ppm correspond to the carbon atoms at $–SiCH_2CH_2CH_2NH_2$ [32]. In the ^{29}Si MAS NMR spectra of the hybrid particles, the peak signal at -66 ppm corresponds to the silicon connected to the amino group (Figure 4.3B), suggesting the condensation of APTES in HMS. It is noted that signals of incompletely hydrolysed silanes and templates which would appear around 59 and 14 ppm are absent in ^{13}C CP/MAS NMR, indicating the completely hydrolysed silanes and the template removal.[33]

The amino-functionalization of mesoporous silica was further confirmed by the ATR-FTIR characterization (Figure 4.3C). Take HMS as examples, the most intensive band, centred at 1052 cm^{-1} is associated with the SiO_4 $v_3(F_2)$ stretching vibration. The band at 806 cm^{-1} corresponds to the SiO_4 $v_1(A)$ stretching vibration. The peak at 1628 cm^{-1} is due to the stretching and bending vibrations of water molecules adsorbed on the surface of HMS. When HMS was functionalized by amino-group, in addition to peaks associated with mesoporous silica, new peaks centred at 2934 and 2877 cm^{-1} were detected, corresponding to the stretching vibrations of the CH group, while the peaks at 1449 and 1388 cm^{-1} belong to the bending vibrations of those groups. Furthermore, the unique peak at 1554 cm^{-1} belongs to the bending vibration of N-H groups. It should be noticed that the C-N stretching vibration in the region of 1030 – 1230 cm^{-1} overlap with the broad peak of silanol groups and the Si-O-Si vibration.[34] The results indicate that the $–NH_2$ group has been successfully anchored onto the surface of mesoporous silica.

4.3.2 Properties of amino-functionalized mesoporous silica based PES-PVP composite membranes

Figure 4.4 shows micrographs of cross-sections of the pristine PES-PVP membrane and silica/PES-PVP composite membranes. The pristine PES-PVP membrane shows smooth cross-sectional morphology (Figure 4.4A), indicating dense and

homogeneous *micro*-structure. After the addition of 2.0 wt.% of inorganic silica fillers into PES-PVP membrane, individual spheres of HMS (Figure 4.4B), NH_2-*meso*-silica (Figure 4.4C) and NH_2-HMS (Figure 4.4D) were clearly observed in the polymer matrix instead of aggregation. That indicates that silica spheres are homogeneously dispersed on the polymer matrix with good interfacial contact with the matrix, although the addition of inorganic fillers increases the roughness of the membrane (inset images). Nevertheless, when excess inorganic mesoporous materials are added into the polymer matrix, it would aggregate in the polymer host [35, 36], which prevents the proton transportation in the polymer matrix [37]. Consequently, the silica filler in the PES-PVP matrix is fixed at a low loading of 2 wt.%. Occasionally, void structure of HMS was observed (indicated by arrow, Figure 4.4B).

The characteristic peak of C=O stretching vibration was observed at 1648 cm^{-1} in the ATR-FTIR spectrum of PVP in the PES-PVP membrane (Figure 4.5A) [38]. And a strong peak at 1149 cm^{-1} can be assigned to the symmetric stretch peak of O=S=O in PES [39]. Moreover, the absorption peaks at 1461 and 1422 cm^{-1} were characteristic adsorptions of the pyrrolidinyl groups in PVP, as shown in Table 4.2.[40] Two characteristic intense bands associated with aromatic CH vibration are present at 3096 and 3068 cm^{-1}, and aromatic skeletal and asymmetric stretching vibrations at 1577 and 1486 cm^{-1} are characteristic of PES [41]. When silica fillers

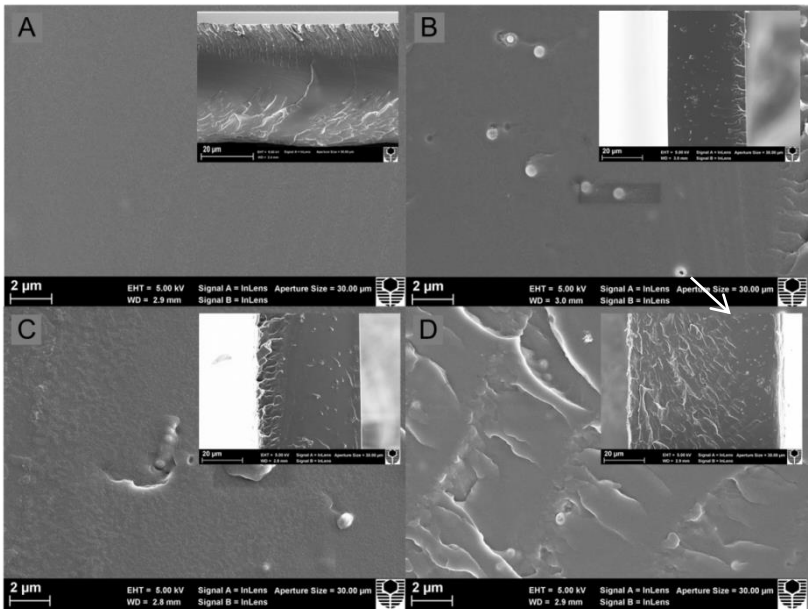

Figure 4.4 Cross-sectional SEM images of the PES-PVP composite membranes with (A) pristine PES-PVP, (B) PES-PVP-H, (C) PES-PVP-NS and (D) PES-PVP-NH. Insets are cross-section images of the composite membranes in large scale.

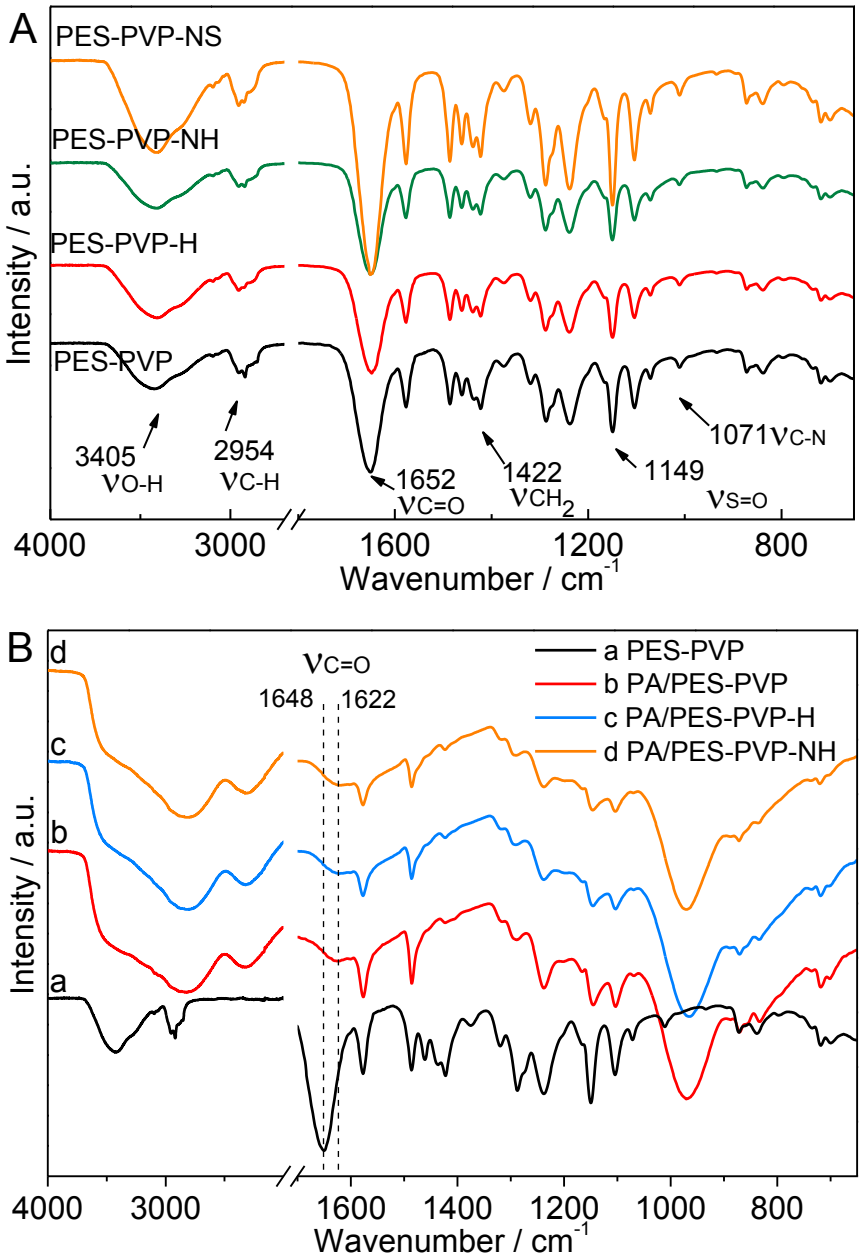

Figure 4.5 ATR-FTIR profiles of (A) PES-PVP composite membranes and (B) PA-doped PES-PVP composite membranes with different silica materials.

were incorporated into the PES-PVP matrix, they could not be distinguished by the ATR-FTIR spectroscopy due to the inherent existence of the amide group in PVP and the overlap for the O-Si-O bands. However, as compared with the corresponding absorption peak of the pristine PES-PVP membrane, the peak at 1652 cm^{-1} red-shifted to 1648 cm^{-1} in the PES-PVP-H membrane. On the contrary, the peak was fixed in PES-PVP-NH and PES-PVP-NS membranes. Consequently, the red-shift in wavenumber for the C=O absorption derives from OH groups and is likely due to the donation of O in C=O to OH groups in HMS, an indication of the formation of

hydrogen bonding between OH and C=O groups.

For the PA-doped PES-PVP composite membrane, there was a broad peak in the range of 1050 – 900 cm^{-1}, which is attributed to the free phosphoric acid molecules (Figure 4.5B) [42]. Moreover, the C=O bond in PES-PVP red-shifted from 1652 to 1624 cm^{-1} after PA doping. The red shift of C=O bond suggest weak interaction with OH group of PA molecules via hydrogen bonding. Furthermore, the peak was shift to 1622 and 1620 cm^{-1} in PA/PES-PVP-HMS and PA/PES-PVP-NH membranes, respectively. Generally, -OH and -NH_2 groups are protonated under acid condition to form –OH_2^+ and -NH_3^+.[43] And the protonated groups tend to form the hydrogen bond with C=O in PVP, leading the red shift of the peak of C=O. Table 4.2 lists the peak positions of the PES-PVP composite membranes with different silica fillers.

The thermal stability of the silica/PES-PVP composite membranes is another critical criterion for the elevated temperature fuel cells application, as shown in Figure 4.6. For the pristine PES-PVP membrane, the weight loss below 100 ^oC is due to the evaporation of adsorbed moisture. The second weight loss started from around 300 ^oC corresponds to the degradation of PVP, while the third weight loss about 500 ^oC results from the degradation of PES [16]. Nevertheless, PES-PVP-H, PES-PVP-NH and PES-PVP-NS membranes show higher degradation temperature for PVP than the pristine PES-PVP membrane, as shown in Figure 4.6. The result indicates that the addition of mesoporous silica materials indicates the positive effect of inorganic silica materials on the thermal stability of PVP.

Table 4. 2 Peaks of PES-PVP membranes with different fillers.

Peaks	Wavenumber	polymer
S=O symmetric stretch	1149	PES
CSO_2C asymmetric stretch	1319	PES
C-O asymmetric stretch	1238	PES
C_6H_6 ring stretch	1577, 1486	PES
C-H stretch	3098, 3068	PES
C-H phenyl	1011	PES
C-S stretch	719	PES
O-H stretch	3405	PVP, PES
C=O stretch	1648	PVP
C-H asymmetric stretch	2954	PVP
C-N vibration	1011	PVP
pyrrolidinyl	1461,1422	PVP

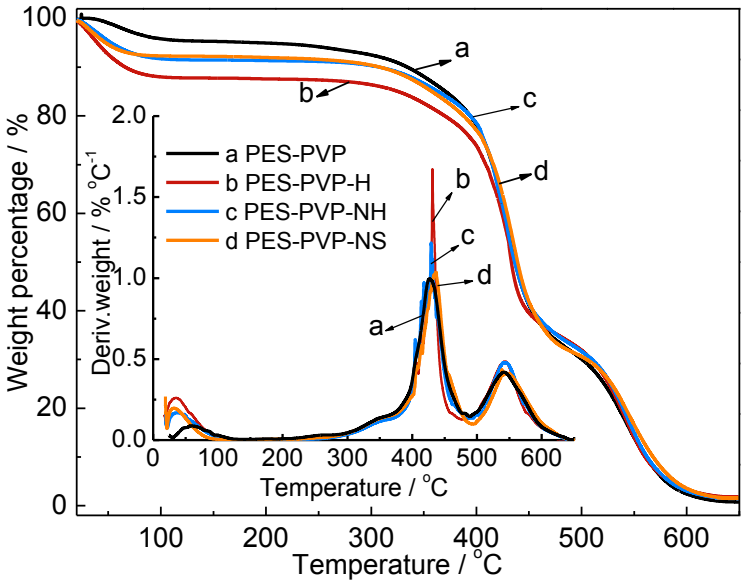

Figure 4.6 TGA profiles of the PES-PVP composite membranes with different types of silica fillers. Inset is the image of derivation weight as a function of temperatures.

Table 4.3 Volume swelling, acid doping of the blend composite membranes and proton conductivity of PA-doped PES-PVP composite membranes under anhydrous condition at different temperatures.

Samples	Volume Swelling,%	Acid doping, wt.%	Proton conductivity, × 10^{-2} S cm^{-1}			
			120 °C	140 °C	160 °C	180 °C
PA/PES-PVP	263	303	7.80	9.20	10.6	11.4
PA/PES-PVP-H	149	252	9.90	12.3	13.7	14.2
PA/PES-PVP-NH	217	245	11.8	13.7	14.8	15.2
PA/PES-PVP-NS	253	246	8.90	10.4	12.4	12.8

Table 4.3 summarizes the PA uptake and volume swelling ratios of PES-PVP composite membranes. The PA uptake of pristine PES-PVP composite membrane was 303 wt.%, and the volume swelling ratio was 263 %. When inorganic materials were added into the composite membranes, the PA uptake slightly decreased to 252 wt.%, 245 wt.% and 246 wt.% for PA/PES-PVP-H, PA/PES-PVP-NH, and PA/PES-PVP-NS composite membranes, respectively. This may be due to the diluted acid adsorption sites after the addition of silica materials in polymer matrix [44]. Moreover, PA/PES-PVP-NH and PA/PES-PVP-NS shows higher volume swelling ratio than that of PA/PES-PVP-H, but lower than that of the pristine PES-PVP composite membrane, indicating the hindrance effect of silica fillers for the volume swelling of the PES-PVP membrane. The lower volume swelling of PES-PVP composite membranes after the addition of silica fillers is likely due to the weak interaction of silica and PVP molecules, as indicated by ATR-FTIR characterization.

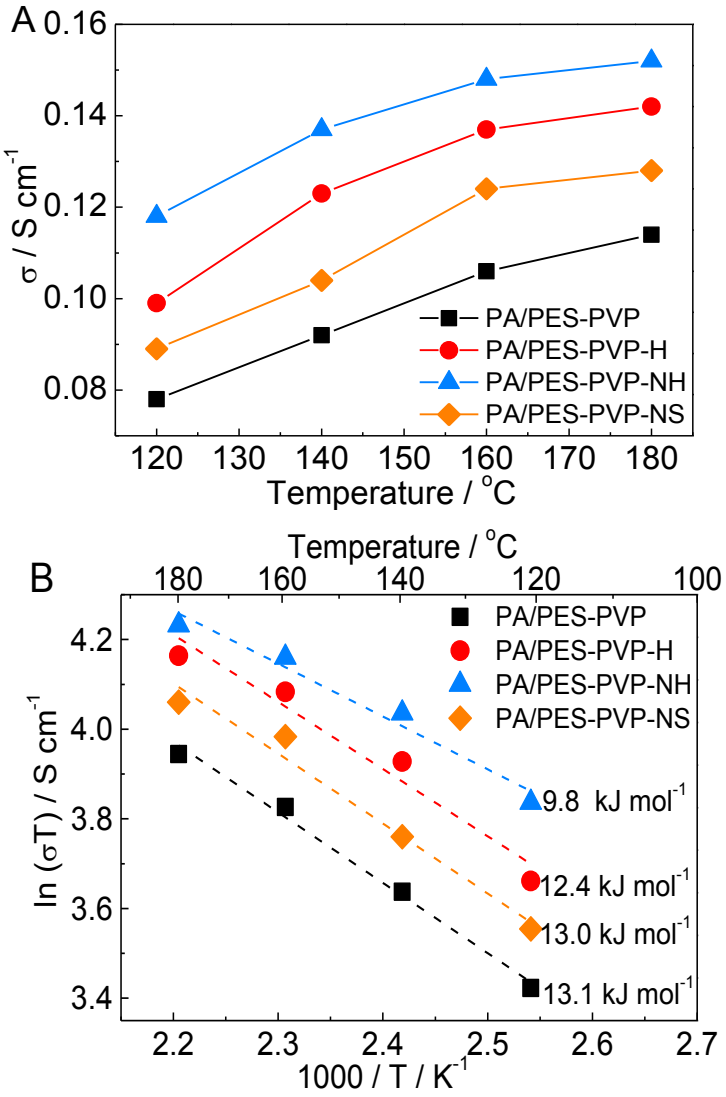

Figure 4.7 (A) Proton conductivity and (B) activation energy for proton transportation of PA-doped based PES-PVP composite membranes under anhydrous conditions.

Figure 4.7 shows the proton conductivity of the PA-doped PES-PVP composite membranes. The proton conductivity of the pristine PA/PES-PVP membrane was 7.80×10^{-2} S cm^{-1} at 120 °C, anhydrous condition. And it increased to 1.14×10^{-1} S cm^{-1} when the temperature was improved to 180 °C. The conductivity value is between the reported proton conductivity of PA-doped PES-PVP composite membranes with 60 wt.% and 80 wt.% PVP. The addition of inorganic silica fillers to the PA/PES-PVP membrane enhances the proton conductivity of the membrane. The proton conductivity of the PA/PES-PVP-H composite membrane increased to 1.42×10^{-1} S cm^{-1} at 180 °C. And the proton conductivity further increased to 1.52×10^{-1} S

cm^{-1} for the PA/PES-PVP-NH membrane. The proton conductivity of the PA/PES-PVP-NH membrane is significantly better than ~2.0×10^{-2} S cm^{-1} of the state-of-the-art PA/PBI membranes measured under the similar condition [44, 45]. The excellent conductivity of the PA/PES-PVP-NH membrane can be contributed to the fact that –NH_2 groups in the highly ordered channels of mesoporous silica are favour to form effective proton conducting paths to improve the proton conductivity [25]. The PA/PES-PVP-NH membrane also shows superior proton conductivity as compared to the PA/PES-PVP-NS membrane, although NH_2-HMS and NH_2-*meso*-silica have the comparable –NH_2 content and both of the membranes have similar PA uptake.

To further investigate the proton conduction mechanism, the activation energy for the proton transportation in different PA-doped silica/PES-PVP composite membranes was calculated via the Arrhenius equations, as shown in Figure 4.7B. The activation energy for the PA/PES-PVP membrane was 13.1 kJ mol^{-1}, which is slightly higher than that of PA/PES-PVP-H and PA/PES-PVP-NS membranes. For the pristine PA/PES-PVP membrane, protons in PA molecules tend to interact with oxygen in the C=O group of PVP molecules via hydrogen bond, and then protons are hopped to neighbour units[46]. On the other hand, protons in free acid at a high PA doping level hop along the mixed anion chains of $H_2PO_4^-$/HPO_4^{2-} under the anhydrous condition [47]. The high activation energy of PA/PES-PVP membrane indicates that the proton transportation in the membranes is primarily via Grotthuss mechanism [48]. On the other hand, in the case of PA/PBI membranes, it has been revealed that when the activation energy of PA/PBI is in the range of 8 – 10 kJ mol^{-1} that is close to that of H_3PO_4 solution with a concentration range of 85 – 93 wt.%, PA would perform in the state of quasi-liquid like conductor due to the presence of water molecules [49]. Thus, the low activation energy of PA/PES-PVP-NH membrane indicates the high water retention capability of NH_2-HMS for the PES-PVP membrane at elevated temperatures under anhydrous conditions.

Figure 4.8 shows the cell performance of PA-doped silica/PES-PVP composite membranes based fuel cells. The open circuit voltage for all the fuel cells was ~0.9 V, indicating the low H_2 permeation. That is likely attributed to the dense structure of the silica/PES-PVP inorganic-organic hybrid composite membranes. The peak power density of the PA/PES-PVP membrane fuel cell was 105 mW cm^{-2} at 120 ^oC without external humidification (Figure 4.8A). And it increased to 249 mW cm^{-2} when the temperature arose to 180 ^oC. Fuel cells based on PES-PVP composite membranes

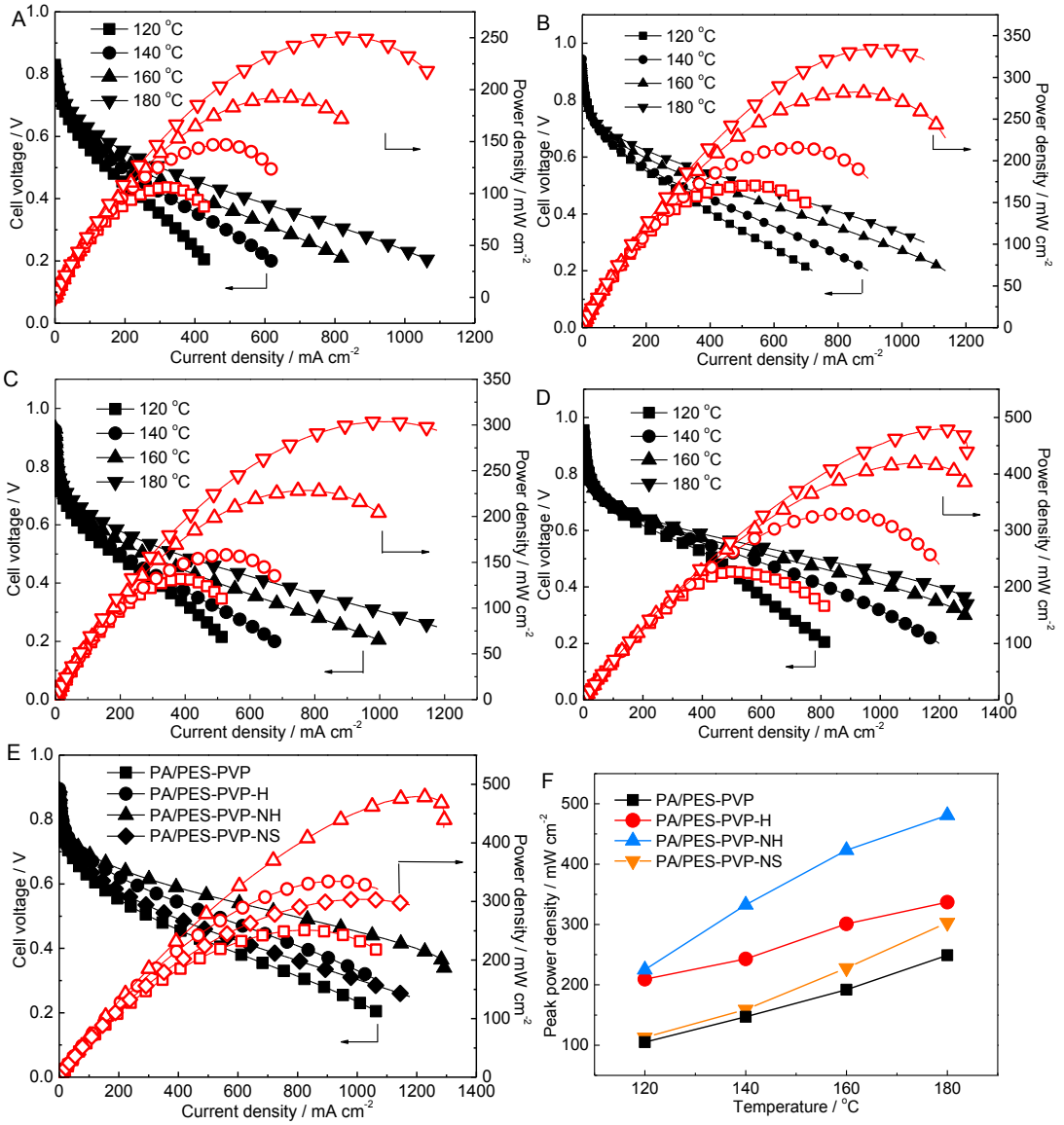

Figure 4.8 Single cell performance of PA-doped silica/PES-PVP composite membranes for (A) PA/PES-PVP, (B) PA/PES-PVP-H, (C) PA/PES-PVP-NS, and (D) PA/PES-PVP-NH. (E) is the comparison of the cell performance at 180 °C and (F) is the peak power density as a function of temperature.

with inorganic fillers demonstrate higher power output than the pristine PA/PES-PVP membrane fuel cell because of the increased proton conductivity, as shown in Figure 4.8E. The peak power density of PA/PES-PVP-H membrane fuel cell increased to 337 mW cm^{-2} at 180 °C (Figure 4.8B). Furthermore, the power density significantly increased to 480 mW cm^{-2} for PA/PES-PVP-NH (Figure 4.8D), which is 92.7 % higher than that of the pristine PA/PES-PVP membrane measured under the identical condition. The peak power density of the fuel cells at different temperatures are summarized in Figure 4.8F, and the value follows the order of PA/PES-PVP-NH > PA/PES-PVP-H> PA/PES-PVP-NS (Figure 4.8C) > PA/PES-PVP.

In the PES-PVP composite membrane, PES primarily functions as the support for the mechanical property and stability of the composite membrane, while PVP plays the role as the proton transportation network in nanoscale domains. Figure 4.9 shows schematically the proton conduction mechanism and role of amino-functionalized mesoporous silica in PES-PVP composite membranes, taking NH_2-HMS as example. First, functionalized amino group favours to form the hydrogen-bond network with PA in the mesoporous channels and the void in NH_2-HMS might serve as an acidic reservoir [17]. Second, the superior water retention capability at elevated temperatures and anhydrous conditions of NH_2-HMS promotes the proton transportation and cell performance for the PES-PVP membrane. Third, the short distance in the mesoporous shell improves the efficiency for proton diffusion than long channels in NH_2-*meso*-silica [5]. Due to the low proton activation energy of the PA/PES-PVP-NH, protons are transferred along the functional unit in PVP and mixed anion chains of $H_2PO_4^-/HPO_4^{2-}$ in the polymeric matrix. Furthermore, the presence of water in the NH_2-HMS structure also provides the quasi-liquid like conduction of protons.

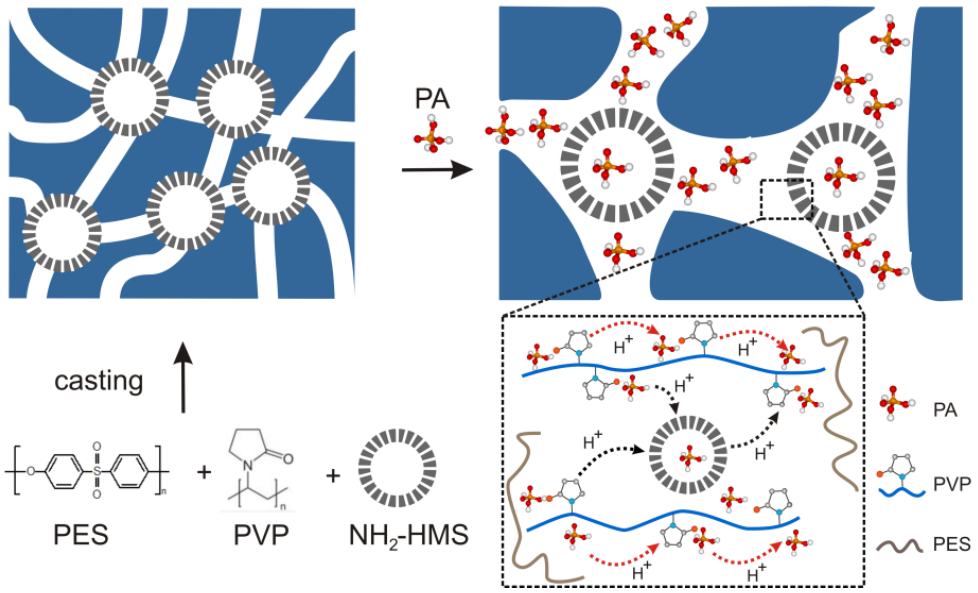

Figure 4.9 The scheme for the formation and proton transportation of mesoporous silica based PES-PVP composite membranes.(Take PA/PES-PVP-NH as example.)

4.4 Conclusions

Three types of mesoporous silica materials were incorporated into the matrix of PES-PVP membrane. In comparison with the pristine PA-doped PES-PVP membrane, the inorganic-organic hybrid composite membranes showed lower PA uptake and higher proton conductivity, which was up to 1.52×10^{-1} S cm^{-1} at 180 ^{o}C with the addition of NH_2-HMS. The high proton conductivity is due to the facilitated proton transportation in the ordered mesoporous channels via the hydrogen bonds between the $–NH_2$ groups and H_3PO_4. Furthermore, the PA-doped PES-PVP composite membrane with NH_2-HMS showed low activation energy (9.8 kJ mol^{-1}), indicating the presence of water for the assistance of proton transportation. Cell performance also confirms the superiority of the addition of inorganic fillers in the PES-PVP membrane, and the highest peak power density at 180 ^{o}C without external humidification reached up to 480 mW cm^{-2} for the PA/PES-PVP-NH membrane, which is 92.7 % higher than that of PA/PES-PVP tested at the same condition. Overall, the inorganic-organic composite membranes based on amino-functionalized hollow mesoporous silica materials show promising potential in the application of elevated temperature proton exchange membrane fuel cells.

References

[1] K. Jiao, X. Li, Water transport in polymer electrolyte membrane fuel cells, Progress in Energy and Combustion Science 37 (3) (2011) 221-291.

[2] B.P. Tripathi, V.K. Shahi, Organic–inorganic nanocomposite polymer electrolyte membranes for fuel cell applications, Progress in Polymer Science 36 (7) (2011) 945-979.

[3] Q. Li, R.H. He, J.O. Jensen, N.J. Bjerrum, Approaches and recent development of polymer electrolyte membranes for fuel cells operating above 100 degrees C, Chemistry of Materials 15 (26) (2003) 4896-4915.

[4] J. Zeng, B. He, K. Lamb, R. De Marco, P.K. Shen, S.P. Jiang, Phosphoric acid functionalized pre-sintered meso-silica for high temperature proton exchange membrane fuel cells, Chemical Communications 49 (41) (2013) 4655-4657.

[5] Y.-S. Ye, G.-W. Liang, B.-H. Chen, W.-C. Shen, C.-Y. Tseng, M.-Y. Cheng, J. Rick, Y.-J. Huang, F.-C. Chang, B.-J. Hwang, Effect of morphology of mesoporous silica on characterization of protic ionic liquid-based composite membranes, Journal of Power Sources 196 (13) (2011) 5408-5415.

[6] R. Marschall, M. Sharifi, M. Wark, Proton conductivity of imidazole functionalized ordered mesoporous silica: Influence of type of anchorage, chain length and humidity, Microporous and Mesoporous Materials 123 (1–3) (2009) 21-29.

[7] S.J. Park, D.H. Lee, Y.S. Kang, High temperature proton exchange membranes based on triazoles attached onto SBA-15 type mesoporous silica, Journal of Membrane Science 357 (1-2) (2010) 1-5.

[8] E. Quartarone, P. Mustarelli, Polymer fuel cells based on polybenzimidazole/H3PO4, Energy & Environmental Science 5 (4) (2012) 6436-6444.

[9] Q. Li, J.O. Jensen, R.F. Savinell, N.J. Bjerrum, High temperature proton exchange

membranes based on polybenzimidazoles for fuel cells, Prog. Polym. Sci. 34 (5) (2009) 449-477.
[10] T. Steenberg, H.A. Hjuler, C. Terkelsen, M.T.R. Sanchez, L.N. Cleemann, F.C. Krebs, Roll-to-roll coated PBI membranes for high temperature PEM fuel cells, Energy & Environmental Science 5 (3) (2012) 6076-6080.
[11] J.K. Kallitsis, M. Geormezi, S.G. Neophytides, Polymer electrolyte membranes for high-temperature fuel cells based on aromatic polyethers bearing pyridine units, Polymer International 58 (11) (2009) 1226-1233.
[12] D. Aili, L.N. Cleemann, Q. Li, J.O. Jensen, E. Christensen, N.J. Bjerrum, Thermal curing of PBI membranes for high temperature PEM fuel cells, Journal of Materials Chemistry 22 (12) (2012) 5444-5453.
[13] Z. Guo, R. Xiu, S. Lu, X. Xu, S. Yang, Y. Xiang, Submicro-pore containing poly(ether sulfones)/polyvinylpyrrolidone membranes for high-temperature fuel cell applications, Journal of Materials Chemistry A 3 (16) (2015) 8847-8854.
[14] S. Yu, L. Xiao, B.C. Benicewicz, Durability Studies of PBI-based High Temperature PEMFCs, Fuel Cells 8 (3-4) (2008) 165-174.
[15] Z. Guo, X. Xu, Y. Xiang, S. Lu, S.P. Jiang, New anhydrous proton exchange membranes for high-temperature fuel cells based on PVDF-PVP blended polymers, Journal of Materials Chemistry A 3 (1) (2015) 148-155.
[16] X. Xu, H. Wang, S. Lu, Z. Guo, S. Rao, R. Xiu, Y. Xiang, A novel phosphoric acid doped poly(ethersulphone)-poly(vinyl pyrrolidone) blend membrane for high-temperature proton exchange membrane fuel cells, Journal of Power Sources 286 (2015) 458-463.
[17] Y. Zhao, H. Yang, H. Wu, Z. Jiang, Enhanced proton conductivity of hybrid membranes by incorporating phosphorylated hollow mesoporous silica submicrospheres, Journal of Membrane Science 469 (2014) 418-427.
[18] Suryani, Y.-N. Chang, J.-Y. Lai, Y.-L. Liu, Polybenzimidazole (PBI)-functionalized silica nanoparticles modified PBI nanocomposite membranes for proton exchange membranes fuel cells, Journal of Membrane Science 403–404 (2012) 1-7.
[19] A.K. Mishra, N.H. Kim, J.H. Lee, Effects of ionic liquid-functionalized mesoporous silica on the proton conductivity of acid-doped poly(2,5-benzimidazole) composite membranes for high-temperature fuel cells, Journal of Membrane Science 449 (2014) 136-145.
[20] L. Zhang, H.Q. He, R.K. S/O Abdul Rasheed, W.J. Zhou, Y.H. Xue, O.L. Ding, S.H. Chan, Fabrication of novel phosphotungstic acid functionalized mesoporous silica composite membrane by alternative gel-casting technique, Journal of Power Sources 221 (2013) 318-327.
[21] Y. Zhao, H. Yang, H. Wu, Z. Jiang, Enhanced proton conductivity of the hybrid membranes by regulating the proton conducting groups anchored on the mesoporous silica, Journal of Power Sources 270 (2014) 292-303.
[22] Y. Yin, W. Deng, H. Wang, A. Li, C. Wang, Z. Jiang, H. Wu, Fabrication of hybrid membranes by incorporating acid-base pair functionalized hollow mesoporous silica for enhanced proton conductivity, Journal of Materials Chemistry A 3 (31) (2015) 16079-16088.
[23] Q. Li, H. Zhang, Z. Tu, J. Yu, C. Xiong, M. Pan, Impregnation of amine-tailored titanate nanotubes in polymer electrolyte membranes, Journal of Membrane Science 423 (2012) 284-292.
[24] S. Ghosh, S. Maity, T. Jana, Polybenzimidazole/silica nanocomposites: Organic-inorganic hybrid membranes for PEM fuel cell, Journal of Materials Chemistry 21 (38) (2011) 14897-14906.
[25] S. Singha, T. Jana, Structure and Properties of Polybenzimidazole/Silica Nanocomposite Electrolyte Membrane: Influence of Organic/Inorganic Interface, Acs Applied Materials & Interfaces 6 (23) (2014) 21286-21296.
[26] S. Zhu, L. Yan, D. Zhang, Q. Feng, Molecular dynamics simulation of microscopic structure and hydrogen bond network of the pristine and phosphoric acid doped polybenzimidazole, Polymer 52 (3) (2011) 881-892.
[27] X. Fang, Z. Liu, M.-F. Hsieh, M. Chen, P. Liu, C. Chen, N. Zheng, Hollow Mesoporous Aluminosilica Spheres with Perpendicular Pore Channels as Catalytic Nanoreactors, ACS Nano 6 (5) (2012) 4434-4444.
[28] A. Danon, P.C. Stair, E. Weitz, FTIR Study of CO2 Adsorption on Amine-Grafted SBA-15: Elucidation of Adsorbed Species, The Journal of Physical Chemistry C 115 (23) (2011) 11540-11549.
[29] X. She, L. Chen, C. Li, C. He, L. He, L. Kong, Functionalization of Hollow Mesoporous

Silica Nanoparticles for Improved 5-FU Loading, Journal of Nanomaterials 2015 (2015) 9.
[30] N. Venkatathri, Synthesis of a mesoporous silica hollow microsphere using polyvinyl alcohol, Materials Science and Engineering: C 28 (8) (2008) 1260-1264.
[31] X. Ma, Y. Zhao, K.W. Ng, Y. Zhao, Integrated Hollow Mesoporous Silica Nanoparticles for Target Drug/siRNA Co-Delivery, Chemistry – A European Journal 19 (46) (2013) 15593-15603.
[32] J.L. Blin, C. Gérardin, L. Rodehüser, C. Selve, M.J. Stébé, Influence of Alkyl Peptidoamines on the Structure of Functionalized Mesoporous Silica, Chemistry of Materials 16 (24) (2004) 5071-5080.
[33] J. Gao, X. Zhang, Y. Lu, S. Liu, J. Liu, Selective Functionalization of Hollow Nanospheres with Acid and Base Groups for Cascade Reactions, Chemistry – A European Journal 21 (20) (2015) 7403-7407.
[34] N. Shadjou, M. Hasanzadeh, Amino functionalized mesoporous silica decorated with iron oxide nanoparticles as a magnetically recoverable nanoreactor for the synthesis of a new series of 2,4-diphenylpyrido[4,3-d]pyrimidines, RSC Advances 4 (35) (2014) 18117-18126.
[35] M.X. Reinholdt, S. Kaliaguine, Proton Exchange Membranes for Application in Fuel Cells: Grafted Silica/SPEEK Nanocomposite Elaboration and Characterization, Langmuir 26 (13) (2010) 11184-11195.
[36] M.J. Kayser, M.X. Reinholdt, S. Kaliaguine, Amine Grafted Silica/SPEEK Nanocomposites as Proton Exchange Membranes, Journal of Physical Chemistry B 114 (25) (2010) 8387-8395.
[37] Y.-F. Lin, C.-Y. Yen, C.-C.M. Ma, S.-H. Liao, C.-H. Lee, Y.-H. Hsiao, H.-P. Lin, High proton-conducting Nafion (R)/-SO3H functionalized mesoporous silica composite membranes, Journal of Power Sources 171 (2) (2007) 388-395.
[38] K.M. Koczkur, S. Mourdikoudis, L. Polavarapu, S.E. Skrabalak, Polyvinylpyrrolidone (PVP) in nanoparticle synthesis, Dalton Transactions 44 (41) (2015) 17883-17905.
[39] I. Ahmed, A. Idris, M.Y. Noordin, R. Rajput, High Performance Ultrafiltration Membranes Prepared by the Application of Modified Microwave Irradiation Technique, Industrial & Engineering Chemistry Research 50 (4) (2011) 2272-2283.
[40] H. Liu, B. Zhang, H. Shi, Y. Tang, K. Jiao, X. Fu, Hydrothermal synthesis of monodisperse Ag2Se nanoparticles in the presence of PVP and KI and their application as oligonucleotide labels, Journal of Materials Chemistry 18 (22) (2008) 2573-2580.
[41] S. Belfer, R. Fainchtain, Y. Purinson, O. Kedem, Surface characterization by FTIR-ATR spectroscopy of polyethersulfone membranes-unmodified, modified and protein fouled, Journal of Membrane Science 172 (1–2) (2000) 113-124.
[42] J.A. Asensio, S. Borrós, P. Gómez-Romero, Proton-conducting polymers based on benzimidazoles and sulfonated benzimidazoles, Journal of Polymer Science Part A: Polymer Chemistry 40 (21) (2002) 3703-3710.
[43] H. Tang, M. Pan, S.P. Jiang, Self assembled 12-tungstophosphoric acid-silica mesoporous nanocomposites as proton exchange membranes for direct alcohol fuel cells, Dalton Transactions 40 (19) (2011) 5220-5227.
[44] D. Aili, J. Zhang, M.T. Dalsgaard Jakobsen, H. Zhu, T. Yang, J. Liu, M. Forsyth, C. Pan, J.O. Jensen, L.N. Cleemann, S.P. Jiang, Q. Li, Exceptional durability enhancement of PA/PBI based polymer electrolyte membrane fuel cells for high temperature operation at 200 [degree]C, Journal of Materials Chemistry A 4 (11) (2016) 4019-4024.
[45] C. Xu, X. Liu, J. Cheng, K. Scott, A polybenzimidazole/ionic-liquid-graphite-oxide composite membrane for high temperature polymer electrolyte membrane fuel cells, Journal of Power Sources 274 (2015) 922-927.
[46] J.C. Lassegues, in: C. Philippe (Ed.), Proton conductors: Solids, Membranes and Gels-Materials and Devices, Cambridge University Press, 2008, p. 318.
[47] M.F.H.S. and, W.H. Meyer, Anhydrous Proton-Conducting Polymers, Annual Review of Materials Research 33 (1) (2003) 233-261.
[48] Y. Liu, J. Wang, H. Zhang, C. Ma, J. Liu, S. Cao, X. Zhang, Enhancement of proton conductivity of chitosan membrane enabled by sulfonated graphene oxide under both hydrated and anhydrous conditions, Journal of Power Sources 269 (2014) 898-911.
[49] R.H. He, Q. Li, G. Xiao, N.J. Bjerrum, Proton conductivity of phosphoric acid doped polybenzimidazole and its composites with inorganic proton conductors, Journal of Membrane

Science 226 (1-2) (2003) 169-184.

Chapter 5 Facile synthesis of amino-functionalized hollow mesoporous silica with oriented mesoporous channels

5.1 Introduction

Phosphoric acid[1, 2] and phosphotungstic acid[3, 4] impregnated mesoporous silica membranes have been developed for high temperature PEMFC applications. PEMFCs have shown promising potential to replace fossil fuels in the future because of their high theoretical efficiency, simple water management, high tolerance to CO and flexible for the non-precious metal catalysts.[5, 6] The intrinsic inorganic mesoporous silica (*meso*-silica) based PEM shows the high performance and low dependence on relative humidity at elevated temperatures.[7, 8] Nevertheless, when PWA is impregnated into *meso*-silica (PWA-*meso*-silica), the hybrid particles tend to suffer the proton conductivity loss due to the leach of PWA during the flush of water in fuel cell operation.[9] On the other hand, Shiju et al. revealed that PWA could be tightly anchored on the surface of mesoporous silica with the assistance of amino-groups.[10] Furthermore, in comparison with HMS and NH_2-*meso*-silica materials, amino-functionalized hollow mesoporous silica showed superior fuel cell performance, as discussed in Chapter 4.

There are two strategies to synthesis NH_2-HMS including post-synthesis and co-condensation.[11] For the post-synthesis protocol, the surface modification is required for the as-synthesized HMS to introduce the $–NH_2$ groups. Moreover, the $–NH_2$ groups tend to anchor on the pore openings due to the hindering diffusion of the silane compounds further into the inner pore channels, leading to the inhomogeneous distribution of the $–NH_2$ groups throughout the materials.[12] In comparison, via the co-condensation method, the $–NH_2$ groups can be anchored on both the exterior and the interior surfaces of the mesopores with a homogeneous distribution.[13] Yin et al. [14] synthesized NH_2-HMS via a one-step method. Besides, Liu et al. [15] fabricated the amino-functionalized silica material via step-by-step post-grafting, and then transformed it into NH_2-HMS by cationic surfactant-assisted selective etching strategy [16]. However, those strategies either lead to disordered mesoporous channels in the shell, or require further surface modification to introduce $–NH_2$ groups to the materials. Achieving ordered pore channels in the shell and homogenous distribution of $–NH_2$ on HMS simultaneously still remains a critical

challenge for the synthesis of NH_2-HMS.

Herein, a simple strategy was proposed for the synthesis of NH_2-HMS. The NH_2-*meso*-silica was first prepared via the co-condensation of ATPES and TEOS with the assistant by CTAB. Then it was transformed into NH_2-HMS with a hollow core and a highly ordered mesoporous shell by a simple alkaline etching process. The role of CTAB, amino group content, etching time, and concentration of etching agents were investigated in details. And the formation mechanism of NH_2-*meso*-silica and NH_2-HMS were revealed by *in situ* time-resolved synchrotron SAXS.

5.2 Experiment section

5.2.1 NH_2-HMS synthesis procedures

The synthesis of NH_2-HMS can be controlled by tuning several parameters. A typical recipe for the synthesis of NH_2-*meso*-silica is H_2O: ethanol: $NH_3 \bullet H_2O$: CTAB: APTES: TEOS = 2756: 518: 3.9: 0.4: 0.1: 1.0 in molar ratio. CTAB was dissolved in a mixed solution of 250 mL Milli-Q water and 150 mL ethanol. Then, $NH_3 \bullet H_2O$ (28 wt.%) was added into the solution, followed by the addition of TEOS and ATPES. The mixed solution was stirred at room temperature for 6 hours. The transparent solution was observed to turn into an opaque suspension. The white solid was collected from the suspension by centrifugation at 10 000 rpm for 10 min, named as NH_2-*meso*-silica/CTAB. After that, the white solid was dispersed into 50 mL of water after being washed twice with water and ethanol. Then the suspension was stirred at a Na_2CO_3 solution at 60 ^oC for 2 hours, followed by filtration. The collected solid, named as NH_2-HMS/CTAB, were washed by water and ethanol and dried overnight at 50 ^oC.

The CTAB surfactant was extracted from the solid with 100 mL of ethanol and 3.0 mL of HCl (32 wt.%) at 80 ^oC for 3 hours. After the CTAB extraction, NH_2-*meso*-silica/CTAB and NH_2-HMS/CTAB were marked as NH_2-*meso*-silica and NH_2-HMS, respectively. All the chemicals were purchased from Sigma-Aldrich, Australia and used as received without any further purification.

The molar ratio of the NH_2 groups in the NH_2-HMS materials can be varied from 0 % to 30 %, while the amount of silanes was fixed at 14 mmol L^{-1} in the solution. The concentration of CTAB was tuned from 4 to 16 mmol L^{-1} to investigate its effect on the formation of NH_2-HMS material. The concentration of the etching agent,

Na_2CO_3, was varied from 0.1 to 0.4 mol L^{-1}.

5.2.2 Characterizations

N_2 isotherms, the thermal stability and the synchrotron SAXS measurements are the same way as described in Section 3.2.3. Characterizations of TEM (JEOL 2100), attenuated total reflectance Fourier Transform Infrared spectroscopy (ATR-FTIR), ^{13}C CP/MAS NMR and ^{29}Si MAS NMR are the same way as described in Section 4.2.4.

For the *in situ* time-resolved SAXS characterizations, liquids were pumped into a capillary in the beamline via a syringe pump. And the temperatures of the liquids were precisely controlled by a water bath. The beam energy is 12 KeV, and the camera length is 500 mm with *q* range from 0.022 to 1.151 $Å^{-1}$.

5.3 Results and discussions

5.3.1 Synthesis of NH_2-HMS

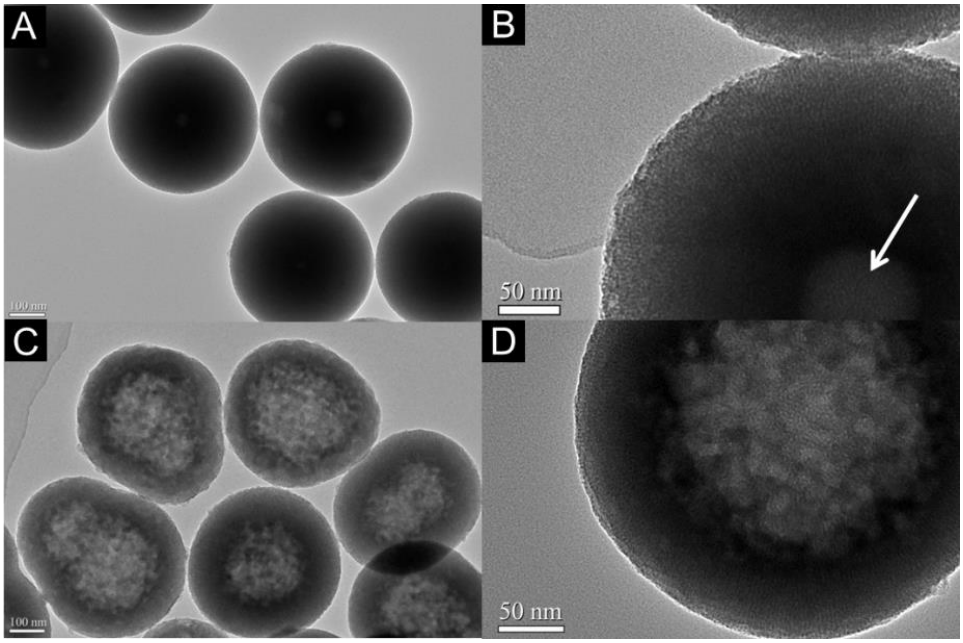

Figure 5.1 TEM images of NH_2-*meso*-silica (A and B) and NH_2-HMS spheres (C, and D) fabricated via co-condensation method with 8 mmol L^{-1} CTAB and 10 % molar ratio APTES. Etching condition: 0.2 M Na_2CO_3, 60 ^oC 2h.

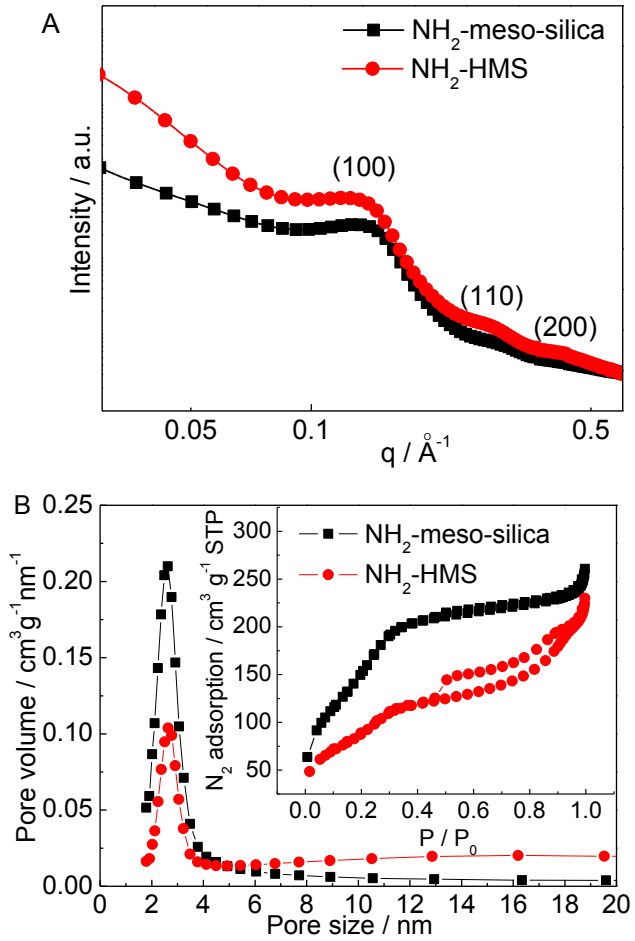

Figure 5.2 (A) SAXS profiles and (B) N_2 isotherms of NH_2-*meso*-silica and NH_2-HMS particles. Synthesis condition: 8 mmol L^{-1} CTAB and 10 % molar ratio APTES. Etching condition: 0.2 M Na_2CO_3, 60 ^oC, 2h.

Amine-functionalized mesoporous silica spheres were synthesized via the co-condensation of TEOS and APTES with a molar ratio of 10 % for APTES. It can be seen from Figure 5.1A that the size of the NH_2-*meso*-silica spheres was about 400 nm. According to the HR-TEM image in figure 5.1B, the mesoporous structure is ordered in short range. What should be noted is the cavity structure of the NH_2-*meso*-silica spheres. Each NH_2-*meso*-silica particle contained a centred small void the size of which varies, as pointed out by the arrows in Figure 5.1B. Moreover, there were two or three voids in the combined NH_2-*meso*-silica particles, indicating the central position of the cavity. One possible reason for the cavernous chamber in the NH_2-*meso*-silica particle is due to the hydrophobicity of TEOS [14, 17]. When TEOS is dispersed in the H_2O/ethanol solution, it tends to from hydrophobic droplets and hydrolyses to silica colloids. The silica colloids that are negatively charged deposit on the positively charged CTAB micelles, forming a shell and at the same time acting as a morphological stabilizer. The further consumption of the TEOS

hydrophobic droplet increases the thickness of the shell, resulting in the formation of mesoporous silica spheres with small voids.[14]

After etched by 0.2 M Na_2CO_3 at 60 ^oC for 2h, the NH_2-*meso*-silica material was transformed into hollow mesoporous spheres of NH_2-HMS. According to the TEM image shown in Figure 5.1C, the hollow chamber was enclosed by a mesoporous shell. Lattice fringes were observed as parallel lines running across the surface of the wall and worm-like channels were observed at the edge of the spheres, as shown in Figure 5.1D. The average diameter of the spheres was about 360 nm, and the thickness of the shell was about 40 nm.

The mesoporous structure of NH_2-*meso*-silica and NH_2-HMS were confirmed by the SAXS and BET characterizations, as shown in Figure 5.2. It can be seen in Figure 5.2A that a broad peak centred at q = 0.128 $Å^{-1}$ was detected for NH_2-*meso*-silica, while the peak shifted to 0.124 $Å^{-1}$ for NH_2-HM. The d spacing calculated from the peak positions were 4.9 nm and 5.1 nm for NH_2-*meso*-silica and NH_2-HMS, respectively. The mesoporous structure was also detected by the nitrogen isotherm curves with type IV adsorption curves with the capillary condensation effect for mesoporous structure and H1 type hysteresis corresponding to cylindrical mesoporous structures (Figure 5.2B). The BET surface area and pore volume of NH_2-*meso*-silica were 601.6 m^2g^{-1} and 0.47 cm^3g^{-1}, respectively, and dropped to 342.5 m^2g^{-1} and 0.37 cm^3g^{-1} upon the formation of NH_2-HMS through etching. The results are likely due to the hollow chamber of NH_2-HMS particles. Nevertheless, the pore size increased from 2.5 nm for NH_2-*meso*-silica to 4.5 nm for NH_2-HMS, in consistent with the results of SAXS.

The successful incorporation of the amine groups was confirmed by the solid-state ^{13}C CP/MAS NMR and the ATR-FTIR spectra in Figure 5.3A. The relevant carbon signals at 10, 22, 42 ppm correspond to the carbon atoms at –$SiCH_2CH_2CH_2NH_2$.[18] In the ^{29}Si MAS NMR spectrum of the NH_2-HMS particles, the peak signal at -66 ppm corresponds to the integration of the amine groups (Figure 5.3B), suggesting the condensation of APTES in the hybrid particles. It should be noted that the peak at around 59 ppm was absent, indicating the completely hydrolysed silanes and template removal.[15] The presence of the –NH_2 groups was also confirmed by ATR-FTIR. As shown in Figure 5.3C, the peaks at 1630, 1045 and 960 cm^{-1} correspond to the framework of mesoporous silica. The most intensive peak, centred at 1045 cm^{-1} is associated with the SiO_4 $v_3(F_2)$ stretching vibration.

The peak at 796 cm^{-1} corresponds to the SiO_4 v_1(A) stretching vibration. The peak at 1630 cm^{-1} is due to the stretching and bending vibrations of the water molecules adsorbed on the surface of the mesoporous materials. The peak centred at 960 cm^{-1} corresponds to the Si-OH stretching of terminal silanol. Peaks detected at 2937 and 2858 cm^{-1} are attributed to the stretching vibrations of the CH group, while the peaks at 1450 and 1391 cm^{-1} are associated with the bending vibrations of those groups. The peak at 1531 cm^{-1} belongs to the bending vibration of the N-H bond. It should be noted that the C-N stretching vibration in the region of 1030 – 1230 cm^{-1} overlap with the broad peak of silanol and the Si-O-Si vibration.[19]

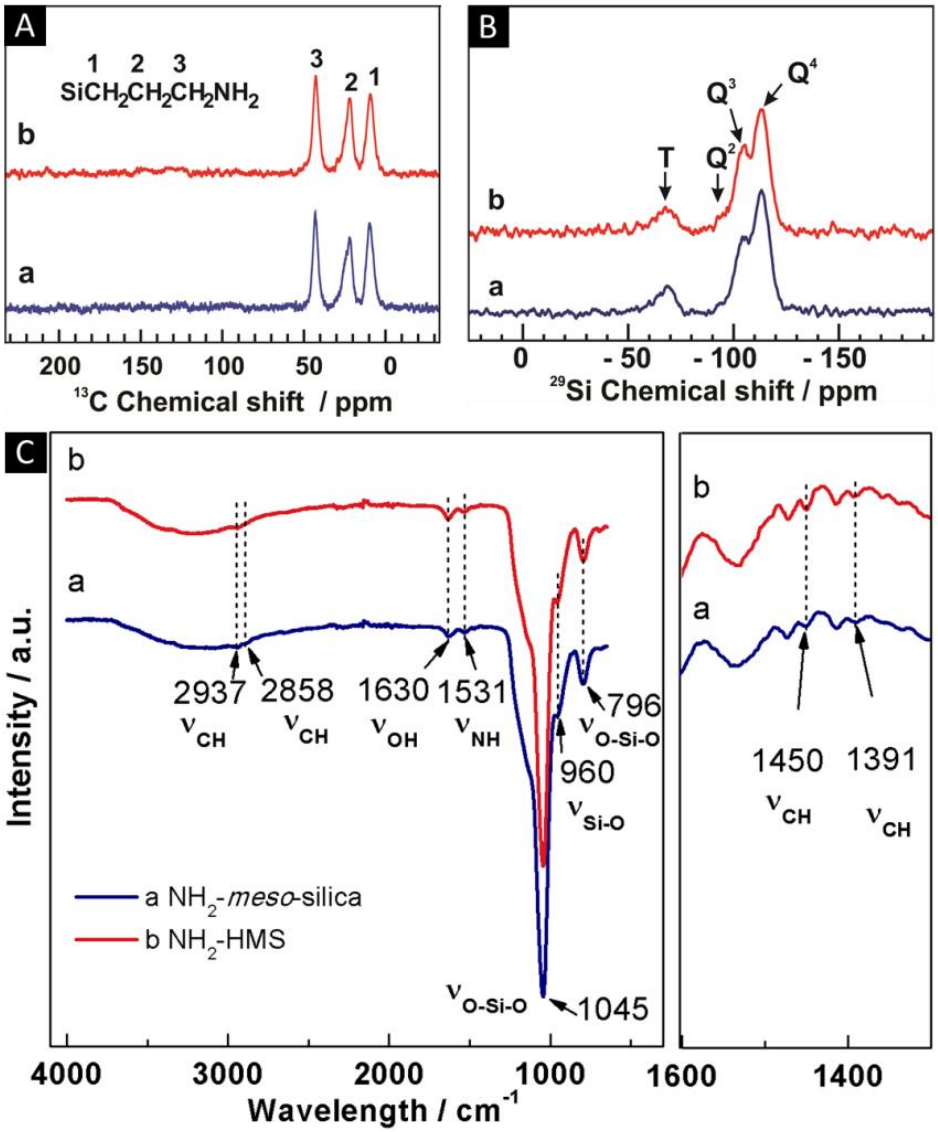

Figure 5.3 (A) ^{13}C CP/MAS, (B) ^{29}Si MAS NMR spectra and (C) ATR-FTIR spectra of NH_2-*meso*-silica (a) and NH_2-HMS(b). Synthesis condition: 8 mmol L^{-1} CTAB and 10 % molar ratio APTES. Etching condition: 0.2 M Na_2CO_3, 60 ^oC, 2h.

5.3.2 *Factors for the synthesis of NH_2-HMS*

5.3.2.1 Roles of CTAB

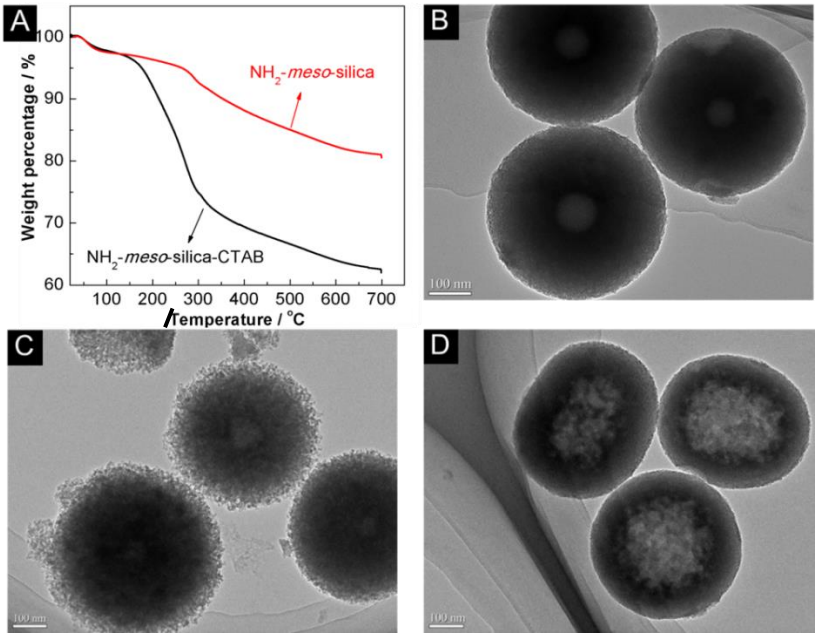

Figure 5.4 (A) TGA profiles of NH_2-*meso*-silica/CTAB and NH_2-*meso*-silica spheres. (B) The TEM image of NH_2-*meso*-silica. TEM images of (C) NH_2-*meso*-silica and (D) NH_2-*meso*-silica/CTAB etched at 0.2 M Na_2CO_3 at 60 °C for 10 h. The molar ratio of APTES is 10 %.

According to the comparison of the TGA profiles, shown in Figure 5.4A, between the pristine NH_2-*meso*-silica/CTAB and NH_2-*meso*-silica, it can be concluded that CTAB is removed from the mesoporous channels of NH_2-*meso*-silica after the EtOH/HCl reflux treatment. Figure 5.4B shows that after the reflux treatment, the mesoporous structure of NH_2-*meso*-silica remains intact and cavity remains centred. However, as shown in Figure 5.4C, when the NH_2-*meso*-silica particles were etched in an alkaline solution, the mesoporous structure substantially deteriorated and the surface of sphere became rough. On the contrary, when the NH_2-*meso*-silica/CTAB material was etched in the same condition, the NH_2-HMS/CTAB sphere with a hollow chamber and a mesoporous shell were obtained (Figure 5.4D). These results indicate that CTAB plays an important role in the transformation of NH_2-*meso*-silica/CTAB into NH_2-HMS/CTAB.

Besides transforming NH_2-*meso*-silica/CTAB into NH_2-HMS/CTAB, CTAB also affects the particle size of NH_2-*meso*-silica/CTAB. For instance, the average particle size of the NH_2-*meso*-silica sphere/CTAB spheres was 726 nm with no void observed when the concentration of CTAB was 4 mmol L^{-1}, as shown in Figure

5.5A. When the concentration of CTAB increased to 8 to16 mmol L^{-1}, the average particle size of the NH_2-*meso*-silica/CTAB spheres decreased from 400 to 236 nm and the void structure emerged (Figure 5.5C, E and G). The reduced particle size is likely due to the fact that the increase of the concentration of CTAB decreases the interfacial energy of the silane droplet.[17] Moreover, the *d* spacing of the mesoporous structures in NH_2-*meso*-silica/CTAB calculated from SAXS curves was 4.3 nm at the concentration of 4 mmol L^{-1} CTAB. And it increased to 4.8 nm at the concentration of 16 mmol L^{-1} CTAB. This may result from enhanced micelle size with increasing the concentration of CTAB.

After the etching process, the NH_2-*meso*-silica/CTAB spheres were transformed into the hollow mesoporous particles except for those at the concentration of 4 mmol L^{-1} CTAB (Figure 5.5B). The results indicate that it is more difficult to etch the mesoporous silica synthesized at the low CTAB concentration (4 mmol L^{-1}) than those synthesized at the high CTAB concentration (Figure 5.5D and F).

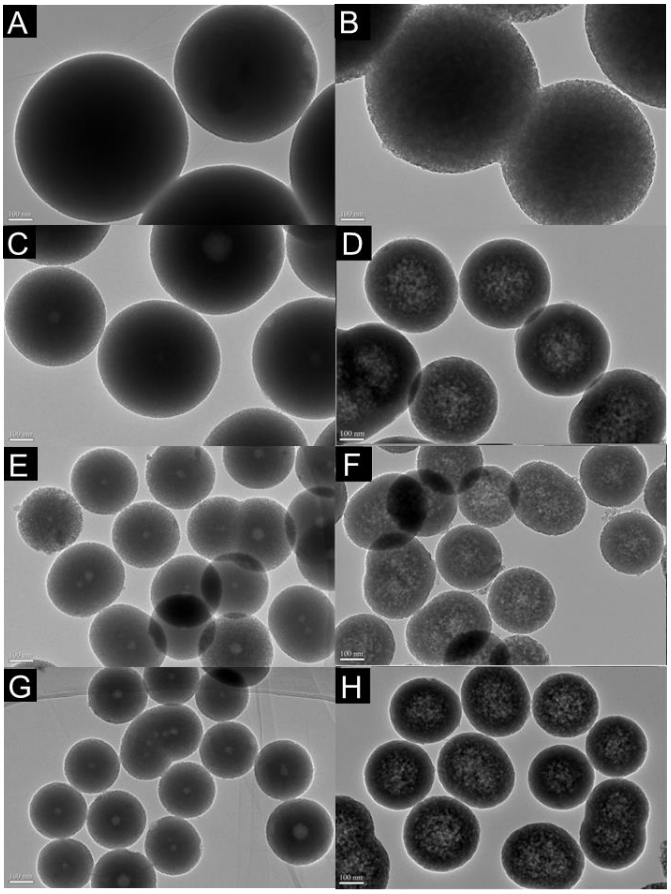

Figure 5.5 TEM images of NH_2-*meso*-silica/CTAB synthesised by the CTAB concentration of (A) 4 mmol L^{-1}, (C) 8 mmol L^{-1}, (E) 12 mmol L^{-1} and (G) 16 mmol L^{-1}. (B), (D), (F) and (H) are the TEM images for the corresponding samples etched at 0.2 M Na_2CO_3, 60 ^oC for 2h. The molar ratio of APTES is 10 %.

Figure 5.6 compares the SAXS profiles of NH_2-*meso*-silica/CTAB spheres before and after the etching process. In comparison with the pristine samples, the peak intensity for all the materilas substantially decreased after the etching process, and the peaks became broadened. The results indicate that the orderly arranged mesoporous structure of the NH_2-HMS/CTAB spheres is impaired compared with the pristine NH_2-*meso*-silica/CTAB spheres. Nevertheless, the peak position for the materials at the CTAB concentration of 8 and 12 mmol L^{-1} remained nearly unchanged after etching. According to the results, the optimum CTAB concentration is in the range of 8 to 12 mmol L^{-1}. The physical properties for the NH_2-*meso*-silica/CTAB materials are listed in Table 5.1. Although 8 and 12 mmol L^{-1} CTAB both enable the fabrication of amine-functionalized HMS, the yield of NH_2-HMS/CTAB at 8 mmol L^{-1} is higher than at 12 mmol L^{-1}. Therefore, 8 mmol L^{-1} CTAB will be used in the subsequent studies.

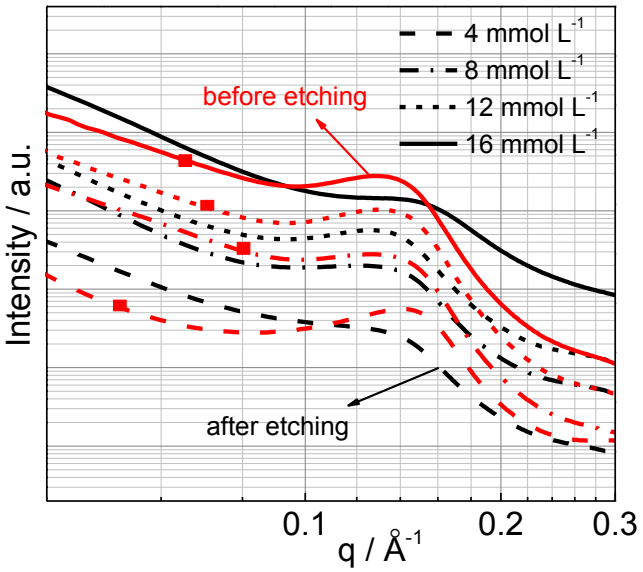

Figure 5.6 SAXS profiles of NH_2-*meso*-silica/CTAB spheres before (red line) and after etching (black line) against CTAB concentration. Etching condition: 0.2 M Na_2CO_3, 60 °C for 2h. The molar ratio of APTES is 10 %.

Table 5.1 Physical properties for the mesoporous NH_2-*meso*-silica/CTAB spheres with various CTAB concentrations in terms of particle size and d spacing before and after etching process. d_1 before etching process, and d_2 after etching process.

C_{CTAB}, mmol L^{-1}	Particle size, nm	d_1 space, nm	d_2 space, nm
4	726	4.3	-
8	409	4.6	4.6
12	296	4.7	4.7
16	236	4.8	-

5.3.2.2 Molar ratios of amine groups

Figure 5.7 shows the SAXS profiles of NH_2-*meso*-silica/CTAB with the molar ratio of the amine groups in the range of 10 – 30 %. A broad peak around $q = 0.12$ Å^{-1} was observed for 10 – 20 % NH_2-*meso*-silica/CTAB, indicating the presence of the mesoporous structure. However, when the ratio increased to 30 %, the peak was absent, which indicates the deterioration of the mesoporous structure. The loss of mesoporous structure is attributed to the fact that excess organosilane molecules can disrupt the packing of surfactants, and consequently, alter the geometry of structure-directing micelles and affect the assembly between the silica-micelle complexes.[20, 21] When the particles were etched at an alkaline condition (0.2 M Na_2CO_3, 60 °C for 2h), the broad peak for 10 % NH_2-HMS/CTAB remained the same as that for the pristine NH_2-*meso*-silica/CTAB. However, the peak for 20 % NH_2-*meso*-silica/CTAB disappeared, indicating the deterioration of the mesoporous structure. Overall, the optimum ratio of APTES for the synthesis of NH_2-*meso*-silica and NH_2-HMS is 10 %, which will be used in the subsequent studies.

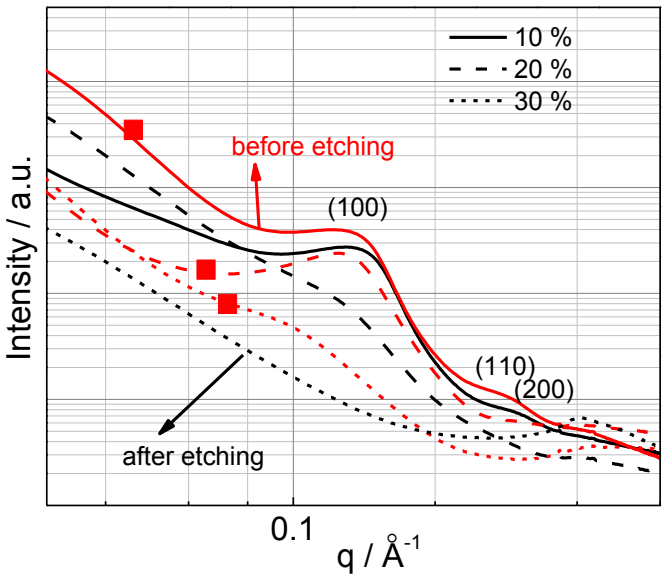

Figure 5.7 Effects of molar ratios of APTES for the synthesis of the NH_2-*meso*-silica/CTAB spheres before (red line) and after etching (black line) at 0.2 M Na_2CO_3, 60 °C for 2h.

5.3.2.3 Concentration of Na_2CO_3

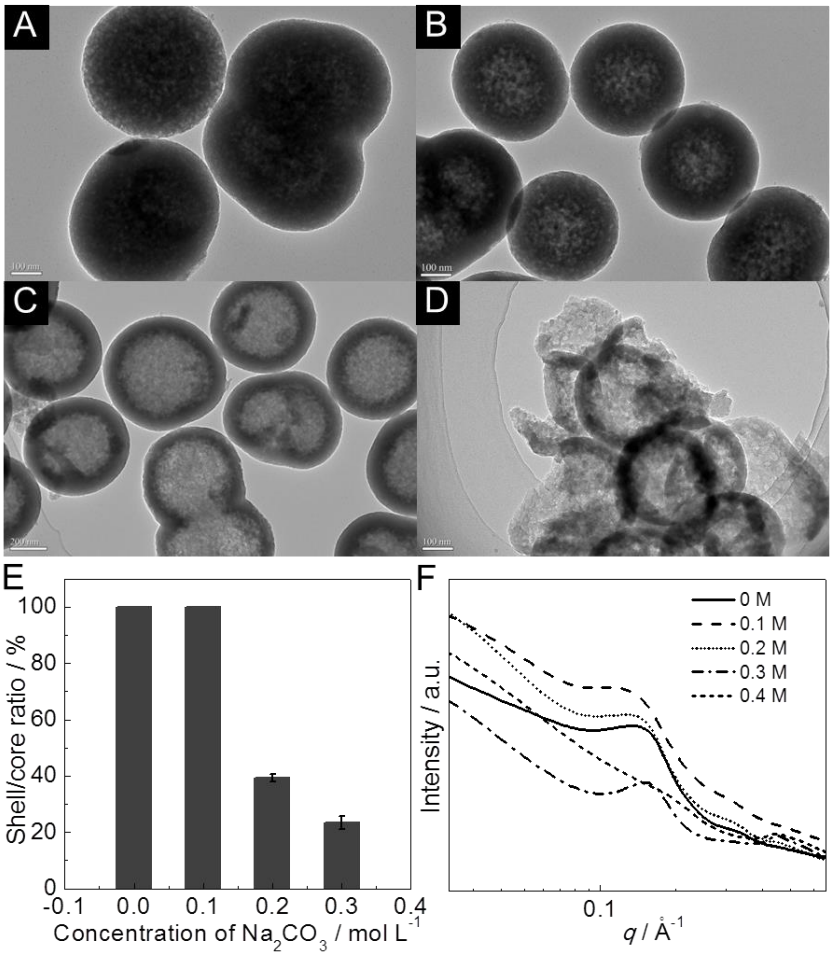

Figure 5.8 TEM images of the NH_2-*meso*-silica/CTAB spheres etched at various Na_2CO_3 concentrations at 60 ^oC for 2h (A) 0.1 M, (B) 0.2 M (C), 0.3 M (D) 0.4 M. (E) and (F) are the shell/core ratio and the SAXS profile of NH_2-HMS/CTAB against the concentration of Na_2CO_3, respectively.

The concentration of Na_2CO_3 plays a critical role in etching the NH_2-*meso*-silica/CTAB spheres. The centre of the NH_2-*meso*-silica/CTAB spheres collapsed into silica colloids while the outer parts of the sphere still remained intact after being etched in the 0.1 M Na_2CO_3 solution (Figure 5.8A). And the void became clear as the concentration of the etching agent increased, as shown in Figure 5.8B and C, which is consistent with the peak changes of NH_2-HMS/CTAB, as shown in Figure 5.8F. Moreover, it can be seen in Figure 5.8E that the shell thickness decreased with the increase of the Na_2CO_3 concentration. However, when the concentration of the Na_2CO_3 solution increased to 0.4 M, the spherical structure of NH_2-*meso*-silica/CTAB broke into silica fragments, as shown in Figure 5.8D. Moreover, the mesoporous structure also deteriorated, as indicated by the absence of the peak around 0.13 $Å^{-1}$ in the SAXS curve (Figure 5.8F). Based on these results, the size of

the hollow chamber in the NH_2-HMS sphere can be easily controlled through tuning the concentration of the Na_2CO_3 solution. For our case, the optimum concentration for the Na_2CO_3 solution is 0.2 – 0.3 M.

As the inner part of the silica spheres is less exposed to the alkaline solution than the outermost layer during the transformation process, the fact that the inner part of the spheres preferentially dissolved is very interesting. Figure 5.9 shows the ^{29}Si MAS NMR spectra of NH_2-HMS obtained from different concentrations of etching agent after acid extraction. The signals at -93, -100 and -110 ppm correspond to the $Q_2[(SiO)_2Si(OX)_2$, X= H or Et], $Q_3[(SiO)_3SiOH$, X= H or Et] and $Q_4[(SiO)_4Si$, X= H or Et] silicate species, respectively.[22] The T signal at -66 ppm is ascribed to the integration of organic functional groups, indicating the existence of the -NH_2 groups in the HMS spheres.[15] Quantitative analysis shows that 14.1% of the silicon atoms in the mesoporous hybrid spheres are at the T sites, and 85.9 % of the silicon atoms are at the Q sites, which is consistent with the percentage composition given by the APTES and TEOS precursors. However, after the etching treatment, the silicon atoms at the T sites decreased with the increase of the concentration of the etching agent. Particularly, only 4.5% of the silicon atoms remained at the T sites when the spheres were etched in 0.4 M Na_2CO_3 at 60 ^oC for 2h. The decrease of the T peaks after the etching process is most likely to result from the partial dissolution of silica condensed from APTES.

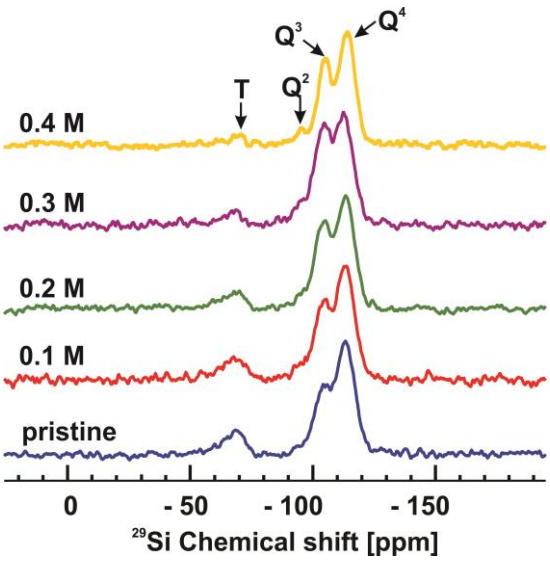

Figure 5.9 Solid state ^{29}Si MAS NMR spectra of NH_2-HMS obtained from different concentrations of etching agent at 60 ^oC for 2h.

Table 5.2 Contents of amine groups and Si groups analysed from NMR results.

Sample	T (mol%)	Q_2 (mol%)	Q_3 (mol%)	Q_4 (mol%)	$Q_4/(Q_3+Q_2)$
Pristine	14.1	2.3	26.2	57.4	2.0
0.1M	12.1	5.3	29.6	53.1	1.5
0.2M	9.3	5.0	34.2	51.4	1.3
0.3M	6.3	7.6	38.1	48.0	1.1
0.4M	4.5	5.1	33.8	56.5	1.5

Furthermore, according to Table 5.2, the ratio of $Q_4/(Q_3+Q_2)$ of the NH_2-HMS was obviously lower than that of the as-made NH_2-*meso*-silica material, which suggests that the condensation degree of the framework decreases after the etching process. It also indicates that silica condensed from TEOS is partially dissolved during the etching treatment. Teng et al. described a self-transformation of mesoporous silica spheres to hollow structured mesoporous silica spheres in hot water, which is induced by a low degree of silica condensation in their inner section.[23] Based on their ^{29}Si MAS NMR, the degree of condensation of the mesoporous silica spheres was much lower than the hollow mesoporous silica spheres. In our case, the degree of condensation of NH_2-*meso*-silica is higher than that of the NH_2-HMS spheres, which indicates the transformation is not due to the low condensation degree in the inner spheres.

Nitrogen sorption characterization was conducted on the acid-extracted materials, as shown in Figure 5.10. All the samples show type IV isotherms, indicating the capillary condensation effect of the mesoporous structure (Figure 5.10A). The BET surface area of pristine NH_2-*meso*-silica was 601.6 m^2g^{-1}, and decreased to 481.7 m^2g^{-1} when the spheres were treated in the 0.1 M Na_2CO_3 solution. With further increase of the concentration of the etching agent to 0.2 M, the BET surface area dropped to 342.5 m^2g^{-1}. The decrease of the surface area suggests the dissolution of the silicate-CTAB under the alkaline solutions. It is interesting to note that the BET surface of the spheres treated in 0.4 M is higher than that of the material treated in 0.2M. The possible reason is the diminishment of the silica colloids in the mesopores in the broken silicate fragments generated at the high concentration of the etching agent.

The BJH method assumes the pores are cylindrical pores in shape. The pore size of the NH_2-*meso*-silica material treated in 0 to 0.2 M Na_2CO_3 is almost the same (2.5 to 2.8 nm), while that of the sample treated in 0.4 M is smaller than 2.0 nm obtained from the pore size distribution (Figure 5.10B). The results confirm the excess etching

agent tend to destroy the mesoporous structure, in consistent with the results from TEM in Figure 5.8D. And the physical properties of the particles are list in Table 5.3.

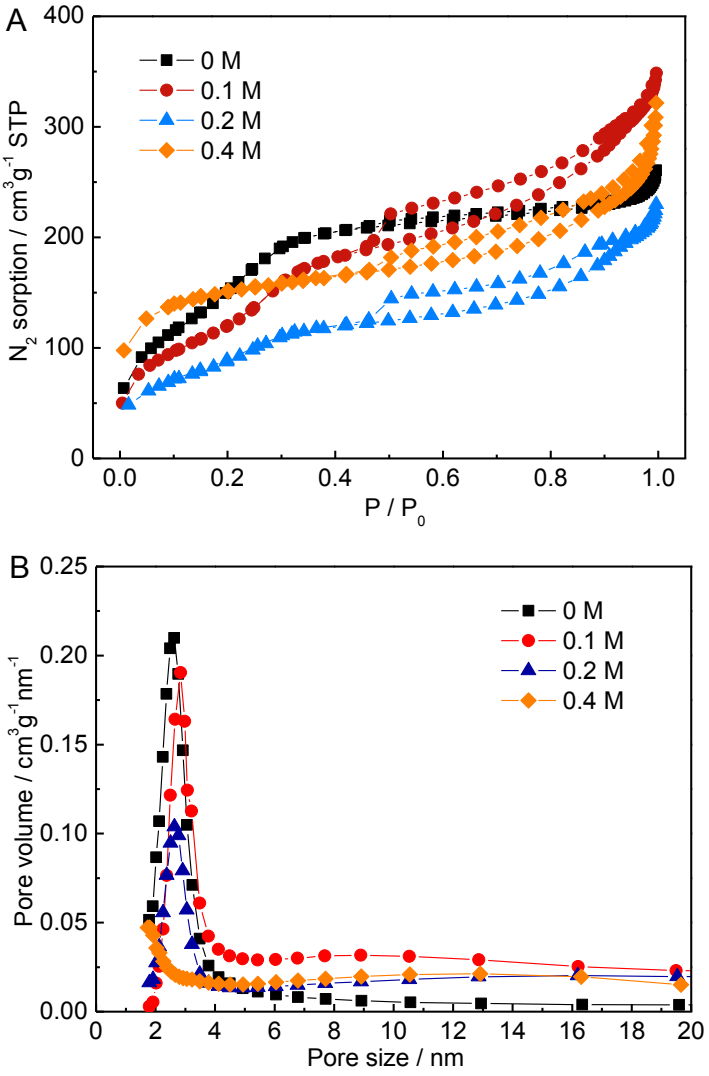

Figure 5.10 (A) N_2 adsorption isotherms and (B) pore size distributions of NH_2-HMS etched from different concentrations of the Na_2CO_3 solution.

Table 5.3 Physical properties of NH_2-*meso*-silica sphere after etching by Na_2CO_3 with different concentrations.

Sample	BET surface area, m^2g^{-1}	pore size[a], nm	pore volume[b], cm^3g^{-1}
0 M	601.6	2.5	0.47
0.1 M	481.7	2.8	0.6
0.2 M	342.5	2.6	0.37
0.4 M	491.1	-	-

[a] Value from the pore size distribution; [b] BJH adsorption.

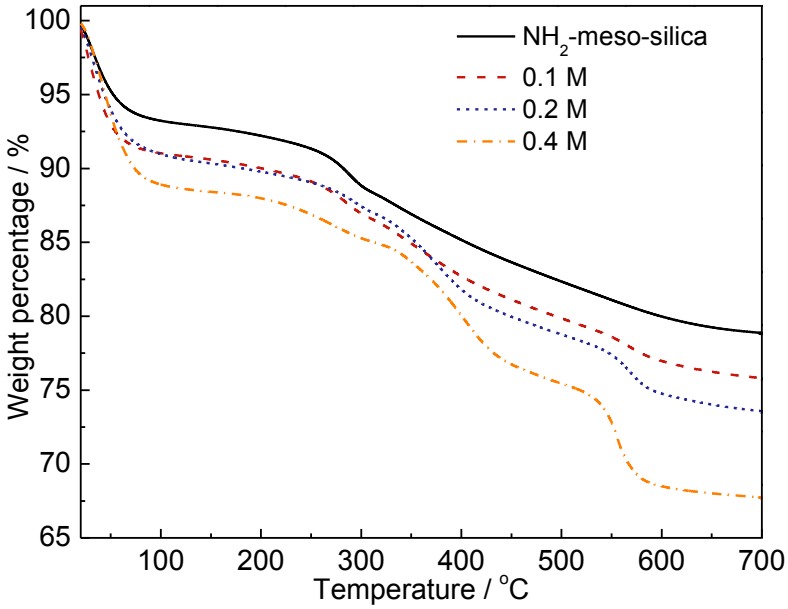

Figure 5.11 TGA profiles of the NH_2-HMS obtained from different concentration of etching agents.

In general, there are three weight loss regimes observed in the TGA profiles of the NH_2-HMS samples, as shown in Figure 5.11. The weight loss at the temperature lower than 120 ^oC is attributed to the loss of a small amount of residual ethanol and moisture adsorbed on the surface of the materials. The weight loss from 250 to 500 ^oC is due to the decomposition of amino-groups on the surface of the materials.[24] The slight weight loss after 500 ^oC is due to the dehydration of the hydroxyl groups on the surface and the further co-condensation of the silica matrix.[25] The further weight loss after 500 ^oC for the samples treated at 0.4 M is associated with the low condensation degree of the silica framework, as suggested based on the ^{29}Si MAS NMR analysis.

5.3.2.4 Etching time

Generally, when the etching agent of Na_2CO_3 is added into the suspension of NH_2-*meso*-silica/CTAB, it reacts with the material and transforms NH_2-*meso*-silica/CTAB into NH_2-HMS/CTAB. Nevertheless, it is critical to answer the question that when the transformation is finished. Figure 5.12 shows the particle size distributions of the NH_2-*meso*-silica/CTAB spheres against the reaction time in the range of 0 to 20 h. At the initial stage, individual NH_2-*meso*-silica/CTAB particles were observed with mesoporous structure, and the particle size was in the range of 350 – 500 nm (Figure

5.12A). When the silicate-CTAB spheres were etched at the alkaline solution for 60 min, the interior parts of the silicate-CTAB particle were dissolved to a hollow chamber (Figure 5.12B). However, the particle size distribution decreased to 300 – 450 nm. When the reaction time was extended to 120 min, the particle size distribution was almost the same as at 60 min (Figure 5.12C). Furthermore, the particle size and shell to diameter ratio were almost constant during the next 18 h (Figure 5.12D). The results indicate that the transformation of the NH_2-*meso*-silica/CTAB material to the NH_2-HMS/CTAB material finishes at 1 – 2 h, resulting in the hollow structure and the decrease of the particle size.

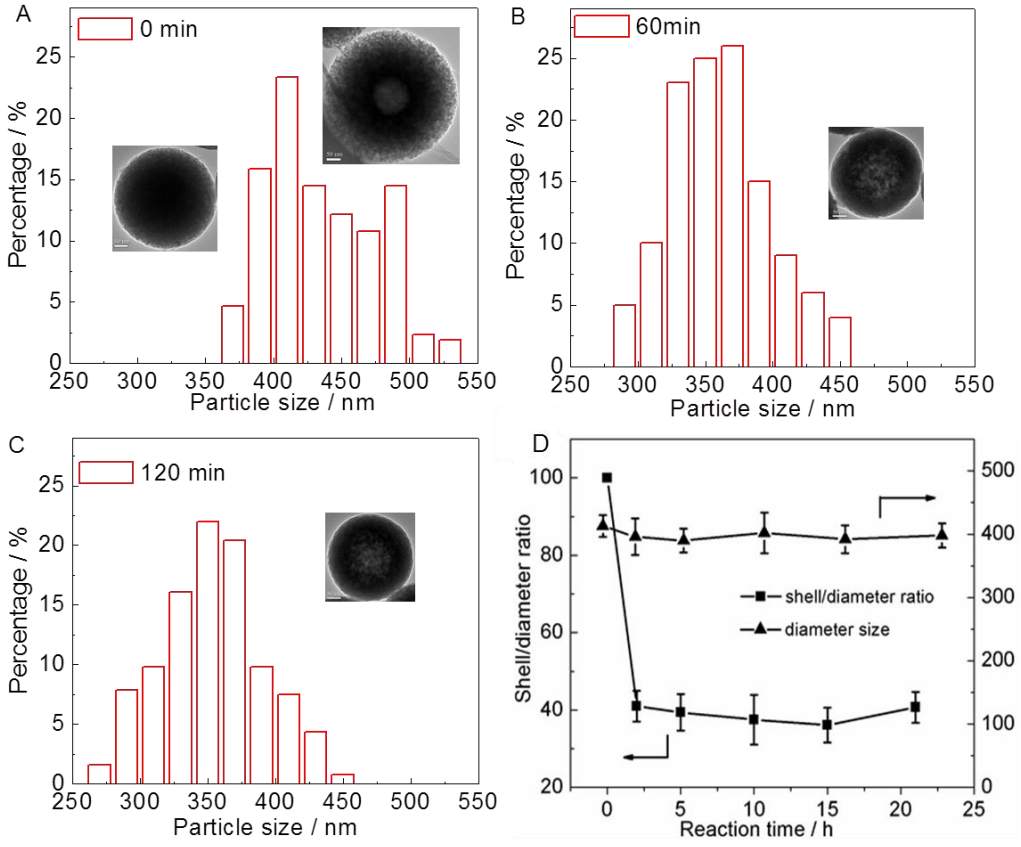

Figure 5.12 Particle size distributions of NH_2-*meso*-silica/CTAB after 0.3 M Na_2CO_3 etching under different time. (A) 0 min, (B) 60 min, (C) 120 min and (D) 2-20 h. (D) also includes the shell/diameter ratio of the particles. The Insets are corresponding TEM images of the particles in difference etching time.

5.3.2.5 *In situ* time-resolved synchrotron SAXS characterizations

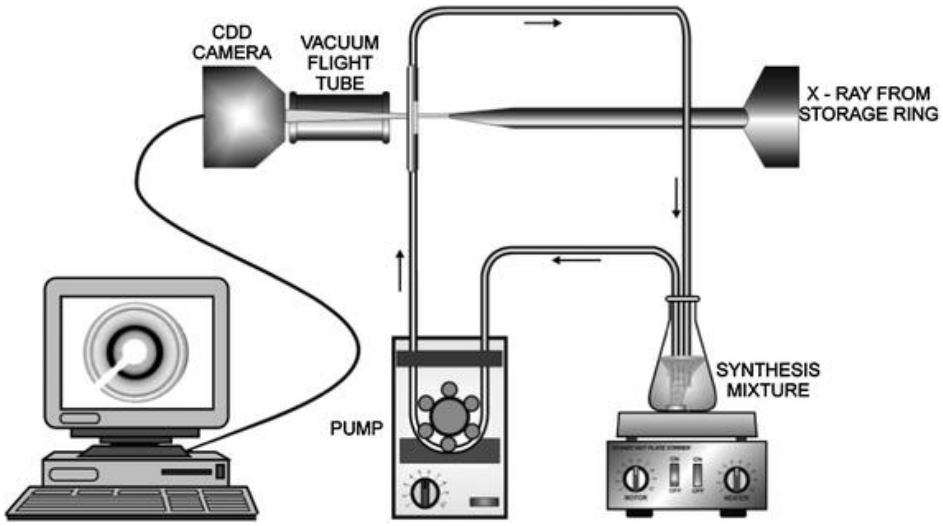

Figure 5.13 Scheme of the time-resolved synchrotron SAXS characterization.[26]

In order to investigate the formation of the NH_2-*meso*-silica/CTAB spheres and the NH_2-HMS/CTAB spheres, *in situ* time-resolved synchrotron SAXS characterizations were conducted. Figure 5.13 shows a scheme for the experiment.

Figure 5.14A shows the *in situ* time-resolved synchrotron SAXS profile for the formation of the NH_2-*meso*-silica/CTAB nanoparticles. At the initial stage (t = 1min), the solution was transparent and a broad peak centred at q = 0.140 $Å^{-1}$ was observed, as shown in Figure 5.14B. That corresponds to the contribution of the globular CTAB micelles.[27] Upon addition of inorganic precursors of TEOS and APTES, silica oligomers are formed by the hydrolysis of silanes in the alkaline condition. The intensity and the position of the peak kept constant from t = 1 to 5 min, implying that the oligomeric silanes are randomly distributed in the solution. Nevertheless, the peak intensity significantly increased from t = 5 to 9 min, while the peak position was the same. At the same time, the solution changes from transparent to opaque. During this period, negatively charged oligomeric silanes are self-assembled with positively charged CTAB globular micelles via electrostatic force. The formed inorganic-organic pairs increase the contrast between the surface and the core of the CTAB micelles, leading to increase in peak intensity. Then, the globular micelles were extended into the enlongated rod-like shape micelles started from t = 9 min, which slightly shifted the peak to q = 0.142 $Å^{-1}$. Then, the rod-like shape micelles packed into a 2D hexagonal structure and formed the small nucleus at t = 14

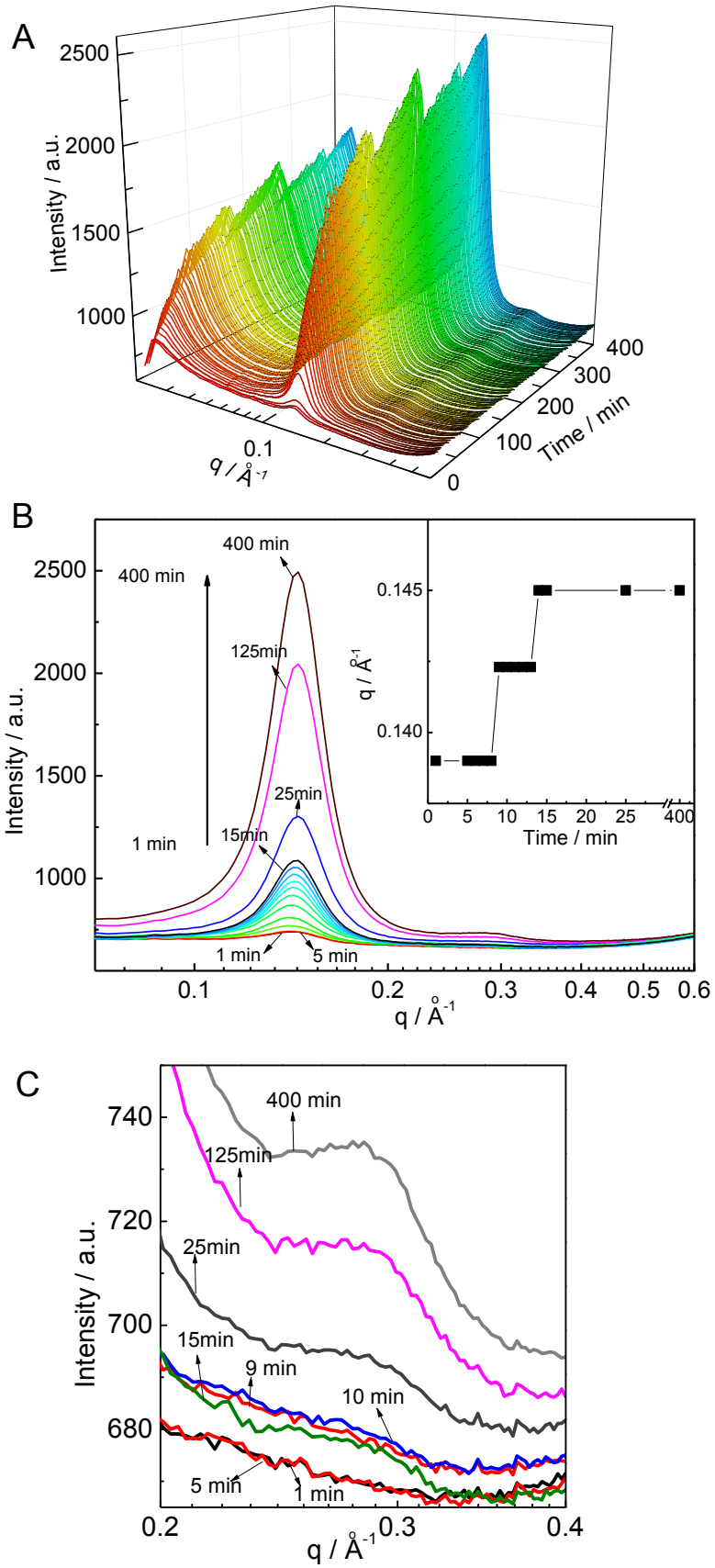

Figure 5.14 (A) *In situ* time-resolved synchrotron SAXS for the formation of the NH_2-*meso*-silica/CTAB material. SAXS curves comparison of the NH_2-*meso*-silica/CTAB material against the time in (B) the (100) plane and (C) the (110) and (200) planes. The inset in (B) is the peak position *vs.* time.

min, as indicated by the peak shift from q = 0.142 Å^{-1} to 0.145 Å^{-1}. Moreover, a broad peak centred at q = 0.280 Å^{-1} was also present, as shown in Figure 5.14C. The sharp peak at q = 0.145 Å^{-1} reflects the plane of (100), indicating good ordering on a local scale. However, the overlapping lines of the broad peak at q = 0.280 Å^{-1} correspond to the (100) and (200) planes. That is likely due to the distortion of the hexagonal symmetry of second- and higher-order neighbour pores around a central pore on a large scale.[28] The distortion of the pores was clearly observed from the worm-like mesoporous of the as-synthesized NH_2-*meso*-silica/CTAB nanoparticles in Figure 5.1B. Besides, the amino-groups also destruct the regularity of arrays of micelles.[29]

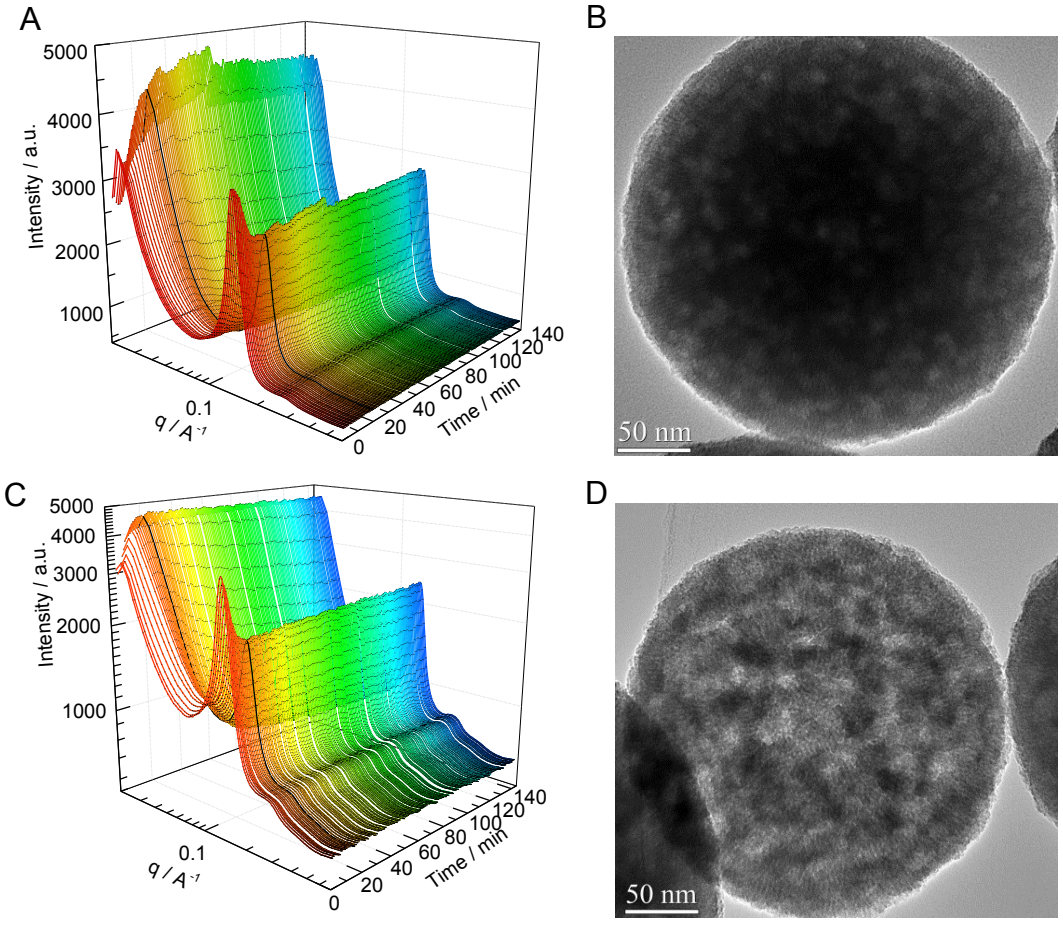

Figure 5.15 (A) *In situ* time-resolved synchrotron SAXS for NH_2-*meso*-silica/CTAB etching process under 0.1 M Na_2CO_3 at 60 ^oC, (B) TEM image of the particle in A at t = 130 min. (C) *In situ* time-resolved synchrotron SAXS for NH_2-*meso*-silica/CTAB etching process under 0.3 M Na_2CO_3 at 60 ^oC, and (D) TEM image of the particle in C at t = 130 min. Black line in A and C shows the lowest peak intensity during the etching process.

Moreover, the transformation of NH_2-*meso*-silica/CTAB into NH_2-HMS was also investigated by the *in situ* time-resolved synchrotron SAXS technique, as shown in Figure 5.15. Figure 5.15A shows the SAXS curves of the NH_2-*meso*-silica/CTAB particles within 130 min under 0.1M Na_2CO_3 at 60°C. The unique peak centred at q = 0.145 $Å^{-1}$, corresponding to the (100) plane of the NH_2-*meso*-silica/CTAB particles, decreased against the etching time and reached the bottom at t = 20 min, as marked in black in Figure 5.15A. And then the peak intensity slightly increased until the end of the experiment, while the peak position kept constant during the whole etching treatment (Figure 5.16A). On the contrary, the intensity of the overlapping peak at q= 0.280 $Å^{-1}$ was almost the same from t = 1 to 20 min, and then it slightly increased until the end of the experiment (Figure 5.16A inset).

Figure 5.15B shows the TEM image for an individual NH_2-*meso*-silica/CTAB particle after finishing the etching treatment. The sphere shape and mesoporous structure of the etched NH_2-*meso*-silica/CTAB particles are intact with smooth edge. Besides, the particle size distribution of the NH_2-*meso*-silica/CTAB particles is almost the same before and after the etching treatment, as shown in Figure 5.16B. N-

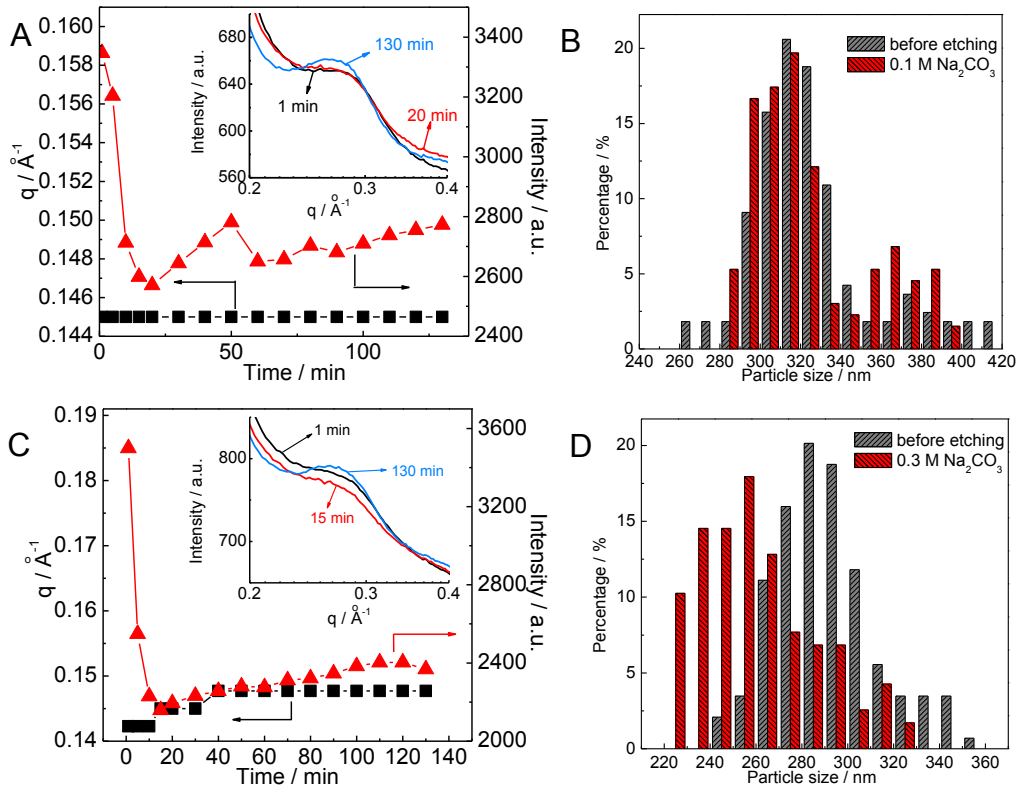

Figure 5. 16 The peak position and intensity of the NH_2-*meso*-silica/CTAB particles against etching time in (A) 0.1 M Na_2CO_3, and (C) 0.3 M Na_2CO_3. The particle size comparison before and after the etching treatment under (B) 0.1 M Na_2CO_3, and (D) 0.3 M Na_2CO_3 .

evertheless, the interior of the particle was etched to some extent, as indicated by the light colour areas in the interior of the particles. The results demonstrate that the alkaline solution reacts with silicate only in the interior of the NH_2-*meso*-silica/CTAB particles. Nevertheless, the alkaline solution is too low in concentration to transform NH_2-*meso*-silica/CTAB to NH_2-HMS. It should be noted that after the 20 min reaction, the ordering of NH_2-*meso*-silica/CTAB was slightly increase until the end of the experiment, which is likely due to the decrease of the distortion of the *meso*-channels during the alkaline etching reaction.

However, when the concentration of Na_2CO_3 solution increased to 0.3 M, the NH_2-*meso*-silica/CTAB particles were transformed into the NH_2-HMS/CTAB particles. Similarly, the intensity of the unique peak for the (100) plane and the overlapping peak for the (110) and (200) planes in the NH_2-*meso*-silica/CTAB particles shows the same bell-shape as the previous experiment. Both peak intensities decreased to the bottom at t = 15 min, marked as black in Figure 5.15C, which is faster than the previous sample. However, the peak position for the (100) plane shifted from 0.142 $Å^{-1}$ (t = 1 min) to 0.145 $Å^{-1}$ (t = 15 min), and then shifted to 0.145 $Å^{-1}$ (t = 40 min), as shown in Figure 5.16C. Moreover, Figure 5.15D shows that the interior of the NH_2-*meso*-silica/CTAB particles is thoroughly etched and only a mesoporous shell with thickness of ~ 40 nm is left. Furthermore, the average particle size changed from 285 nm for the NH_2-*meso*-silica/CTAB particles to 255 nm for the NH_2-HMS particles (Figure 5.16D).

5.3.3 Formation mechanism

Generally, the HMS and organic groups functionalized HMS materials are synthesized by the template strategy [30] and the self-templating strategy [11]. The synthesis, properties and applications of hollow mesoporous silica materials are concluded comprehensively by a few reviews [31-34]. In our case, templates are not employed, thus the template strategy is eliminated. For the self-templating strategy, a number of approaches for hollow structures silica materials have been developed, including surface protected etching [35, 36], structural difference-based selective etching [37], and cationic surfactant assisted self-etching [16]. Before the discussion on the formation mechanism of the NH_2-HMS material, let us first examine the self-templating mechanism in our case.

- Surface protected etching. When the surface of a solid silica sphere is covered by protecting agents such as PVP and PEI polyelectrolytes, it would be stabilized by the protecting agents. On the other hand, etching species, OH^-, is able to permeate to the interior of the silica spheres because of the relatively loose structure of sol-gel based the silica spheres, and selectively etch the interior of silica spheres. In our case, the CTAB molecules are confined in the mesoporous channels of the NH_2-*meso*-silica/CTAB spheres instead of the surface of the spheres. Moreover, the surface protecting etching method is limited for the solid silica spheres, rather than the mesoporous NH_2-*meso*-silica/CTAB particles. Therefore, the surface protecting etching principle is not suitable for the transformation of NH_2-*meso*-silica/CTAB to NH_2-HMS/CTAB in our case.
- Structural difference-based selective etching. Generally, a hybrid silica layer is covered on the silica template for this approach. It is based on the stability difference between the surface layer and interior of the hybrid silica spheres. When etching agents, such as water, ammonium hydroxide solution, Na_2CO_3 and HF etc., are employed, the interior parts of the hybrid silica spheres are selectively etched to form the HMS. ^{29}Si NMR analysis confirmed that the as-synthesized HMS showed fewer defects than the pristine silica spheres.[23, 38] In our case, the NH_2-*meso*-silica/CTAB spheres are homogeneous without surface covering. However, for the sol-gel based silica spheres, it is believed that the silicates located in the central parts are loose while the outer parts are dense, because the inner part is formed in the early stages of nucleation and growth. Given that the interior parts of the NH_2-*meso*-silica/CTAB spheres are less dense than the outer parts of the spheres, the interior parts tend to be etched by the etching agents, which is consistent with our results for the formation of NH_2-HMS. However, ^{29}Si MAR NMR in Figure 5.10 shows that the defects of the NH_2-HMS material is higher than the pristine NH_2-*meso*-silica/CTAB material. Thus, the structural difference-based selective etching approach cannot explain the formation of NH_2-HMS in our case.

After excluding the self-etching hypotheses, let us have a discussion about the roles of CTAB in the NH_2-*meso*-silica/CTAB particles. Generally, CTAB plays two

important roles during the formation of HMS. The first role is to redeposit the silicate species to form HMS. Zheng et al. [16] proposed an etching-redeposition mechanism for the formation of HMS from the solid SiO_2 spheres via the cationic surfactant-assisted selective etching strategy. According to the strategy, solid SiO_2 releases negatively charged soluble silicate species upon alkaline etching. The silicate species are covered by positively charged CTAB micelles via the electrostatic force and then redeposit on the surface of SiO_2. The etching-redeposition path facilitates the etching of SiO_2 and eventually leads to the formation of a mesostructured CTAB/SiO_2 shell, that is, HMS. The second role of CTAB is to stabilize the CTAB/SiO_2 *meso*-structure against the alkaline etching. [11, 16] When the core-shell SiO_2@CTAB/SiO_2 spheres are etched in the alkaline solution, solid SiO_2 core is selectively etched while the oriented mesoporous CTAB/SiO_2 shell is intact.

In our case, NH_2-HMS is transformed from NH_2-*meso*-silica/CTAB. Radical and cylindrical mesoporous channels filled with CTAB micelles are embedded in the NH_2-*meso*-silica/CTAB particles, and CTAB molecules are homogeneously distributed in the mesopores of NH_2-*meso*-silica/CTAB particles, as illustrated in Figure 5.17A. When the NH_2-*meso*-silica/CTAB particle is immersed in the alkaline solution, the Br^- ions in CTAB molecules will fast exchange with OH^- ions in the alkaline solution. OH^- ion, therefore, are homogeneously anchored on the surface of mesopores, as shown in Figure 5.17B. And the density of OH^- ions in the NH_2-*meso*-silica/CTAB particle with distance r from the centre of the sphere, ρ, can be calculated from the equation 5.1.

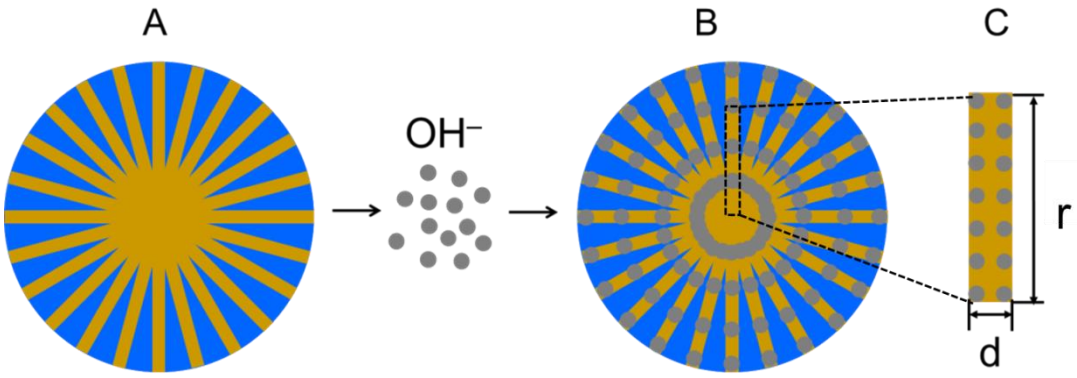

Figure 5. 17 The scheme for the cross-sectional image of a NH_2-*meso*-silica/CTAB particles; B, the particle of NH_2-*meso*-silica/CTAB after the OH^- ions exchange via CTAB molecules; C, the enlarged tubes for the mesopores in the NH_2-*meso*-silica/CTAB particles.

$$\rho = \frac{3nd^2\rho_0}{16r^2} \quad (0 < r \leq R) \tag{5.1}$$

Where ρ_0 is the density of OH^- ions in the mesopores; n is the number of mesopores in the sphere; d is the diameter of a mesopores; r is the radius started from the centre of the sphere, and R is the radius of the NH_2-*meso*-silica/CTAB, as illustrated in Figure 5.17C. Then the differential function can be calculated from equation 5.2.

$$\frac{d\rho}{dr} = -\frac{3nd^2\rho_0}{8r^3} < 0 \quad (0 < r \leq R) \tag{5.2}$$

From equation 5.2 we can obtain that the density of OH^- decreases with increase of r from 0 to R, that is, from the interior part to the outer part of the spheres.

Based on all the results regarding the synthesis and characterizations, a possible formation mechanism for NH_2-HMS is proposed, as shown in Figure 5.17. After the addition of TEOS and APTES in the CTAB solution, the hydrolysis of silanes forms the silica oligomers around the globular CTAB micelles, as named as stage 1. Then the negatively charged silica oligomers are self-assembled with positively charged CTAB globular micelles via electrostatic force (stage 2). And the globular micelles are extended into the enlongated rod-like shape micelles, and pack into a 2D hexagonal structure, leading to the small nucleus (stage 3). After that, the silica oligomers continuously assemble on the surface of the nucleus to form the NH_2-*meso*-silica/CTAB spheres (stage 4).

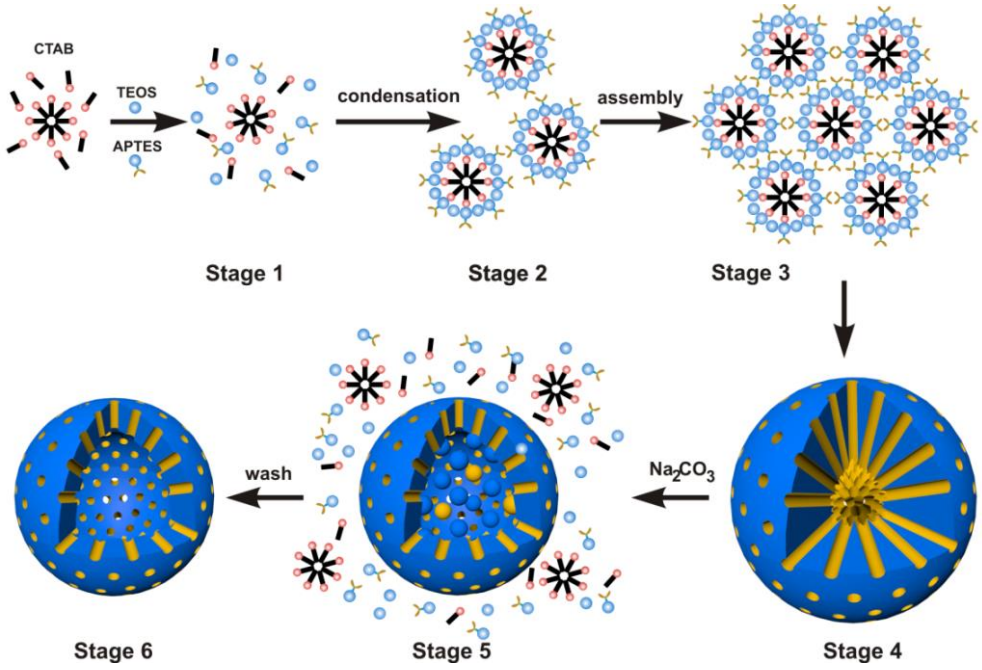

Figure 5.18 Proposed mechanism for the formation of NH_2-*meso*-silica/CTAB nanoparticles.

When the NH_2-*meso*-silica/CTAB spheres are immersed in a Na_2CO_3 solution, the OH^- ions are fast exchanged with the Br^- ions in the CTAB molecules that are confined in the mesopores of the NH_2-*meso*-silica/CTAB spheres. And the concentration of the OH^- decreases from the core to the outer parts of the sphere because of the gradient of the CTAB concentrations in the spheres. The high concentration of the OH^- ions in the interior parts leads to dissolve silicates. The hollow structure is formed after the dissolving of the interior parts of the spheres. Although the outer parts of the sphere are stable, they also could be dissolved by the high concentration of OH^- ions in the solution, resulting in the decrease of the particle size (stage 5). That is why the size of the NH_2-*meso*-silica/CTAB spheres is stable under the 0.1 M Na_2CO_3 solution, while it descends under the 0.3 M Na_2CO_3 solution. The etching process follows the sequence of the interior parts and then the outer parts of the spheres and the NH_2-HMS/CTAB spheres are formed (stage 6).

5.4 Conclusions

Amino-functionalized hollow mesoporous silica was fabricated through a simple alkaline etching treatment from the functionalized mesoporous silica spheres. And the transformation of NH_2-*meso*-silica to NH_2-HMS is largely dependent on the concentration of the surfactant and etching agent. Without the assistance of CTAB, the final NH_2-HMS could not be obtained. Besides, the particle size and the thickness of the shell can be controlled by tuning the concentration of CTAB and that of the etching agents, respectively. For the formation mechanism, it suggested that upon the exposure of the silica spheres to an alkaline solution, the OH^- ions are concentrated in the interior parts of the NH_2-*meso*-silica/CTAB spheres because of the enrichment effect induced by CTAB. The high concentration of OH^- ions in the interior parts of the spheres enables the reaction of silicate and OH^-. The OH^- ions in the alkaline solution also attack the outer parts of the sphere and reduce the particle size to some extent. However, further research is required to examine in details the reasons for the transformation of organic mesoporous silica spheres to hollow structures.

References

[1] J. Zeng, B. He, K. Lamb, R. De Marco, P.K. Shen, S.P. Jiang, Anhydrous Phosphoric

Acid Functionalized Sintered Mesoporous Silica Nanocomposite Proton Exchange Membranes for Fuel Cells, Acs Applied Materials & Interfaces 5 (21) (2013) 11240-11248.
[2] J. Zeng, B. He, K. Lamb, R. De Marco, P.K. Shen, S.P. Jiang, Phosphoric acid functionalized pre-sintered meso-silica for high temperature proton exchange membrane fuel cells, Chemical Communications 49 (41) (2013) 4655-4657.
[3] S. Lu, D. Wang, S.P. Jiang, Y. Xiang, J. Lu, J. Zeng, HPW/MCM-41 Phosphotungstic Acid/Mesoporous Silica Composites as Novel Proton-Exchange Membranes for Elevated-Temperature Fuel Cells, Advanced Materials 22 (9) (2010) 971-+.
[4] H. Tang, M. Pan, S.P. Jiang, Self assembled 12-tungstophosphoric acid-silica mesoporous nanocomposites as proton exchange membranes for direct alcohol fuel cells, Dalton Transactions 40 (19) (2011) 5220-5227.
[5] J. Yang, D. Aili, Q. Li, Y. Xu, P. Liu, Q. Che, J.O. Jensen, N.J. Bjerrum, R. He, Benzimidazole grafted polybenzimidazoles for proton exchange membrane fuel cells, Polymer Chemistry 4 (17) (2013) 4768-4775.
[6] Q. Li, R.H. He, J.O. Jensen, N.J. Bjerrum, Approaches and recent development of polymer electrolyte membranes for fuel cells operating above 100 degrees C, Chemistry of Materials 15 (26) (2003) 4896-4915.
[7] Y. Zhou, J. Yang, H. Su, J. Zeng, S.P. Jiang, W.A. Goddard, Insight into Proton Transfer in Phosphotungstic Acid Functionalized Mesoporous Silica-Based Proton Exchange Membrane Fuel Cells, Journal of the American Chemical Society 136 (13) (2014) 4954-4964.
[8] J. Zeng, S.P. Jiang, Characterization of High-Temperature Proton-Exchange Membranes Based on Phosphotungstic Acid Functionalized Mesoporous Silica Nanoconnposites for Fuel Cells, Journal of Physical Chemistry C 115 (23) (2011) 11854-11863.
[9] J. Zeng, Y. Zhou, L. Li, S.P. Jiang, Phosphotungstic acid functionalized silica nanocomposites with tunable bicontinuous mesoporous structure and superior proton conductivity and stability for fuel cells, Physical Chemistry Chemical Physics 13 (21) (2011) 10249-10257.
[10] N.R. Shiju, A.H. Alberts, S. Khalid, D.R. Brown, G. Rothenberg, Mesoporous Silica with Site-Isolated Amine and Phosphotungstic Acid Groups: A Solid Catalyst with Tunable Antagonistic Functions for One-Pot Tandem Reactions, Angewandte Chemie International Edition 50 (41) (2011) 9615-9619.
[11] X. Fang, X. Zhao, W. Fang, C. Chen, N. Zheng, Self-templating synthesis of hollow mesoporous silica and their applications in catalysis and drug delivery, Nanoscale 5 (6) (2013) 2205-2218.
[12] K. Cheng, C.C. Landry, Diffusion-Based Deprotection in Mesoporous Materials: A Strategy for Differential Functionalization of Porous Silica Particles, Journal of the American Chemical Society 129 (31) (2007) 9674-9685.
[13] W. Huang, Functionalized mesoporous silica nanoparticles (MSNs) for applications in drug delivery and catalysis., (2010).
[14] N. Hao, K.W. Jayawardana, X. Chen, M. Yan, One-Step Synthesis of Amine-Functionalized Hollow Mesoporous Silica Nanoparticles as Efficient Antibacterial and Anticancer Materials, ACS Applied Materials & Interfaces 7 (2) (2015) 1040-1045.
[15] J. Gao, X. Zhang, Y. Lu, S. Liu, J. Liu, Selective Functionalization of Hollow Nanospheres with Acid and Base Groups for Cascade Reactions, Chemistry – A European Journal 21 (20) (2015) 7403-7407.
[16] X. Fang, C. Chen, Z. Liu, P. Liu, N. Zheng, A cationic surfactant assisted selective etching strategy to hollow mesoporous silica spheres, Nanoscale 3 (4) (2011) 1632-1639.
[17] Z. Teng, Y. Han, J. Li, F. Yan, W. Yang, Preparation of hollow mesoporous silica spheres by a sol–gel/emulsion approach, Microporous and Mesoporous Materials 127 (1–2) (2010) 67-72.
[18] J.L. Blin, C. Gérardin, L. Rodehüser, C. Selve, M.J. Stébé, Influence of Alkyl Peptidoamines on the Structure of Functionalized Mesoporous Silica, Chemistry of Materials 16 (24) (2004) 5071-5080.
[19] N. Shadjou, M. Hasanzadeh, Amino functionalized mesoporous silica decorated with iron oxide nanoparticles as a magnetically recoverable nanoreactor for the synthesis of a new series of 2,4-diphenylpyrido[4,3-d]pyrimidines, RSC Advances 4 (35) (2014) 18117-18126.
[20] T. Suteewong, H. Sai, M. Bradbury, L.A. Estroff, S.M. Gruner, U. Wiesner, Synthesis

and Formation Mechanism of Aminated Mesoporous Silica Nanoparticles, Chemistry of Materials 24 (20) (2012) 3895-3905.
[21] T. Suteewong, H. Sai, R. Cohen, S. Wang, M. Bradbury, B. Baird, S.M. Gruner, U. Wiesner, Highly Aminated Mesoporous Silica Nanoparticles with Cubic Pore Structure, Journal of the American Chemical Society 133 (2) (2011) 172-175.
[22] Z. Teng, S. Wang, X. Su, G. Chen, Y. Liu, Z. Luo, W. Luo, Y. Tang, H. Ju, D. Zhao, G. Lu, Facile Synthesis of Yolk–Shell Structured Inorganic–Organic Hybrid Spheres with Ordered Radial Mesochannels, Advanced Materials 26 (22) (2014) 3741-3747.
[23] Z. Teng, X. Su, Y. Zheng, J. Sun, G. Chen, C. Tian, J. Wang, H. Li, Y. Zhao, G. Lu, Mesoporous Silica Hollow Spheres with Ordered Radial Mesochannels by a Spontaneous Self-Transformation Approach, Chemistry of Materials 25 (1) (2013) 98-105.
[24] M.C. Burleigh, M.A. Markowitz, M.S. Spector, B.P. Gaber, Amine-Functionalized Periodic Mesoporous Organosilicas, Chemistry of Materials 13 (12) (2001) 4760-4766.
[25] M.C. Burleigh, M.A. Markowitz, M.S. Spector, B.P. Gaber, Direct Synthesis of Periodic Mesoporous Organosilicas: Functional Incorporation by Co-condensation with Organosilanes, The Journal of Physical Chemistry B 105 (41) (2001) 9935-9942.
[26] A.Y. Khodakov, V.L. Zholobenko, M. Impéror-Clerc, D. Durand, Characterization of the Initial Stages of SBA-15 Synthesis by in Situ Time-Resolved Small-Angle X-ray Scattering, The Journal of Physical Chemistry B 109 (48) (2005) 22780-22790.
[27] V.K. Aswal, J. Kohlbrecher, P.S. Goyal, H. Amenitsch, S. Bernstorff, Counterion condensation on charged micelles in an aqueous electrolyte solution as studied with combined small-angle neutron scattering and small-angle x-ray scattering, Journal of Physics: Condensed Matter 18 (50) (2006) 11399.
[28] B. Pauwels, G. Van Tendeloo, C. Thoelen, W. Van Rhijn, P.A. Jacobs, Structure Determination of Spherical MCM-41 Particles, Advanced Materials 13 (17) (2001) 1317-1320.
[29] T.M. Suzuki, T. Nakamura, K. Fukumoto, M. Yamamoto, Y. Akimoto, K. Yano, Direct synthesis of amino-functionalized monodispersed mesoporous silica spheres and their catalytic activity for nitroaldol condensation, Journal of Molecular Catalysis A: Chemical 280 (1–2) (2008) 224-232.
[30] X.W. Lou, L.A. Archer, Z. Yang, Hollow Micro-/Nanostructures: Synthesis and Applications, Advanced Materials 20 (21) (2008) 3987-4019.
[31] X. Wang, J. Feng, Y. Bai, Q. Zhang, Y. Yin, Synthesis, Properties, and Applications of Hollow Micro-/Nanostructures, Chemical Reviews (2016).
[32] X. Du, J. He, Spherical silica micro/nanomaterials with hierarchical structures: Synthesis and applications, Nanoscale 3 (10) (2011) 3984-4002.
[33] Y. Li, J. Shi, Hollow-Structured Mesoporous Materials: Chemical Synthesis, Functionalization and Applications, Advanced Materials 26 (20) (2014) 3176-3205.
[34] Y. Ye, C. Jo, I. Jeong, J. Lee, Functional mesoporous materials for energy applications: solar cells, fuel cells, and batteries, Nanoscale 5 (11) (2013) 4584-4605.
[35] T. Zhang, J. Ge, Y. Hu, Q. Zhang, S. Aloni, Y. Yin, Formation of Hollow Silica Colloids through a Spontaneous Dissolution–Regrowth Process, Angewandte Chemie International Edition 47 (31) (2008) 5806-5811.
[36] Q. Zhang, T. Zhang, J. Ge, Y. Yin, Permeable Silica Shell through Surface-Protected Etching, Nano Letters 8 (9) (2008) 2867-2871.
[37] Y. Chen, H. Chen, L. Guo, Q. He, F. Chen, J. Zhou, J. Feng, J. Shi, Hollow/Rattle-Type Mesoporous Nanostructures by a Structural Difference-Based Selective Etching Strategy, ACS Nano 4 (1) (2010) 529-539.
[38] Z. Teng, X. Su, B. Lee, C. Huang, Y. Liu, S. Wang, J. Wu, P. Xu, J. Sun, D. Shen, W. Li, G. Lu, Yolk–Shell Structured Mesoporous Nanoparticles with Thioether-Bridged Organosilica Frameworks, Chemistry of Materials 26 (20) (2014) 5980-598.

Chapter 6 Phosphotungstic acid impregnated amino-functionalized hollow mesoporous silica particles for the elevated temperature fuel cells application

6.1 Introduction

Phosphoric acid employed as a proton conductor in high temperature proton exchange membranes has attracted great attentions because of its high proton conductivity and stability at elevated temperatures.[1] Polybenzimidazole is the state-of-the-art membrane suitable for PA-doping because of the weak basic properties of its heterocyclic functional groups.[2] Although PBI shows a high glass transition temperature and high stability at the temperature up to 435 ^{o}C, the complicated fabrication process largely hinders the wide application of PBI membrane as a PEM in elevated temperature fuel cells.[3] Recently, Lu et al.[4] developed a composite membrane simply by blending polyethersulfone and polyvinylpyrrolidone to form the PES-PVP composite membrane. The membrane was successfully employed in elevated temperature fuel cells. PA-doped PES-PVP composite membranes showed the high performance at the temperature as high as 180 ^{o}C.[5] The higher proportion of PVP, the higher content of PA is adsorbed, leading to the high proton conductivity. However, the chemical and mechanical stabilities of the PA-doped PES-PVP composite membranes with a high content of PVP tend to seriously deteriorate at elevated temperatures. Hence, there is a trade-off between the stability of the polymer membrane and its cell performance.

Incorporation of inorganic nanoparticles and proton conductors into proton exchange membranes substantially improves the properties of PEMs.[6, 7] For instance, the addition of mesoporous silica materials into PA-doped polymer composite membranes facilitates the proton conduction and improves the cell performance.[8] According to our previous research, PA-doped inorganic-organic PES-PVP hybrid membranes with hollow mesoporous silica, amino-functionalized mesoporous silica and amino-functionalized hollow mesoporous silica showed superior performance over the pristine PA-doped PES-PVP membrane. And the hybrid PES-PVP membrane with NH_2-HMS showed the best performance among these three types of composite membranes. It is suggested that it was the $–NH_2$ groups in the mesopores which facilitated proton transportation in the mesopores of

the silica materials. Although functionalized mesoporous silica materials can improve the proton conductivity of the proton exchange membranes, their intrinsic non-conductive characteristic limits their applications in the polymer matrix. In other words, excess mesoporous silica deteriorates the mechanical structure of the polymer membrane as well as the proton conductivity and cell performance.[9, 10]

Heteropolyacids are well known inorganic solid acids with high acidity and proton conductivity.[11] For instance, phosphomolybdic acid favours increase the PA uptake of poly(2,5-benzimidazole) (ABPBI), and consequently, improves the proton conductivity of the resulting membranes.[12, 13] Li et al. comprehensively studied the effects of the inorganic proton conductors on the proton conductivity of PA-doped PBI composite membranes.[14] They found that the addition of phosphotungstic acid and silicotungstic acid into PBI enhanced the mechanical strength and the proton conductivity of the PA/PBI membrane at temperatures up to 110 ^{o}C.[14] However, the HPAs are easy to dissolve in water generated in the fuel cell operation, leading the decrease of the proton conductivity of PEMs.[15] One protocol to reduce the loss of HPAs in PEMs is to transfer the HPAs into insoluble caesium salts. The Cs salts of HPAs are good candidates to form composite membranes with PBI for elevated temperature fuel cell applications.[16] However, the introduction of Cs salts into HPAs substantially reduce the proton conductivity of HPAs. Another protocol to fix the HPAs is employing the amino group with weak basicity. The amino group is an effective agent to anchor the heteropolyacid tightly on the walls of the mesoporous silica materials, such as PWA, via the acid-base pairs.[17]

Herein, PWA impregnated NH_2-HMS (named as PWA-NH_2-HMS) was employed to improve the performance of the PES-PVP composite membranes. PWA was confined in the mesopores of the amino-functionalized hollow mesoporous silica material via a vacuum impregnation method. The interactions between the PWA-NH_2-HMS particles and the PES-PVP membrane were comprehensively investigated. Moreover, the loading of PWA-NH_2-HMS was also optimized for the PA-doped PES-PVP composite membranes in terms of stability, proton conductivity and single cell performance. The results showed that the addition of PWA-NH_2-HMS filler significantly improved the performance of the PES-PVP composite membrane. And it shows great potential for the applications in elevated temperature fuel cells.

6.2 Experimental section

6.2.1 HPW-NH_2-HMS preparation

PWA was impregnated into the mesopores of the NH_2-HMS spheres via the vacuum impregnation method.[18] The loading of PWA in NH_2-HMS is 40.0 wt.%.

6.2.2 Membrane preparation

Certain amounts of inorganic fillers were mixed into the PES-PVP solution in NMP. The dispersion was casted in a petri dish at 100 ^oC for 24 h and 120 ^oC for 24 h. Then the membrane was detached from the petri dish with the assistance of Milli-Q water. The weight contents of PWA-NH_2-HMS in the PES-PVP membranes are 5.0, 10.0 and 15.0 wt.%. NH_2-HMS is employed as the control group, and the content of NH_2-HMS in the PES-PVP matrix is 10.0 wt.%.

6.2.3 Characterizations

Microstructure and element distribution of inorganic powders were examined by high-angle annular dark field (HAADF) scanning transmission electron microscopy (STEM) using FEI Titan G2 STEM in the accelerate voltage of 200 kV. The powder was dispersed in hexane and dropped on a copper grid for the HAADF STEM characterization.

TGA was conducted in the same way as described in Section 3.2.3. ATR-FTIR, SAXS, PA uptake and volume swelling, SEM for the cross-sectional morphology of the composite membrane, proton conductivity and cell performance analysis were conducted in the same way as described in Section 4.2.4.

Stress–strain curves were recorded using a Testometric Micro 350 under ambient conditions and a crosshead speed of 10.00 mm min^{-1}. The specimens were die-cut to a dog-bone shape with a gauge length and width of 28 and 2 mm, respectively.

6.3 Results and discussion

6.3.1 Morphology and structure

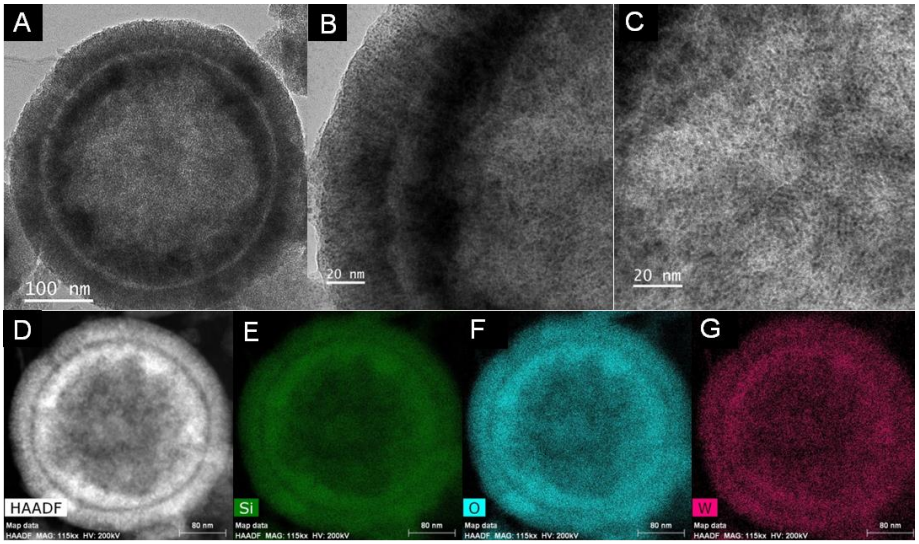

Figure 6.1 (A), (B) and (C) Bright field TEM images, and (D) HAADF STEM images of a PWA-NH_2-HMS particle. (E), (F) and (G) are the Si, O, and W element mapping for a PWA-NH_2-HMS particle, respectively.

After impregnation, the PWA molecules were confined homogeneously in the mesopores of the NH_2-HMS nanoparticles. As shown in Figure 6.1A-C, the hollow structure and the mesopores in the shell were clearly observed in the bright field TEM images. It can be seen that a large number of black dots with a size of 1-2 nm were confined in the mesopores. The high angle annular dark field scanning transmission electron microscopy image of PWA-NH_2-HMS (Figure 6.1D) further confirms the distribution of PWA in NH_2-HMS. More specifically, according to the silicon (Figure 6.1E) and the tungsten (Figure 6.1G) element mapping, the mesoporous channels of the NH_2-HMS were filled with PWA. This may due to the hydrogen bonds between PWA and amino groups in the mesoporous channels of NH_2-HMS.[19]

The mesoporous structure of NH_2-HMS and the confinement of PWA in the mesopores were also confirmed by the synchrotron small angle X-ray scattering results. Figure 6.2A shows a broad peak centred at 0.14 $Å^{-1}$ for NH_2-HMS, indicating the mesoporous structure of the shell. And the SAXS result is consistent with the STEM images in Figure 6.1. The presence of the mesoporous structure was further confirmed by the N_2 isotherm in Figure 6.2B. Type IV curve for the N_2 adsorption indicates the capillary condensation effect of the mesoporous structures, while H1 type hysteresis is an indication of cylindrical mesoporous structures. The Brunauer-Emmett-Teller surface area of the NH_2-HMS was 417.6 m^2g^{-1}, and the pore size calculated from Barrett-Joyner-Halenda adsorption method was 4.6 nm. After the

PWA impregnation, the peak position for the mesopores of NH_2-HMS remained unchanged, indicating the mesoporous structure of the host remains intact. However, the peak intensity was substantially reduced due to the reduced contrast between the silicate framework and the mesoporous channels.[20] The pore size and BET surface area of the PWA-NH_2-HMS particle decreased to 4.4 nm and 147.5 m^2g^{-1}, respectively. Furthermore, the pore volume of PWA-NH_2-HMS dropped to 0.28 cm^3g^{-1}, which is much lower than 0.87 cm^3g^{-1} of the pristine NH_2-HMS material. The decrease of BET surface area and pore volume confirms the occupation of PWA in the mesopores of the NH_2-HMS particles. And the physical properties of NH_2-HMS and PWA-NH_2-HMS are listed in Table 6.1.

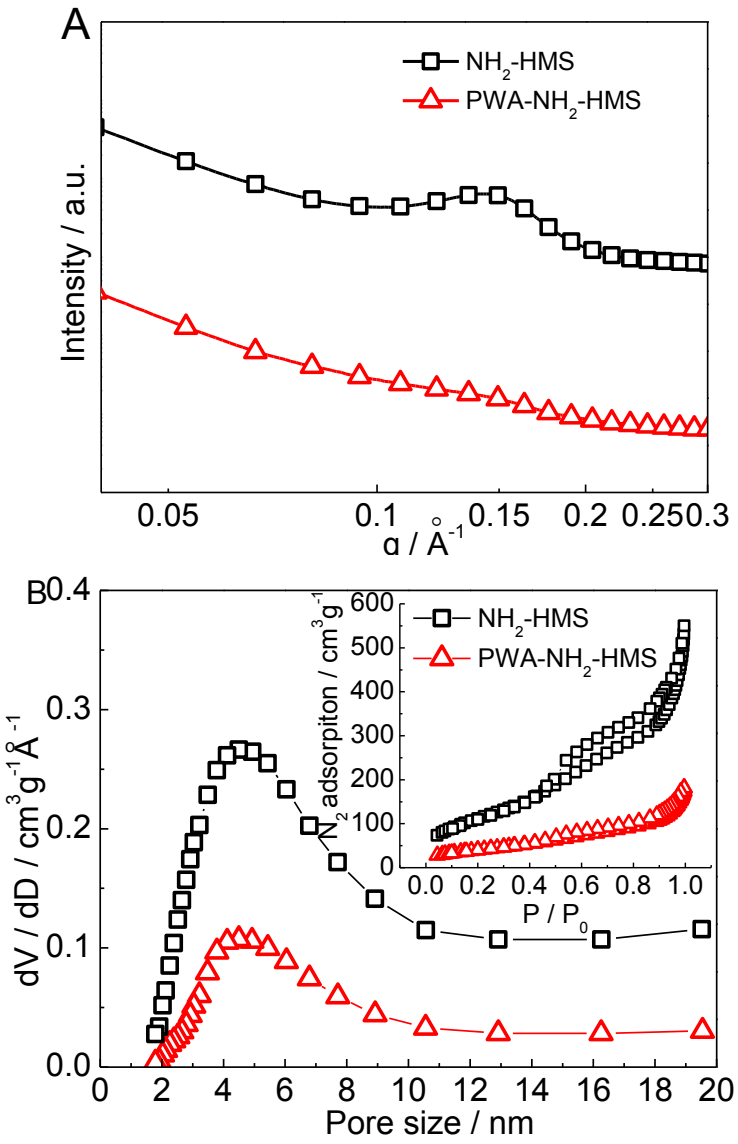

Figure 6.2 (A) SAXS profiles and (B) BET characterizations of NH_2-HMS particles impregnated by HPW.

Table 6.1 Physical properties of NH_2-HMS and PWA-NH_2-HMS with 40 wt.% PWA loading.

Sample	BET surface area, m^2g^{-1}	BJH adsorption average pore size, nm	BJH adsorption average pore volume, cm^3g^{-1}
NH_2-HMS	417.6	4.6	0.87
PWA-NH_2-HMS	147.5	4.4	0.28

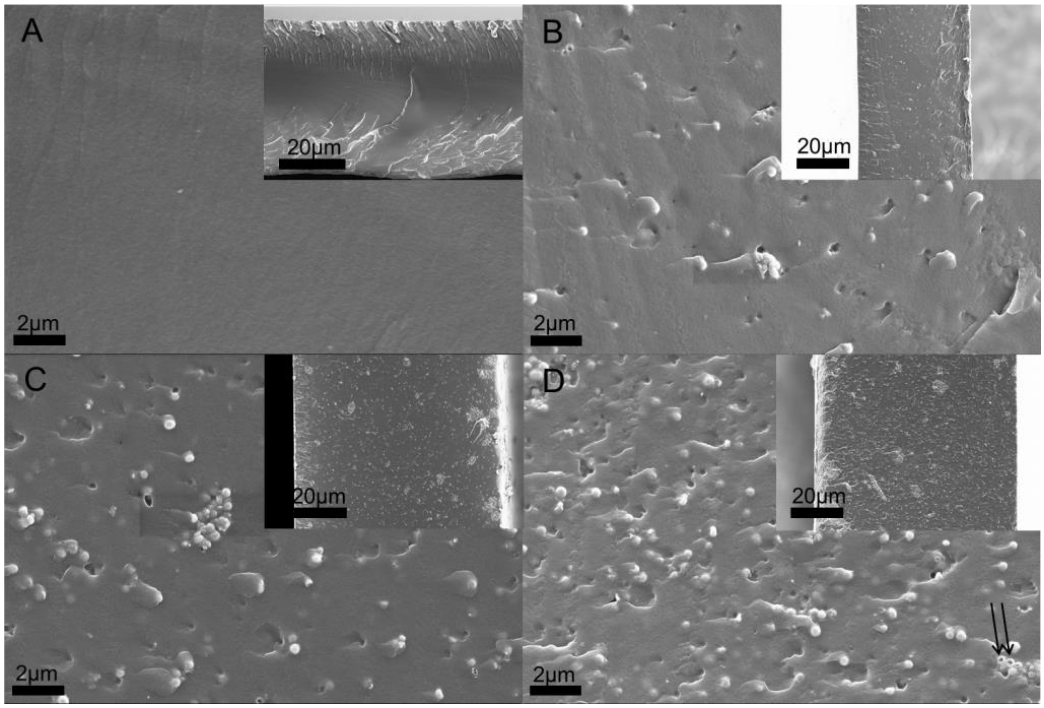

Figure 6.3 Cross section SEM images of the PES-PVP composite membranes with various PWA-NH_2-HMS loading (A) pristine PES-PVP, (B) 5 wt.%, (C) 10 wt.%, and (D) 15 wt.%. Inset images are the picture of the corresponding membranes at large scales.

Figure 6.3 shows the morphology of the PES-PVP composite membranes with different loading of PWA-NH_2-HMS. As can be seen in Figure 6.3A, the pristine PES-PVP composite membrane shows dense and smooth structure. When 5 wt.% PWA-NH_2-HMS was added into the matrix, the particles were found to be individually embedded on the PES-PVP membrane with a homogenous distribution (Figure 6.3B). Furthermore, according to Figure 6.3C and D, as the filler loading increased from 5 to 15 wt.%, increasingly dense particle distribution was observed. However, aggregates of the particles were found in the membrane with the filler loading of 15 wt.%, indicating an excess of the PWA-NH_2-HMS filler for the PES-PVP composite membrane. It should be noted that the hollow structure of PWA-NH_2-HMS particles was clearly observed on some broken particles, as pointed out by the arrows in Figure 6.3D.

6.3.2 *Thermal stability*

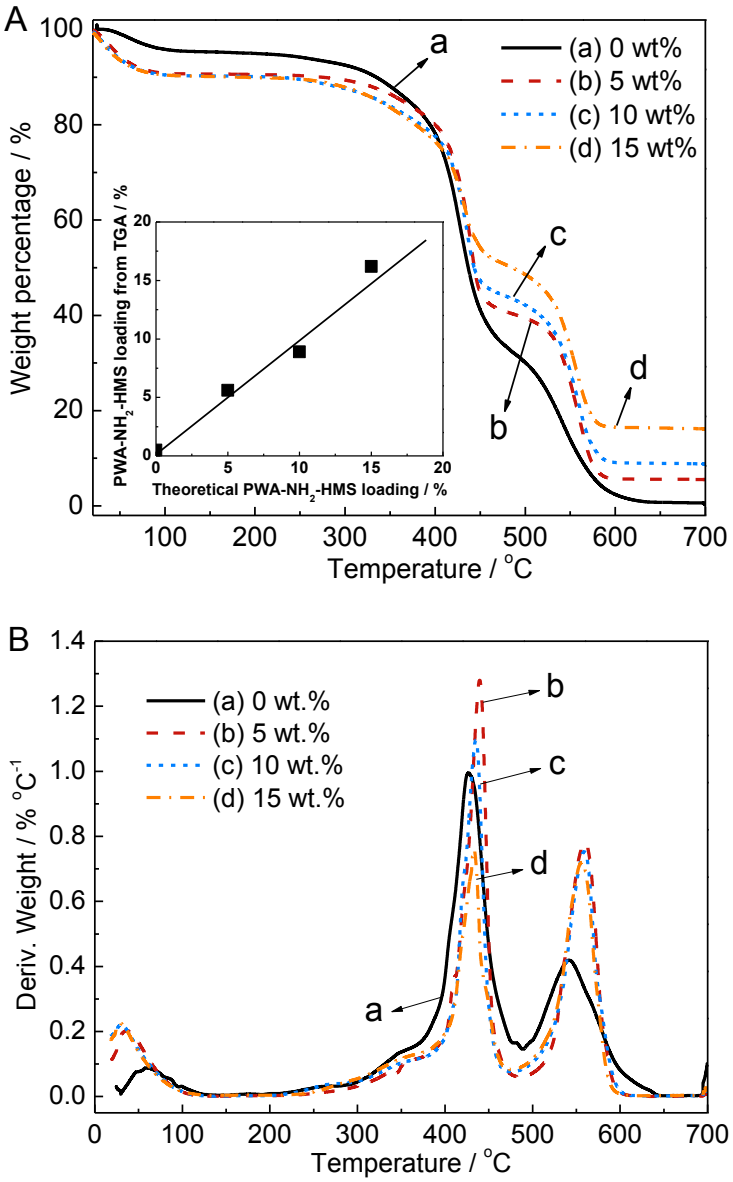

Figure 6.4 TGA profiles of the PWA-NH_2-HMS based PES-PVP composite membrane (A) weight and (B) derivation weight as a function of temperature.

Thermogravimetric analysis was employed to confirm the PWA-NH_2-HMS composition after casting and examine the thermo-oxidative stability of the composite membranes. The loading of PWA-NH_2-HMS determined by the calcination of the composite membrane in air is consistent with the calculated value, as shown in the inset of Figure 6.4A. The weight loss below 100 °C of all the composite membranes is due to the evaporation of adsorbed moisture. The second weight loss started from around 300 °C is due to the degradation of PVP. And the third weight loss at around 500 °C results from the decomposition of PES.[5] By

adding the PWA-NH_2-HMS fillers, the thermal stability of the PES-PVP composite membranes is improved in terms of the decomposition temperature of PVP and PES. For instance, the decomposition temperature of PVP increased from 426 to 439 ^oC, and that of PES raised from 541 to 559 ^oC after the addition of 5 wt.% PWA based mesoporous silica filler. Consequently, the addition of the PWA-NH_2-HMS fillers enhances the thermal stability of the PES-PVP composite membrane, which shows great potential for the application of these composite membranes in elevated temperature proton exchange membrane fuel cells.

6.3.3 ATR-FTIR

The characteristic ATR-FTIR adsorptions of PWA with Keggin unit in the PES-PVP membrane are shown in Figure 6.5. Compared with the adsorption band of W-O_b-W at 880 cm^{-1} in pristine PWA, the peak shifted to 895 cm^{-1} when PWA was added into the PES-PVP membrane. The results indicate that the proton of PWA is transferred to the PVP molecules. In the PVP molecule, only the electronegative nitrogen and the ketonic oxygen atom could interact with protons in PWA, while the C=O bonds (1650 cm^{-1}) in PVP remained unchanged by the addition of PWA.[21] Lu et al.[22] investigated the chemical interaction between PWA and the PES-PVP membrane, an-

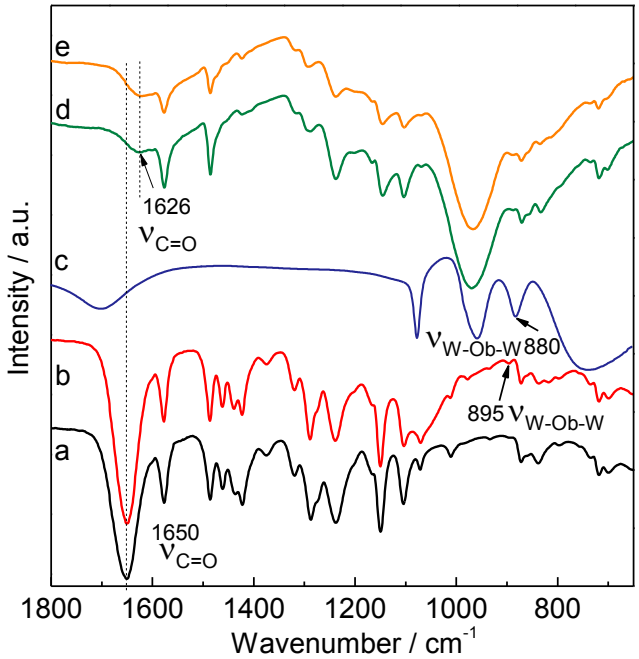

Figure 6.5 ATR-FTIR profiles of the PES-PVP composite membranes with different inorganic fillers.(A) pristine PES-PVP; (B) PES-PVP with PWA; (C) pristine PWA; (D) PA-PES-PVP; and (E) PA-PES-PVP with PWA-NH_2-HMS.

d revealed that it was H-O_b in the PWA molecule that interacted with the N atom in the N-heterocycle side chain of PVP. When the PES-PVP composite membrane was doped by PA, there was a broad peak in the range of 1050 – 900 cm^{-1}, which is attributed to the free phosphoric acid molecules.[23] Moreover, the C=O bonds in PVP red-shifted to 1626 cm^{-1} after the PA adoption both in PES-PVP and the PES-PVP membrane with the PWA-NH_2-HMS filler. The red shift of the C=O bond suggests strong interaction between C=O and the OH groups of the PA molecules via hydrogen bonding. Overall, it is the O atom and the N atom in PVP that tend to interact with PA and PWA molecules, respectively.

6.3.4 PA uptake, volume swelling and mechanical stability

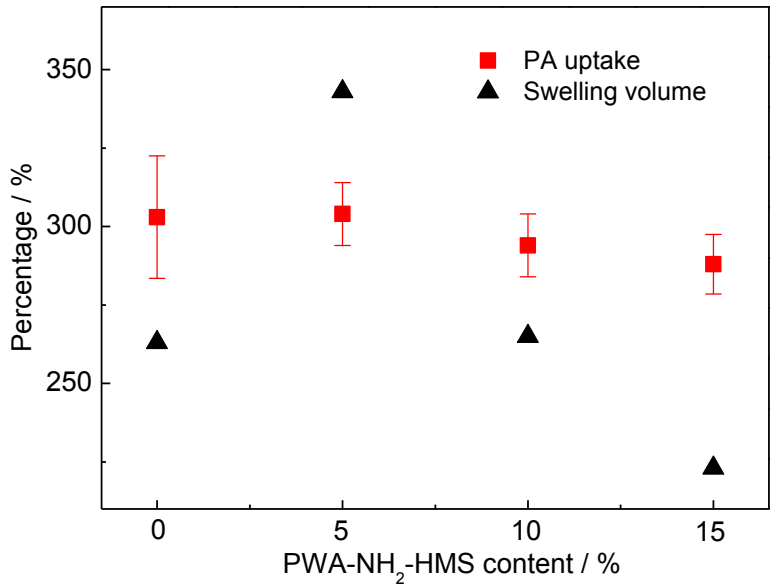

Figure 6.6 The PA uptake and volume swelling for the PES-PVP composite membranes with various loading of PWA-NH_2-HMS filler.

Table 6.2 Properties of the PES-PVP composite membranes with various loading of PWA-NH_2-HMS filler. NH_2-HMS was employed as the control group.

Inorganic filer	Loading, %	PA uptake, wt.%	volume swelling, %	PA per Unit	Elastic modulus, MPa
PWA-NH_2-HMS	0	303	213	4.9	16
	5.0	304	343	4.9	30
	10.0	294	265	4.8	23
	15.0	288	223	4.7	28
NH_2-HMS	10.0	278	179	4.5	–

The composite membranes were immersed in 85 wt.% PA for one week at room temperature for PA doping. PA uptake was determined gravimetrically relative to the weight of the dry membrane, as shown in Figure 6.6. The PA uptake of the composite membrane was found to slightly decrease with the addition of the inorganic PWA-NH_2-HMS filler. The PA uptake for the pristine PES-PVP composite membrane was 303 wt.%, corresponding to 4.9 PA per polymer repeat unit. Generally, the inorganic fillers show low PA uptake and weak interaction with the polymer membrane.[24] In this regards, by adding PWA-NH_2-HMS, the PA uptake would be expected to decrease. However, after the addition of 5 wt.% of PWA-NH_2-HMS into the PES-PVP membrane, the PA uptake remained almost the same as the pristine PES-PVP membrane, while the volume swelling ratio increased from 263 % of PES-PVP to 343 %. The possible reasons are when a certain amount of the inorganic particles are homogenously distributed on the polymer matrix, the particles weaken the interactions among the polymer molecules, resulting in the increase of the swelling ratio and consequently increased PA uptake. Moreover, $–NH_2$ group in the mesopores of the functionalized HMS also absorbed the PA molecules via the acid-base pair interaction. With further increase of the filler content, excessive inorganic particles tend to aggregate, leading to a reduced swelling ratio of the polymer matrix. For instance, when 15 wt.% of PWA-NH_2-HMS was added into the PES-PVP composite membrane, the volume ratio decreased to 223%. In that case, nevertheless, the positive effect on PA uptake contributed by the $–NH_2$ groups is not sufficiently significant to compensate the negative effect caused by the aggregation of the fillers, leading to a slight decrease of the PA uptake to 288 % for the composite membrane.

It should be noted that the PES-PVP membranes with the PWA-NH_2-HMS show superior PA uptake than the NH_2-HMS modified membrane. For instance, the addition of 10 wt.% of NH_2-HMS into the PES-PVP membrane resulted in a PA uptake of 278 wt.% and correspondingly 4.5 PA per polymer repeat unit. However, the PA uptake increased to 294 wt.% and 4.8 PA per polymer repeat unit with the same loading of PWA-NH_2-HMS in the membrane. Moreover, we have recently concluded that the addition of PWA into the pure PES-PVP membrane, with weight content of 1.2 –30 %, increased the PA uptake of the membrane. The addition of PWA in NH_2-HMS, therefore, substantially compensates the loss of the PA uptake caused by the addition of the NH_2-HMS in the composite membrane. The properties

in terms of the PA uptake, volume swelling ratio and the mechanical strengths of the composite membranes are listed in Table 6.2.

The strain-stress curves and the corresponding elastic modules for the PA-doped PES-PVP composite membranes with inorganic fillers are shown in Figure 6.7. In Figure 6.7A, the pristine PA-PES-PVP membrane shows high tensile stress at break of the membrane. After the addition of PWA-NH_2-HMS particles, the tensile stress of the composite membranes was lower than that of the pristine PA-PES-PVP membrane. Moreover, the tensile stress decreased with increasing the inorganic fillers. That is likely due to the discontinuities in the polymer phase.[24] On the contrary, the elastic modulus of the PA-PES-PVP membrane increased after the addition of the inorganic fillers (Figure 6.7B). For example, the elastic modulus of the phosphoric acid doped pure PBI membrane was 16 MPa as compared with 28 MPa for the membrane with a PWA-NH_2-HMS loading of 15 wt.% (Table 6.2). That indicates that the PES-PVP composite membranes with inorganic fillers become soft after the addition of the PWA-NH_2-HMS particles, which are still sufficient for processing and membrane electrode assembly fabrication.

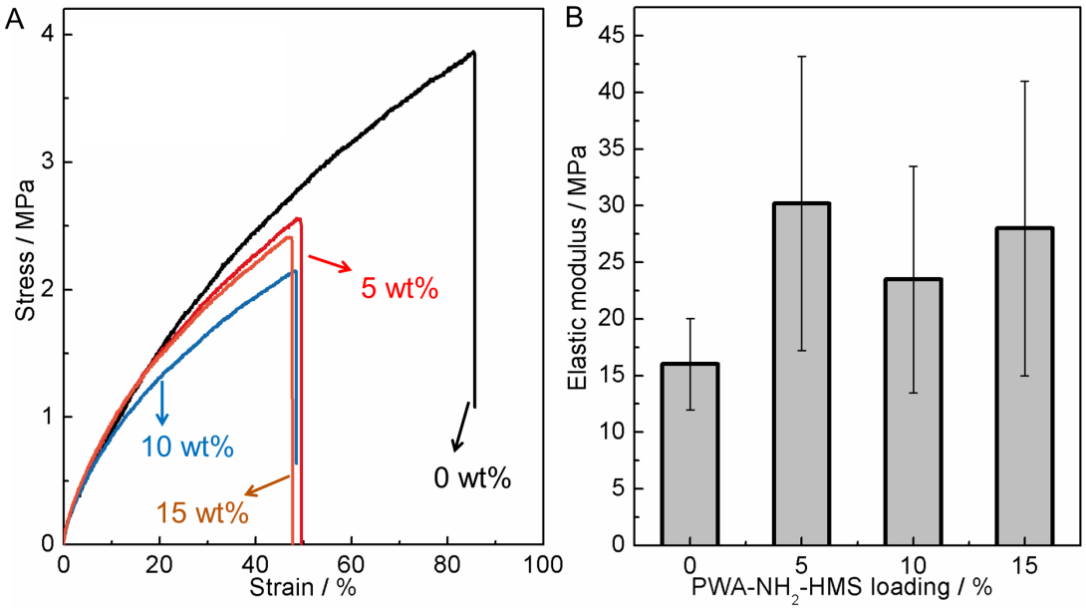

Figure 6. 7 (A) Selection of stress-strain curves for the composite membranes with PWA-NH_2-HMS loading of 0 – 15 wt.% after PA doping and (B) the corresponding elastic modulus for each membrane. The standard deviations are indicated by the error bars.

6.3.5 Proton conductivity

The *in situ* proton conductivity of the PES-PVP composite membranes with different fillers and filler loadings were tested at different temperatures (Figure 6.8A). For the PA-PES-PVP membrane, the proton conductivity of the membrane was 7.8×10^{-2} S cm^{-1} at 120 ^{o}C without external humidification, and it increased to 1.14×10^{-1} S cm^{-1} at 180 ^{o}C. When either NH_2-HMS or PWA-NH_2-HMS was added into the matrix, the proton conductivity of the composite membrane increased, compared with that of the PA-PES-PVP membrane. Mustarelli et al.[25] suggested that the entrance of PA into the mesopores of the silica materials had a positive effect on the proton conduction of the polymer membrane. In our case, when either the PWA-NH_2-HMS or NH_2-HMS particle was homogenously added into the PES-PVP membrane, PA also entered the mesopores of the fillers and facilitated the proton transportation in the polymer matrix.

Moreover, the PES-PVP membrane with 10 wt.% PWA-NH_2-HMS shows a proton conductivity of 1.75×10^{-1} S cm^{-1} at 180 ^{o}C under anhydrous condition, 35% higher than that of the membrane with 10 wt.% NH_2-HMS as the filler at the same condition (1.29×10^{-1} S cm^{-1}). Therefore, such enhanced proton conduction of the former membrane is considered to result from PWA. This is confirmed by examining the proton conductivity of the PES-PVP membrane with different loadings of the PWA-NH_2-HMS filler. As the PA uptake, the value decreased with increasing the filler loading. The proton conductivity would be expected to be reduced with the decrease of the PA uptake. However, the proton conductivity of the PES-PVP composite membranes increased from 1.61 to 1.75×10^{-1} S cm^{-1} at 180 ^{o}C, as the loading of PWA-NH_2-HMS increased from 5 wt.% to 10 wt.%. The result indicates that it is PWA that contribute to the improvement of the proton conductivity when the loading of the fillers is lower than 10 wt.%. Nevertheless, with the further increase of the loading to 15 wt.%, the proton conductivity reduced to 1.55×10^{-1} S cm^{-1} at the same test condition. These results demonstrate that under this condition, the improvement of proton conductivity contributed by PWA is insufficient to compensate the loss of proton conductivity resulting from the decrease of PA uptake.

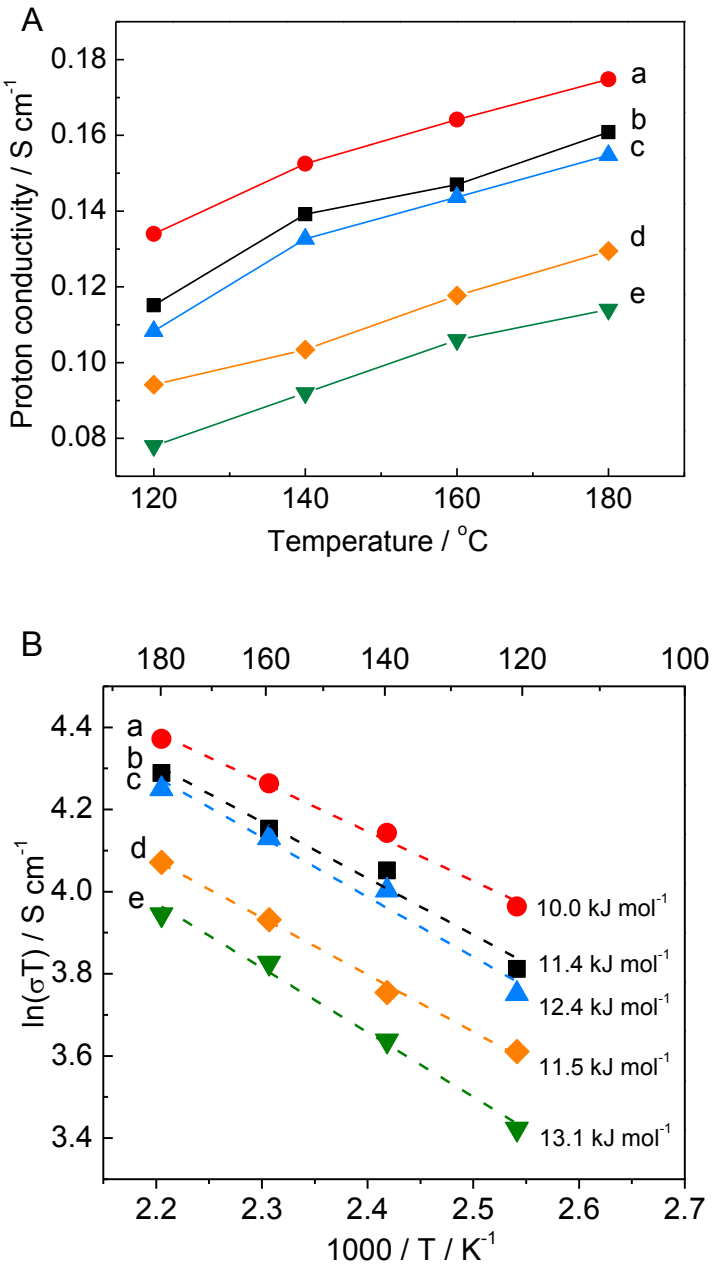

Figure 6.8 (A) Proton conductivity and (B) activation energy for proton transportation in PA-doped PES-PVP composite membranes. (a) ● 10 % PWA-NH_2-HMS; (b) ■ 5 % PWA-NH_2-HMS; (c) ▲ 15% PWA-NH_2-HMS; (d) ♦ 10 % NH_2-HMS; (e) ▼ pristine PES-PVP composite membrane.

Figure 6.8B shows the activation energy of proton transportation for the PA-doped PES-PVP composite membranes. The PA-doped PES-PVP membrane with 10 wt.% of NH_2-HMS shows lower activation energy than the PA-PES-PVP membrane, indicating a positive effect of the inorganic filler on proton diffusion in the PES-PVP composite membranes. When PWA-NH_2-HMS was added into the PES-PVP membrane, the activation energy for proton transportation was further reduced in comparison with that of NH_2-HMS. More specifically, the activation energy of PES-

PVP composite membranes shows a U-shape against the loading of PWA-NH_2-HMS. The PES-PVP membrane with 10 wt.% of PWA-NH_2-HMS shows the lowest activation energy of 10.0 kJ mol^{-1}, suggesting the highest proton diffusion rate of the membrane. The results also confirm the positive effect of the inorganic fillers for proton transportation in the PA-doped PES-PVP composite membrane, especially with the PWA-NH_2-HMS fillers. However, the excess filler loading of PWA-NH_2-HMS (> 10 wt.%) hinders the diffusion of protons in the membrane, resulting from the reduced PA adsorption ratio.

6.3.6 Cell performance

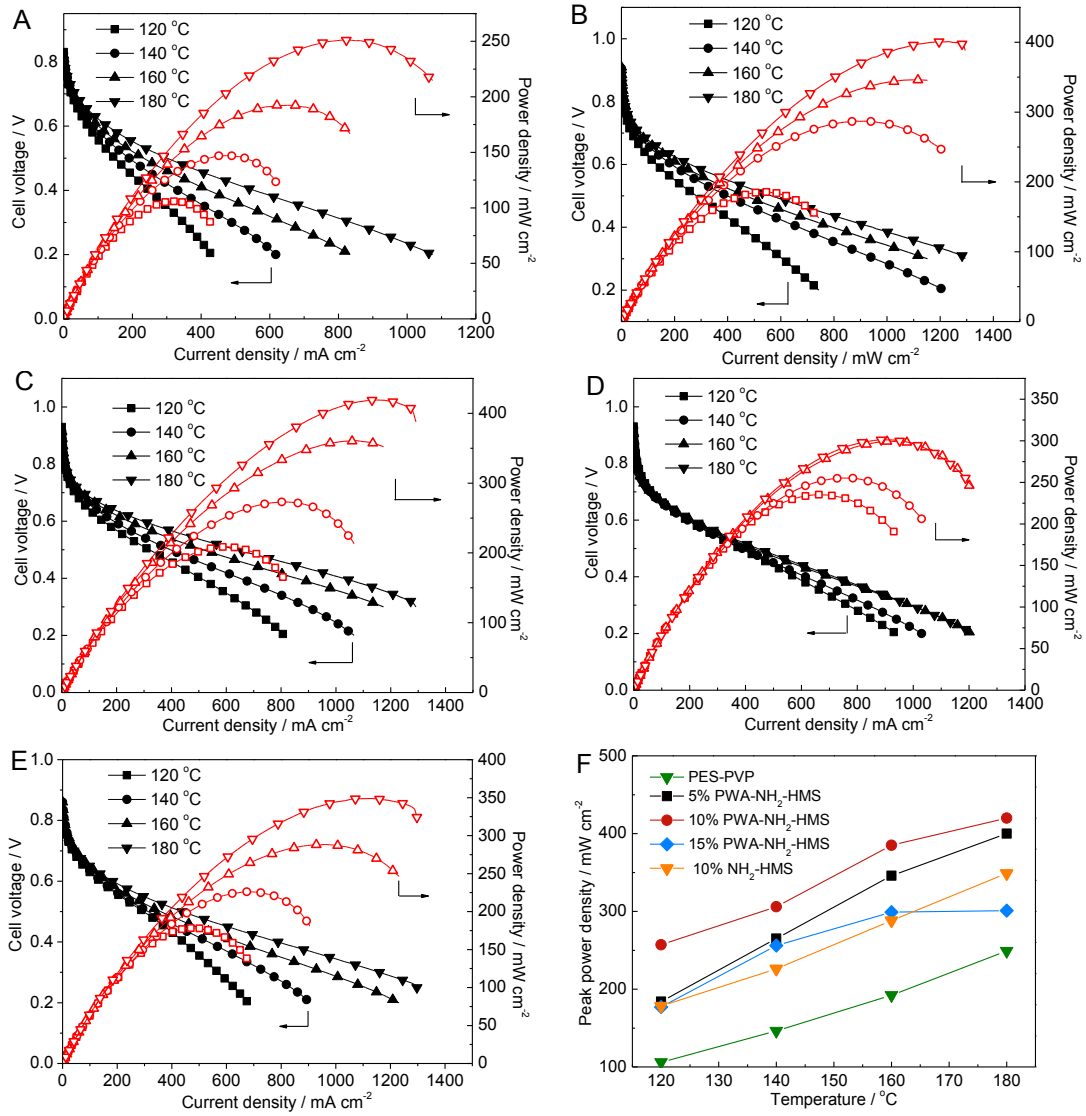

Figure 6.9 Single cell performance of PA-doped PES-PVP composite membranes with (A) pristine PES-PVP; (B) 5 % PWA-NH_2-HMS; (C) 10 % PWA-NH_2-HMS; (D) 15 % PWA-NH_2-HMS; (E) 10 % NH_2-HMS pristine and (F) peak power density conclusion of PES-PVP based composite membranes.

The single cell performance of the PA-doped PES-PVP composite membranes was evaluated at different temperatures, as shown in Figure 6.9. The peak power density of the PA-PES-PVP membrane was 105.9 mW cm^{-2} at 120 ^{o}C, and improved to 249.1 mW cm^{-2} at 180 ^{o}C (Figure 6.9A). When NH_2-HMS was added into the polymer host, the composite membrane shows superior peak power density than the PA-PES-PVP membrane at the temperatures ranging from 120 to 180 ^{o}C. For instance, the peak power density of PES-PVP membrane with 10 wt.% of NH_2-HMS reached up to 348.7 mW cm^{-2} at 180 ^{o}C, which is 40.0 % higher than that of the PA-PES-PVP membrane. This is due to the facilitated proton conductivity in the mesopores of the NH_2-HMS particles via the hydrogen bond network between the -NH_2 groups and the PA molecules. However, when 5 wt.% of PWA-NH_2-HMS was added into the PES-PVP membrane, the peak power density of the membrane was raised to 400 mW cm^{-2} at 180 ^{o}C without external humidification, 14.7 % higher than that of the PES-PVP membrane with NH_2-HMS. That is contributed to the positive effect of PWA for NH_2-HMS in terms of proton conductivity. Moreover, the highest cell performance reached up to 420 mW cm^{-2} at 180 ^{o}C for PES-PVP with 10 wt.% of PWA-NH_2-HMS. However, further increasing the loading of PWA-NH_2-HMS to 15 wt.% leaded to a decrease of the cell performance. Overall, the variation of the cell performance is subject to the positive effect of PWA and the negative effect of NH_2-HMS on the proton conductivity of the composite membrane.

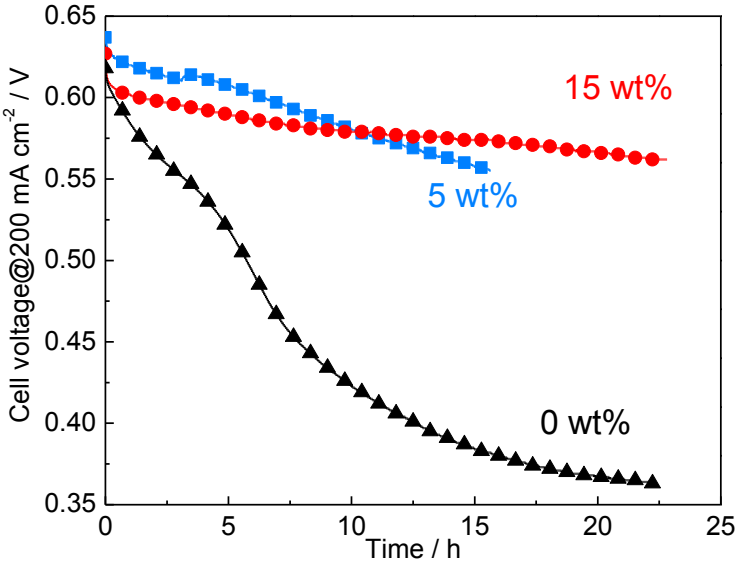

Figure 6.10 Durability test of PES-PVP based composite membranes with different loading of PWA-NH_2-HMS filler in the range of 0 to 15 wt.%. Both H_2 and O_2 have flow rate of 100 mL min^{-1}, 0 % RH, 90 ^{o}C, while the fuel cell was tested at 200 ^{o}C.

Durability of the single cell performance is also a critical criterion for the operation of PEMs in fuel cells. Figure 6.10 shows the durability of the PES-PVP composite membranes that were operated at 200 ^{o}C without external humidification. With the constant current loading of 200 mA cm^{-2}, the cell voltage of the PA-PES-PVP composite membrane sharply dropped from 0.62 V to 0.36 V during the period of 22 h. The substantial degradation of the durability is likely due to the dehydration and out-leaching of the acid in PA-PES-PVP membrane cells at the high temperature of 200 ^{o}C.[26] Moreover, as calculated and confirmed by Lu et al., the glass transition temperature of the PES-PVP membrane with the weight ratio of 3:7 is 190 ^{o}C,[5] which is lower than the operation temperature of the fuel cell. Thus, the high temperature might lead to the loss of thermal stability of the composite membrane, and consequently, the degradation of the membrane performance. By adding 5 wt.% of PWA-NH_2-HMS to the PES-PVP membrane, the degradation was significantly reduced as shown in Figure 6.10. By increasing the amount of PWA-NH_2-HMS to 15 wt.%, the durability was significantly improved. In comparison with the membrane with a 5 wt.% filler loading, the low cell voltage during the first 10 h is due to the low proton conductivity of the membrane with a 15 wt.% filler loading. Nevertheless, its durability was significantly higher than that with a 5 wt.% filler loading. This is likely to be attributed to the enhanced thermal stability after the addition of the inorganic fillers and *in situ* formation of phosphosilicate [24] in the composite membrane.

6.4 Conclusions

PWA impregnated NH_2-HMS were homogenously embedded in the matrix of the PES-PVP membrane with different loading up to 15 wt.%. PWA tended to donate the protons to the N atom in the heterocyclic carbon ring of PVP, while PA was favour to attack the ketonic O atom in the PVP molecules. Because of the facilitated proton transportation in the mesopores of NH_2-HMS, the addition of the filler significantly increased the proton conductivity and cell performance of the polymer host. Moreover, the impregnation of PWA into the amino-functionalized hollow mesoporous silica further improved the properties of the polymer matrix in terms of proton conductivity and single cell performance. The optimum loading of the PWA-NH_2-HMS in PES-PVP was determined to be 10 wt.%. Overall, PWA-NH_2-HMS

shows promising potential application with simple fabrication process and outstanding cell performance.

References

[1] Q. Li, J.O. Jensen, R.F. Savinell, N.J. Bjerrum, High temperature proton exchange membranes based on polybenzimidazoles for fuel cells, Prog. Polym. Sci. 34 (5) (2009) 449-477.

[2] S. Yu, L. Xiao, B.C. Benicewicz, Durability Studies of PBI-based High Temperature PEMFCs, Fuel Cells 8 (3-4) (2008) 165-174.

[3] B.G. Dawkins, F. Qin, M. Gruender, G.S. Copeland, High Temperature Polymer Blends, Woodhead Publishing, 2014, pp. 174-212.

[4] S. Lu, R. Xiu, X. Xu, D. Liang, H. Wang, Y. Xiang, Polytetrafluoroethylene (PTFE) reinforced poly(ethersulphone)–poly(vinyl pyrrolidone) composite membrane for high temperature proton exchange membrane fuel cells, Journal of Membrane Science 464 (2014) 1-7.

[5] X. Xu, H. Wang, S. Lu, Z. Guo, S. Rao, R. Xiu, Y. Xiang, A novel phosphoric acid doped poly(ethersulphone)-poly(vinyl pyrrolidone) blend membrane for high-temperature proton exchange membrane fuel cells, Journal of Power Sources 286 (2015) 458-463.

[6] X. Wu, M. Mamlouk, K. Scott, A PBI-Sb0.2Sn0.8P2O7-H3PO4 Composite Membrane for Intermediate Temperature Fuel Cells, Fuel Cells 11 (5) (2011) 620-625.

[7] S. Singha, T. Jana, Structure and Properties of Polybenzimidazole/Silica Nanocomposite Electrolyte Membrane: Influence of Organic/Inorganic Interface, Acs Applied Materials & Interfaces 6 (23) (2014) 21286-21296.

[8] Suryani, Y.-N. Chang, J.-Y. Lai, Y.-L. Liu, Polybenzimidazole (PBI)-functionalized silica nanoparticles modified PBI nanocomposite membranes for proton exchange membranes fuel cells, Journal of Membrane Science 403–404 (2012) 1-7.

[9] Y.-F. Lin, C.-Y. Yen, C.-C.M. Ma, S.-H. Liao, C.-H. Lee, Y.-H. Hsiao, H.-P. Lin, High proton-conducting Nafion (R)/-SO3H functionalized mesoporous silica composite membranes, Journal of Power Sources 171 (2) (2007) 388-395.

[10] Q. Li, R.H. He, J.O. Jensen, N.J. Bjerrum, Approaches and recent development of polymer electrolyte membranes for fuel cells operating above 100 degrees C, Chemistry of Materials 15 (26) (2003) 4896-4915.

[11] M.-Q. Li, Z.-G. Shao, K. Scott, A high conductivity Cs2.5H0.5PMo12O40/polybenzimidazole (PBI)/H3PO4 composite membrane for proton-exchange membrane fuel cells OPE-rating at high temperature, Journal of Power Sources 183 (1) (2008) 69-75.

[12] J.A. Asensio, S. Borrós, P. Gómez-Romero, Enhanced conductivity in polyanion-containing polybenzimidazoles. Improved materials for proton-exchange membranes and PEM fuel cells, Electrochemistry Communications 5 (11) (2003) 967-972.

[13] P. Gomez-Romero, J.A. Asensio, S. Borros, Hybrid proton-conducting membranes for polymer electrolyte fuel cells phosphomolybdic acid doped poly(2,5-benzimidazole)-(ABPBI-H3PMo12O40), Electrochimica Acta 50 (24) (2005) 4715-4720.

[14] R. He, Q. Li, G. Xiao, N.J. Bjerrum, Proton conductivity of phosphoric acid doped polybenzimidazole and its composites with inorganic proton conductors, Journal of Membrane Science 226 (1–2) (2003) 169-184.

[15] S.-Y. Oh, T. Yoshida, G. Kawamura, H. Muto, M. Sakai, A. Matsuda, Inorganic-organic composite electrolytes consisting of polybenzimidazole and Cs-substituted heteropoly acids and their application for medium temperature fuel cells, Journal of Materials Chemistry 20 (30) (2010) 6359-6366.

[16] C. Xu, X. Wu, X. Wang, M. Mamlouk, K. Scott, Composite membranes of polybenzimidazole and caesium-salts-of-heteropolyacids for intermediate temperature fuel cells, Journal of Materials Chemistry 21 (16) (2011) 6014-6019.

[17] N.R. Shiju, A.H. Alberts, S. Khalid, D.R. Brown, G. Rothenberg, Mesoporous Silica with Site-Isolated Amine and Phosphotungstic Acid Groups: A Solid Catalyst with Tunable Antagonistic Functions for One-Pot Tandem Reactions, Angewandte Chemie 123 (41) (2011) 9789-9793.

[18] X. Ji, K.T. Lee, R. Holden, L. Zhang, J. Zhang, G.A. Botton, M. Couillard, L.F. Nazar, Nanocrystalline intermetallics on mesoporous carbon for direct formic acid fuel cell anodes, Nat Chem 2 (4) (2010) 286-293.
[19] N.R. Shiju, A.H. Alberts, S. Khalid, D.R. Brown, G. Rothenberg, Mesoporous Silica with Site-Isolated Amine and Phosphotungstic Acid Groups: A Solid Catalyst with Tunable Antagonistic Functions for One-Pot Tandem Reactions, Angewandte Chemie International Edition 50 (41) (2011) 9615-9619.
[20] S. Lu, D. Wang, S.P. Jiang, Y. Xiang, J. Lu, J. Zeng, HPW/MCM-41 Phosphotungstic Acid/Mesoporous Silica Composites as Novel Proton-Exchange Membranes for Elevated-Temperature Fuel Cells, Advanced Materials 22 (9) (2010) 971-+.
[21] I. Szaraz, W. Forsling, Interaction between a capacitor electrolyte and gamma-aluminum oxide studied by Fourier transform infrared spectroscopy, Applied spectroscopy 57 (6) (2003) 622-627.
[22] S. Lu, X. Xu, J. Zhang, S. Peng, D. Liang, H. Wang, Y. Xiang, A Self-Anchored Phosphotungstic Acid Hybrid Proton Exchange Membrane Achieved via One-Step Synthesis, Advanced Energy Materials 4 (17) (2014) n/a-n/a.
[23] J.A. Asensio, S. Borrós, P. Gómez-Romero, Proton-conducting polymers based on benzimidazoles and sulfonated benzimidazoles, Journal of Polymer Science Part A: Polymer Chemistry 40 (21) (2002) 3703-3710.
[24] D. Aili, J. Zhang, M.T. Dalsgaard Jakobsen, H. Zhu, T. Yang, J. Liu, M. Forsyth, C. Pan, J.O. Jensen, L.N. Cleemann, S.P. Jiang, Q. Li, Exceptional durability enhancement of PA/PBI based polymer electrolyte membrane fuel cells for high temperature operation at 200 [degree]C, Journal of Materials Chemistry A 4 (11) (2016) 4019-4024.
[25] A.S. Cattaneo, D.C. Villa, S. Angioni, C. Ferrara, E. Quartarone, P. Mustarelli, Structure and Interactions in Polybenzimidazole Composite Membranes for High-Temperature Polymer Fuel Cells: A Full Multinuclear Solid-State NMR Study, The Journal of Physical Chemistry C 119 (33) (2015) 18935-18944.
[26] J. Zeng, B. He, K. Lamb, R. De Marco, P.K. Shen, S.P. Jiang, Anhydrous Phosphoric Acid Functionalized Sintered Mesoporous Silica Nanocomposite Proton Exchange Membranes for Fuel Cells, Acs Applied Materials & Interfaces 5 (21) (2013) 11240-11248.

Chapter 7 Phosphotungstic acid impregnated mesoporous silica for polybenzimidazole based polymer electrolyte membrane fuel cells at 200 °C

7.1 Introduction

High temperature operation of polymer electrolyte membrane fuel cells allows for better fuel impurity tolerance and catalyst kinetics as well as simplified cooling systems.[1] Membranes of phosphoric acid doped polybenzimidazole [2-4] or pyridine containing aromatic polyethers[5] are among the most promising electrolyte systems in this connection, showing high proton conductivity at low water activity as well as good thermal and oxidative stability. Great progress has been achieved in this field and lifetimes of up to 18,000 h have been reported by several groups at constant current load as well as under dynamic operation at intermediate temperatures up to about 160 °C.[6-11] While electrode related degradation seem to be the most significant during idling[12] or shut-down/start-up,[13] membrane degradation or acid redistribution predominate during the operation at high current loads.[14-16]

In the higher end of the operating temperature regime (180 – 200 °C) the PA loss rate increases considerably, eventually leading to acid depletion and proton conductivity decay.[6, 17] High water activities, *i.e.* operation at high current loads, further promote this mechanism,[6, 18] due to suppressed pyrophosphate formation.[19] For example, the PA leaching rate at the cathode at 190 °C has been found to be about an order of magnitude higher than at 160 °C.[6, 20] As a result, the durability data reported in the literature at 190 – 200 °C do not extend to much more than a few hundred hours of operation.[3, 6, 9] Nevertheless, increasing the operating temperature from 160 to 200 °C is strongly beneficial due to further improved catalyst kinetics and fuel impurity tolerance in combination with better possibilities for thermal integration with fuel processing units.[21-24] It is, therefore, of great interest to improve the long term stability under such challenging operating conditions, where the utilization of composite membranes has proven a successful approach.[25-27]

The proton conductivity and cell performance of the composite membranes can be improved by incorporating functionalized mesoporous silica materials into polyelectrolyte matrix.[28-30] That is due to their high water retention capability and

facilitated proton transportation in the functionalized mesoporous channels. Phosphotungstic acid ($H_3PW_{12}O_{40}\cdot nH_2O$) functionalized mesoporous silica (PWA-*meso*-SiO_2) shows a high proton conductivity of 3.4×10^{-2} S cm^{-1} and encouraging fuel cell performance at 200 °C.[31] Although PWA is water soluble and cannot be used as PEM on its own, leaching of the PWA is prevented by anchoring the heteropolyacid to the mesoporous silica network through ionic interactions. As a result, such composites show good stability and nearly unchanged ion exchange capacity after 200 h in water for the composites with low initial PWA contents of 10 – 15 wt.% [31].

Herein, we introduced PWA-*meso*-SiO_2 into the PA/PBI matrix to improve the fuel cell durability in the high end of the operating temperature regime. Stable operation was achieved under dry conditions at 200 °C for 2,700 h, which is a significant milestone in the high temperature PEM fuel cell development. Furthermore, the reasons for the exceptional durability of the composite membrane were investigated in details, and revealed that the *in situ* formed phosphosilicate and stabile Pt catalyst in the electrode were the critical factors.

7.2 Experimental

7.2.1 Membrane preparation

The PWA-*meso*-SiO_2 (40 wt.% PWA, 2.0 g) was prepared as described elsewhere [32] and dispersed in 100 mL methanol (Sigma-Aldrich) containing 2.0 g dequalinium chloride hydrate (DCH, Sigma-Aldrich), as shown in Figure 7.1. The mixture was stirred mechanically for 1 h and further ultrasonicated for 3 h to form a fine dispersion. The mixture was subsequently dried at 160 °C for 20 h *in vacuo* yielding an off-white powder. Composite membranes were prepared by dispersing the modified PWA-*meso*-SiO_2 in a *N*,*N*-dimethylacetamide (DMAc, Sigma-Aldrich) solution of *m*PBI (6.1 wt.%) from Danish Power Systems (inherent viscosity 0.95 dL g^{-1} at 30.0 °C and 500 mg dL^{-1} in 96 wt.% H_2SO_4), to give PWA-*meso*-SiO_2:*m*PBI weight ratios of 0, 5, 10, 15, 20, 30 and 40 wt.%. The mixtures were ultrasonicated for 20 h and cast on Petri dishes from room temperature to 120 °C. The obtained composite membranes were treated with methanol at 50 °C in order to wash out the DCH modifier and further dried at 180 °C for 3 h. The membranes were imbibed with PA in 85 wt.% H_3PO_4 (Sigma-Aldrich) for at least 2 weeks.

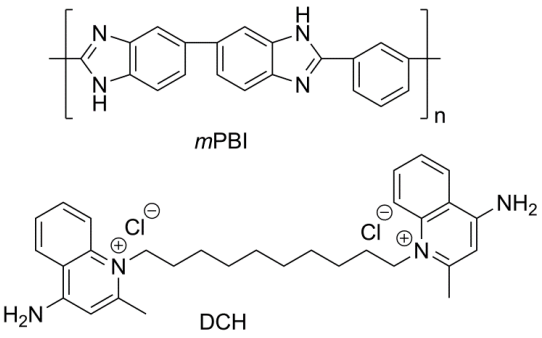

Figure 7.1 Chemical structure of the poly[2,2′-m-(phenylene)-5,5′-bibenzimidazole] (*m*PBI) repeat unit and dequalinium chloride hydrate modifier.

7.2.2 PWA-meso-SiO_2 and composite Membrane characterization

N_2 adsorption/desorption isotherms, ATR-FTIR, the acid uptake and volume swelling are the same way as described in Section 4.2.4. Mechanical performance and HAADF STEM are the same way as described in Section 6.2.3.

All the single pulse ^{1}H NMR and the ^{1}H PFG-NMR diffusion experiments were carried out on a Bruker Advance III 300 MHz wide bore spectrometer (with proton Larmor frequency of 300.13 MHz) equipped with a 5 mm diff50 pulse-field gradient (PFG) probe. The 90 degree pulse lengths for single pulse ^{1}H NMR were 15 μs, and the recycle delays were 10s to allow the system to recover to the equilibrium state. The pulse-field gradient stimulated echo (PFG-STE) pulse sequence was used to obtain diffusion coefficients. The maximum gradient strength is 29.454 T m^{-1}. The sample temperatures in the probe for the ^{1}H NMR variable temperature experiments were calibrated by using the relative chemical shift separation between the OH resonance and CH_3 resonance of dry methanol.

Scanning electron microscopy imaging was carried out using a Carl Zeiss EVO MA10 scanning electron microscope equipped with an INCA energy-dispersive X-ray spectroscopy system from Oxford Instruments. The membrane cross-sections for the SEM imaging were prepared by sandwiching the membrane samples between two pieces of non-woven carbon cloth followed by ion-milling using a Hitachi E-3500, and sputter coated with carbon.

Thermogravimetric data were acquired using a Netzsch STA 409 PC. The thermograms were recorded at a heating rate of 10 °C min^{-1} in air. The thermogravimetric curves were normalized with respect to the dry membrane basis at 210 °C.

7.2.3 Proton conductivity and fuel cell tests

The gas diffusion electrodes were supplied by Danish Power Systems. They consisted of 57.33 wt.% Pt/C from Johnson Matthey, applied on a nonwoven carbon substrate (Freudenberg H2315 C2) by a spray technique using *m*PBI as binder. The loading of platinum and *m*PBI was 1.6 and 0.1 mg cm^{-2}, respectively. Membrane-electrode assemblies with an active area of 4 cm^2 were fabricated by sandwiching the phosphoric acid doped membrane between two pieces of the gas diffusion electrodes followed by hot-pressing (4.9 MPa) at 180 °C for 10 minutes.

The fuel cell hardware was made of graphite plates with parallel gas channels. Two aluminum end plates with attached heaters were used to clamp the graphite plates and current collecting plates. Hydrogen and air were supplied to the anode and cathode, respectively. The polarization curves were obtained by current step potentiometry. The area specific resistance was obtained from the polarization data in the region where no mass trans limitations were present by fitting to Equation 7.1 by regression, where E is the cell voltage, i is the current density, a is a constant, b is the Tafel slope and R_{ASR} is the area specific resistance.

$$E = a - b\log(i) - iR_{ASR} \quad (7.1)$$

The proton conductivity of the composite membranes, σ was subsequently calculated according to Equation 7.2, where t is the thickness of the membrane and R_{ASR} is area specific resistance as obtained from Equation 7.1.

$$\sigma = t / R_{ASR} \quad (7.2)$$

7.3 Results

7.3.1 Morphology of the inorganic particles and membranes

The bright field TEM image in Figure 7.2A shows (100) plane of PWA-*meso*-SiO_2 particle. And the corresponding HAADF-STEM image clearly shows hexagonal mesoporous channels of the PWA-*meso*-SiO_2 particle along [100] direction (Figure 7.2B). From the silicon (Figure 7.2D) and tungsten (Figure 7.2C) element mapping it can be seen that the mesoporous channels of *meso*-SiO_2 are filled with PWA, anchored to the mesoporous silica network through ionic interactions.[33] The parallel white lines in the STEM image of PWA-*meso*-SiO_2 (Figure 7.2 E) compliments Figure 7.2 B by further confirming that the pores of *meso*-SiO_2 are

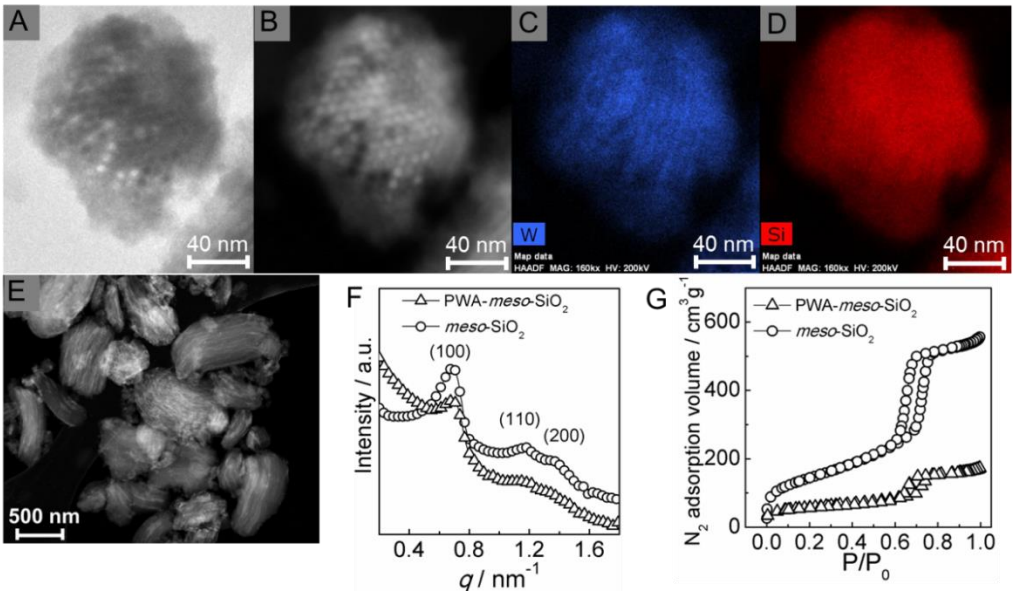

Figure 7.2 (A) Bright field TEM, (B) HAADF STEM image and corresponding (C) Si and (D) W element mapping for the PWA-*meso*-SiO_2; (E) large scale HAADF STEM image for PWA-*meso*-SiO_2; (F) SAXS patterns and (G) N_2 adsorption isotherm of *meso*-SiO_2 and PWA-*meso*-SiO_2.

filled with PWA along the [001] direction in large scales. The small angle X-ray scattering of *meso*-SiO_2 after PWA impregnation shows reduced intensity of the *meso*-SiO_2 matrix (Figure 7.2 F), indicating an aggregation of PWA within the *meso*-SiO_2 structure.[34] Moreover, the scattering peak position after PWA impregnation remains unchanged, suggesting structural integrity. The N_2 adsorption/desorption isotherms of *meso*-SiO_2 and PWA-*meso*-SiO_2 show type IV adsorption curves with capillary condensation effect for the mesoporous structure and H 1 type hysteresis for cylindrical mesoporous structures (Figure 7.2 G). The BET surface area and BJH pore volume of *meso*-SiO_2 were 507 $m^2\ g^{-1}$ and 0.89 $cm^3\ g^{-1}$, respectively, while they sharply reduced to 196 $m^2\ g^{-1}$ and 0.25 $cm^3\ g^{-1}$ after the PWA functionalization (Figure 7.2 G), which is consistent with the STEM/TEM and SAXS results.

The pristine PBI membrane shows a smooth and dense structure as evidenced from the cross-sectional scanning electron microscopy imaging (Figure 7.3A). After a surface modification of PWA-*meso*-SiO_2 with dequalinium chloride hydrate, homogenous PBI composite membranes were obtained with low PWA-*meso*-SiO_2 loading of 5 wt.% (Figure 7.3B). That is due to the great dispersion of the particles in PBI solution. Further increase the loadings of PWA-*meso*-SiO_2 to 10 – 15 wt.% resulted in anisotropic structures and pore formation (Figure 7.3C and D), likely due to the agglomeration of the inorganic component at high concentrations.

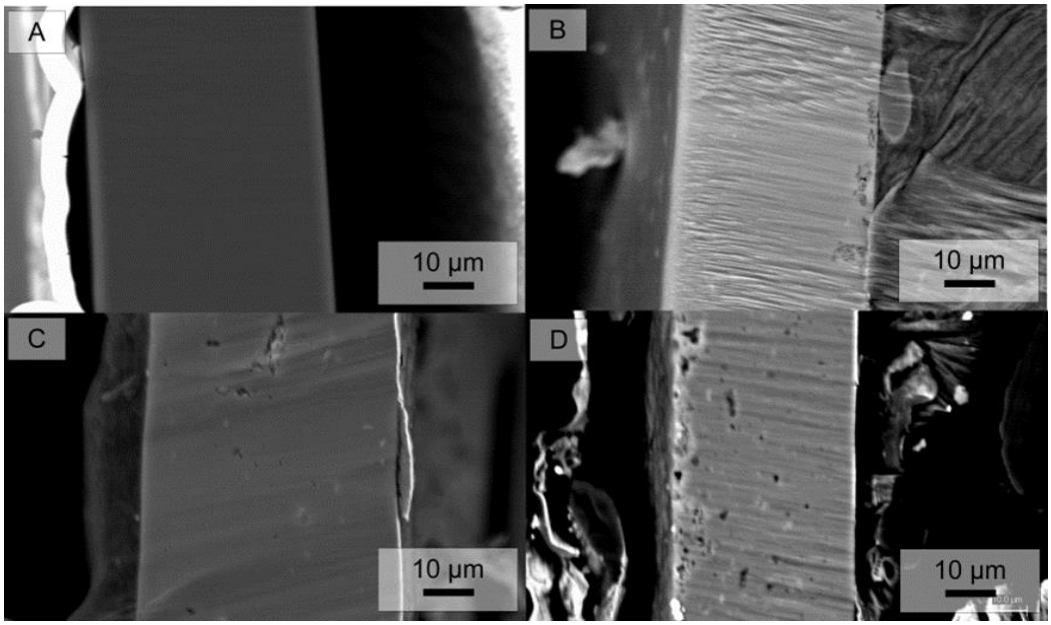

Figure 7.3 Cross sectional SEM images of (A) PBI, and PBI membranes with (B) 5 wt.%, (C) 10 wt.% and (D) 15 wt.% PWA-*meso*-silica.

7.3.2 PA uptake and mechanical properties

The composite membranes were subsequently equilibrated in 85 wt.% PA at room temperature. The PA uptake was determined gravimetrically relative to the weight of the dry membrane. It was found to decrease gradually with increasing the PWA-*meso*-SiO_2 loading (Table 7.1) More specifically, the PA uptake of the pristine PBI membrane was 341 wt.%, corresponding to about 10.5 PA per polymer repeat unit. When 5 wt.% PWA-*meso*-SiO_2 was added, the PA of the membrane dropped to 308 wt.%, indicating the negative effect of silica materials on the PA uptake of PA/PBI composite membranes.[35] That is also confirmed by the decrease of the PA uptake to 215 wt.% for the composite with a PWA-*meso*-SiO_2 loading of 40 wt.%.

Generally, the mechanical property of the composite membrane is a critical criterion for the membrane to be used in fuel cells. The mechanical properties of PBI composite membranes before and after PA-doping were tested, as shown in Figure 7.4. Before PA doping, the PBI composite membrane shows outstanding mechanical properties and dimensional stability, as shown in Figure 7.4A1 and A2. With increment of the PWA-*meso*-silica content in PBI membrane, the mechanical strength of the composite membrane dropped. That may be due to a porous structure of the composite membrane, resulting from the aggregation of the inorganic filler. On the other hand, when the PBI based composite membranes were doped by PA,

the mechanical strength of the composite membrane sharply dropped (Figure 7.4B1 and B2). That is due to the swelling of the membrane and the reduced intermolecular force among the polymer backbones. The elastic modulus and engineering tensile stress at break of the PA equilibrated composites was found to decrease with increasing PWA-*meso*-SiO_2, likely due to discontinuities in the polymer phase. For example, the elastic modulus of the phosphoric acid doped pure PBI membrane was 52 MPa as compared with 25 MPa for the membrane with a PWA-*meso*-SiO_2 loading of 40 wt.%, which is still sufficient for the processing and membrane electrode assembly fabrication. Overall, the results indicate that the inorganic filler reduce the mechanical strength of PBI membrane, where the mechanical strength of the PBI composite membranes is still sufficient to be operated in elevated temperature fuel cells.

Table 7.1 Phosphoric acid uptake and volume swelling after doping in 85 wt.% H_3PO_4 at room temperature for at least 2 weeks.

PWA-*meso*-SiO_2 loading / wt.%	0	5	10	15	20	30	40
H_3PO_4 uptake / wt.%	341	308	284	242	226	219	215
Volume swelling / vol.%	203	167	163	137	128	130	100

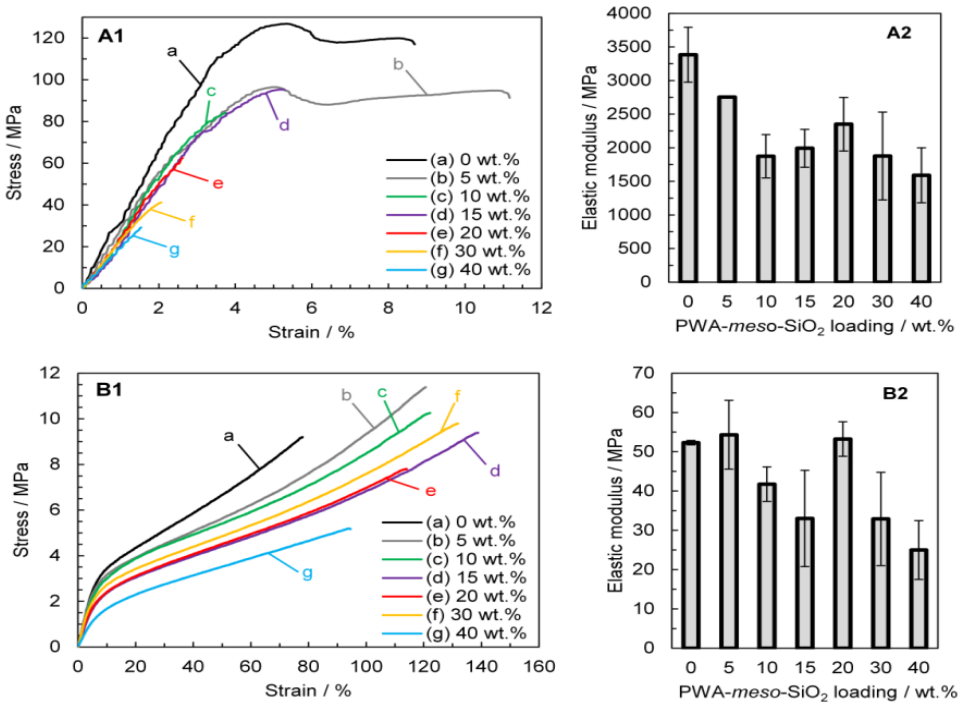

Figure 7.4 Tensile strength of PBI composite membranes with different PWA-*meso*-silica loading before (A1 and A2) and after (B1 and B2) PA-doping.

7.3.3 Proton conductivity

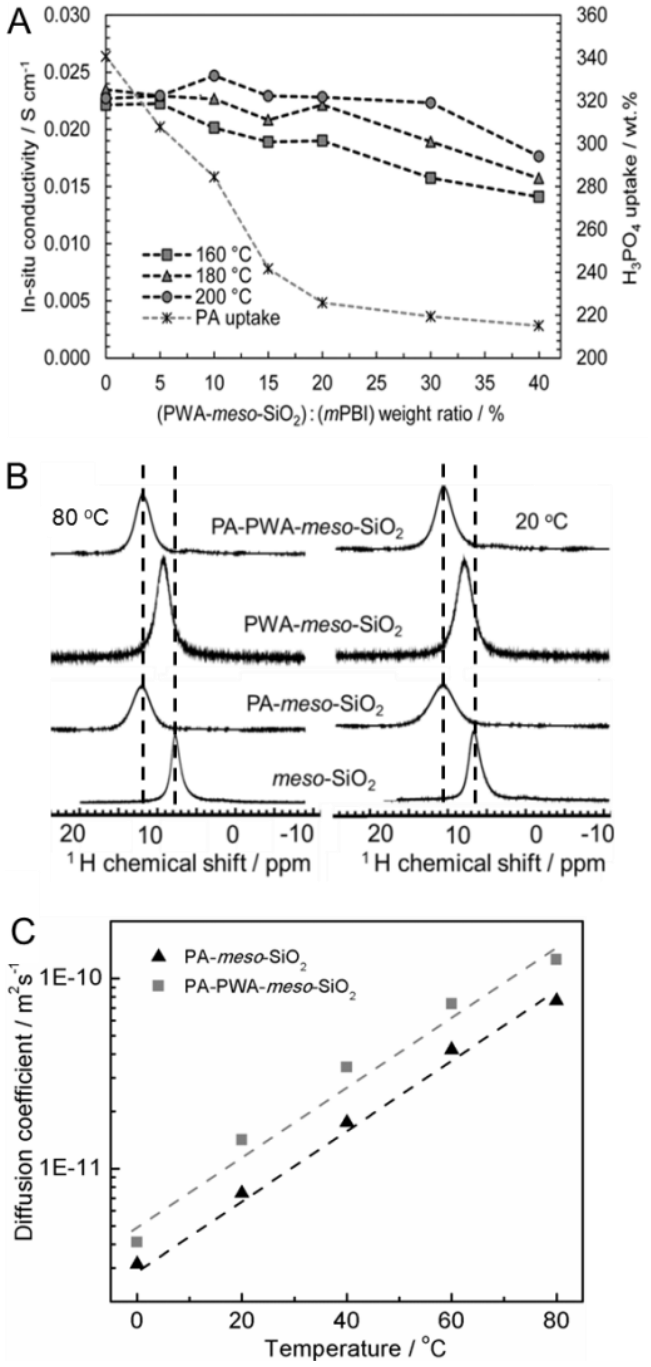

Figure 7.5 *In situ* proton conductivity PA-doped membranes with PWA-*meso*-SiO_2 loadings ranging from 0 – 40 wt.%; (B) ^{1}H chemical shift of *meso*-SiO_2 and (C) Proton diffusion coefficient in PA-*meso*-SiO_2 and PA-PWA-*meso*-SiO_2 at different temperatures.

The *in situ* cross-sectional proton conductivity of the composite membranes at 160, 180 and 200 °C was calculated from the fuel cell polarization data without humidification of the feed gases. The pristine PA/PBI membrane with PA uptake of 341 wt.% shows proton conductivity in the range of 2.2 – 2.4 × 10^{-2} S cm^{-1} at 160 –

200 °C (Figure 7.5A), in consistence with the data in the literature.[36] Although the PA uptake of the composite membranes significantly decreased with increasing the PWA-*meso*-SiO_2 loading, the conductivity was still in a practically useful range. For example, the membrane with a PWA-*meso*-SiO_2 loading of 40 wt.%, had a PA uptake of 215 wt.% and a *in-situ* cross-sectional proton conductivity of 1.4 and 1.7×10^{-2} S cm^{-1} at 160 °C and 200 °C, respectively. Moreover, the decrease in the PA uptake significantly reduces the volume swelling. For the membrane with a PWA-*meso*-SiO_2 loading of 15 wt.%, the volume swelling ratio was 137%, much lower than 203 % of the pristine PA/PBI membrane (Table 7.1). The substantially reduced volume swelling is critical for the long-term stable operation of the PA/PBI membrane based fuel cells.

In order to better understand the origin to the proton conductivity properties of the PWA-*meso*-SiO_2 composite membranes, the proton mobility (Figure 7.5B) and diffusion coefficients (Figure 7.5C) of *meso*-SiO_2 with different proton conductors were examined by pulse field gradient nuclear magnetic resonance spectroscopy. The ^1H chemical shifts were found to move downfield with increasing acidity. Similarly, the ^1H resonance signals shifted downfield as the temperature was increased from 20 to 80 °C due to the weakening of the hydrogen bonding, which in turn indicates that the increased temperature promotes the acid dissociation. In comparison with PWA-*meso*-SiO_2, PA-*meso*-SiO_2 shows higher ^1H chemical shift at both 20 and 80 °C, suggesting that PA is more dissociated than PWA. It is known that the proton line of water or organic solvent in micro-porous media is usually broad due to the restricted molecular motions, as well as the residual homonuclear dipolar couplings and the susceptibility effect from the pore surfaces.[37] Therefore, the proton line width is sensitive to the molecular motions, and faster motions would lead to a narrower line width. The PA-PWA-*meso*-SiO_2 shows a slightly narrower proton line in comparison with PA-*meso*-SiO_2, indicating that the proton in the former system is more mobile than the later one. In addition, the PA-PWA-*meso*-SiO_2 shows systematically higher proton diffusion coefficients at all the different temperatures measured than PA-*meso*-SiO_2 (Figure 7.5C), suggesting a higher proton translational mobility with the addition of PA. Both experimental and theoretical modelling demonstrate that PWA-*meso*-SiO_2 has the capability of high proton conductivity and high water retention due to the stability of PWA within the confined and ordered mesoporous silica structure.[33, 38]

7.3.4 Durability

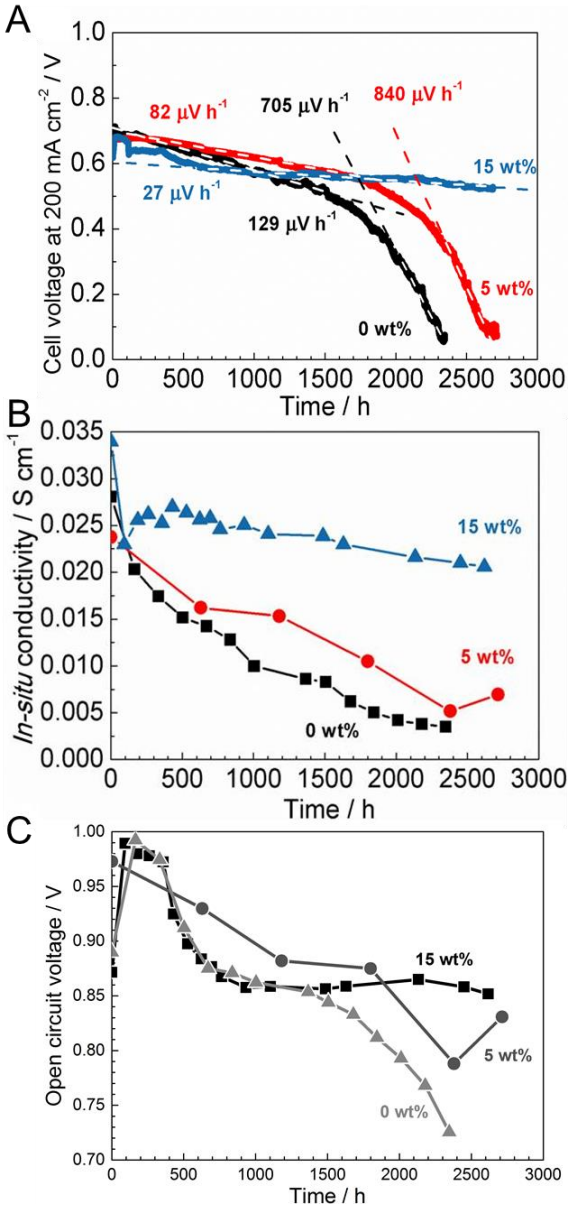

Figure 7.6 (A) Long-term stability tests of corresponding fuel cell operated at 200 mA cm^{-2} and 200 °C; (B) Variation of the *in situ* membrane conductivity and (C) open circuit voltage with time.

Fuel cell durability studies were conducted at 200 °C and 200 mA cm^{-2}, using the isotropic composite membranes with PWA-*meso*-SiO_2 loadings of 0, 5, and 15 wt.%. For the cell based the pure PA/PBI membrane the cell voltage at 200 mA cm^{-2} decreased from 0.71 to 0.53 V during the first 1450 h, corresponding to a degradation rate of 130 µV h^{-1} (Figure 7.6A). It was followed by a rapid voltage drop of about 705 µV h^{-1}. The impedance, as recorded on the pristine PA/PBI membrane cell operated in parallel, was measured every 8 hrs, showing a significant increase of

the cell internal resistance of about 350 – 400 % after 320 h and a much smaller (about 40 – 50 %) increase of the electrode polarization resistance, likely a consequence of reduced proton conductivity due to the dehydration and out-leaching of the acid of pristine PA/PBI membrane cells at this high operational temperature (200 ^{o}C).[17] By adding 5 % PWA-*meso*-SiO_2 to the membrane, the degradation was significantly reduced to 82 μV h^{-1} during the first 1660 h. Thereafter the cell voltage decay rate increased dramatically to 840 μV h^{-1}.

The membrane degradation via the dehydration and leaching of the acid[17] can be substantially suppressed by increasing the loading of PWA-*meso*-SiO_2. By increasing the amount of PWA-*meso*-SiO_2 in the membrane to 15 wt.%, the durability was significantly improved as further supported by the stable *in-situ* conductivity (Figure 7.6B). Except for the initial reduction of performance, the cell voltage decay during 2700 h was found to be as low as 27 μV h^{-1}, which is comparable and significantly better than the degradation rate of 25 μV h^{-1} at 160 ^{o}C,[39] 44 μV h^{-1} at 170 ^{o}C[6] and 60 μV h^{-1} at 190 ^{o}C,[40] for cells based on *p*-PBI or commercial PA/PBI MEA, P-1000. It should also be mentioned that the durability data for the cells in the present work were acquired at significantly higher gas-stoichiometry for both hydrogen and air, which is an additional stress-factor.

The performance was evaluated from their steady state characteristics and from polarization curves periodically during the test. From the representative polarization curves (Figure 7.7A), it can be seen that the characteristics of the membrane-electrode assemblies are initially quite similar for the cells based on the composites with PWA-*meso*-SiO_2 loadings of 0 and 5 wt.%. The initial performance was slightly lower for the cell based on the composite with a PWA-*meso*-SiO_2 loading of 15 wt.%, apparently due to interfacial contact limitations with the electrodes due to the stiffness of the membrane. However, after 1750 h durability test, the cell performance of the pristine PA-doped PBI composite membrane was sharply dropped, which is much lower than that of PBI membranes with PWA-*meso*-SiO_2 tested at the same conditions. Moreover, after 2400 h durability test, only the composite membrane of PBI with 15 wt.% PWA-*meso*-SiO_2 showed comparable cell performance than the pristine PA-doped PBI membrane at the initial stage. Overall, the results indicated that PBI composite membrane with PWA-*meso*-SiO_2 shows higher stability than the pristine PBI membrane, and the stability increases with the increment of the loading of the inorganic filler.

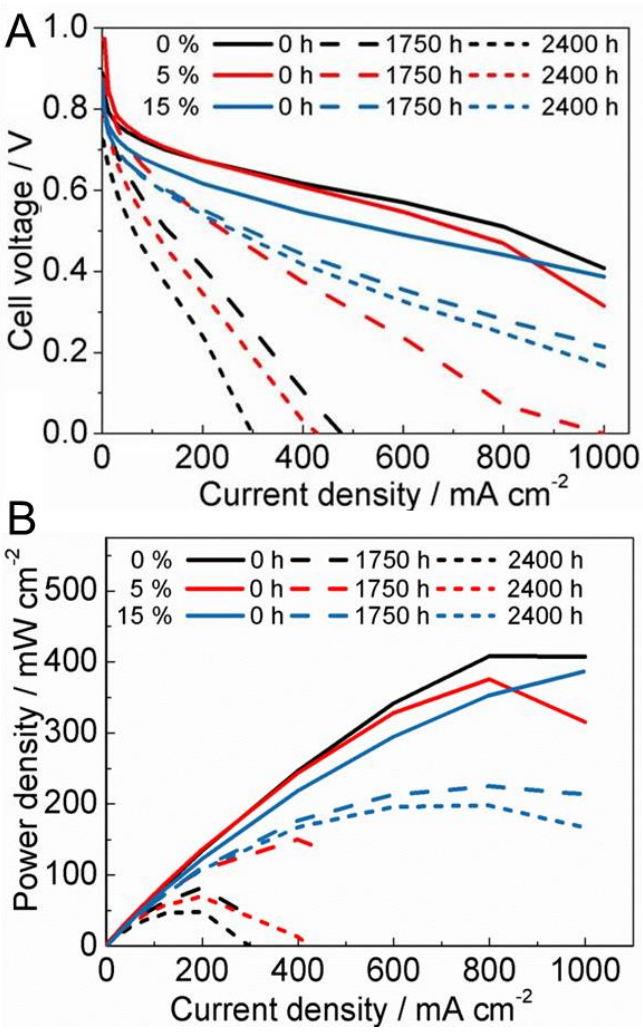

Figure 7.7 (A) Polarization curves and (B) power output curves for fuel cells based on the composites with PWA-*meso*-SiO_2 loadings of 0, 5 and 15 wt.%.

7.4 Discussion

Evidently, the stability of the PA/PBI composite membrane based fuel cell increases substantially with the addition of the PWA-*meso*-silica fillers. This is also supported by a high stability of the open circuit voltage of the PA/PBI composite membrane cells with the addition of 15 wt.% PWA-*meso*-silica (Figure 7.6C). Thus, the reasons for the exceptional durability of the PA/PBI composite membrane modified with PWA-*meso*-silica were discussed as follows.

7.4.1 Effects of the proton exchange membrane

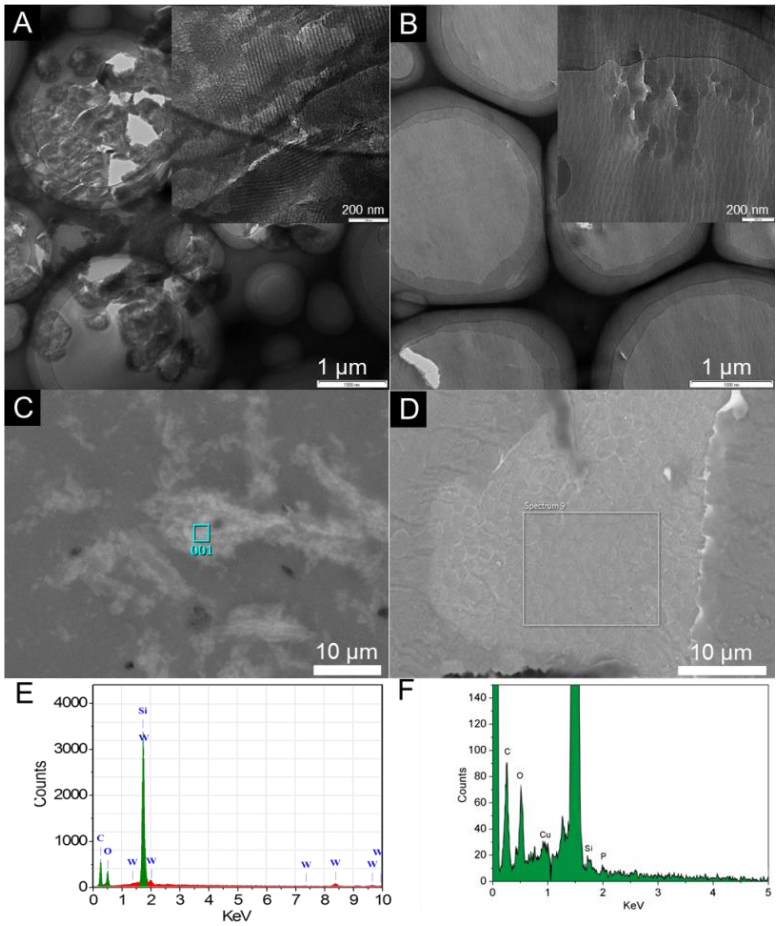

Figure 7.8 TEM images of (A) the PWA-*meso*-silica/PBI composite membrane, and (B) the composite membrane after 2700 h fuel cell test. (C) and (D) are the SEM images of the PWA-*meso*-silica/PBI composite membrane before and after the 2700 h fuel cell test, respectively, while (E) and (F) are the corresponding EDS for the selected area in (C) and (D). The loading for the filler is 15 wt.%.

Figure 7.8A shows the TEM image of the pristine PWA-*meso*-silica/PBI composite membrane with a loading of 15 wt.%. The TEM samples for the composite membranes were cut via microtome technique. The hexagonal mesoporous channels of the PWA-*meso*-silica along [100] and [110] directions were clearly observed in the TEM images of Figure 7.8A. And bright areas in Figure 7.8C and the corresponding Si and W elements mapping in Figure 7.8E confirmed the existence of the PWA and silica materials in PWA-*meso*-silica. Nevertheless, when the membrane was operated in fuel cell for over 2700 h at 200 ^{o}C, the mesoporous structure of the PWA-*meso*-silica particles was deteriorated (Figure 7.8B and D). Moreover, the elements of Si and P were detected in Figure 7.8F, likely due to the reaction between silica and phosphoric acid during the fuel cell operation. It should be noted that the sharp peak in Figure 7.8D corresponding to the element of Al, resulting from a special holder for the TEM grid in SEM characterization.

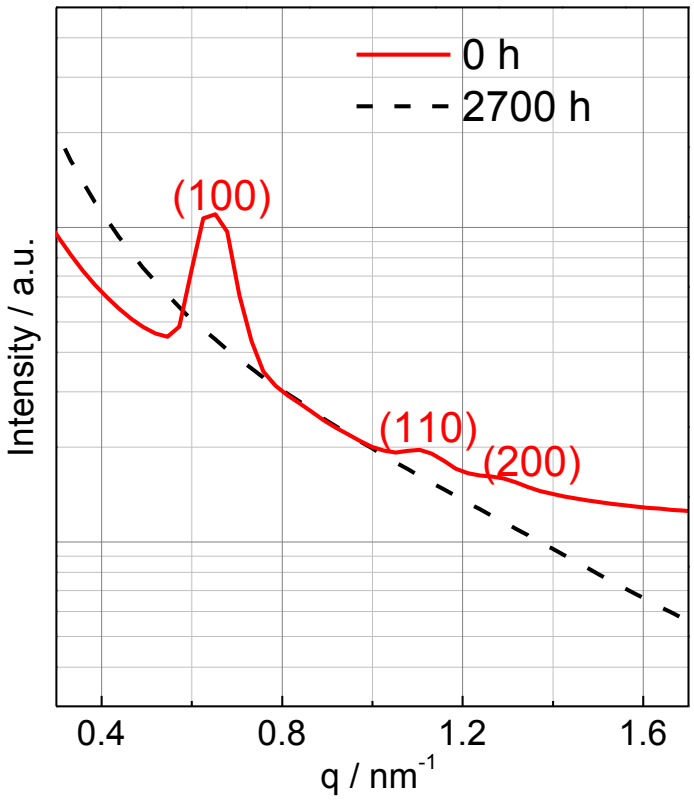

Figure 7.9 SAXS profiles of a PA-doped PWA-*meso*-silica/PBI composite membranes before and after 2700 h fuel cell test. The loading for the inorganic filler is 15 wt.%.

Figure 7.9 compares the SAXS curves of the PWA-*meso*-silica/PBI composite membrane with 15 wt.% of PWA-*meso*-silica .before and after the 2,700 h fuel cell operation. After the fuel cell operation, the unique peaks of *meso*-silica corresponding to planes of (100), (110) and (200) were vanished. The result demonstrates that the mesoporous structure of the inorganic fillers in PBI matrix is destroyed after the fuel cell operation, which is consistent with observation in Figure 7.8.

Figure 7.10 shows the X-ray diffraction patterns of different PA/PBI membrane cells after the durability test at 200 ^{o}C. In the case of the pristine PA/PBI membrane cells, the peaks for P_2O_5 and P_2O_7 emerged, which is an indication of the thermal instability of phosphoric acid at 200^{o}C. Therefore, the considerable degradation of the pristine PA/PBI membrane cells is mainly attributed to the decomposition of PA. However, after the addition of PWA-*meso*-silica, a new peak centred at 23.5^{o} corresponding to the phosphosilicate phase, $Si_5O(PO_4)_6$ was detected. The intensity of the peak of $Si_5O(PO_4)_6$ increased with increasing the PWA-*meso*-silica loading. Meanwhile, the peak intensity associated with P_2O_5 clearly decreased, indicating the

suppression for the formation of P_2O_5. Phosphosilicate has been reported to have a high proton conductivity and stability at medium temperature[41], similar as the effect of Al_2O_3[42] and TiO_2[43] in phosphoric acid based high temperature PEMs on reducing the acid loss and the cell resistance.

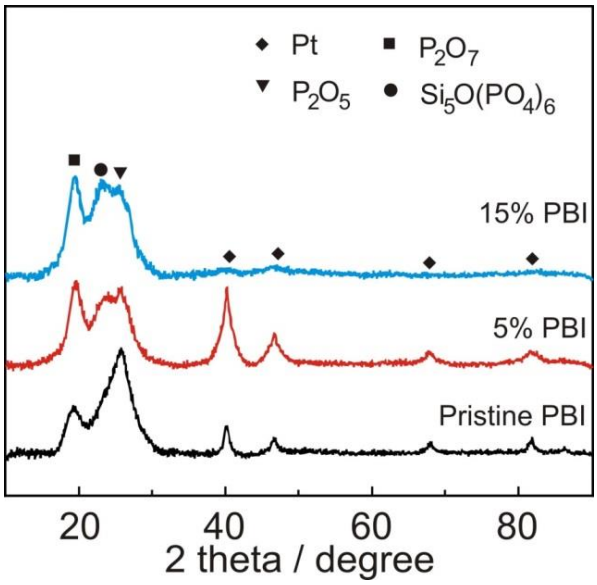

Figure 7.10 XRD profiles of various PA/PBI composite membranes with 0, 5 and 15 wt.% PWA-*meso*-SiO_2 after durability test.

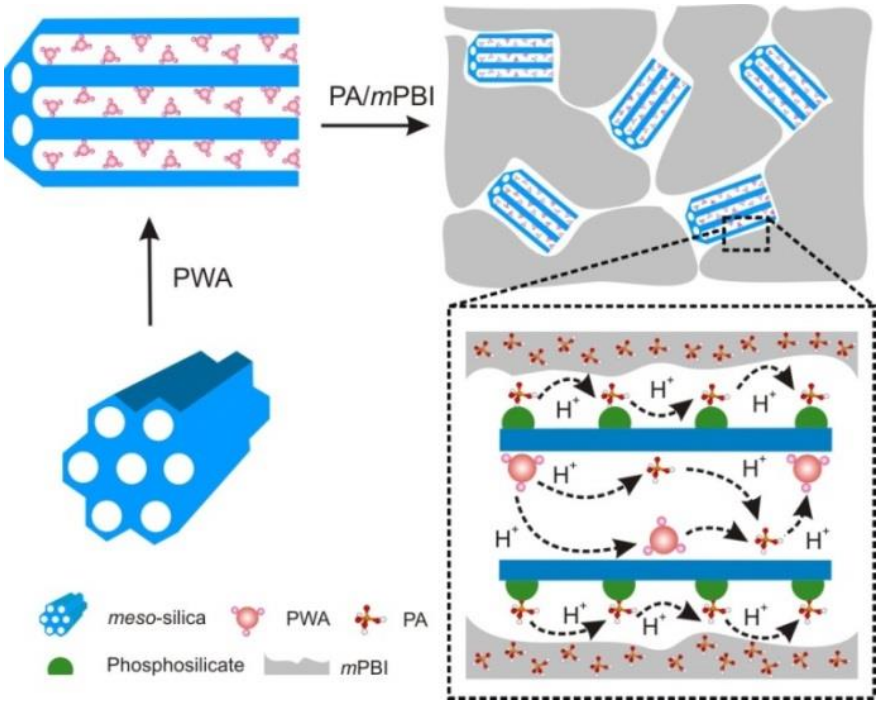

Figure 7.11 Scheme of proton conduction paths through the attached and stabilized PA and PWA anchored inside the mesoporous channels of *meso*-silica at high temperatures.

Though the exact reasons for the substantially enhanced stability of the PWA-*meso*-SiO_2 modified PA/PBI membrane cells are not clear at this stage, there are sufficient evidences that the inclusion of mesoporous silica to the PA/PBI composite membranes reduces the loss of PA during fuel cell operation at 200 ^oC most likely by stabilizing phosphoric acid in the form of phosphosilicate. On the other hand, the facile and high proton diffusion ability of PWA in the mesopores of silica facilitates and maintains the high conductivity of the composite membranes, despite the reduction of the PA uptake (Figure 7.5A).[44] Proton conductivity can occur simultaneously through stabilized PA and PWA within the mesoporous silica, as shown schematically in Figure 7.11. Overall, the inclusion of the PWA-*meso*-SiO_2 fillers inhibits the leaching of the acid by forming the immobilized phosphosilicate, resulting in the formation of a composite membrane with a high proton conductivity and excellent stability at 200 ^oC.

7.4.2 Effects of the catalysts

Besides the proton exchange membrane, the catalyst in the electrodes is another critical criterion for the durability of the fuel cells. For instance, Zhang et al. conducted the continuous aging life test on the PA/PBI composite membrane fuel cells at 150 ^oC for 500 h, and found that obvious degradation occurred at the Pt catalyst.[45] Figure 7.12A shows the XRD profiles of the catalysts in the fuel cell after the durability test. The broad peak at around 25.1^o is associated with the amorphous active carbon, while the sharp peaks at 39.8^o, 46.3^o, 67.5^o, 81.4^o and 85.7^o correspond to Pt(111), Pt (200), Pt (220), Pt (311) and Pt (222), respectively. Based on Scherrer equation, the diameter of the Pt catalyst was calculated, as shown in Figure 7.12B. The diameter of the Pt NPs in the cathode was higher than that of the catalyst in anode for all the fuel cells irrespective of the composite membranes employed. Moreover, the particles sizes in both the anode and the cathode decreased with the increase of the loading of the PWA-*meso*-silica particles.

The change of the Pt particle size after the durability test was directly observed from the TEM images, as shown in Figure 7.13. The average particle size determined based on the TEM images was close to the value calculated according to the Scherrer equation. The particle size of the Pt NPs in the anode decreased from 5.5 nm (Figure 7.13A) to 4.0 nm (Figure 7.13E) in the PBI membrane-based fuel cells as the loading

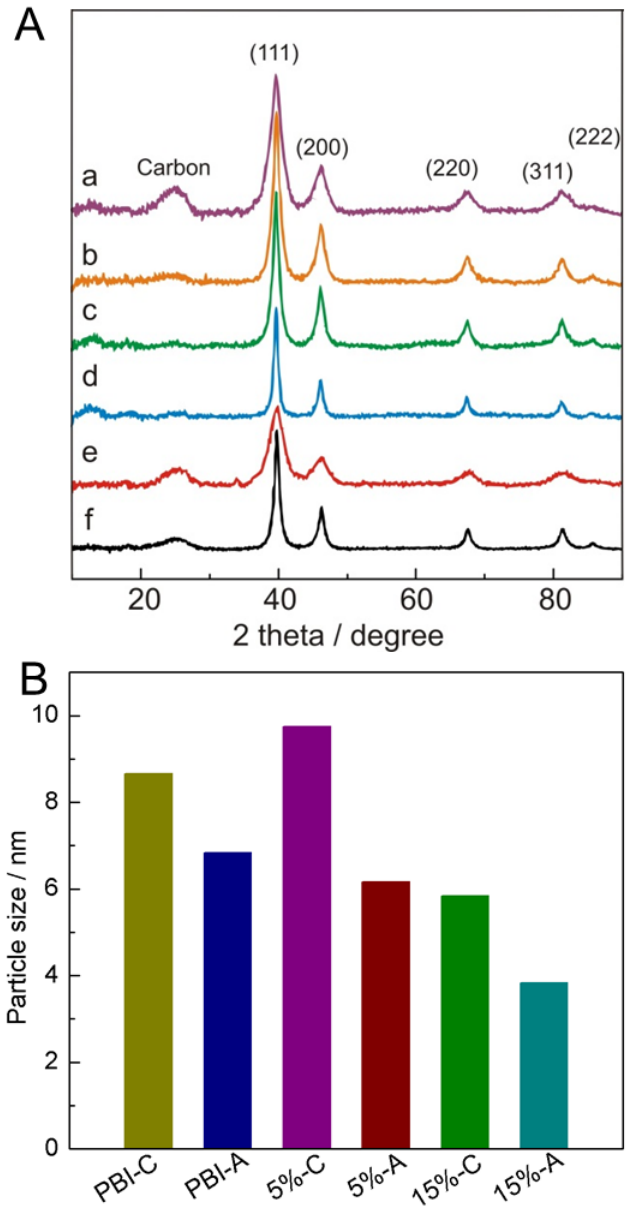

Figure 7.12 (A) XRD patterns of the Pt catalyst after the durability operation with a current load of 200 mA cm^{-2} at 200 ^{o}C. a, 15 % PBI, anode; b, 15% PBI, cathode; c, 5 % PBI, anode; d, 5% PBI, cathode; e, PBI, anode; f, PBI, cathode. (B) The particle size of Pt catalysts derived from the XRD pattern by the Scherrer equation.

of PWA-*meso*-silica increased from 0 to 15 wt.%. Moreover, the average particle size of the Pt NPs in the cathode remained nearly unchanged as the loading of PWA-*meso*-silica increased from 0 to 5 wt.%, being in the range of 7.5 – 8.5 nm (Figure 7.13B and D). However, when the loading increased to 15 %, the size of the Pt NPs in the cathode was substantially reduced to 4.5 nm (Figure 7.13F). The large particle size of the Pt NPs at the low PWA-*meso*-silica loading is likely due to the agglomeration of Pt catalyst, especially for the cathode catalyst. Qi et al. operated the PA/PBI based fuel cell at OCV for 50h, and found that the Pt crystallite size in the c-

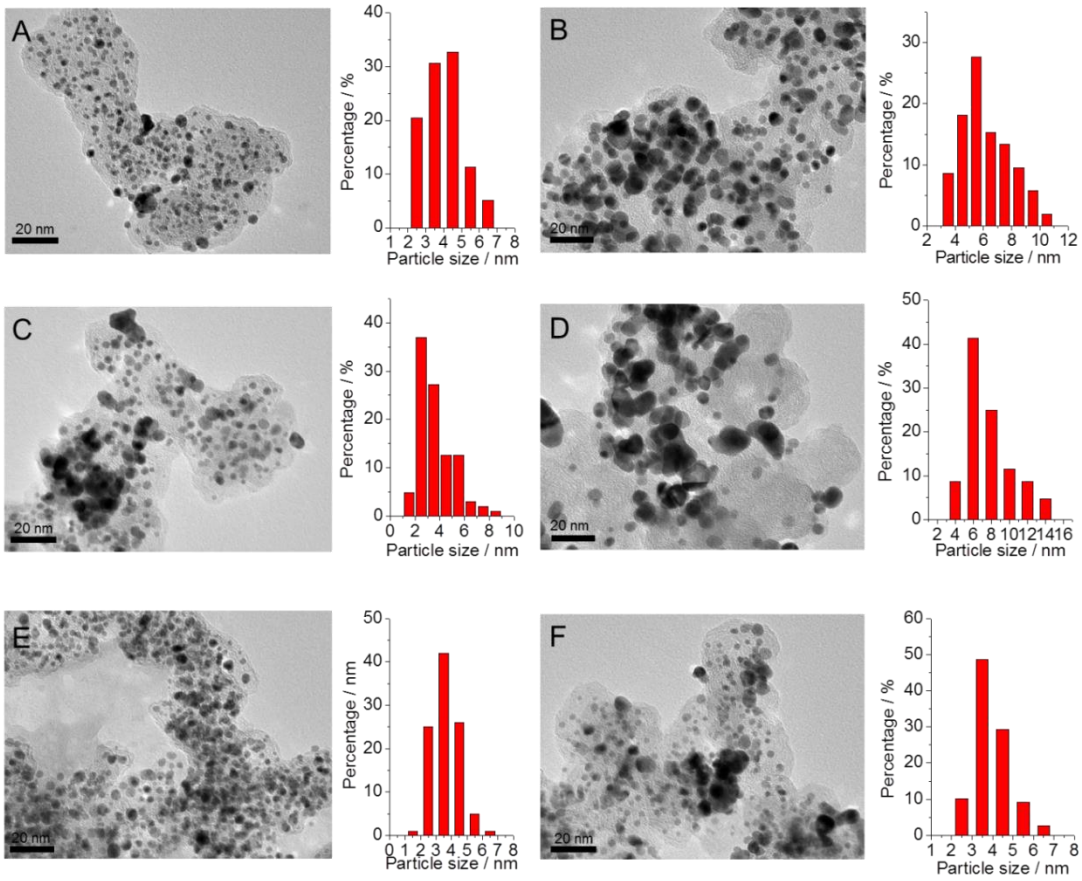

Figure 7.13 TEM images of Pt catalysts after over 2700 h operation with a current load of 200 mA cm^{-2} at 200 ^{o}C. A, the pristine PBI, anode; B, the pristine PBI, cathode. C, 5 wt.% PBI, anode; D, 5 wt.% PBI, cathode; E, 15 wt.% PBI, anode; F, 15wt.% PBI, cathode.

athode increased by as much as 5.3 times of its original value, while the anode Pt crystallite size only slightly changed. On one hand, high temperatures and current loadings elevate the rate of Pt dissolution and re-deposition [46]. On the other hand, the Pt/C catalyst is transferred from one crystallite to another, resulting in a decrease of platinum crystallite density and the growth of platinum particles [47].

7.5 Conclusions

In this work, we developed a novel type of composite membranes based on the incorporation of PWA functionalized mesoporous silica into a matrix of phosphoric acid doped polybenzimidazole. The composite membranes with the 15 wt.% of the PWA-*meso*-silica showed high proton conductivity and exceptional performance durability at a significantly reduced phosphoric acid uptake, which resulted in low volume swelling and sufficient mechanical robustness. As a result of the stabilization of phosphoric acid by the filler, a decay rate of the fuel cell voltage as low as 27 μV

h^{-1} was recorded during the operation at 200 °C and 200 mA cm^{-2} for 2,700 h. It is suggested that it was the *in situ* formed phosphosilicate and the stable Pt NPs on the cathode that contributed to the exceptional durability of the PA/PBI composite membrane based elevated temperature fuel cell.

References

[1] Q. Li, R.H. He, J.O. Jensen, N.J. Bjerrum, Approaches and recent development of polymer electrolyte membranes for fuel cells operating above 100 degrees C, Chemistry of Materials 15 (26) (2003) 4896-4915.

[2] E. Quartarone, P. Mustarelli, Polymer fuel cells based on polybenzimidazole/H3PO4, Energy & Environmental Science 5 (4) (2012) 6436-6444.

[3] Q. Li, J.O. Jensen, R.F. Savinell, N.J. Bjerrum, High temperature proton exchange membranes based on polybenzimidazoles for fuel cells, Prog. Polym. Sci. 34 (5) (2009) 449-477.

[4] T. Steenberg, H.A. Hjuler, C. Terkelsen, M.T.R. Sanchez, L.N. Cleemann, F.C. Krebs, Roll-to-roll coated PBI membranes for high temperature PEM fuel cells, Energy & Environmental Science 5 (3) (2012) 6076-6080.

[5] J.K. Kallitsis, M. Geormezi, S.G. Neophytides, Polymer electrolyte membranes for high-temperature fuel cells based on aromatic polyethers bearing pyridine units, Polymer International 58 (11) (2009) 1226-1233.

[6] S. Yu, L. Xiao, B.C. Benicewicz, Durability Studies of PBI-based High Temperature PEMFCs, Fuel Cells 8 (3-4) (2008) 165-174.

[7] J. Mader, L. Xiao, T.J. Schmidt, B.C. Benicewicz, Fuel Cells Ii, 2008, pp. 63-124.

[8] T.J. Schmidt, J. Baurmeister, Properties of high-temperature PEFC Celtec (R)-P 1000 MEAs in start/stop operation mode, Journal of Power Sources 176 (2) (2008) 428-434.

[9] Y. Oono, T. Fukuda, A. Sounai, M. Hori, Influence of operating temperature on cell performance and endurance of high temperature proton exchange membrane fuel cells, Journal of Power Sources 195 (4) (2010) 1007-1014.

[10] Y. Oono, A. Sounai, M. Hori, Long-term cell degradation mechanism in high-temperature proton exchange membrane fuel cells, Journal of Power Sources 210 (0) (2012) 366-373.

[11] Y. Oono, A. Sounai, M. Hori, Prolongation of lifetime of high temperature proton exchange membrane fuel cells, Journal of Power Sources 241 (0) (2013) 87-93.

[12] Z. Qi, S. Buelte, Effect of open circuit voltage on performance and degradation of high temperature PBI-H3PO4 fuel cells, Journal of Power Sources 161 (2) (2006) 1126-1132.

[13] T. Engl, L. Gubler, T.J. Schmidt, Think Different! Carbon Corrosion Mitigation Strategy in High Temperature PEFC: A Rapid Aging Study, Journal of the Electrochemical Society 162 (3) (2015) F291-F297.

[14] T. Arlt, W. Maier, C. Tötzke, C. Wannek, H. Markötter, F. Wieder, J. Banhart, W. Lehnert, I. Manke, Synchrotron X-ray radioscopic in situ study of high-temperature polymer electrolyte fuel cells - Effect of operation conditions on structure of membrane, Journal of Power Sources 246 (0) (2014) 290-298.

[15] S.H. Eberhardt, M. Toulec, F. Marone, M. Stampanoni, F.N. Büchi, T.J. Schmidt, Dynamic Operation of HT-PEFC: In-Operando Imaging of Phosphoric Acid Profiles and (Re)distribution, Journal of the Electrochemical Society 162 (3) (2015) F310-F316.

[16] D. Aili, L.N. Cleemann, Q. Li, J.O. Jensen, E. Christensen, N.J. Bjerrum, Thermal curing of PBI membranes for high temperature PEM fuel cells, Journal of Materials Chemistry 22 (12) (2012) 5444-5453.

[17] C. Wannek, B. Kohnen, H.F. Oetien, H. Lippert, J. Mergel, Durability of ABPBI-based MEAs for high temperature PEMFCs at different operating conditions, Fuel Cells 8 (2) (2008) 87-95.

[18] M.K. Daletou, M. Geormezi, E. Vogli, G.A. Voyiatzis, S.G. Neophytides, The interaction of H_3PO_4 and steam with PBI and TPS polymeric membranes. A TGA and Raman

study, Journal of Materials Chemistry A 2 (4) (2014) 1117-1127.
[19] W. Maier, T. Arlt, C. Wannek, I. Manke, H. Riesemeier, P. Kruger, J. Scholta, W. Lehnert, J. Banhart, D. Stolten, In-situ synchrotron X-ray radiography on high temperature polymer electrolyte fuel cells, Electrochemistry Communications 12 (10) (2010) 1436-1438.
[20] S.H. Eberhardt, T. Lochner, F.N. Büchi, T.J. Schmidt, Correlating Electrolyte Inventory and Lifetime of HT-PEFC by Accelerated Stress Testing, Journal of The Electrochemical Society 162 (12) (2015) F1367-F1372.
[21] Q. Li, R.H. He, J.A. Gao, J.O. Jensen, N.J. Bjerrum, The CO poisoning effect in PEMFCs operational at temperatures up to 200 degrees C, Journal of the Electrochemical Society 150 (12) (2003) A1599-A1605.
[22] Q. Li, R.H. He, J.O. Jensen, N.J. Bjerrum, PBI-Based Polymer Membranes for High Temperature Fuel Cells - Preparation, Characterization and Fuel Cell Demonstarion, Fuel Cells 4 (3) (2004) 147-159.
[23] C. Pan, R. He, Q. Li, J.O. Jensen, N.J. Bjerrum, H.A. Hjulmand, A.B. Jensen, Integration of high temperature PEM fuel cells with a methanol reformer, Journal of Power Sources 145 (2) (2005) 392-398.
[24] G. Qian, B.C. Benicewicz, in: H.A. Gasteiger, A. Weber, S.R. Narayanan, D. Jones, P. Strasser, K. SwiderLyons, F.N. Buchi, P. Shirvanian, H. Nakagawa, H. Uchida, S. Mukerjee, T.J. Schmidt, V. Ramani, T. Fuller, M. Edmundson, C. Lamy, R. Mantz (Eds.), Polymer Electrolyte Fuel Cells 11, Electrochemical Soc Inc, Pennington, 2011, pp. 1441-1448.
[25] J. Lobato, P. CaÃ±izares, M.A. Rodrigo, D. Ãšbeda, F.J. Pinar, Enhancement of the fuel cell performance of a high temperature proton exchange membrane fuel cell running with titanium composite polybenzimidazole-based membranes, Journal of Power Sources 196 (20) (2011) 8265-8271.
[26] F.J. Pinar, P. Canizares, M.A. Rodrigo, D. Ubeda, J. Lobato, Titanium composite PBI-based membranes for high temperature polymer electrolyte membrane fuel cells. Effect on titanium dioxide amount, RSC Advances 2 (4) (2012) 1547-1556.
[27] F.J. Pinar, P. Cañizares, M.A. Rodrigo, D. Úbeda, J. Lobato, Long-term testing of a high-temperature proton exchange membrane fuel cell short stack operated with improved polybenzimidazole-based composite membranes, Journal of Power Sources 274 (0) (2015) 177-185.
[28] Y. Zhao, H. Yang, H. Wu, Z. Jiang, Enhanced proton conductivity of hybrid membranes by incorporating phosphorylated hollow mesoporous silica submicrospheres, Journal of Membrane Science 469 (2014) 418-427.
[29] Y. Zhao, H. Yang, H. Wu, Z. Jiang, Enhanced proton conductivity of the hybrid membranes by regulating the proton conducting groups anchored on the mesoporous silica, Journal of Power Sources 270 (2014) 292-303.
[30] A.K. Mishra, N.H. Kim, J.H. Lee, Effects of ionic liquid-functionalized mesoporous silica on the proton conductivity of acid-doped poly(2,5-benzimidazole) composite membranes for high-temperature fuel cells, Journal of Membrane Science 449 (2014) 136-145.
[31] H. Tang, M. Pan, S.P. Jiang, Self assembled 12-tungstophosphoric acid-silica mesoporous nanocomposites as proton exchange membranes for direct alcohol fuel cells, Dalton Transactions 40 (19) (2011) 5220-5227.
[32] H. Tang, M. Pan, S. Lu, J. Lu, S.P. Jiang, One-step synthesized HPW/meso-silica inorganic proton exchange membranes for fuel cells, Chemical Communications 46 (24) (2010) 4351-4353.
[33] Y.H. Zhou, J. Yang, H.B. Su, J. Zeng, S.P. Jiang, W.A. Goddard, Insight into Proton Transfer in Phosphotungstic Acid Functionalized Mesoporous Silica-Based Proton Exchange Membrane Fuel Cells, Journal of the American Chemical Society 136 (13) (2014) 4954-4964.
[34] S.F. Lu, D.L. Wang, S.P. Jiang, Y. Xiang, J.L. Lu, J. Zeng, HPW/MCM-41 Phosphotungstic Acid/Mesoporous Silica Composites as Novel Proton-Exchange Membranes for Elevated-Temperature Fuel Cells, Advanced Materials 22 (9) (2010) 971-976.
[35] Suryani, Y.-N. Chang, J.-Y. Lai, Y.-L. Liu, Polybenzimidazole (PBI)-functionalized silica nanoparticles modified PBI nanocomposite membranes for proton exchange membranes fuel cells, Journal of Membrane Science 403–404 (2012) 1-7.
[36] D. Aili, T. Allward, S.M. Alfaro, C. Hartmann-Thompson, T. Steenberg, H.A. Hjuler, Q. Li, J.O. Jensen, E.J. Stark, Polybenzimidazole and sulfonated polyhedral oligosilsesquioxane

composite membranes for high temperature polymer electrolyte membrane fuel cells, Electrochimica Acta 140 (2014) 182-190.
[37] H. Zhu, H.P. Huinink, S.J.F. Erich, V. Baukh, O.C.G. Adan, K. Kopinga, High spatial resolution NMR imaging of polymer layers on metallic substrates, Journal of Magnetic Resonance 214 (2012) 227-236.
[38] J. Zeng, S.P. Jiang, Characterization of High-Temperature Proton-Exchange Membranes Based on Phosphotungstic Acid Functionalized Mesoporous Silica Nanoconnposites for Fuel Cells, Journal of Physical Chemistry C 115 (23) (2011) 11854-11863.
[39] A.D. Modestov, M.R. Tarasevich, V.Y. Filimonov, N.M. Zagudaeva, Degradation of high temperature MEA with PBI-H3PO4 membrane in a life test, Electrochimica Acta 54 (27) (2009) 7121-7127.
[40] W. Maier, T. Arlt, C. Wannek, I. Manke, H. Riesemeier, P. Krüger, J. Scholta, W. Lehnert, J. Banhart, D. Stolten, In-situ synchrotron X-ray radiography on high temperature polymer electrolyte fuel cells, Electrochemistry Communications 12 (10) (2010) 1436-1438.
[41] A. Matsuda, T. Kanzaki, K. Tadanaga, M. Tatsumisago, T. Minami, Medium temperature range characterization as a proton conductor for phosphosilicate dry gels containing large amounts of phosphorus, Electrochimica Acta 47 (6) (2001) 939-944.
[42] H.-S. Oh, Y. Cho, W.H. Lee, H. Kim, Modification of electrodes using Al2O3 to reduce phosphoric acid loss and increase the performance of high-temperature proton exchange membrane fuel cells, Journal of Materials Chemistry A 1 (7) (2013) 2578-2581.
[43] F. Javier Pinar, P. Canizares, M.A. Rodrigo, D. Ubeda, J. Lobato, Long-term testing of a high-temperature proton exchange membrane fuel cell short stack operated with improved polybenzimidazole-based composite membranes, Journal of Power Sources 274 (2015) 177-185.
[44] J. Zeng, B. He, K. Lamb, R. De Marco, P.K. Shen, S.P. Jiang, Anhydrous Phosphoric Acid Functionalized Sintered Mesoporous Silica Nanocomposite Proton Exchange Membranes for Fuel Cells, Acs Applied Materials & Interfaces 5 (21) (2013) 11240-11248.
[45] J. Hu, H. Zhang, Y. Zhai, G. Liu, B. Yi, 500h continuous aging life test on PBI/H3PO4 high-temperature PEMFC, International Journal of Hydrogen Energy 31 (13) (2006) 1855-1862.
[46] G. Liu, H. Zhang, J. Hu, Y. Zhai, D. Xu, Z.-g. Shao, Studies of performance degradation of a high temperature PEMFC based on H3PO4-doped PBI, Journal of Power Sources 162 (1) (2006) 547-552.
[47] J.A. Bett, K. Kinoshita, P. Stonehart, Crystallite growth of platinum dispersed on graphitized carbon black, Journal of Catalysis 35 (2) (1974) 307-316.

Chapter 8 Conclusions and Recommendations for future work

8.1 Conclusions and achievements

The aim of this thesis is to develop novel proton exchange membranes with high proton conductivity at low relative humidity and elevated temperatures. It has been successfully achieved by introducing the mesoporous structures into Nafion and new types of mesoporous inorganic-organic hybrid composite membranes. The main achievements from the present study are listed below.

1) The mesoporous structures were introduced into the Nafion membrane via a soft template method with the assistance of the silica colloidal mediator. Silica colloids were critical for the formation of the highly ordered mesoporous structured phase in the precursor solution. Four mesoporous Nafion membranes with highly ordered mesoporous structures were synthesized including 2D hexagonal, 3D face-centred, 3D cubic-bicontinuous and 3D body-centred. The mesoporous Nafion membrane showed a high water retention capability that was indicated by S-shaped dependence on RH for power output of the mesoporous Nafion membrane cells. The best result was observed on the Nafion membranes with the 2 D hexagonal structure by the high proton conductivity at low RH and the outstanding fuel cell stability under anhydrous condition.

2) Inorganic-organic nanostructured hybrid membranes of polyethersulfone–polyvinylpyrrolidone were prepared with mesoporous silica materials. The inorganic-organic composite membranes after PA doping showed superior proton conductivity than that of the pristine PA-PES-PVP composite membrane. This is most likely due to the facilitated proton transportation in the ordered mesoporous channels via the hydrogen bond between the $–NH_2$ groups and H_3PO_4. The highest peak power density reached up to 480 mW cm^{-2} for the NH_2-HMS based composite membrane for dry gas at 180 ^oC, which is 92.7 % higher than that of PA-doped PES-PVP composite membrane at the identical condition.

3) A novel method was developed to synthesize amino-functionalized hollow mesoporous silica. Different from conventional approaches, the amino functionalized hollow mesoporous silica was transformed from amino-factionalized mesoporous silica. Because of the enrichment of OH^- induced by CTAB and the gradient of OH^- concentration in the mesoporous spheres, the interior parts of the mesoporous silica

spheres were etched by OH^- while the shell of the sphere was intact, and consequently resulting in the amino functionalized hollow mesoporous silica. The novel method not only simplifies the synthesis procedures of NH_2-HMS fabrication, but also reveals a novel mechanism for functionalized mesoporous silica.

4) Novel proton exchange membranes based on phosphotungstic acid impregnated amino-functionalized hollow mesoporous silica were fabricated for elevated temperature fuel cells. The interaction between the proton conductors and the polymer matrix was also investigated in details. PWA tended to donate the protons to the N atom in the heterocyclic carbon ring of PVP, while PA was favour to attack the ketonic O atom in the PVP molecules. Incorporation of PWA-NH_2-HMS improved the proton conductivity and single cell performance of the polymer membranes with an optimum loading of 10 wt.%.

5) Phosphotungstic acid functionalized mesoporous silica particles were successfully incorporated into PA/PBI membranes and an exceptional performance durability up to 2700 h was achieved (27 $\mu V\ h^{-1}$) at 200 ^oC. The exception durability of the PA-doped PBI composite membrane with PWA-*meso*-silica is due to the *in situ* formation of phosphosilicate and the diminished aggregation of Pt nanoparticles, especially on the cathode. The development of PWA-*meso*-silica based PA/PBI PEMs operated at 200 ^oC represents a significant milestone in the development of elevated temperature PEMFCs.

6) The role of the inner tubes of CNTs was revealed with significant promotion effects on the activity of supported Pd nanoparticles for alcohol oxidation reactions of direct alcohol fuel cells. The Pd NPs supported on the CNTs with the wall number of 3 – 7 showed significant higher activity and stability for the oxidation reaction of methanol, ethanol, and ethyl glycol than that of Pd NPs on single wall and multi wall carbon nanotubes. A facile charge transfer mechanism via electron tunnelling between the outer wall and inner tubes of CNTs under an electrochemical driving force was proposed for the significant promotion effects of CNTs for the alcohol oxidation reactions in alkaline solutions.

8.2 Recommendations for future work

Mesoporous materials including mesoporous Nafion, amino functionalized hollow mesoporous silica and PWA functionalized *meso*-silica etc. significantly improve the proton conductivity of polymer matrix at low relative humidity and even at

anhydrous conditions. However, the research still needs further investigations.

1) Amino-functionalized hollow mesoporous silica was fabricated by a novel synthesis method from the transformation of amino-functionalized mesoporous silica spheres. And the synthesis conditions including concentration of surfactant and etching agents etc. were optimized. However, the mechanism of the transformation from NH_2-*meso*-silica to NH_2-HMS is still unclear. The distribution of $–NH_2$ groups in NH_2-HMS still needs confirmation evidences. For instance, $–NH_2$ groups can be stained and then characterized by STEM to find out the distribution of functional groups.

2) Expand the applications of NH_2-HMS. Besides $–NH_2$ group, the second functional group can be introduced into the surface of NH_2-HMS, such as thiol group and carboxyl group etc. to form the acid-base bifunctionalized NH_2-HMS. It can be employed as agents for the waste water treatment including heavy metal ions adsorption. Besides, it can be introduced to the PA/PBI composite membranes.

3) PES-PVP composite membranes with PWA-NH_2-HMS particles indicated outstanding proton conductivity and stability at temperature up to 200 ^oC. However, the reasons for the high stability of PES-PVP membrane with 15 wt.% of the filler is unclear and further investigations are required, such as TEM and XRD characterizations for the membranes after the durability test.

4) Development of PES-PVP composite membranes with high stability at 200 ^oC. The addition of mesoporous silica materials increased the proton conductivity of the PES-PVP composite membranes. However, it contributes small for the thermal stability of the PES-PVP matrix. Moreover, the glass transition temperature (T_g) of the PES-PVP composite membrane with 70 wt.% PVP is only 192 ^oC, and it decreases with increasing PVP content. Thus, in order to improve the stability of PES-PVP composite membrane at high temperatures, the PVP content should be reduced. After the addition of the mesoporous silica materials to PES-PVP composite membranes with low content of PVP, PES-PVP hybrid membranes with great stability will be obtained in fuel cells operated at high temperatures.

5) Fundamental understanding is required for the mechanism of phosphosilicate phase formation in the *meso*-silica-PA/PBI composite membranes and the effects of *meso*-silica loading and distribution on proton conductivity.

Appendix

Copyrights for Figure 2.2

7/27/2016 Rightslink® by Copyright Clearance Center

Copyright Clearance Center RightsLink® Home Account Info Help Live Chat

ACS Publications Most Trusted. Most Cited. Most Read.

Title: Structure−Properties Relationship in Proton Conductive Sulfonated Polystyrene −Polymethyl Methacrylate Block Copolymers (sPS−PMMA)

Author: Laurent Rubatat, Chaoxu Li, Hervé Dietsch, et al

Publication: Macromolecules

Publisher: American Chemical Society

Date: Nov 1, 2008

Copyright © 2008, American Chemical Society

Logged in as: JIN ZHANG
Account #: 3000977716
LOGOUT

PERMISSION/LICENSE IS GRANTED FOR YOUR ORDER AT NO CHARGE

This type of permission/license, instead of the standard Terms & Conditions, is sent to you because no fee is being charged for your order. Please note the following:

- Permission is granted for your request in both print and electronic formats, and translations.
- If figures and/or tables were requested, they may be adapted or used in part.
- Please print this page for your records and send a copy of it to your publisher/graduate school.
- Appropriate credit for the requested material should be given as follows: "Reprinted (adapted) with permission from (COMPLETE REFERENCE CITATION). Copyright (YEAR) American Chemical Society." Insert appropriate information in place of the capitalized words.
- One-time permission is granted only for the use specified in your request. No additional uses are granted (such as derivative works or other editions). For any other uses, please submit a new request.

If credit is given to another source for the material you requested, permission must be obtained from that source.

BACK CLOSE WINDOW

Copyright © 2016 Copyright Clearance Center, Inc. All Rights Reserved. Privacy statement. Terms and Conditions.
Comments? We would like to hear from you. E-mail us at customercare@copyright.com

https://s100.copyright.com/AppDispatchServlet 1/1

Copyrights for Figure 2.3

ROYAL SOCIETY OF CHEMISTRY LICENSE TERMS AND CONDITIONS

Jul 27, 2016

This Agreement between JIN ZHANG ("You") and Royal Society of Chemistry ("Royal Society of Chemistry") consists of your license details and the terms and conditions provided by Royal Society of Chemistry and Copyright Clearance Center.

License Number	3916970245621
License date	Jul 27, 2016
Licensed Content Publisher	Royal Society of Chemistry
Licensed Content Publication	Journal of Materials Chemistry A
Licensed Content Title	Fabrication of hybrid membranes by incorporating acid–base pair functionalized hollow mesoporous silica for enhanced proton conductivity
Licensed Content Author	Yongheng Yin,Wanyu Deng,Hongyan Wang,Anping Li,Chongbin Wang,Zhongyi Jiang,Hong Wu
Licensed Content Date	Jun 30, 2015
Licensed Content Volume Number	3
Licensed Content Issue Number	31
Type of Use	Thesis/Dissertation
Requestor type	academic/educational
Portion	figures/tables/images
Number of figures/tables/images	1
Format	print and electronic
Distribution quantity	2
Will you be translating?	no
Order reference number	
Title of the thesis/dissertation	Development of novel mesoporous proton exchange membranes for fuel cells
Expected completion date	Aug 2016
Estimated size	200
Requestor Location	JIN ZHANG 1 Turner Ave Technology Park Curtin University, Bentley Perth, WA 6102 Australia Attn: JIN ZHANG
Billing Type	Invoice
Billing Address	JIN ZHANG 1 Turner Ave Technology Park Curtin University, Bentley Perth, Australia 6102 Attn: JIN ZHANG
Total	0.00 AUD
Terms and Conditions	

Copyrights for Figure 2.3

ROYAL SOCIETY OF CHEMISTRY LICENSE TERMS AND CONDITIONS

Jul 27, 2016

This Agreement between JIN ZHANG ("You") and Royal Society of Chemistry ("Royal Society of Chemistry") consists of your license details and the terms and conditions provided by Royal Society of Chemistry and Copyright Clearance Center.

License Number	3916970427355
License date	Jul 27, 2016
Licensed Content Publisher	Royal Society of Chemistry
Licensed Content Publication	Journal of Materials Chemistry A
Licensed Content Title	A "H2O donating/methanol accepting" platform for preparation of highly selective Nafion-based proton exchange membranes
Licensed Content Author	Kai Feng,Beibei Tang,Peiyi Wu
Licensed Content Date	Aug 3, 2015
Licensed Content Volume Number	3
Licensed Content Issue Number	36
Type of Use	Thesis/Dissertation
Requestor type	academic/educational
Portion	figures/tables/images
Number of figures/tables/images	1
Format	print and electronic
Distribution quantity	2
Will you be translating?	no
Order reference number	
Title of the thesis/dissertation	Development of novel mesoporous proton exchange membranes for fuel cells
Expected completion date	Aug 2016
Estimated size	200
Requestor Location	JIN ZHANG 1 Turner Ave Technology Park Curtin University, Bentley Perth, WA 6102 Australia Attn: JIN ZHANG
Billing Type	Invoice
Billing Address	JIN ZHANG 1 Turner Ave Technology Park Curtin University, Bentley Perth, Australia 6102 Attn: JIN ZHANG
Total	0.00 AUD

Terms and Conditions

This License Agreement is between {Requestor Name} ("You") and The Royal Society of Chemistry

Copyrights for Figure 2.4

ELSEVIER LICENSE
TERMS AND CONDITIONS

Jul 27, 2016

This Agreement between JIN ZHANG ("You") and Elsevier ("Elsevier") consists of your license details and the terms and conditions provided by Elsevier and Copyright Clearance Center.

License Number	3916970698009
License date	Jul 27, 2016
Licensed Content Publisher	Elsevier
Licensed Content Publication	Journal of Power Sources
Licensed Content Title	High proton-conducting Nafion®/−SO3H functionalized mesoporous silica composite membranes
Licensed Content Author	Yu-Feng Lin,Chuan-Yu Yen,Chen-Chi M. Ma,Shu-Hang Liao,Chia-Hsun Lee,Yi-Hsiu Hsiao,Hong-Ping Lin
Licensed Content Date	27 September 2007
Licensed Content Volume Number	171
Licensed Content Issue Number	2
Licensed Content Pages	8
Start Page	388
End Page	395
Type of Use	reuse in a thesis/dissertation
Portion	figures/tables/illustrations
Number of figures/tables/illustrations	1
Format	both print and electronic
Are you the author of this Elsevier article?	No
Will you be translating?	No
Order reference number	
Original figure numbers	figure 6
Title of your thesis/dissertation	Development of novel mesoporous proton exchange membranes for fuel cells
Expected completion date	Aug 2016
Estimated size (number of pages)	200
Elsevier VAT number	GB 494 6272 12
Requestor Location	JIN ZHANG 1 Turner Ave Technology Park Curtin University, Bentley Perth, WA 6102 Australia Attn: JIN ZHANG
Total	0.00 AUD
Terms and Conditions	

Copyrights for Figure 2.5

ELSEVIER LICENSE
TERMS AND CONDITIONS

Jul 27, 2016

This Agreement between JIN ZHANG ("You") and Elsevier ("Elsevier") consists of your license details and the terms and conditions provided by Elsevier and Copyright Clearance Center.

License Number	3916970820227
License date	Jul 27, 2016
Licensed Content Publisher	Elsevier
Licensed Content Publication	Journal of Power Sources
Licensed Content Title	Proton-conducting electrolyte membranes based on organosiloxane network/sulfonated poly(ether ether ketone) interpenetrating polymer networks embedding sulfonated mesoporous benzene–silica
Licensed Content Author	Sung Yeon Han,Junghwa Park,Dukjoon Kim
Licensed Content Date	1 December 2013
Licensed Content Volume Number	243
Licensed Content Issue Number	n/a
Licensed Content Pages	9
Start Page	850
End Page	858
Type of Use	reuse in a thesis/dissertation
Intended publisher of new work	other
Portion	figures/tables/illustrations
Number of figures/tables/illustrations	1
Format	both print and electronic
Are you the author of this Elsevier article?	No
Will you be translating?	No
Order reference number	
Original figure numbers	fugure 10b
Title of your thesis/dissertation	Development of novel mesoporous proton exchange membranes for fuel cells
Expected completion date	Aug 2016
Estimated size (number of pages)	200
Elsevier VAT number	GB 494 6272 12
Requestor Location	JIN ZHANG 1 Turner Ave Technology Park Curtin University, Bentley Perth, WA 6102 Australia Attn: JIN ZHANG

Copyrights for Figure 2.7

PERMISSION/LICENSE IS GRANTED FOR YOUR ORDER AT NO CHARGE

This type of permission/license, instead of the standard Terms & Conditions, is sent to you because no fee is being charged for your order. Please note the following:

- Permission is granted for your request in both print and electronic formats, and translations.
- If figures and/or tables were requested, they may be adapted or used in part.
- Please print this page for your records and send a copy of it to your publisher/graduate school.
- Appropriate credit for the requested material should be given as follows: "Reprinted (adapted) with permission from (COMPLETE REFERENCE CITATION). Copyright (YEAR) American Chemical Society." Insert appropriate information in place of the capitalized words.
- One-time permission is granted only for the use specified in your request. No additional uses are granted (such as derivative works or other editions). For any other uses, please submit a new request.

If credit is given to another source for the material you requested, permission must be obtained from that source.

BACK CLOSE WINDOW

Copyrights for Figure 2.8

Copyright Clearance Center RightsLink®

Home | Account Info | Help | Live Chat

ACS Publications Most Trusted. Most Cited. Most Read.

Title: Enhancement of Proton Transport by High Densification of Sulfonic Acid Groups in Highly Ordered Mesoporous Silica

Author: Satoru Fujita, Akihiko Koiwai, Masaya Kawasumi, et al

Publication: Chemistry of Materials

Publisher: American Chemical Society

Date: May 1, 2013

Copyright © 2013, American Chemical Society

Logged in as: JIN ZHANG
Account #: 3000977716
LOGOUT

PERMISSION/LICENSE IS GRANTED FOR YOUR ORDER AT NO CHARGE

This type of permission/license, instead of the standard Terms & Conditions, is sent to you because no fee is being charged for your order. Please note the following:

- Permission is granted for your request in both print and electronic formats, and translations.
- If figures and/or tables were requested, they may be adapted or used in part.
- Please print this page for your records and send a copy of it to your publisher/graduate school.
- Appropriate credit for the requested material should be given as follows: "Reprinted (adapted) with permission from (COMPLETE REFERENCE CITATION). Copyright (YEAR) American Chemical Society." Insert appropriate information in place of the capitalized words.
- One-time permission is granted only for the use specified in your request. No additional uses are granted (such as derivative works or other editions). For any other uses, please submit a new request.

If credit is given to another source for the material you requested, permission must be obtained from that source.

BACK | CLOSE WINDOW

Copyright © 2016 Copyright Clearance Center, Inc. All Rights Reserved. Privacy statement. Terms and Conditions.
Comments? We would like to hear from you. E-mail us at customercare@copyright.com

Copyrights for Figure 2.9

ELSEVIER LICENSE
TERMS AND CONDITIONS

Jul 27, 2016

This Agreement between JIN ZHANG ("You") and Elsevier ("Elsevier") consists of your license details and the terms and conditions provided by Elsevier and Copyright Clearance Center.

License Number	3916971301660
License date	Jul 27, 2016
Licensed Content Publisher	Elsevier
Licensed Content Publication	Microporous and Mesoporous Materials
Licensed Content Title	Proton conductivity of imidazole functionalized ordered mesoporous silica: Influence of type of anchorage, chain length and humidity
Licensed Content Author	Roland Marschall,Monir Sharifi,Michael Wark
Licensed Content Date	1 July 2009
Licensed Content Volume Number	123
Licensed Content Issue Number	1-3
Licensed Content Pages	9
Start Page	21
End Page	29
Type of Use	reuse in a thesis/dissertation
Intended publisher of new work	other
Portion	figures/tables/illustrations
Number of figures/tables/illustrations	1
Format	both print and electronic
Are you the author of this Elsevier article?	No
Will you be translating?	No
Order reference number	
Original figure numbers	figure 3
Title of your thesis/dissertation	Development of novel mesoporous proton exchange membranes for fuel cells
Expected completion date	Aug 2016
Estimated size (number of pages)	200
Elsevier VAT number	GB 494 6272 12
Requestor Location	JIN ZHANG 1 Turner Ave Technology Park Curtin University, Bentley Perth, WA 6102 Australia Attn: JIN ZHANG
Total	0.00 AUD

Copyrights for Figure 2.10

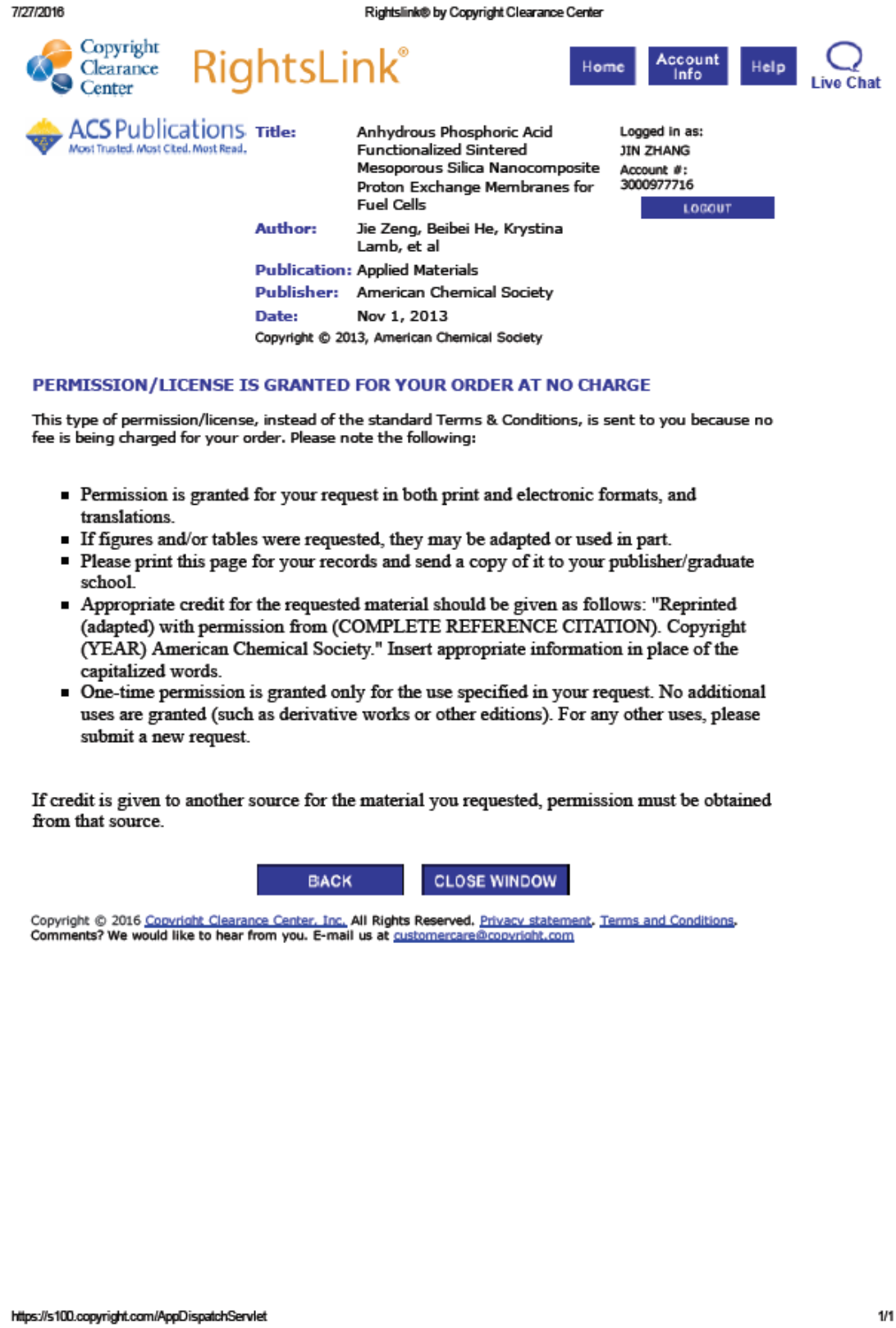

7/27/2016 Rightslink® by Copyright Clearance Center

Copyright Clearance Center RightsLink®

Home | Account Info | Help | Live Chat

ACS Publications Most Trusted. Most Cited. Most Read.

Title: Anhydrous Phosphoric Acid Functionalized Sintered Mesoporous Silica Nanocomposite Proton Exchange Membranes for Fuel Cells

Logged in as: JIN ZHANG
Account #: 3000977716
LOGOUT

Author: Jie Zeng, Beibei He, Krystina Lamb, et al

Publication: Applied Materials

Publisher: American Chemical Society

Date: Nov 1, 2013

Copyright © 2013, American Chemical Society

PERMISSION/LICENSE IS GRANTED FOR YOUR ORDER AT NO CHARGE

This type of permission/license, instead of the standard Terms & Conditions, is sent to you because no fee is being charged for your order. Please note the following:

- Permission is granted for your request in both print and electronic formats, and translations.
- If figures and/or tables were requested, they may be adapted or used in part.
- Please print this page for your records and send a copy of it to your publisher/graduate school.
- Appropriate credit for the requested material should be given as follows: "Reprinted (adapted) with permission from (COMPLETE REFERENCE CITATION). Copyright (YEAR) American Chemical Society." Insert appropriate information in place of the capitalized words.
- One-time permission is granted only for the use specified in your request. No additional uses are granted (such as derivative works or other editions). For any other uses, please submit a new request.

If credit is given to another source for the material you requested, permission must be obtained from that source.

BACK | CLOSE WINDOW

Copyright © 2016 Copyright Clearance Center, Inc. All Rights Reserved. Privacy statement. Terms and Conditions.
Comments? We would like to hear from you. E-mail us at customercare@copyright.com

https://s100.copyright.com/AppDispatchServlet 1/1

Copyrights for Figure 5.13

Title: Characterization of the Initial Stages of SBA-15 Synthesis by in Situ Time-Resolved Small-Angle X-ray Scattering

Author: Andrei Y. Khodakov, Vladimir L. Zholobenko, Marianne Impéror-Clerc, et al

Publication: The Journal of Physical Chemistry B

Publisher: American Chemical Society

Date: Dec 1, 2005

Copyright © 2005, American Chemical Society

Logged in as:
JIN ZHANG
Account #:
3000977716

LOGOUT

PERMISSION/LICENSE IS GRANTED FOR YOUR ORDER AT NO CHARGE

This type of permission/license, instead of the standard Terms & Conditions, is sent to you because no fee is being charged for your order. Please note the following:

- Permission is granted for your request in both print and electronic formats, and translations.
- If figures and/or tables were requested, they may be adapted or used in part.
- Please print this page for your records and send a copy of it to your publisher/graduate school.
- Appropriate credit for the requested material should be given as follows: "Reprinted (adapted) with permission from (COMPLETE REFERENCE CITATION). Copyright (YEAR) American Chemical Society." Insert appropriate information in place of the capitalized words.
- One-time permission is granted only for the use specified in your request. No additional uses are granted (such as derivative works or other editions). For any other uses, please submit a new request.

If credit is given to another source for the material you requested, permission must be obtained from that source.

BACK CLOSE WINDOW